SPECTRAL SAMPLING TECHNIQUES
FOR ATMOSPHERIC MODELING

VRIJE UNIVERSITEIT

SPECTRAL SAMPLING TECHNIQUES
FOR ATMOSPHERIC MODELING:
Modeling and Retrieval of Atmospheric Water Vapor

ACADEMISCH PROEFSCHRIFT

ter verkrijging van de graad van doctor aan
de Vrije Universiteit Amsterdam,
op gezag van de rector magnificus
prof.dr. T. Sminia,
in het openbaar te verdedigen
ten overstaan van de promotiecommissie
van de faculteit der Exacte Wetenschappen
op donderdag 31 oktober 2002 om 13.45 uur
in de aula van de universiteit,
De Boelelaan 1105

door

Rüdiger Lang

geboren te Schwäbisch Hall, Duitsland

promotoren: prof.dr. W.J. van der Zande
                prof.dr. W.M.G. Ubachs
copromotor: prof.dr. E.A.A. Aben

Für Mareike und
für meine Eltern, Anne und Ulrich.

Contents

Chapter 1

Introduction

1.1 Modeling of Water Vapor Absorption in the Atmosphere

1.1.1 Some Aspects of Atmospheric Modeling and the Role of Water Vapor in the Atmosphere

Modeling of the earth climate system is a difficult and complex task. The only tool that provides reasonable quantitative estimates of future developments of our climate system (*climate change*) are numerical models based on both observations and on our principal, analytical understanding of the energy balance of the earth system. This is because the complexity of the system prevents us from using simple extrapolations of statistical trends from the past or from using other empirical projection methods [*IPCC*, 2001]. It is important to keep in mind that useful projections of future climates by numerical modeling require simplified mathematical representation of the Earth climate system. All predictive methods make use of simplifications and model approaches. These approaches require, in turn, a good understanding of the fundamental physical, chemical and biological processes that govern the present climate system. In addition, the response of numerical climate models is very sensitive to a specific input scenario, i.e. accurate predictions of future changes depend on accurate measurements of the current state of the climate. Estimates of, for example, *feedback mechanisms* and regional detail can therefore only come from very elaborate climate models in conjunction with very accurate measurements outside and inside of the laboratory.

Many basic climate processes of importance are well-known and modeled exceedingly well [*IPCC*, 2001]. However, positive or negative feedback processes amplify or reduce, respectively, changes in the climate system in response to a perturbation. For example, such a perturbation is the continuous forcing of the *radiation balance* by a steady increase of *greenhouse gas* emissions like CO_2 in the atmosphere and the subsequent climate response in terms of temperature adjustment, which brings the atmosphere back to a new radiative equilibrium. Relatively independent atmospheric layers with respect to heat transport, like, for example, the troposphere (from the surface up to about 13 km) and the stratosphere (from 13 to about 50 km) possess different response times to perturbations in order to find their individual radiative equilibrium. Whereas the stratosphere finds such radiative equilibrium within a few months after applying a perturbation, this can take in the order of decades in the case of the troposphere (due to the large heat capacity of the oceans) [*van Dorland*, 1999]. Perturbations, causing temperature changes in the troposphere as a response, are best measured by the change in the net flux (*radiative forcing*) at the top of the troposphere, the tropopause. Radiative forcing measures are
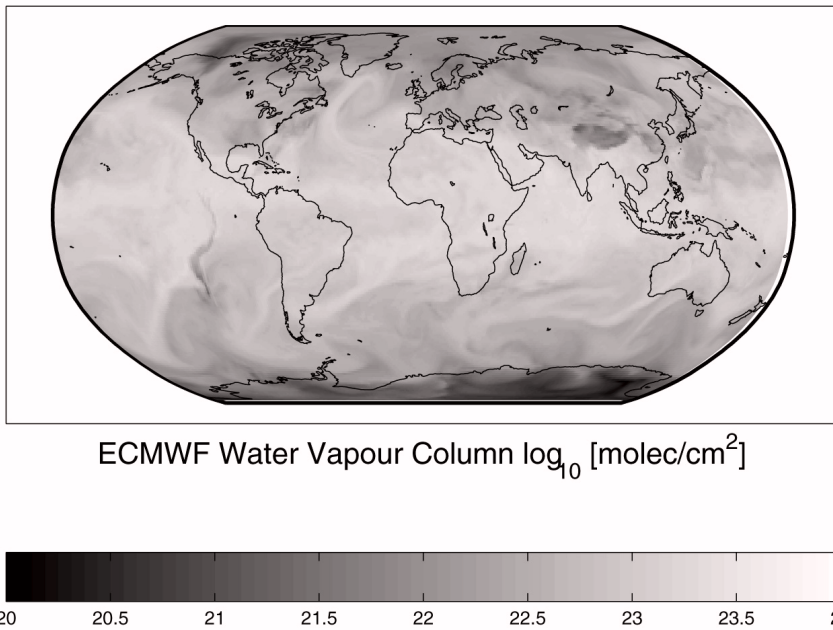
Figure 1.1: Global water vapor column density as given by European Center of Medium-Range Weather Forecast (ECMWF) on the 23rd of October, 1998, 18:00 UT. ECMWF data is based on meteorological data from various sources as, for example, from radiosonde data and satellite measurements.

frequently expressed in units of Watts per square meter. For example, doubling the CO_2 content will lead to an imbalance of about 4 Watts per square meter [*van Dorland*, 1999]. Such a perturbation is predicted by climate models to be followed by an increase in atmospheric water vapor due to the induced temperature change and the subsequent change of the water-holding capacity of the atmosphere. However, most parts of the atmosphere are not saturated, meaning that an increase in temperature does not necessarily mean that also water vapor, itself, must increase. Stable predictions with respect to this can only be made for the first 2 km in altitude (the boundary layer), where the water vapor content generally increases with increasing temperature. Above the boundary layer the situation is harder to quantify. Here, an enhancement in the water vapor content would cause more absorption of the terrestrial radiation and, therefore, affect the efficiency with which the Earth radiates to space. This result is called a *positive* radiative forcing effect or an enhancement of the *greenhouse effect*.

Due to its high abundance in the atmosphere, water vapor is the strongest greenhouse gas (about three times stronger than CO_2 in terms of the overall radiative forcing). Its abundance varies between roughly 10^{20} (3 mg) and more than 10^{23} (more than 3 g) molecules in a column above one square centimeter of the earth surface (WVC) depending on geolocation. The lowest WVC can be measured above the poles and the highest around the equatorial region (Figure 1.1). The water vapor density is rapidly decreasing with

altitude. Roughly 98% of the water vapor is situated below the 5 km altitude level (Figure 1.2). Here, water vapor is the third most abundant specie apart from oxygen and nitrogen. Therefore, the role of water vapor in feedback mechanisms triggered by perturbations of the climate system (as described for the case of CO_2) is very important, but can - because of its complexity - still not accurately be modeled in all its aspects. One large problem concerns the modeling of the radiative forcing of clouds. Cloud formation depends, of course, on the water vapor content of the atmosphere. If we consider the earth being a sphere, the irradiated solar flux (the radiation averaged over time, photon energy and solid angle) is about 340 Watts per square meter. From this amount about 50% is absorbed by the surface, 23% is reflected to the top of the atmosphere by clouds, 19% is absorbed in the atmosphere, and 8% is reflected in the atmosphere [*Andreae et al.*, 2002]. These numbers emphasize the importance of clouds for the radiation balance. The negative radiative forcing due to reflection of shortwave irradiation by clouds dominates the positive radiative forcing: the reflection of longwave radiation coming from the surface. On average, low and optically thick clouds predominantly reflect the light coming from the sun and have a cooling effect whereas high and optically thin clouds act effectively as a greenhouse gas and have a warming effect. So far, considering solely these two radiative forcing mechanisms, the net effect predicted by numerical models is a cooling of the surface temperature due to the presence of clouds by about 6 degrees [*van Dorland*, 1999]. In contrast, if water vapor, as an atmospheric greenhouse gas, would be removed from the atmosphere the global mean surface temperature would decrease by 20 degrees. Hence, the overall effect due to the presence of water vapor in the atmosphere for the described scenario is a warming of the surface temperature. However, clouds represent a significant source of potential error in such climate simulations, predominantly due to uncertainties in the precipitation process and difficulties in correctly simulating the diurnal cycle and precipitation amounts and frequencies [*IPCC*, 2001].

Due to these remaining uncertainties and, more in general, due to the important role of water vapor as a greenhouse gas in the described feedback mechanisms, as well as due to its role in the formation of clouds, the knowledge of the water vapor density distribution in the atmosphere is a crucial parameter for the understanding and modeling of climate forcing and climate change.

1.1.2 Measuring Atmospheric Water Vapor

Ground based, airborne and balloon radiosonde measurements are frequently performed to measure locally the amount of water vapor in the atmosphere. The most important measurement techniques are: (i) the *frost point* technique, which is already more than 50 years old but still in use, measuring the temperature difference between the surrounding air and a reflecting surface which is cooled to the point where the water vapor condenses on the surface. From both temperatures the relative humidity is calculated. (ii) the *Lyman α*-technique photolyses water vapor utilizing a Lyman-α light (121.6 nm) emitting lamp, to atomic hydrogen and an excited OH* radical, which subsequently emits light in the region around 300 nm of which the intensity is measured and related to the amount of water vapor molecules [*Kley & Stone*, 1978]. (iii) tunable *diode laser spectroscopy* measuring the amount of absorption of the laser light by water vapor at a specific wavelength [*Kessler et al.*, 1998]. (iv) *infrared* and *microwave radiometry*, the most important
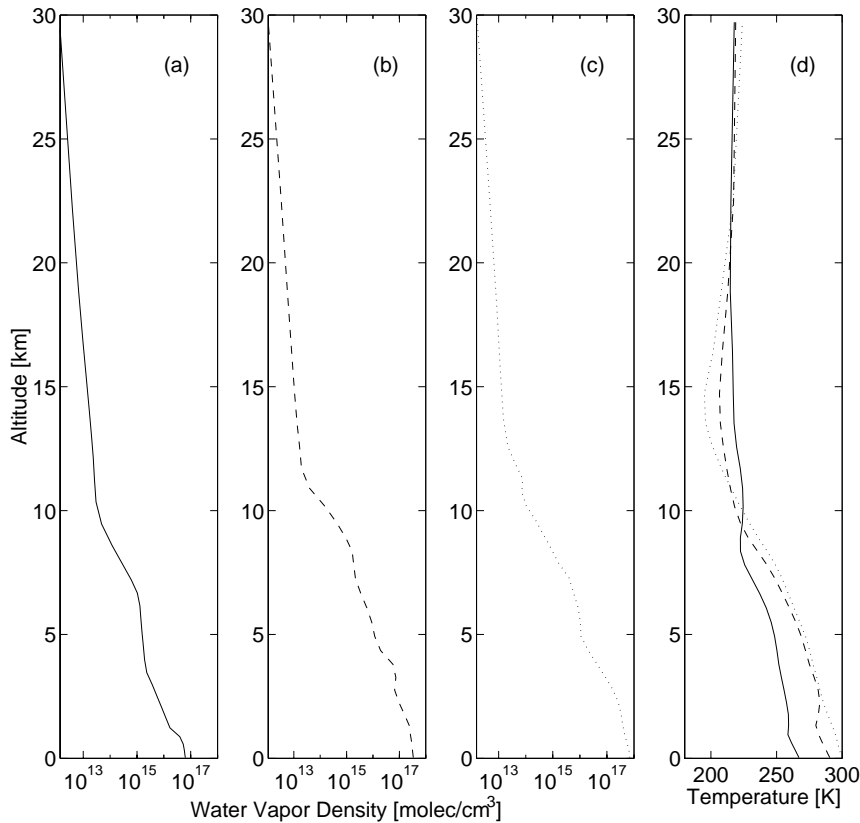
Figure 1.2: Water vapor density and temperature profiles as given by ECMWF. Panel (a) shows a profile for a low total WVC of $2.85 \times 10^{22} molec/cm^2$ over the northern part of the united states, panel (b) shows a medium total WVC of $7.21 \times 10^{22} molec/cm^2$ measured over the pacific at 21° south and panel (c) shows a high WVC of $1.34 \times 10^{23} molec/cm^2$ over the pacific close to the californian coast. The corresponding temperature profiles are shown in panel (d). The minima of those profiles denote the altitudes where the tropopause occurs, i.e. the end of the troposphere and the turbulent mixing of atmospheric gases. Above the tropopause, in the stratosphere, ECMWF WV-density values are fixed for all geolocations.

tools for satellite-based remote sensing of water vapor concentrations achieving global coverage. Non-satellite-based techniques have accuracies between 0.5 and 15%, whereas inter-comparison studies between satellite and ground based or airborne techniques reveal differences of up to 50% and more [*Vesperini et al.*, 1998; *Chaboureau et al.*, 1998]. The studies presented in this thesis focus on measurements of back-scattered solar radiation in the visible of such a satellite based remote sensing instrument introduced briefly in the following.

The Global Ozone Monitoring Experiment (GOME) is situated on board ESA's second Environmental Research Satellite platform (ERS-2), which was launched in April, 1995. The ERS-2 platform observes the earth atmosphere from a polar, sunsynchronous orbit at an altitude of 780 km. It's velocity with respect to the surface is 6.7 km/s. The equator is crossed in descending mode for each orbit at around 10:30 AM local time. Its scanning mirror allows a maximum scanning angle of $\pm 31^o$ with respect to nadir. A total scan over this angle is performed within 4.5 seconds for integration times of 1.5 seconds. The scanned surface areas are referred to as 'West', 'Nadir' and 'East' ground pixel covering an area of 320 by 40 km^2 each. After such a forward scan a backward scan is performed with an integration time of 1.5 seconds covering the whole swath width of 960 km.

The reflected light that enters GOME via the scan mirror and an input slit is split in four parts (channels) using prisms and a dichroic mirror. After the spectral decomposition of the light by gratings it is projected onto diode-arrays consisting of 1024 detector-pixels for each channel. The four channels cover a wavelength region between 240 and 790 nm with a spectral resolution of roughly 0.2 to 0.4 nm. For each orbit a direct sun measurement is performed where the light enters the instrument via an additional sun viewing mirror, a diffuser, and then enters the spectrometer through the same entrance slit as is used for the measurement of the reflected light. In this way the solar irradiance spectrum is obtained. GOME has an on-board wavelength calibration unit using a Pt-Cr-Ne lamp. Due to the construction of the optics of the instrument, GOME is sensitive to the polarization of the incoming light. In order to correct for this effect, three broadband Polarization Measurement Devices (PMDs) have been added measuring the polarization between 300–400, 400–600, and 600–800 nm. From the combined data absolute radiances and reflectivity (radiance divided by irradiance normalized with the cosine of the solar zenith angle (SZA)) spectra can be obtained. Figure 1.3 shows such a reflectivity measurement for the whole wavelength region covered by GOME. More details about the instrument can be found in the GOME Users manual [*ESA*, 1995].

The SCanning Imaging Absorption spectroMeter for Atmospheric CartograpHY (SCIA-MACHY) [*Bovensmann et al.*, 1999] launched on the 1st of March, 2002, on board of ESA's environmental satellite ENVISAT, is a similar type of instrument. It extends the spectral region to the near infrared up to 1750 nm while adding two additional channels in regions between 1.9 and 2.4 microns. It therefore covers absorption bands of a number of additional atmospheric species, when compared to the GOME instrument, which include a number of important near-infrared water vapor bands especially in the 1.9 and 2.4 micron region.

1.1.3   Water Vapor Spectroscopy

Water vapor absorption takes place predominantly over the first ten kilometer (Figure 1.2) where the temperature drops from about 300 K to a minimum of around 200 K. Light absorption by water vapor corresponds to excitations from a ro-vibrational state of the electronic ground state to a higher lying ro-vibrational state of the sane electronic ground state [*Learner et al.*, 2000]. The bands which are covered by the GOME and SCIAMACHY instrument are relatively weak, as we are concerned with transitions equal to several (3 to 10) vibrational quanta. Due to the moderate temperatures involved their rotational quantum numbers rarely exceed 15. In order to characterize a transition of
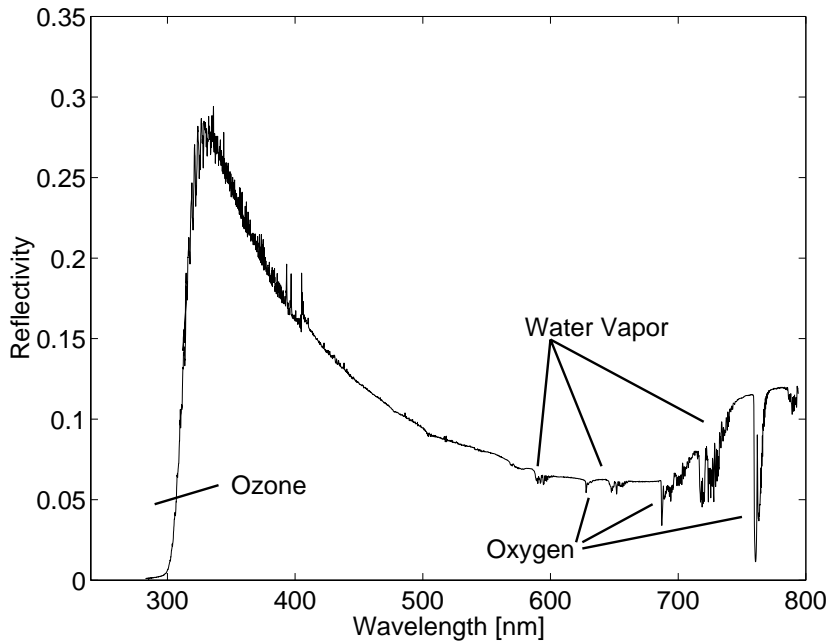
Figure 1.3: Clear sky GOME measurement at 30° latitude and -120° longitude over the Californian coast with a solar zenith angle (SZA) of 37°. One can identify the strong ozone absorption at wavelength shorter than 330 nm. Above this wavelength the decreasing reflectivity is due to Rayleigh- and Mie-scattering until about 700 nm where a sharply increasing ground surface reflectivity starts to significantly contribute to the total reflectivity. Water vapor absorption bands are situated and visible around 590, 640 and 720 nm. The oxygen γ, B and A band are visible around 630, 680 and 760 nm, respectively.

such a triatomic molecule, vibrational quantum numbers of three vibrational states for both the upper and lower states are needed. For example, absorptions around 500 nm are partly due to the $(4,2,1) \leftarrow (0,0,0)$ vibrational transition, where the numbering order corresponds to the symmetric stretch v_1, bend v_2, and asymmetric stretch v_3 quanta. In the region between 3 and 10 vibrational quanta from the ground state the two stretching modes happen to have similar transition energies which appear to be equal to roughly twice the value of the bend energy. Therefore, in this energy region, the absorption bands of water vapor appear as clumps of superimposed bands where all bands with the value of

$$v_1 + 2v_2 + v_3 \cong kv_1 \qquad (1.1)$$

involve transitions of similar energy. In this case, each absorption band can be labelled by k and is called a $k\nu$ polyad. In order to make it "as complicated as possible" [*Learner et al.*, 2000], the bands with odd v_2 are called the $k\nu + \delta$ polyads. Figure 1.4 shows all
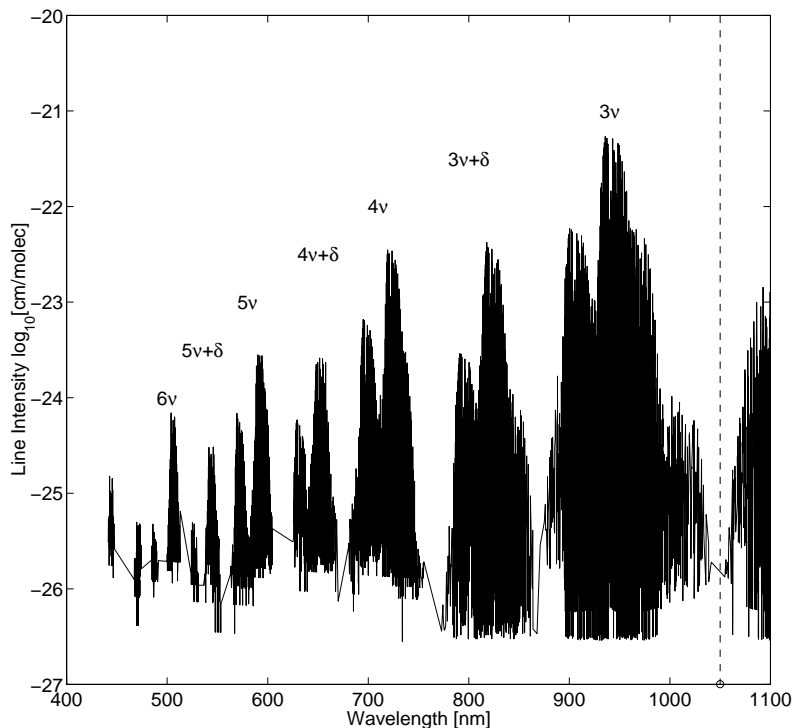
Figure 1.4: Water vapor absorption bands in the visible and near infrared region, for transitions with more than 3 vibrational quanta for the stretch vibrations from the ground state (0,0,0). For lower energies (dashed line) the bands are not clearly separated anymore and water vapor absorption lines can be found over the entire wavelength range. Line-intensities are taken from the HITRAN 96 database.

water vapor absorption bands for $k > 2$ and within the wavelength region accessible by the GOME and SCIAMACHY instrument. The line intensities are taken from the HIGH-resolution TRANSmission database, HITRAN, issued 1996 (later on referred to as HITRAN 96) [*Rothman et al.*, 1998], which is frequently used for modeling of atmospheric absorption and transmission spectra (for definition of line intensities see section 1.4 and appendix A).

For this thesis water vapor absorptions in the atmosphere by the 4ν, $4\nu + \delta$ and 5ν polyad around 720, 640 and 590 nm, respectively, are studied with a special focus on the weak 5ν polyad absorption band. The latter is similar in strength to the $4\nu + \delta$ polyad and about 5 times weaker than the 4ν polyad. All of these bands are measured by GOME resulting in significant absorption signatures for water vapor columns larger than 10^{20} molec/cm^2. Polyads for higher vibrational quanta are hardly visible in the GOME spectrum, even for high water vapor columns. Figure 1.5 shows the absorption signature of a GOME measurement of the 5ν polyad for a water vapor column of about 1.34×10^{23}
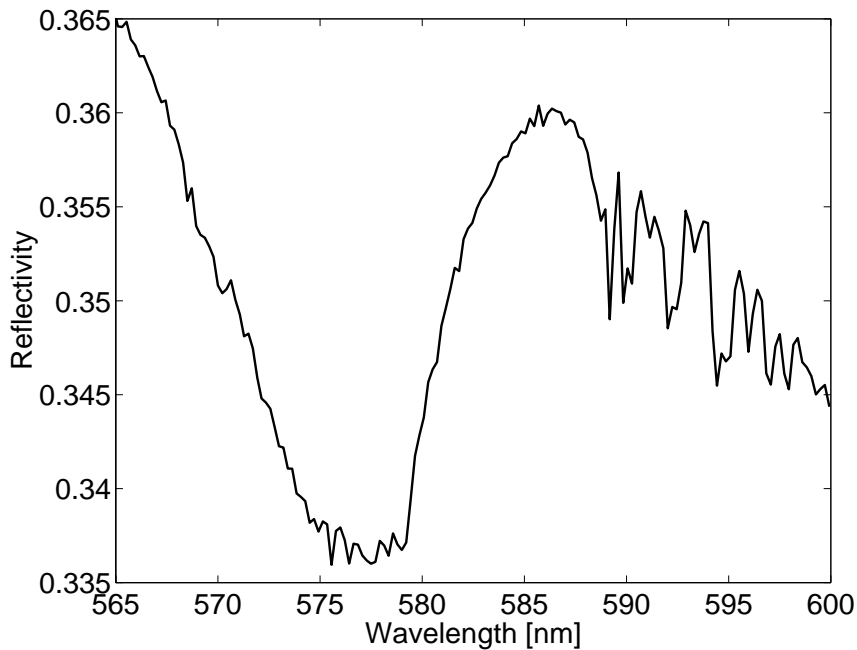
Figure 1.5: Reflectivity measured by GOME at $62°N$ for a relatively high solar zenith angle of $73°$. Additional absorbers contributing to the background signal are $(O_2)_2$ (540–690 nm), O_3 (Chappuis Band; 450–700 nm) and Sodium (590 nm). The stronger of the two broad $(O_2)_2$ absorption peaks in this region is clearly visible around 577 nm with part of the water vapor absorption band between 565 and 580 nm superimposed on it.

molec/cm^2 distributed over altitude as modeled by ECMWF and shown in panel (c) of Figure 1.2.

In order to perform a first rough estimate of the relative absorption strength of the three relevant water vapor absorptions seen by GOME, we may model their optical density utilizing a simple direct path approximation neglecting scattering. In this case we assume that the light is travelling from the top of the atmosphere (TOA) to the earth surface and back to the satellite. The increase of the path length due to the fact that the sun is not directly in the zenith and the removal of photons by absorption of the earth surface is also accounted for in order to obtain a realistic estimate. The result is shown in Figure 1.6. It is clearly visible from the upper panel that the absorption band around 590 nm and the absorption band around 640 nm are approximately equal in strength, whereas the band around 720 nm is about 5 times stronger as the former (upper panel). The lower panel includes a modeling of the redistribution of photon-energy by the entrance-slit and the optics of the detector (convolution). For this purpose, the instrumental slit function of GOME for detector channel 3 and 4 was applied. The shot noise level of the

GOME instrument detectors (counting the photons which passed through the optics of the instrument) around 3×10^{-4} [*ESA*, 1995] is also indicated in the lower panel by a dashed line. From the results it follows that photons are detected at all energies by the instrument detectors for all three absorption bands. Whereas individual absorption lines of water vapor of the 720 nm may easily be *saturated*, meaning only a fraction of down to 10^{-20} of the incident photons for specific wavelength reach the detector (which is way below the sensitivity of the detectors), all of the minima of the convolved lines are still detectable due to the redistribution of photon-energy by the optics of the instrument. This situation changes, for example, for the significantly stronger WV-bands in the IR region of the SCIAMACHY instrument. There, also part of the convolved spectrum is below the detectable limit.

1.2   Measuring Radiances

The extinction of light over a direct path ℓ and for a specific wavenumber ν can be written using Lambert-Beers law by

$$I(\nu) = I_0(\nu) \exp(-\sigma_{e,tot} n_{tot} \ell), \qquad (1.2)$$

where $\sigma_{e,tot}$ is the total extinction cross-section for all scatterers and absorbers with total density n_{tot}, I is the radiated and I_0 is the irradiated specific intensity in units of photons per wavenumber, surface, time and solid angle (see also Appendix A, Eq. A.1).

For this specific case of photons traversing over a direct path, only scattering out of the light path is considered to contribute to the total extinction, whereas scattering into the light path by single or multiple scattering is neglected. Radiative transfer processes in the lower and middle atmosphere are predominately un-coupled (defined as "frequency coherent" by *Fu & Liou*, [1992]) in wavenumber or energy, i.e. that no energy-redistribution and no significant energy-shifts occur during the photon transfer. The only exception to this are resonant scattering events, where the re-emission occurs at slightly different energies over a wide spectral region, like, for example, in rotational and vibrational Raman-scattering processes, which can play a weak but nevertheless significant role during the transfer process. Neglecting the latter processes as well as the convolution and spectral sampling by the optics of a measuring instrument the physically appropriate, principal parameter is wavenumber [*Fu & Liou*, 1992]. This means that the photon intensity at a specific point in the atmosphere may be calculated for each wavenumber or energy separately, using the same transport model. Such calculations of the photon intensity are called line-by-line (lbl) calculations.

Whereas the scattering cross-section σ_s for non-resonant scattering on molecules (Rayleigh scattering) varies smoothly with wavenumber the situation changes for photon energies close to the energy of a molecular transition (resonant case). There, both the scattering cross-section and the imaginary part of the refractive index (the absorption cross-section σ_a, which from now on will be referred to by simply σ) may vary significantly with respect to energy depending on the nature of the involved molecular transition and, more specifically, the lifetimes of the excited states. Non-resonant scattering events and absorptions, which are highly structured (strongly varying) with respect to energy, i. e. possessing long lifetimes of the excited states, are usually referred to as *nongray gaseous absorptions* and
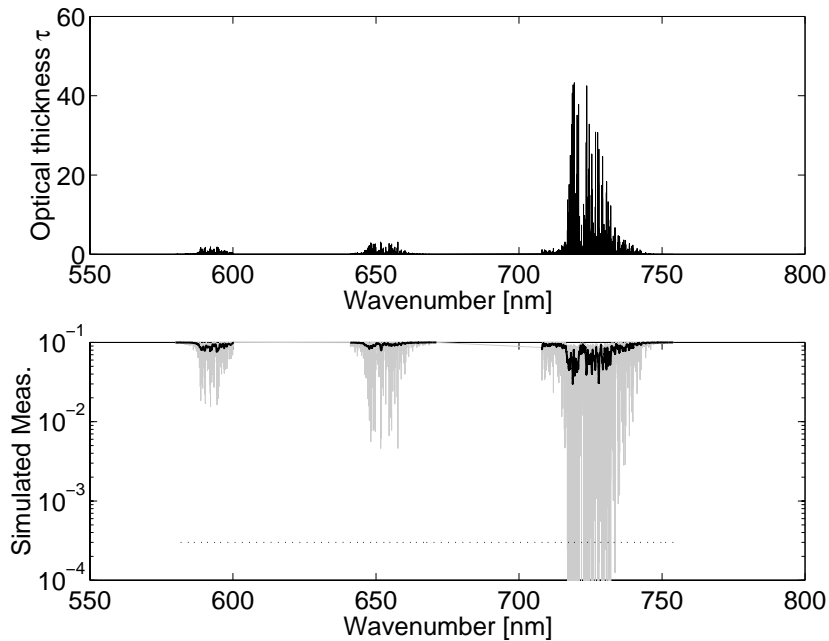
Figure 1.6: Optical thickness of the three water vapor absorption bands relevant for GOME (upper panel). For the calculation, the water vapour profile from panel (c) of Figure 1.2 with a total column of 1.34×10^{23} molec/cm^2 is used. The lower panel estimates the fraction of photons reaching the entrance slit of the satellite instrument in arbitrary units (gray spectrum) assuming a direct path from TOA to the surface, under an angle with respect to the zenith of 40°, and back to the instrument, under an angle of 0° (nadir viewing). It is also assumed that 90 % of the photons are removed by absorption at the earth surface. A convolution of this spectrum using the instrumental response function is shown by the black spectrum. Note the apparent absence of saturation in the final, black spectrum while individual lines can be heavily saturated (gray spectrum). The dashed line in the lower panel indicates the shot-noise level of the GOME instrument.

the spectral region where such absorption occur is, in the atmospheric context, called a *nongray atmosphere* [*Lacis & Oinas*, 1991]. For example, ro-vibrational overtone band transitions of low lying electronic bound states usually possess relatively long radiative lifetimes (as is, for example, the case for radiative lifetimes of the 5ν polyad transitions of water vapor around 17000 cm^{-1} which are on the order of minutes). Therefore, in the lower and middle atmosphere, these transitions are usually interrupted by collisions before they radiate. In contrast, highly pre-dissociative states (like in the case of O$_3$) result in very short lifetimes and, therefore, in broad spectral dependencies of the absorption cross-section. Also, collision complexes like (O$_2$)$_2$ give rise to broad absorption features corresponding to continuum states related to the O$_2$–O$_2$ interaction potential [*Naus &*

Ubachs, 1999]. (For a more detailed description of the quantities involved see appendix A.3.)

In order to represent the transmitted radiance numerically correct, the spectral, numerical representation of σ has to be performed on a sufficient fine grid in order to accurately model the variations of the nongray spectrum, i.e. the variation in photon intensity between each wavenumber grid point should be small enough to represent the real intensity by a lbl calculation. The non-linear exponential relationship between the extinction σ_e and the radiance (Eq. 1.2) increases the demand for an accurate spectral representation. The optical density τ, which is also frequently referred to as the *opacity*, is expressed as

$$\tau(\nu) = \int_s \sigma_{e,tot}(\nu, s) n_{tot}(s) ds, \tag{1.3}$$

where s describes an arbitrary photon path. However, measurements of radiances always possess a finite resolution in photon-energy and may very often not resolve the narrowest absorption features. For spectrally resolved measurements it holds that the optics of the instrument redistribute the photon-energy according to the width of the entrance slit and the principal spectral resolution of the dispersive components. In the case of spatially resolved spectral measurements, utilizing for example gratings as dispersive components, there is finally some spectral sampling by the discrete detector pixels involved counting photons within a specific spectral sampling interval.

The measured radiance for one specific spectral sampling interval $\Delta\nu'$ may then be written as

$$I_{\Delta\nu'} = \int_{\Delta\nu'} \int_{-\infty}^{\infty} I_0 \exp\left(-\tau(\nu)\right) \times \mathcal{H}(\nu - \nu^\star;\Sigma) d\nu^\star \frac{d\nu}{\Delta\nu'}, \tag{1.4}$$

where $\mathcal{H}(\nu - \nu^\star;\Sigma)$ is the spectral function representing the energy re-distribution by the entrance slit and the optics of the instrument with a Full-Width at Half-Maximum (FWHM) of Σ, $\tau(\nu)$ is the optical density and $\Delta\nu'$ is the spectral interval covered by the photon counting detector. Performing the convolution and the sampling integral in Eq. (1.4) may cost a significant amount of computational time depending on the number of numerical realization points needed to accurately represent τ within $\Delta\nu'$ in the sense of a monochromatic representation. For example, about 1000 realization points are needed to accurately resolve the absorption lines of water vapor monochromatically in the visible region around 17000 cm^{-1} over a region of 6 cm^{-1} and for pressures relevant for significant atmospheric water vapor absorption. Therefore, it is convenient to reduce the number of realization points before the convolution is performed by introducing a numerical sampling integral covering a spectral range which is sufficiently smaller than the FWHM of the instrumental function (satisfying the Nyquist criterium) but broad enough to efficiently reduce the amount of calculations needed for the convolution. In order to do so we write

$$I_{\Delta\nu'} = \int_{\Delta\nu'} \int_{-\infty}^{\infty} \int_{\Delta\nu} I_0 \exp\left(-\tau(\nu)\right) \frac{d\nu}{\Delta\nu} \times \mathcal{H}(\nu' - \nu^\star;\Sigma) d\nu^\star \frac{d\nu'}{\Delta\nu'}, \tag{1.5}$$

where $\Delta\nu$ is the numerical sampling interval reducing the resolution.

The exponent of the opacity is the basic function representing the absorption over a specific light path including paths traversed by multiple scattered photons. The benefit in

numerical efficiency by reducing the resolution of the exponential opacity therefore also affects the efficiency with which a full solution of the scalar equation of radiative transfer may be calculated (see chapter 2 and 3).

For the specific case of measuring a direct path transmittance T we may write,

$$T_{\Delta\nu'} = \frac{I}{I_0}\bigg]_{\Delta\nu'} = \int_{\Delta\nu'} \int_{-\infty}^{\infty} \int_{\Delta\nu} \exp\left(-\tau(\nu)\right) \frac{\mathrm{d}\nu}{\Delta\nu} \times \mathcal{H}(\nu' - \nu^\star;\Sigma)\mathrm{d}\nu^\star \frac{\mathrm{d}\nu'}{\Delta\nu'}. \qquad (1.6)$$

Here, we assume that I_0 is constant within $\Delta\nu'$. For the measurement of transmitted solar irradiation this is of course very often not true. The solar Fraunhofer lines cause structure in I_0. Fortunately, the integrated Fraunhofer line contribution to the total opacity within $\Delta\nu'$ is often much weaker than the terrestrial opacity contribution. Nevertheless, one has to judge carefully this assumption before utilizing Eq. (1.6) (see, for example, chapter 3, section 3.4.2).

In the following sections some standard techniques are introduced used to perform the integral over the exponent of the opacity efficiently. Band models, which were among the first techniques used for modeling stellar atmospheres in order to solve this sampling problem, are discussed first in the following section. After this, the frequently used *k-distribution* sampling technique is discussed in some detail. The Opacity Coefficient Method (OCM), proposed by *Maurellis*, [1998], discussed in detail in chapter 2 and used for forward modeling and retrieval purposes (chapter 3) in this thesis, is a new and original way in dealing with the opacity-sampling problem, even though some of its aspects are conceptually comparable with the k-distribution method. The Spectral Structure Parameterization (SSP), introduced in this thesis for the first time in detail (chapter 4) is utilized for forward modeling and retrieval purposes in chapter 5, deals also with an efficient solution of the spectral opacity sampling, but is conceptually more similar to a *band-model* approach which makes SSP significantly faster but less accurate than OCM.

1.3   Band Models

Already as early as 1936, Ambartzumian proposed the first idea of grouping spectral intervals according to absorption coefficient strength [*Ambartzumian*, 1936]. Later on, this basic idea for opacity-sampling methods turned out to be useful especially for applications to nongray atmospheres in combination with absorptions over nonhomogeneous paths where pressure, temperature and absorber amount change significantly over the path. Around the same time, band models became first successful for their ability to efficiently describe absorption of nongray atmospheres along homogenous paths [*Elsasser*, 1942; *Goody*, 1952] and, later on, also along nonhomogeneous paths where the difference in pressure and temperature is not that big [*Malkmus*, 1967].

The essence of band modeling is the introduction of averaged line parameters representing the individual parameters of the individual lines contained within a certain spectral window $[\nu_0, \nu_1]$ [*Lacis & Oinas*, 1991]. These average band parameters may be derived directly from the individual line parameters or by a fit to a lbl calculation of the transmittance. One representative example of such a band model is the Malkmus band model [*Malkmus*, 1967], where the transmission function is a two-parameter formula:

$$T(n) = \exp(-\pi \frac{B}{2}[(1 + \frac{4}{\pi} S n \pi B)^{\frac{1}{2}} - 1]), \tag{1.7}$$

where B is the effective line halfwidth, S is the effective line strength and n is the particle density. The parameters B and S are now in turn related to three statistical line parameters, s, b, and d, with the relation $B = b/d$ and $S = s/d$. Here s is the mean absorption line strength with

$$s = \frac{1}{N} \sum_i^N s_i, \tag{1.8}$$

and b is the mean absorption line width, with

$$b = \frac{4}{\pi s} \left[\frac{1}{N} \sum_i^N (s_i b_i)^{\frac{1}{2}} \right]^2. \tag{1.9}$$

The additional parameter d, the mean line spacing, is not related to the individual line parameters but to the total absorption band covered by $[\nu_0, \nu_1]$ and is given by

$$d = \Delta\nu/N, \tag{1.10}$$

where N is the total number of lines within $\Delta\nu = [\nu_0, \nu_1]$. The temperature and pressure dependence of these parameters may be explicitly taken into account through the line-intensity partition function, Boltzmann factors, and Voigt line shape parameters with

$$s_i = s_{i0} \frac{V_0 R_0}{V R} \exp\left[\frac{hc}{k_B} E'' \left[\frac{1}{T_0} - \frac{1}{T} \right] \right], \tag{1.11}$$

and

$$b_i = b_{i0} \frac{P}{P_0} \left[\frac{T}{T_0} \right]^{\tilde{n}}, \tag{1.12}$$

where k_B is the Boltzmann factor, h is Planck's constant, c the speed of light, E'' is the energy of the lower lying state and P_0 and T_0 are reference pressure and temperature, respectively. $\frac{V_0}{V}$ and $\frac{R_0}{R}$ are vibrational and rotational partition functions respectively. s_{i0} and b_{i0} are tabulated values of line strength and line intensity at the reference temperature and pressures and $\tilde{n}$ characterizes the temperature dependence of the line width parameter and must also be tabulated. For a direct calculation of s and d at specific pressures and temperatures the reference values may be taken from a line parameter database like HITRAN '96 [*Rothman et al.*, 1998] which provides this parameters explicitly (see also appendix A and section 1.4. For an example of the usage of band models for the calculation of averaged transmittances see also appendix C).

However, significant changes of temperature and pressure for nonhomogeneous paths cause problems for the specific form of the Malkmus band model (Eq. 1.7), which requires "randomly distributed, overlapping Lorentz lines" where the distribution function of all individual line strength s_i within $\Delta\nu$ must be "exponentially tailed" by s^{-1}. If this is not the case large errors in the transmittances can be expected. *Lacis & Oinas*, [1991], report
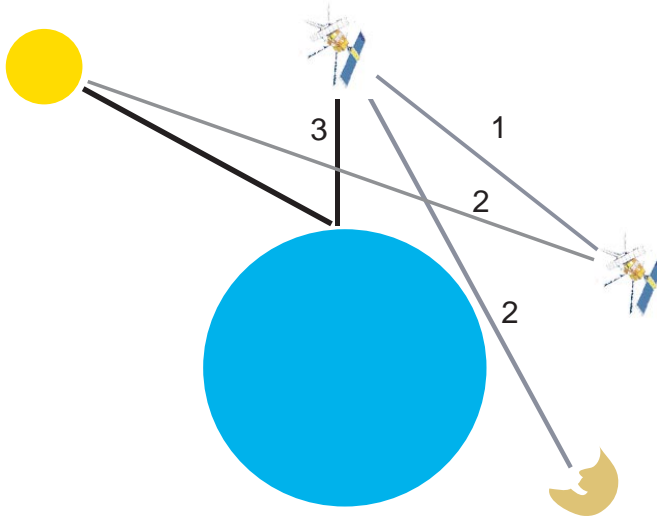
Figure 1.7: Schematic examples of three different measurement geometries. (1) Direct path measurement with active emitter and receiver on both ends of the path: towards homogeneous paths with low multiple-scattering contribution (GPS systems). (2) Moon/Sun occultation measurement: Nonhomogeneous paths but low multiple-scattering contribution (e.g. SCIAMACHY). (3) Nadir measurement geometry: highly nonhomogeneous paths and significant contribution of multiple scattering over different paths (e.g. GOME, SCIAMACHY).

errors up to 10 to 20% in the troposphere increasing with altitude from a direct calculation of S and B by equations (1.8) to (1.12). By utilizing a fitting optimization scheme to lbl calculations of transmittances they improve the accuracy of the band model to accuracies of, for example, 1% in the case of water vapor at 6.3 μm and low altitudes (T=296K). For high altitude cases, i.e. narrower absorption lines, accuracies decrease to around 6% in the case of CO at 240K. Other band models introduced by, for example, *Elsasser*, [1942], and *Goody*, [1989], also achieve good results for homogeneous path absorptions and may be optimized by fitting to monochromatically calculated transmittances for nonhomogeneous paths. Similar conclusions hold for the SSP band model introduced in this thesis. In this case a two parameter scheme of weighted opacity functions is introduced where the two averaged line parameters are directly related to the mean width and strength of the individual absorption lines within a spectral window $\Delta\nu$. Both direct calculations and optimizations to lbl calculations of transmittances of the two parameters are possible. The calculated parameter scheme results in accuracies of better then 2% in transmittance in the case of water vapor absorption in the visible around 590 nm and includes single-scattering photon contributions (chapter 4 + 5).

Measurement geometries, where the total amount of measured photons travel through a homogeneous atmosphere rarely exist. Occultation measurements (e.g. moon occultation measurements are performed by SCIAMACHY and star occultation measurements are performed by GOMOS both on ENVISAT) as well as specific limb geometries, with

emitter and receiver on different ends of the path (e.g. GPS measurements with satellite based emitter and receiver; Limb measurements are performed by SCIAMACHY on ENVISAT) may come closest to the ideal case of a homogeneous atmospheric path (Figure 1.7). For example, for occultation measurements sensing the troposphere the photons travel for the majority of the path length with significant absorption parallel to the pressure surfaces. Nadir measurements in the visible (GOME, SCIAMACHY) and the near infra-red (SCIAMACHY), however, always have to deal with photons travelling via different light paths and through different parts of the atmosphere, where pressure, temperature and absorber amounts may change over orders of magnitudes. Especially in the UV and visible, the multiple-scattering component to the total measured photon amount is not negligible due to the ν^p dependence of the scattering coefficient, where p ranges between 1 for large particles (Mie scattering) and 4 for molecules (Rayleigh scattering).

1.4   Nonhomogeneous Light Paths

Apart from the optimization of band-model parameters by fitting to lbl calculations of transmittances other optimization schemes are introduced to account for significant changes in pressure and temperature over nonhomogeneous paths. The first attempts to account for absorption over nonhomogeneous paths was an "one-parameter" scaling, introduced by e.g. *Howard et al.*, [1956], *Manabe & Moller*, [1961], *Yamamoto et al.*, [1962]. This scaling adds an additional effective pressure scaling to a simple extrapolation of the optical thickness measured in the laboratory to atmospheric pressure situations. This additional scaling of the absorber amount with pressure, however, turns out to be adequate only over limited absorber and pressure ranges.

One other suggestion was the replacement of the nonhomogeneous path by an equivalent homogeneous path which gives good results in the weak and strong line absorption limits [*Goody & Yung*, 1989]. This "two-parameter" scaling originally introduced by *van de Hulst*, [1945], yields higher accuracy than the one-parameter scaling. It is usually referred to as the Curtis-Godson method [*Curtis*, 1952; *Godson*, 1953] and is frequently used in atmospheric radiative transfer calculations [*Goody & Yung*, 1989]. The principle of the method is based on the replacement of an equivalent (or averaged) width of an absorption line through a nonhomogeneous path by an equivalent width through a corresponding homogeneous path. This involves the definition of an equivalent average halfwidth and line intensity (two-parameter scaling) for the path extending from the observer to some point, X, in the path and weighted by the length of the path between observer and X. The changes in the averaged absorption width for different homogeneous paths can then be formulated in closed analytical form [*Lindquist & Simmons*, 1972]. Consequently, measurements of the equivalent width and line-intensity parameter in the laboratory for different homogeneous paths may then be used together with the Curtis-Godson approximation to calculate their corresponding atmospheric values for the nonhomogeneous situation. Together with some improvements introduced by *Armstrong*, [1968], *Yamamoto et al.*, [1972], *Lindquist and Simmons*, [1972], and *Young*, [1975], the Curtis-Godson method is considered to produce reliable results not only in the weak and strong line absorption limits. However, two parameter scaling methods fail in cases of inverse pressure-gas-concentration distribution as is the case, for example, for ozone. They

also fail for all scattering situations where individual photons traverse over different paths [*Lacis & Oinas*, 1991].

Absorptions by nongray and vertically nonhomogeneous atmospheres are therefore best calculated monochromatically utilizing a full solution of the equation of radiative transfer including all forms of scattering. The basic physics of pressure and temperature broadening is sufficiently well understood that altitudes dependent cross-section values might be calculated by utilizing a convolution between a Lorentz and a Gauss line profile (Voigt profile) [*Armstrong*, 1967]. For a normalized Voigt profile $\Upsilon(p,T)$ the principal parameters are the HWHM of the line-transition with $\gamma(p,T)$ and a Doppler halfwidth with

$$\Delta\nu_D = \nu_0 \sqrt{\frac{2k_B T}{M}}, \tag{1.13}$$

where ν_0 is the center line position in wavenumbers and M is the mass of the absorbing gas molecule. For a calculation of the absorption cross-section by

$$\sigma(\nu; p, T) = S(T)\Upsilon(\nu; p, T) \tag{1.14}$$

the line-intensity parameter S at a reference temperature, the line-broadening parameters (HWHM) at reference temperature and reference pressure and the temperature scaling parameter $\tilde{n}$ for a scaling of the transition rate with $(T/T_0)^{\tilde{n}}$ (Eq. 1.12) have to be taken from a line parameter database. For a calculation of the line intensity S at a specific temperature T partition functions are calculated according to Eq. A.40 and A.43 in appendix A. (For a detailed description of line parameters and their relation to fundamental quantities of the theory of quantum electrodynamics, as well as how they are used and defined in the HITRAN 96 database, see appendix A.)

Monochromatic (lbl) high resolution calculations of pressure and temperature dependent cross-sections used in Eq. 1.3 and including all individual absorption lines with

$$\sigma(\nu; p, T) = \sum_i^N \sigma_i(\nu; p, T) \tag{1.15}$$

provide a reliable and accurate standard for comparison with other approximate methods over nonhomogeneous paths. However, as pointed out in section 1.2, monochromatic integrations of the radiance (Eq. 1.4) together with monochromatic (lbl) calculations of cross-sections (Eq. 1.15) need a significant amount of computational time. They might be useful for accurate one-time calculations of transmittances but they are unpractical or impossible to handle for inverse modeling, i.e. for the retrieval of atmospheric gas concentrations.

The use of band model for an efficient solution of Eq. 1.4 in the case of homogeneous direct path absorptions has already been discussed. The well known k-distribution method as well as the opacity coefficient method (OCM) described in this thesis in full detail provide a computationally efficient procedure for computing average opacities (Eq. 1.5) in vertically nonhomogeneous, multiple-scattering atmospheres. In the following section a more general introduction on the principles of the k-distribution method will be given. A detailed description of the theoretical aspects of OCM can be found in the following chapter together with a comparison of both methods.

1.5 The k-distribution Method

In the case of nongray atmospheres the cross-section k (from here on the previously used symbol σ is used) has a highly repetitive character as a function of wavenumber. Because the solution of the scalar equation of radiative transfer is frequency coherent with wavenumber (see section 1.2) there is no need to perform two calculations for two different wavenumbers ν_{k1} and ν_{k2} with corresponding cross-section σ_{k1} and σ_{k2}, lying within a cross-section bin $\Delta\sigma_j$ with mean value ξ_j within which the differences for the calculated transmittance is negligible small. In order to make advantage of the latter, we start off with a realization of the cross-section of a specific absorber (Eq. 1.15) on a sufficient resolution $(\sigma(\nu) \rightarrow \sigma_k(\nu_k))$ to resolve all individual absorption lines. Then we define a number of bins ξ_j covering the whole cross-section range and satisfying the above made assumption. Now a calculation of the corresponding transmittances T_{ξ_j} for individual cross-section bins ξ_j may be performed which are, when properly weighted, directly related to the total transmittance $T_{\Delta\nu}$ within the selected interval $\Delta\nu = [\nu_0, \nu_1]$. Depending on the structure of the cross-section within the selected interval and the number of occurrences of individual σ_k's within a specific cross-section bin, this may reduce the amount of calculations significantly with respect to a lbl calculation.

After having performed the remaining transfer calculations for the T_{ξ_j} within $[\nu_0, \nu_1]$ there are two ways to proceed. The first possibility is to reassign the specific transmittance T_{ξ_j} to all ν_k with $\sigma_k(\nu_k) \in \Delta\sigma_j$. This reveals a reconstruction of T in the original wavenumber resolution of σ_k. The other possibility, on which we will focus here, is to count the number of occurrences of $\sigma_k(\nu_k) \in \Delta\sigma_j$ within $[\nu_0, \nu_1]$. The latter result in a discretized density distribution function $f(\xi_j)$ which gives weight to the relative importance of the transmittance T_{ξ_j}. Upon normalizing $f(\xi_j)$ we may write for the average transmittance over $[\nu_0, \nu_1]$:

$$T_{\Delta\nu} = \sum_{j}^{M} f(\xi_j) e^{-\xi_j N} \Delta\sigma_j \qquad (1.16)$$

where M is the number of subintervals $\Delta\sigma_j$ and N is the layer- (or subcolumn) density of a finite homogeneous atmospheric layer. Using this transformation, the numerical sampling integral over the high-resolution opacity function in Eq. 1.5 is replaced by a sum over M weighted opacity functions.

As mentioned before, the basic idea of grouping absorption coefficients by strength within specific spectral intervals is not new [*Ambartzumian*, 1936]. The same principle has been applied to radiative problems in the terrestrial atmosphere by *Yamamoto et al.*, [1970], *Arking & Grossman*, [1972], *Lacis & Hansen*, [1974], *Chou & Arking*, [1980] and *Wang & Shi*, [1988]. For example, *Lacis & Hansen*, [1974], use empirical band-models with a pressure and temperature scaling correction, similar to the *Curtis-Godson* approximation, for modeling the radiative transfer in clear sky situations. But they use a probability distribution parameterization similar to Eq. 1.16 for the calculation of the transmittance over a large spectral region between 200 nm and 3.2 μm in the case of cloudy skies. There, they use $M = 8$ subintervals to characterize $f(\xi_j)$. *Arking & Grossman*, [1972], also calculate the average transmittance like in Eq. 1.16, but, in contrast to *Lacis & Hansen*, for homogeneous planetary atmospheres. They study the influence of

overlapping and non-overlapping lines, as well as the influence of specific line shapes and their changes due to changes in temperature with analytical derivations of the normalized discrete probability distribution functions $f(\xi_j)$. Finally, *Wang & Shi*, [1988], use Eq. 1.16 to calculate the total band absorption (1-T) for various atmospheric absorbers like CO_2, H_2O and O_3, but for homogeneous atmospheres. They state that this formulation has problems in dealing with inhomogenous atmospheres and overlapping absorptions of different bands and different absorbers. They use $M = 5$ subintervals to characterize $f(\xi_j)$ and use average line parameters for each band (cf. section 1.3) in order to evaluate $f(\sigma_k)$ before the discretization.

Until the end of the eighties, the use of band models was the generally accepted approach usually together with the Curtis-Godson approximation (section 1.3) for modeling nonhomogeneous paths [*Goody et al.*, 1989]. Then, the publications of *Wang & Shi*, [1988], *Goody et al.*, [1989], and *Lacis & Oinas*, [1991], for the use of the k-distribution and correlated k-distribution for calculations in nonhomogeneous and multiple-scattering atmospheres brought wider attention to the usage of probability density functions as in Eq. 1.16. Today, the correlated-k-distribution method (*ck*-method) generally replaces the usage of band models or is used in combination with the latter. Its accuracy becomes now compatible with those of lbl calculations. Numerous authors have been using correlated k-distribution methods since the beginning of the nineties, especially for fast forward or inverse modeling of remote sensing data (see *Kato et al.*, [1999]; *Buchwitz et al.*, [2000a], and references therein). Since the publications by *Goody et al.*, [1989], and *Lacis & Oinas*, [1991], various theoretical discussions or improvements of the *ck*-method have been proposed, for example, by *Fu & Liou*, [1992], *Bennartz & Fischer*, [1999], and *Buchwitz et al.*, [2000], concerning predominantly the correlation assumption needed for performing integrations over nonhomogeneous paths and/or for multiple absorbers (see section 1.5.3).

In general, the summation over the quadrature weights $\Delta\sigma_j$ and the distribution function $f(\xi_j)$ in Eq. (1.16) is called the discretized cumulative density distribution function with

$$g_m = \sum_j^m f(\xi_j)\Delta\sigma_j, \tag{1.17}$$

which can be inverted due to its strictly monotonic character,

$$\xi_j(g) = g^{-1}(\xi_j) \tag{1.18}$$

This inverse discretized cumulative density distribution is supposed to be free of strong variations in contrast to $\sigma_k(\nu_k)$ or $f(\xi_j)$, and it may therefore be handled very easily (see also concluding remarks to this introduction). Using Eq. (1.17) and (1.18) we write Eq. (1.16) as,

$$T = \sum_j^M e^{-\xi_j(g)N}\Delta g_j, \tag{1.19}$$

and $\Delta g_j = f(\xi_j)\Delta\sigma_j$. In the limit to small intervals Δg_j and $\Delta\sigma_j$, Eq. (1.19) becomes generalized to
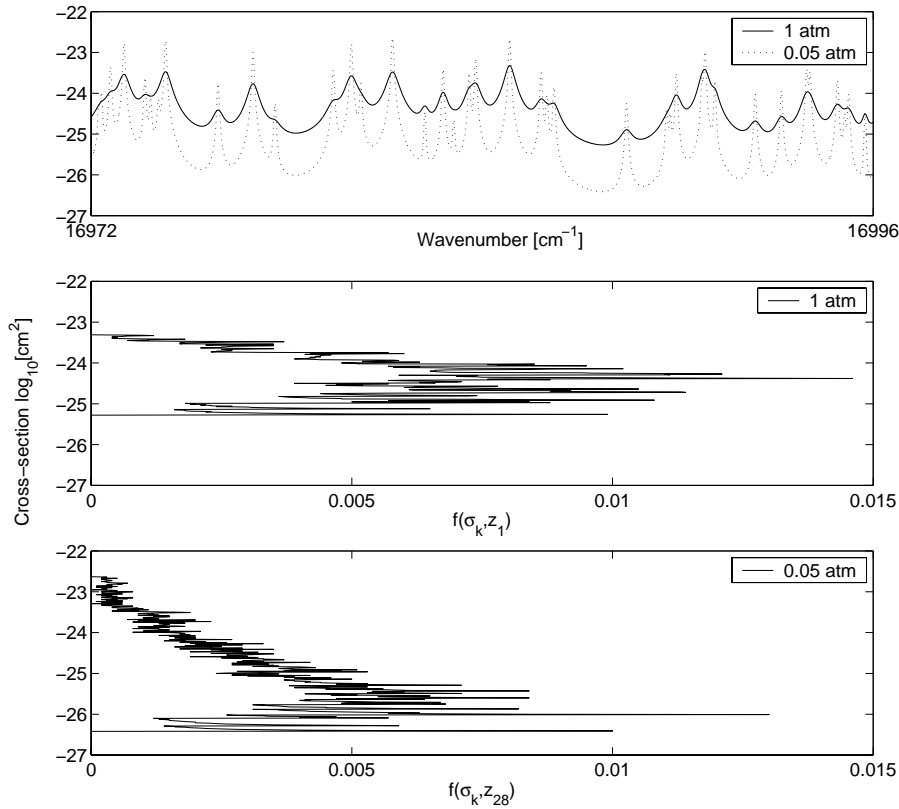
Figure 1.8: Cross-sections and discretized cross-section probability density functions using Eq. (1.22). The upper panel shows two cross-sections of water vapor in the visible for atmospheric altitude levels with a pressure of 1 (solid line) and 0.05 atm (dotted line). The mid and the lower panel show dpdf for each of the cross-sections in the upper panel.

$$T = \int_0^1 e^{-\sigma(g)N} dg, \tag{1.20}$$

and Eq. (1.16) becomes

$$T = \int_0^\infty f(\sigma) e^{-\sigma N} d\sigma. \tag{1.21}$$

The method of calculating spectral-mean transmittances based on Eq. 1.20 (or Eq. 1.19 in the discretized form) is what one refers to as k-distribution method [*Fu & Liou*, 1992].

1.5.1   Use of k-density Distribution Functions

For both, the k-distribution and the OCM method described in detail in this thesis, the nature and representation of the distribution function $f(\sigma)$ is of vital importance. In its discretized form $f(\xi_j)$ can be seen as a histogram function (discretized probability density function: dpdf). I adopt the formulation of *Lacis & Oinas*, [1991], by writing the dpdf as

$$f(\xi_j) = \frac{1}{\nu_1 - \nu_0} \sum_m^N \left| \frac{\Delta \nu_m}{\Delta \sigma_j} \right| W(\sigma_j, \sigma_j + \Delta \sigma_j), \qquad (1.22)$$

where $W(\sigma_j, \sigma_j + \Delta \sigma_j)$ is a window function, which is zero everywhere except in the interval $[\sigma_j, \sigma_j + \Delta \sigma_j]$. The latter σ_j's can be found in N subintervals $\Delta \nu_m$. Hence, the cumulative density intervals $\Delta g_j = f(\xi_j) \Delta \sigma_j$ define the fraction of the interval $[\nu_0, \nu_1]$ for which the cross-section σ_k is within σ_j and $\sigma_j + \Delta \sigma_j$ (see also chapter 2, section 2.2.2 and appendix B). By this we established the before mentioned relationship between cross-sections found in a specific cross-section bin ξ_j and their position in wavenumber space. The total function is normalized in the specific wavenumber interval $[\nu_0, \nu_1]$ within which we count the cross-sections.

The form of the distribution $f(\xi_j)$ (Eq. 1.22) does not change for a transformation $f(\xi_j) \rightarrow f(h(\xi_j))$ introducing just a different scaling of the abscissa providing h is a monotonic function. In other words, counting cross-sections, optical densities or the exponent of optical densities (transmittances), does not change the values of $f(\xi_j)$ (see also chapter 2, section 2.2.2). In addition, the mapping between the latter quantities and the subintervals $\Delta \nu_m$ does not change from quantity to quantity. This histogram property will be used later on for the determination of the opacity coefficients used for OCM (chapter 2).

Other characteristics of the histogram spectrum are its spikes, which reflect local maxima and minima within $[\nu_0, \nu_1]$ (Figure 1.8). These structures evolve from small $\Delta \sigma_j$ which are associated with large subintervals $\Delta \nu_m$. The amplitude of these spikes is dependent on the resolution of the monochromatic spectrum with subintervals $\delta \nu_k$ and binned utilizing the cross-section bins $\Delta \sigma_j$. As mentioned before and in the case of the k-distribution method, the transformation from the histogram to a cumulative density histogram is made exactly because of this structures. From this we get a general transformation $f(\nu) \rightarrow f(g)$, which is often referred to as a "pseudo-absorption" line profile, which has the same nongray transmission properties as the original absorption coefficient spectrum [*Lacis & Oinas*, 1991].

1.5.2   Construction of Quadrature Points and "Pseudo-Absorption" Functions

For nonhomogeneous atmospheres different altitudes traversed by the light give rise to different histogram functions. This means that for modeling transmittances over nonhomogeneous paths the histogram functions becomes explicitly pressure and temperature dependent (and also dependent on the absorber amount in the case of, for example, sampling absorption coefficients instead of cross-sections). From this it follows that at different altitudes z we find different $\sigma(g)$ functions (Figure 1.9).
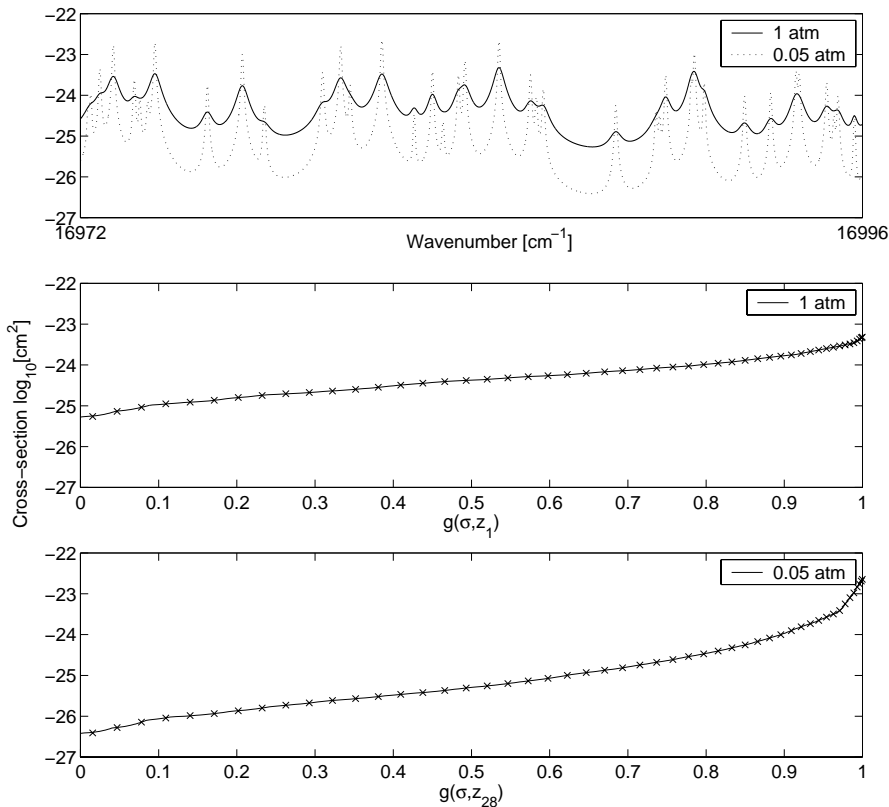
Figure 1.9: Cross-sections and cumulative probability density functions. The upper panel shows two cross-sections of water vapor in the visible for atmospheric altitude levels with a pressure of 1 (solid line) and 0.05 atm (dotted line). The mid and the lower panel show cumulative probability density functions for each of the cross-sections in the upper panel. Both panels also show the discrete $\xi_j(g)$ at 50 quadrature weight positions Δg_j (Figure 1.10)

There are different ways to find $\sigma(g, z)$ functions. *Lacis & Oinas*, [1991], derive an analytical expression for $g(\sigma)$ utilizing the Malkmus band model (section 1.3; appendix C). In this case $g(\sigma)$ becomes a function of the band-model parameters s, p, d derived and optimized by fitting to lbl results at different altitudes. The last step then is a numerical inversion of $g(\sigma)$ in order to receive the required $\sigma(g)$ and a discretization using an appropriate amount of quadrature weights Δg_j to receive $\xi_j(g)$ (Figure 1.9).

There are other possibilities to receive the discretized Δg_j's and $\xi_j(g)$'s directly. *Lacis & Hansen*, [1974], or *Wiscombe & Evans*, [1977], use an exponential sum fitting technique (ESFT) of some, in principle, arbitrary parameters $\xi_j(g)$ and Δg_j to monochromatic (lbl) realizations of the transmittance. After the fitting, $\xi_j(g)$ and Δg_j have similar meaning than the $\xi_j(g)$ functions and weights Δg_j used for the k-distribution method. But, increasing the number of terms M in Eq. (1.19) is much easier for k-distribution methods than

increasing the number of fitting parameters in the case of ESFT [*Kato et al.*, 1999]. *Buchwitz et al.*, [2000], combine both techniques by keeping the quadrature points Δg_j fixed for each altitude (see following section) and fitting $\xi_j(g)$ to monochromatic realizations of the transmittance.

The discretization of the k-distribution method, i.e. going from Eq. (1.20) with smooth $\sigma(g)$ to Eq. (1.19) with discrete $\xi_j(g)$ and quadrature weights Δg_j, has to be addressed by all users of the k-distribution or ESFT methods. It can be performed in different ways. In the case of ESFT the number of fitting parameters simply determines the degree of discretization. *Lacis & Oinas*, [1991], give an analytical relationship between the mean $\xi_j(g)$, the quadrature weights Δg_j and the subintervals $\Delta\sigma_j$ for the dpdfs. This analytical relationship is, in principle, dependent on the absorber amount. However, for large amounts of subintervals Δg_j this dependency becomes weaker. An alternative concept is to use a Gauss-Legendre-Quadrature scheme in order to discretize the integral in Eq. (1.20). In this case Δg_j are the Gauss-Legendre-Quadrature weights [*Press et al.*, 1992] which are given analytically using Legendre Polynomials of degree k, whereas the mean $\xi_j(g)$ are interpolates from $\sigma(g)$ at the zero-point values $x_0 = \Delta g_j$ of the Legendre polynomials.

For all of the latter discretizations it is important that the density of Δg_j subintervals increases with $g \to 1$, as is the case for a Gauss-Legendre quadrature (Figure 1.10), because the steepness of g continuously increases towards 1 (Figure 1.9), especially for low pressure cases, saturation effects [*Lacis & Oinas*, 1991] or non-highly repetitive σ-distributions (for example in cases of small wavenumber intervals $[\nu_0, \nu_1]$; see chapter 2).

1.5.3 The Correlation Problem

Having pre-calculated different $\xi_j(g)$ at different altitudes z, i.e. for different pressures and temperatures, the k-distribution equation can then be re-written for nonhomogeneous paths to

$$T = \sum_j^M e^{-\sum_\ell^L \xi(g,z_\ell)N(z_\ell)}\Delta g_j, \qquad (1.23)$$

where ℓ are L homogeneous altitude layers with subcolumn density $N(z_\ell)$. This assumes that only one g exists for a specific ν at different heights z. This assumption is known as the so-called *correlation assumption* [*Fu & Liou*, 1992] and, as mentioned before, Eq. (1.23) is called the correlated k-distribution, applied to a nonhomogeneous atmosphere. *Fu et al.*, [1992], showed that in order to make this assumption hold, there are two relations required to be satisfied:

$$\sigma(\nu_j,p,T) = \sigma(\nu_i,p,T) \;\; \text{if} \;\; \sigma_{\mathrm{r}}(\nu_{\mathrm{j}}) = \sigma_{\mathrm{r}}(\nu_{\mathrm{i}}), \qquad (1.24)$$

where σ_r is a reference cross-section at a reference pressure and temperature, p_r and T_r, respectively. The second relation is

$$\sigma(\nu_j,p,T) > \sigma(\nu_i,p,T) \;\; \text{if} \;\; \sigma_{\mathrm{r}}(\nu_{\mathrm{j}}) > \sigma_{\mathrm{r}}(\nu_{\mathrm{i}}). \qquad (1.25)$$
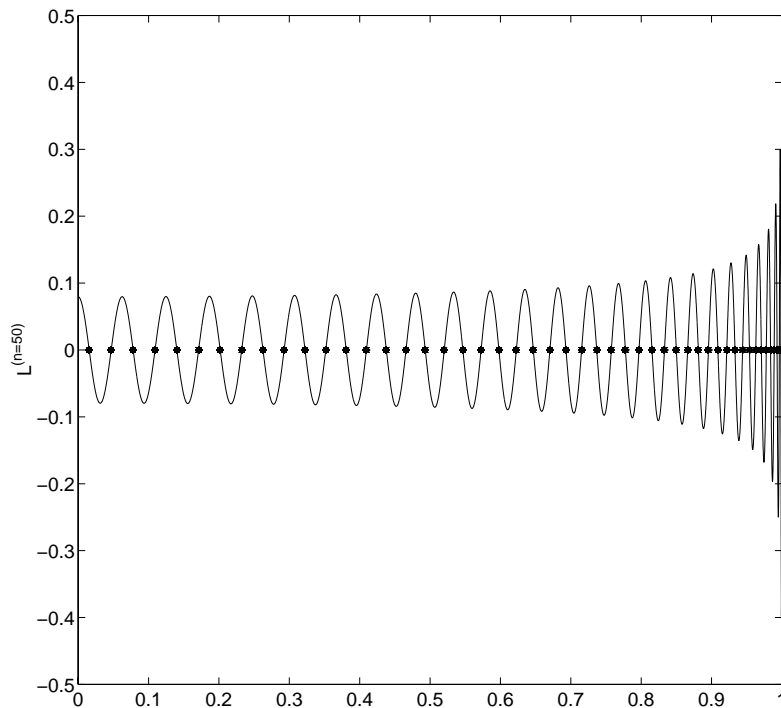
Figure 1.10: Legendre polynomial of degree 50, with 50 zero point values between 0 and 1. The Legendre weights can be found analytically from the Legendre polynomial function and successively associated with Δg_j used for the discretization of $\sigma(g)$ in Figure 1.9

Qualitatively, these relations mean that for a given wavenumber interval $[\nu_0, \nu_1]$ the cross-section distributions at all altitudes are correlated in wavenumber space. From this follows that the monotonic ordering by intensity of absorption for different wavenumbers (or the relative spectral alignment of absorption lines) retains at different levels in the atmosphere. However, for nonhomogeneous paths this one-to-one correspondence between the monotonic ordering of the cross-section and the wavenumber scale relative to the line center might be broken for specific cases.

For single lines this correspondence is rigorously maintained at all levels of the atmosphere with the strongest absorption always occurring at the line center and the weakest absorption in the extreme line wings for all pressures and temperatures. On the other hand, in the case of overlapping lines of different intensity one can produce uncorrelated changes as is shown in Figure 1.11 for an absorption line, covered by the wings of a stronger line for high pressures and becoming distinct for low pressures. Such a developing additional maximum results in two additional maxima in the dpdf (one for the extra peak and one for the extra trough) at lower pressures and therefore affects the monotonic ordering of σ in this specific wavenumber region and therefore also affects $h(\sigma)$ at these specific σ. As a result the second correlation requirement (Eq. 1.25) is not satisfied
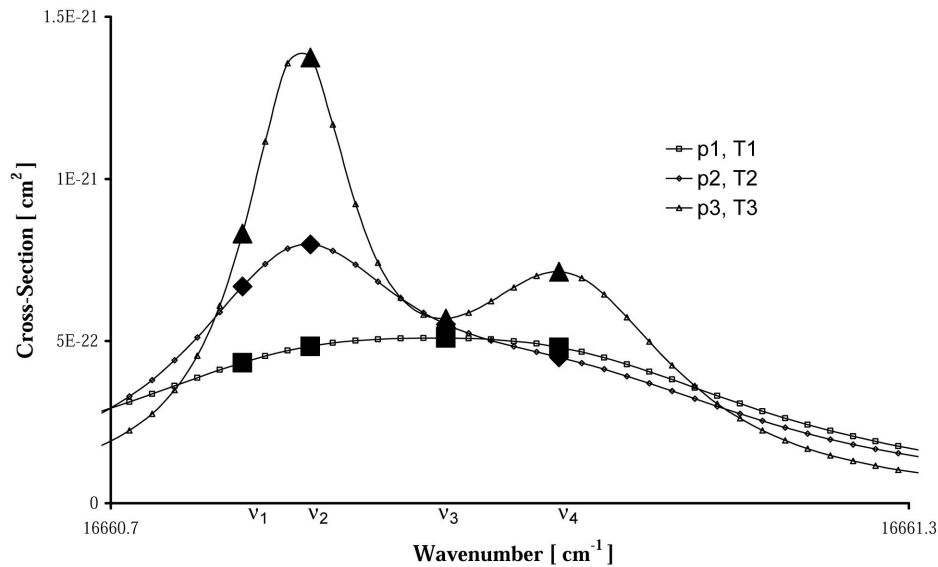
Figure 1.11: Sketch of a typical cross-section of water vapor at three significantly different pressure and temperature situations. As the pressure decreases the lines become narrower and an additional maximum (at ν_4) and an additional trough at ν_3 evolves in the wings of the strong line at ν_2. Whereas the increasing order of the cross-sections for decreasing pressures is conserved for ν_1 and ν_2 ($\sigma(\nu_2)$ always bigger than $\sigma(\nu_1)$) satisfying (1.25), their order is reversed for the lowest pressure p_3 and for cross-sections at ν_3 and ν_4. In this latter case the correlation assumption (1.25) is not satisfied anymore.

anymore (see also chapter 2, section 2.3.2).

This correlation problem predominantly occurs for highly structured line absorbers with high abundances over a wide altitude range covering significant changes in pressure and temperature. In contrast, such a problem does not occur in the case of OCM, for it is not based on any correlation assumption of this kind and may therefore be applied also to absorptions over very nonhomogeneous paths. To this respect, it is superior to the so far introduced band models and the correlated k-distribution method for applications to nongray, nonhomogeneous atmospheres.

It has to be noted that a different type of correlation problem occurs for both methods, correlated-k and OCM, in cases of large scale shifts in line positions in hot-bands or in cases of two overlapping, highly structured line absorbers with significantly different

atmospheric profiles. For example, in the latter case, the simple scalar product of two individual transmissions of two gases, i.e., $T(N_a, N_b) = T(N_a) \times T(N_b)$, loses its validity. To evaluate the nongray product of individual transmissions for overlapping gases, one has to perform the double sum [*Lacis & Oinas*, 1991]

$$T(N_a, N_b) = \sum_m^M \sum_n^M e^{-(\sigma_m(g_m)N_a + \sigma_n(g_n)N_b)} \Delta g_m \Delta g_n. \tag{1.26}$$

Again, computations of dpdf have to be made over the full vertical extent of the atmosphere for each individual component before being summed over k and j to obtain the transmittance. This problem of overlapping line absorbers or hot-band absorption or emissions should not be confused with the method related correlation problem of the correlated k-method as discussed in this chapter. Correlation problems due to different absorbers occur, for example, in the infrared region around 1.9 and 2.4 μm accessed by SCIAMACHY, where three line absorbers like methane, carbon monoxide and water vapor happen to overlap [*Schrijver et al.*, 1995]. Computationally efficient solutions of Eq. 1.26 for such a scenario have been suggested by, for example *Buchwitz et al.*, [2000], utilizing additional parameters for the mixing of lines of different absorbers.

1.6 Conclusions

During the past ten years sampling techniques, like the correlated k-distribution method based on cross-section distribution functions, have replaced other techniques, like for example band models, because of their ability to accurately model nonhomogeneous paths. Such sampled exponential opacity functions may be implemented in solutions of the equation of radiative transfer (both, scalar as well as full Stokes vector solutions) and already showed their ability to calculate efficiently the spectrally averaged transmittance in multiple-scattering atmospheres [*Lacis & Oinas*, 1991; *Stam et al.*, 2000]. An altitude-dependent distribution of histogram functions (ESFT fitted or calculated) may be stored in look-up-tables for different p and T and, if necessary, for different absorber amounts N. Interpolations on such tables are easy to perform because the f-functions vary smoothly with pressure and temperature (and absorber amount). For the first applications of the relatively simple k-distribution method, average line parameters from various band models were used in order to construct the probability density functions. Those combinations of band-model approximations with the k-distribution method result in very smooth probability functions for which a relatively low number of sampling points is needed in order to accurately represent the discretization (1.16). This is also true for combinations of the correlated k-distribution function with band models [*Lacis & Oinas*, 1991]. Also here, the cumulative density distribution functions are smoother when constructed on bases of average line parameters and less sampling points are needed for an accurate discretization (1.21) than is the case for those cumulative density distribution functions which are constructed directly from lbl calculations (see chapter 2). However, the transmittance calculated by correlated k-distribution methods utilizing band-model parameters is less accurate when compared to lbl results, than for those sampling methods utilizing dpdf from monochromatically calculated spectra directly. For the latter there is, of course, no

benefit in computational efficiency to be achieved for one-time calculations of transmittances.

The correlated k-distribution method was already applied for numerous applications. For example, correlated-k was successfully applied to calculate radiative heating and cooling rates of a number of absorbers like water vapor, carbon monoxide and ozone achieving numerical accuracies around 1% when compared to lbl calculations [*Lacis & Oinas*, 1991]. Correlated-k has shown its ability to retrieve water vapor, carbon dioxide, and methane concentrations with a precision of better than 1% and nitrous oxide and carbon monoxide concentrations better than 10% from monochromatically simulated absorption spectra of SCIAMACHY [*Buchwitz et al.*, 2000]. Similar accuracies were achieved for a modified k-distribution method using simulated data from the Medium Resolution Imaging Spectrometer (MERIS) onboard of ESA's environmental satellite (ENVISAT) with accuracies in calculated transmittances of 0.1% in the case of water vapor and 1% in the case of oxygen A-band absorptions [*Bennartz & Fischer*, 1999].

1.7 Outlook

The following two chapters deal with the Opacity Coefficient Method (OCM), which will be theoretically discussed in some detail in chapter 2 and applied to forward modeling of water vapor absorptions measured by GOME and the retrieval of total water vapor columns from the same instrument in chapter 3. Even though the concept of OCM utilizing dpdf of cross-section values for calculation of averaged transmittances is conceptually comparable with the k-distribution method, chapter 2 and 3 will show that OCM explicitly relates the spectroscopy and the inhomogeneity of the absorber along the path to the spectral averaged transmittance and is, therefore, not based on any correlation assumption for nonhomogeneous atmospheres, like the correlated k-distribution method. **Chapter 2** will also show that the discretized representation of the cumulative dpdf may cause problems in the case of using the correlated k-distribution method for instruments with relatively high spectral resolution (like GOME and SCIAMACHY) and, thus, narrow sampling width containing only a few distinct absorption lines. In contrast, the accuracy of the OCM method is solely dependent on the amount of quadrature points and on the accurate representation of the monochromatic reference cross-section. **Chapter 3** discusses the specific implementation of OCM in a radiative transfer scheme, which includes the treatment of singly scattered photons for retrieval and forward modeling purposes, utilizing a water vapour absorption band around 590 nm that has not been used before for the retrieval of WVC. The specific use of the OCM sampling method for such retrieval and forward modeling purposes has been labelled the Optical Absorption Coefficient Spectroscopy (OACS). The sensitivity and accuracy of the method is discussed in some detail, together with the implementation of background absorbers in order to accurately model the spectra measured by the satellite instrument within our spectral region of interest. The impact of the structured solar irradiance spectrum and the Ring effect, the impact of multiple-scattering contributions, aerosols and clouds and the impact of errors in the spectral cross-section database of water vapour on the retrieved WVC, is also discussed in this chapter.

The Spectral Structure Parameterization, introduced for the first time by *Maurellis*

et al., [2000b], (**chapter 4**) and utilized for forward modeling and retrieval purposes in **chapter 5**, deals also with an efficient solution of spectral opacity sampling, but is conceptually similar to a band-model approach. This makes SSP significantly faster but less accurate than OCM. **Chapter 4** describes the basic concept of SSP together with a sensitivity and accuracy study using synthetic spectra. The concept of averaged line parameters, typical for band models, allows a characterization of the spectral structure of different atmospheric absorbers by SSP in terms of the non-linear behavior of their absorption features, which is often referred to as *saturation* and which should not to be confused with saturation effects caused by the sensitivity of the instrument (Figure 1.4). **Chapter 5** will show that, providing some assumptions are made, SSP may easily be implemented in a radiative transfer scheme describing the absorption along nonhomogeneous paths and including first order of scattering. As one of the results, this chapter shows a global retrieval of WVC from more than 40000 GOME measurements using SSP. Both methods, SSP and OACS, retrieve subcolumn profiles, which, in principle, makes the retrieval of water vapor profiles from nadir satellite measurements possible using both methods. Finally, **chapter 6** presents a profile information content study for the three important water vapor absorption bands measured by GOME (Figure 1.4) using singular value decomposition together with a Phillips-Tikhonov regularization scheme. Retrieval results from artificial spectra are shown together with some preliminary results of WV-profile retrieval from GOME measurements using OACS.

Bibliography

Ambartzumian, V., The effect of the absorption lines on the radiative equilibrium of the outer layers of the stars, *Publ. Obs. Astron. Univ. Leningrad*, 6, 7-18, 1936.

Andreae, M. O., O. L. Mayol-Bracero, M. Gondwe, and A. J. Kettle, Aerosols and Climate, *Chemical, Physical and Biogenic Processes in the Atmosphere*, Notes from the 3rd COACh International School, Obernai, France, 2002.

Arking, A. A., and K. Grossman, The influence of line shape and band structure on temperatures in planetary atmospheres, *J. Atmos. Sci., 29*, 937-949, 1972.

Armstrong, B. H., Spectrum Line Profiles: The Voigt Function, *J. Quant. Spect. & Rad. Transfer, 7,* 61-88, 1967.

Armstrong, B. H., Analysis of the Curtis-Godson approximation and radiation transmission through inhomogeneous atmospheres, *J. Atmos. Sci., 25*, 312-322, 1968.

Bennartz, R., J. Fischer, A modified k-distribution, A modified k-distribution approach applied to narrow band water vapor and oxygen absorption estimates in the near infrared, *J. Quant. Spect. & Rad. Transfer, 66*, 539-553, 1999.

Bovensmann, H., J. P. Burrows, M. Buchwitz, J. Frerick, S. Noëll, V. V. Rozanov, K. V. Chance, and A. Goede, SCIAMACHY - Mission Objectives and Measurement Modes, *J. Atmos. Sci., 56*, 127-150, 1999.

Buchwitz, M., V. V. Rozanov, and J.P. Burrows, A correlated-k distribution scheme for overlapping gases suitable for retrieval of atmospheric constituents from moderate resolution radiance measurements in the visible/near-infrared spectral region, *J. Geophys. Res., 105*, 15,247-15,261, 2000.

Chaboureau, J.-P., A. Chédin, and N. A. Scott, Remote Sensing of the vertical distribution

of atmospheric water vapor from the TOVS observations: Method and validation, *J. Geophys. Res., 103,* 8743-8752, 1998.

Chou, M. D., and A. Arking, Computation of infrared cooling rates in the water vapor bands, *J. Atmos. Sci., 37,* 855-867, 1980.

Curtis, A. R., Discussion of "A statistical model for water vapor absorption", *Q. J. R. Metereol. Soc., 78,* 638-640, 1952.

van Dorland, R., Radiation and Climate, From Radiative Transfer Modeling to Global Temperature Response, PhD thesis, 147 pp., *ISBN 90-646-4032-7,* 1999.

Elsasser, W. M., Heat transfer by infrared radiation in the atmosphere, *Harvard Meteorol. Stud., 6,* 107 pp., Harvard University Press, Cambridge, Mass., 1942.

The Global Ozone Monitoring Experiment Users Manual, *Ed. F. Bednarz,* ESA Publication SP-1182, ESA Publication Division, ESTEC, Noordwijk, The Netherlands, 1995.

Fu, Q., and K. N. Liou, On the correlated k-distribution method for radiative transfer in nonhomogeneous atmospheres, *J. Atmos. Sci., 49,* 22, 2139-2156, 1992.

Godson, W. L., The evaluation of infrared-radiative fluxes due to atmospheric water vapor, *Q. J. R. Metereol. Soc., 79,* 367-379, 1953.

Goody, R. M., A statistical model for water vapor absorption, *Q. J. R. Meteorol. Soc., 78,* 165-169, 1952.

Goody, R. M., and Y. L. Yung, Atmospheric Radiation: Theoretical Basis, *Oxford University Press,* Oxford, 1964.

Goody, R. M., R. West, L. Chen, and D. Crisp, The correlated-k-method for radiation calculations in nonhomogeneous atmospheres, *J. Quant. Spect. & Rad. Transfer, 42,* 539-550, 1989.

Howard, J. N., D. E. Burch, and D. Williams, Infrared transmission of synthetic atmospheres, Parts I-V, *J. Opt. Soc. Am., 46,* 186-190, 237-241, 242-245, 334-338, 452-455, 1956.

van de Hulst, H. C., Theory of absorption lines in the atmosphere of the earth, *Ann. Astrophys.,8,* 1-11, 1945.

IPCC Third Assessment Report - Climate Change 2001: The Scientific Basis, Technical Summaries, *Cambridge University Press,* Cambridge, 2001.

Kato, S., T. P. Ackerman, J. H. Mather, and E. E. Clothiaux, The k-distribution method and correlated-k approximation for shortwave radiative transfer model, *J. Quant. Spect. & Rad. Transfer, 62,* 109-121, 1999.

Kessler, W. J., M. G. Allen, S. J. Davis, P. A. Mulhall, and J. A. Polex, Near-IR Diode Laser-Based Sensor for ppb-Level Water Vapor in Industrial Gases, *SPIE Paper No. 3537-A30,* SPIE International Symposium on Industrial and Environmental Monitors and Biosensors, Boston, 1998.

Kley, D., and E. J. Stone, Measurement of water vapor in the stratosphere by photodissociation with Ly (α) (1216 A) light, *Rev. Sci. Instrum.*, 49, 691-697, 1978.

Lacis, A. A., and J. E. Hansen, A parametrization for the absorption of solar radiation in the Earth's atmosphere, *J. Atmos. Sci., 31,* 118-133, 1974.

Lacis, A. A., and V. Oinas, A description of the correlated k distribution method for modeling nongray gaseous absorption, thermal emission, and mutlitple scattering in vertically inhomogeneous atmospheres, *J. Geophys. Res., 96,* D5, 9027-9063, 1991.

Learner, R., R. Schermaul, J. Tennyson, N. Zobov, J. Ballard, D. Newnham, and M. Wickett, Measurement of H_2O Absorption Cross-Sections for the Exploitation of GOME

data, *ESTEC Contract No 13312/9/NL/SF*, Final Presentation, 2000.

Lindquist, G. H., and F. S. Simmons, A band model formulation for very nonuniform paths, *J. Quant. Spect. & Rad. Transfer, 12*, 807-820, 1972.

Malkmus, W., Random Lorentz band model with exponential-tailed s^{-1} line-intensity distribution function, *J. Opt. Soc. Am., 57*, 323-329, 1967.

Manabe, S., and F. Moller, On the radiative-equilibrium and heat balance of the atmosphere, *Mon. Weather Rev., 89*, 503-532, 1961.

Maurellis, A. N., Non-Auroral Models of the Jovian Ionosphere, Ph.D. thesis, 75 pp., University of Kansas, June 1998. Measuring Radiances

Press, W. H., S. A. Teukolsky, W. T. Vetterling, and B. P. Flannery, Numerical recipes in FORTRAN - The art of scientific computing, Cambridge University Press, Cambridge, 140pp., 1992.

Naus H., and W. Ubachs, Visible absorption bands of the $(O_2)_2$-collision complex at pressures below 760 Torr, *Applied Optics, 38*, 3423-3428, 1999.

Rothman, L. S., C. P. Rinsland, A. Goldman, S. T. Massie, D. P. Edwards, J.-M. Flaud, A. Perrin, C. Camy-Peyret, V. Dana, J.-Y. Mandin, J. Schroeder, A. McCann, R. R. Gamache, R. B. Wattson, K. Yoshino, K. V. Chance, K. W. Jucks, L. R. Brown, V. Nemtchino, and P. Varanasi, The HITRAN Molecular Spectroscopic Database and HAWKS (HITRAN Atmospheric Workstation): 1996 Edition, *J. Quant. Spect. & Rad. Transfer, 60,* 665-710, 1998.

Schrijver, H., S. Slijkhuis, M.G.M. Roemer, and A.P.H. Goede, Noise-related limits on the detectability of concentration variations of CH_4 and CO with SCIAMACHY , *Atmospheric Sensing and Modeling*, Richard P. Santer (ed.), Proc. SPIE 2311, 39, 1995.

Stam, D. M., J. F. De Haan, J. W. Hovenier, and P. Stammes, A fast method for simulating observations of polarized light emerging from the atmosphere applied to the oxygen *A* band, *J. Quant. Spect. & Rad. Transfer, 64*, 131-149, 2000.

Vesperini, M., Humidity in the ECMWF model: Monitoring of operational analyses and forecasts using SSM/I observations, *Q. J. R. Meteorol. Soc., 124,* pp.1313-1327, 1998.

Wang, W. C., and G. Y. Shi, Total band absorption and and *k*-distribution function for atmospheric gases, *J. Quant. Spect. & Rad. Transfer, 39*, 387-397, 1988.

Wiscombe, W., and J. Evans, Exponential-sum fitting of radiative transmission functions, *J, Comput. Phys., 24*, 416-444, 1977.

Yamamoto, G., Direct absorption of solar radiation by atmospheric water vapor, carbon dioxide and molecular oxygen, *J. Atmos. Sci., 19*, 182-188, 1962.

Yamamoto, G., M. Tanaka, and S. Asano, Radiative transfer in water clouds in the infrared region, *J. Atmos. Sci., 27*, 282-292, 1970.

Yamamoto, G., M. Aida, and S. Yamamoto, Improved Curtis-Godson approximation in a non-homogeneous atmosphere, *J. Atmos. Sci., 29*, 1150-1155, 1972.

Young, S. J., Band model formulation for inhomogeneous optical paths, *J. Quant. Spect. & Rad. Transfer, 15*, 483-501, 1975.

Chapter 2

A New Determination of Extinction for Nongrey, Nonhomogeneous Atmospheres

The accurate and efficient computation of radiation transmittance in nongrey, nonhomogeneous atmospheric models is frequently complicated by complex bands of line spectra which range in value over many orders of magnitude and depend strongly on either or both of pressure and temperature. In this work we present a new opacity sampling technique called the Opacity Coefficient Method (OCM) which is shown to determine correctly the wavelength-averaged extinction due to path-dependent realizations of a line absorption spectrum. The technique is easy to implement computationally and is applicable to a wide variety of atmospheric problems in which frequent iteration of the radiative transfer model is required. We consider two such instances: modeling of solar fluxes for use in a time-dependent planetary ionosphere model and retrieval from nadir measurements of backscattered solar irradiance. The power of OCM lies in its straightforward analytical treatment of both atmospheric inhomogeneity and spectral complexity. It is thus relevant for both retrieval and radiative transfer modeling purposes.

2.1   Introduction

Analytical models of the transfer of radiation due to highly-structured line spectra saw their first comprehensive formulation in the spectral band models of van de Hulst, Curtis and Godson *van der Hulst* [1945]; *Curtis* [1952]; *Godson* [1953] and have since been extensively reviewed, especially in application to planetary atmospheres, by Goody and Yung *Goody & Yung* [1989] and Lenoble *Lenoble* [1993], among others (see also Thomas & Stamnes *Thomas & Stamnes* [1999]). By *highly-structured* spectra in nongrey atmospheric models we mean cross-section line spectra containing very narrow features and covering a wide range of values. In this work we consider the specific problem of determining an average transmittance over some wavelength interval of an absorption spectrum without employing the technique of analytical band modeling. Analytical formulations of spectral band models (eg. the Malkmus model *Malkmus* [1967]) are usually complicated by the number of lines being considered, the relative strengths of the lines and the degree to which they overlap. They are further complicated by the temperature and pressure dependence of the line widths, which in the case of atmospheric cross-sections translates into a problem of altitude or path dependence.

We treat the above problems by presenting a new opacity sampling technique which we dub the Opacity Coefficient Method (OCM). This method employs numerical realizations or tabulations of pressure- and temperature-dependent absorption cross-sections rather than analytical formulations of the absorption. Numerical realizations can always be computed to arbitrary wavelength resolution in order to obtain a set of discretized cross-sections with an implicit altitude dependence. We show in this work that it is possible to establish a simple but accurate analytical relationship between the discretized cross-sections and a quantity frequently required by atmospheric forward models, namely, wavelength-averaged atmospheric transmittance. Thus OCM can be used to replace path-dependent, nested integrals with exponential sums which are computationally more efficient in highly-iterative atmospheric forward modeling and retrieval schemes.

In fact, OCM is applicable to any set of line spectra which can be tabulated in numerical form as a function of wavelength. For example, a single line profile is often computed using a Voigt line profile *Rees* [1989]. In many cases the total band absorption cross-section is subsequently arrived at by simply adding the cross-sections due to each line. However, OCM, unlike analytical band models, does not depend at all on the method of computation of the line profiles and may be applied to line profile realizations originating in formulations of greater complexity, such as those in which broadening effects other than pressure and temperature are taken into account (eg. collisional broadening or Dicke narrowing *Shapiro et al.* [2001]) or in which considerable line overlap exists.

In section 2.2, we present details of the mathematical analysis underlying OCM. The relationship of OCM to similar existing methods, in particular the k-distribution method, is discussed in section 2.3 along with practical implementation aspects and an evaluation of accuracy and performance in atmospheric modeling.

2.2   The Opacity Coefficient Method: Analysis and Scope

2.2.1   Definitions

In order to model the general transmittance T of radiation after its passage through an attenuating atmosphere we first consider the simple extinction case along an arbitrary path Γ from point P_1 to point P_2 through an attenuating atmosphere, given by

$$T(\Gamma, \lambda) = e^{-\tau(\Gamma, \lambda)} \ , \tag{2.1}$$

for a given wavelength λ. The optical depth τ along the path Γ is defined as the path integral,

$$\tau(\Gamma, \lambda) = \int_\Gamma \beta_{\text{ext}}(P_s, \lambda) ds \ , \tag{2.2}$$

Here, P_s denotes a position on the path Γ, ds represents an infinitesimal path element and β_{ext} is the extinction coefficient along the path.

   In order to evaluate the integral in Eq. (2.2), we assume that the path Γ consists of a chain of $n + 1$ smooth paths, each of which may be parameterized by a function g_l, $l = 1, \cdots n + 1$,

$$\tau(\Gamma, \lambda) = \sum_{l=1}^{n+1} \int_{w_l}^{w_{l+1}} \beta_{\text{ext}}(w, \lambda) g_l'(w) \ dw \ . \tag{2.3}$$

Here, w is a parameter denoting the position along the path and w_l and w_{l+1} indicate the end points of the path segment ℓ. Furthermore, $g_l'(w)$ is the derivative of the parameterization with respect to w. In the remainder of this analysis we will only consider paths of a special type $\Gamma^n = \Gamma(z_0, \cdots, z_{n+1}, \Omega_1, \cdots, \Omega_{n+1})$ consisting of a chain of $n + 1$ straight ray trajectory connected at n scattering points. Each ray trajectory is characterized by altitude levels of the end points z_{l-1} and z_l and the direction $\Omega_l = (\mu_l, \varphi_l)$ with an azimuth angle φ_l and the cosine of the zenith angle μ_l ($\mu_l > 0$ for upward directions and $\mu_l < 0$ for downward directions) . For such a path we may choose altitude z as a suitable parameter. For the l-th path segment, the parameterization is given by

$$g_l(z) = \frac{1}{u_l}(z - z_l) \ , \tag{2.4}$$

with $u_l = |\mu_l|$ (see figure 2.1). In this particular case, the transmittance (2.1) is given by

$$T(\Gamma, \lambda) = \prod_{l=0}^{n} \exp\{-\frac{1}{u_{l+1}} \Delta\tau(z_{l+1}, z_l, \lambda)\} \ , \tag{2.5}$$

where $\Delta\tau(z_{l+1}, z_l, \lambda)$ is the optical depth between altitude z_l and z_{l+1} satisfying

$$\Delta\tau(z_{l+1}, z_l, \lambda) = |\int_{z_{l+1}}^{z_l} \beta_{\text{ext}}(z, \lambda) dz| \ . \tag{2.6}$$

   What is required in many applications of radiative transfer is the transmittance $\bar{T}$ averaged over a wavelength region $[\lambda_1, \lambda_2]$,

$$\bar{T}(\Gamma) = \frac{1}{\Delta\lambda} \int_{\lambda_1}^{\lambda_2} T(\Gamma, \lambda) d\lambda \ . \tag{2.7}$$
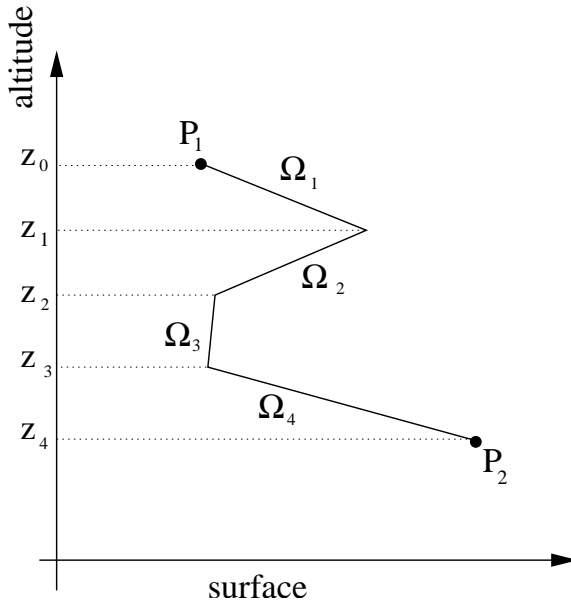
Figure 2.1: A path $\Gamma^{n=3}$ which connects the points P_1 and P_2. Γ consists of a chain of four straight ray trajectories connected at three scattering points, which may be parameterized by the functions g_l in equation (2.4).

The numerical calculation of $\bar{T}$ by a line-by-line model is very time-consuming if the path-dependent extinction coefficient β_{ext} varies strongly with wavelength and the path-dependent cross-section depends strongly on temperature and pressure, i.e.

$$\sigma = \sigma(T(z), p(z), \lambda) .$$

If, for the sake of clarity, we assume absorption by only one atmospheric constituent and further assume that scattering is wavelength-independent within each discretized spectral element $[\lambda_1, \lambda_2]$ then the extinction coefficient is given by

$$\beta_{\text{ext}}(z, \lambda) = n(z)\sigma(z, \lambda) + \beta_{\text{scat}}(z) , \tag{2.8}$$

Here, n denotes the density of the absorber, σ is the absorption cross section and β_{scat} represents the wavelength-independent scattering coefficient. Thus Eq. (2.8) yields an averaged transmittance in the form of

$$\bar{T}(\Gamma) = T_{\text{scat}}(\Gamma)\, \bar{T}_{\text{abs}}(\Gamma) , \tag{2.9}$$

with

$$T_{\text{scat}}(\Gamma) = e^{-\tau_{\text{scat}}(\Gamma)} , \tag{2.10}$$

and

$$\bar{T}_{\text{abs}}(\Gamma) = \frac{1}{\Delta\lambda} \int_{\lambda_1}^{\lambda_2} e^{-\tau_{\text{abs}}(\Gamma, \lambda)} d\lambda . \tag{2.11}$$

The variables τ_{scat} and τ_{abs} represent the path-integrated scattering and absorption optical depth, respectively.

In what follows we show how numerical realizations of "path-dependent" cross-sections can be analytically linked to an average transmittance for any required wavelength interval of an absorption spectrum over a given altitude range. This permits the calculation of total extinction, in the case of scattering which is not highly-structured but absorption which is, to be calculated directly from the cross-sections. The further novelty of OCM is the manner in which it accounts for both the nonhomogeneous and the nongrey nature of the extinction problem as defined here without having to introduce correlation or scaling assumptions. We note that no bias is introduced into the radiative transfer model apart from the numerical error arising out of the discretization of the problem. Thus any accuracy can be achieved if an appropriate discretization is used.

2.2.2   Opacity Sampling

In this section we use ordered Riemann sums to arrive at the averaged transmittance $\bar{T}$ for an arbitrary path and for a given wavelength interval. First we determine the averaged cross-section $\bar{\sigma}(P_s)$ somewhere on the path Γ in Riemann sum form. The averaged transmittance is then linked via an opacity sampling to the cross-section Riemann sum.

The integral of a general function $f(x)$ may be expressed as a Riemann sum

$$\int_{x_1}^{x_2} f(x)dx = \sum_{i=1}^{B} \alpha_i \xi_i \delta x + \epsilon(\mathcal{R}, \delta x) \; , \tag{2.12}$$

as follows. The function is first discretized $f(x) \rightarrow f_k$ by sampling it at K positions $\{x_k, k = 1, \cdots K\}$ with constant grid spacing δx, i.e. f_k is the mean value of $f(x)$ over the domain $x \in [x_k - \frac{\delta x}{2}, x_k + \frac{\delta x}{2}]$. Now assume that a finite ordered, non-overlapping set $\mathcal{R}$ of B bins with centers given by ξ_i may be constructed spanning the space of f_k, viz,

$$\mathcal{R} = \{\xi_i, i = 1, \ldots, B\} \; . \tag{2.13}$$

Then α_i is the number of values of f_k falling into bin i. In fact α_i is an element of a non-normalized discretized probability density function representation (hereafter "dpdf") of values $\{f_k, k = 1, \cdots, K\}$ equal to the product of K and the probability of finding the value f_k. This may be expressed alternatively as

$$\sum_{i=1}^{B} \alpha_i = K \; .$$

Finally, the error ϵ is dependent on both the discretization grid spacing δx as well as the specific choice of $\mathcal{R}$. We formally notate the calculation of dpdf coefficients α_i as follows

$$\alpha_i = \text{dpdf}(f, \mathcal{R}) \; , \tag{2.14}$$

which may be read as "the ith discrete probability density function coefficient of a discretized function $f \rightarrow f_k$ binned in terms of ordered set $\mathcal{R} = \{\xi_i\}$". The above formalism
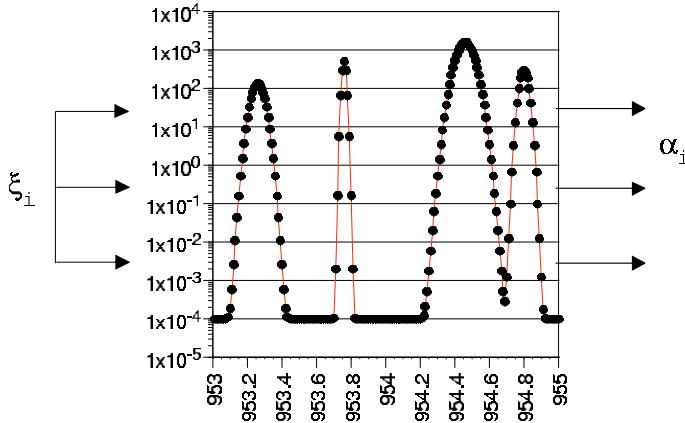
Figure 2.2: A graphical representation of the probability density function sampling technique used here. The method may be applied to any function but here it is shown applied to a typical absorption band, in which case the vertical axis is in arbitrary absorption cross-section units and the horizontal axis is in wavelength. Molecular absorption line strengths often vary over many orders of magnitude and exhibit a certain amount of overlap as well as lines of very different intensity. The filled circles indicate the values at which the cross-section has been discretely sampled. The cross-section scale has been divided into arbitrary bins ξ_i and the number of values that lie within a given bin, when counted, yields a set of coefficients, α_i, ordered with respect to bin index i.

also lends itself to an expression of the following special property of ordered sums (described in more detail in appendix B). For a general, discretized function f_k, binned in terms of an ordered set $\{\xi_i\}$,

$$\mathrm{dpdf}(f_k, \{\xi_i\}) = \mathrm{dpdf}(g(f_k), \{g(\xi_i)\}), \qquad (2.15)$$

providing that g is monotonic and single-valued.

Now we identify f with σ (and x with λ) in order to discretize an absorption cross-section $\sigma(P_s, \lambda) \rightarrow \sigma_k(P_s, \lambda_k)$ (see Figure 2.2). The discretized absorption cross-section is sampled at a grid spacing $\delta\lambda$ over a wavelength region $\lambda_j \in [\lambda_1, \lambda_2]$ with sampling width $\Delta\lambda = (\lambda_2 - \lambda_1)$. Thus ξ_i is an element of a binning set of cross-section values and α_i is the unitless, non-normalized weighting of cross-section value ξ_i. For instance, the wavelength-averaged absorption cross-section,

$$
\begin{aligned}
\bar{\sigma}(P_s) &= \frac{1}{\Delta\lambda} \int_{\lambda_1}^{\lambda_2} \sigma(P_s, \lambda) d\lambda \\
&\approx \frac{\delta\lambda}{\Delta\lambda} \sum_{\mathcal{R}} \alpha_i(P_s)\xi_i \ ,
\end{aligned}
\qquad (2.16)
$$

is a simple mean of the wavelength values. A wavelength-averaged cross-section is not useful for determining wavelength-averaged transmittance. However it is useful in demonstrating that the altitude dependence of the cross-section is now contained within the

coefficient $\alpha_i(P_s)$. As will be shown later this coefficient may be easily interpolated over different altitude ranges in a nonhomogenous atmosphere.

The general aim is to obtain an analytical expression for the wavelength-averaged transmittance at a given altitude due to solar flux entering at the top of an atmosphere (equation 2.1) in terms of the new formalism. We assume just one attenuating species. First we determine an opacity sampling $\bar{\tau}_{\mathrm{abs}}(\Gamma)$, in terms of an ordered Riemann sum, viz,

$$\bar{\tau}_{\mathrm{abs}}(\Gamma) \quad = \quad \frac{1}{\Delta\lambda} \int_{\lambda_1}^{\lambda_2} \tau_{\mathrm{abs}}(\Gamma, \lambda) d\lambda \tag{2.17}$$

$$= \quad \frac{\delta\lambda}{\Delta\lambda} \sum_{i=1}^{B} \gamma_i(\Gamma)\, \zeta_i \ , \tag{2.18}$$

where we assume that a set $\mathcal{Q}$ of B bins, characterized by the values ζ_i, spans the full range of τ, via

$$\zeta_i = \xi_i \int_{\Gamma} n(s)\, ds \ , \tag{2.19}$$

so that the coefficients γ_i are given by

$$\gamma_i(\Gamma) = \mathrm{dpdf}\left(\tau(\Gamma), \mathcal{Q}\right) \ , \tag{2.20}$$

analogous to the dpdf of the cross-section distribution.

Clearly the ordered sum in equation (2.18) is homeomorphic to the corresponding sum (equation 2.16) of the averaged cross-section since the definition of optical depth in equation (2.2) derives from an integral mapping of cross-section to optical depth with the number density $n(s)$ as an integral kernel (see Eqn. B.9 in appendix B). Furthermore, application of the Lemma in appendix B provides an alternative expression for the averaged optical depth, viz,

$$\bar{\tau}_{\mathrm{abs}}(\Gamma) = \frac{\delta\lambda}{\Delta\lambda} \sum_{i=1}^{B} \xi_i \int_{\Gamma} \alpha_i(s) n(s)\, ds \ , \tag{2.21}$$

from which we make the identification

$$\gamma_i(\Gamma) = \frac{\int_{\Gamma} \alpha_i(s) n(s)\, ds}{\int_{\Gamma} n(s)\, ds} \ , \tag{2.22}$$

after a term-by-term comparison of Eqs. (2.18) and (2.21) and substitution of Eq. (2.19).

We note, parenthetically, that the substitution of an average opacity (Eq. 2.18) directly into equation (2.1) for a highly-structured spectrum yields an estimate of transmittance which is weighted in favor of large cross-section values, so that transmittance would be significantly underestimated. As mentioned before, the useful quantity is the transmittance $\bar{T}_{\mathrm{abs}}(\Gamma)$ itself wavelength-averaged over the bandpass of interest (see equation 2.11) which may also be expressed as an ordered Riemann sum,

$$\bar{T}_{\mathrm{abs}}(\Gamma) \approx \frac{\delta\lambda}{\Delta\lambda} \sum_{i=1}^{B} \eta_i\, T_i \tag{2.23}$$

assuming a binning $\mathcal{T}$ in B bin intervals characterized by values T_i with dpdf coefficients

$$\eta_i = \text{dpdf} \left(e^{-\tau_{\text{abs}}(\Gamma)}, \mathcal{T} \right) . \tag{2.24}$$

It remains to show that η_i and T_i may also be expressed in terms of the $\alpha_i(P_s)$ and ξ_i defined earlier for the discretized cross-section. The spectral transmittance may formally be expressed as a combination of the exponential function and the absorption optical depth, which itself depends on cross section. Thus one may define the binning of the transmittance by

$$T_i = e^{-\zeta_i} \tag{2.25}$$

where ζ_i characterizes the corresponding binning of optical depth τ. Because of the monotonic behavior of the exponential the property of ordered Riemann sums (appendix B, Lemma 2; function f should be identified with τ_{abs} and function h with the exponential) may be used to identify the coefficients η_i in (2.23) with the corresponding dpdf coefficients γ_i, viz.

$$\begin{aligned}
\eta_i &= \text{dpdf}(\exp \circ \tau_{\text{abs}}, \mathcal{T}) \\
&= \text{dpdf}(\tau_{\text{abs}}, \mathcal{Q}) \\
&= \gamma_i .
\end{aligned} \tag{2.26}$$

So, equation (2.23) may be written as

$$\bar{T}_{\text{abs}}(\Gamma) \approx \frac{\delta\lambda}{\Delta\lambda} \sum_{i=1}^{B} \gamma_i(\Gamma) \, e^{-\zeta_i} \; , \tag{2.27}$$

which together with equations (2.10) (2.19) and (2.22) represents the basic OCM formulation of the desired average transmittance (2.7). We note that the path-dependence of cross section is now explicitly in the path-integration of the dpdf coefficients α_i so that the OCM representation converges toward the correct solution for increasing bin number B. Thus, no significant bias is introduced by the treatment of the path-dependence of the absorption cross section.

The accuracy of OCM depends primarily on the level of discretization of the wavelength grid. In practical terms, the spectral realization must be achieved with a small enough $\delta\lambda$ so that the very weakest lines are resolved sufficiently at their centers as well as across the wings. The wing profiles should also be computed out to wavelengths sufficiently far from the line centers so that wing profiles overlap and no unassigned regions exist in the cross-section tabulation.

The OCM technique is less dependent on the accuracy of the dpdf representation. It is important to choose $\mathcal{R}$ so that the dynamic range of the function is fully covered. It is also important to choose bin widths which are small enough such that the summation adequately approximates the integral. In addition, $\mathcal{R}$ must truly span the space of interest. An error here may be more crucial than the choice of step size because a minimum value for ξ_i which is too large will force the smallest values of the function into too large a bin yielding a dpdf representation which overestimates the integral.

It remains to develop the scattering formalism in a plane parallel atmosphere more generally in the following section.

2.2.3 Scattering

A common approach to solving the radiative transfer equation is to use the method of successive orders of scattering. Here, the diffuse intensity field at altitude z in a direction $\mathbf{\Omega} = (\mu, \varphi)$ is expressed as *Lenoble* [1993]

$$I(z, \mathbf{\Omega}) = \sum_{n=1}^{\infty} I_n(z, \mathbf{\Omega}) \ , \tag{2.28}$$

where in scalar approximation

$$I_n(z, \mathbf{\Omega}, \lambda) = \int_o^{z_{\text{top}}} dz' \int_{4\pi} d\Omega' K(z, \mathbf{\Omega}; z', \mathbf{\Omega}') \ I_{n-1}(z', \mathbf{\Omega}', \lambda) e^{-\Delta\tau(z', z, \lambda)/u} \tag{2.29}$$

is the part of the intensity scattered n times and $u = |\mu|$, the direction cosine. Here, $d\Omega = d\mu d\varphi$ indicates the integration over solid angle. The integral kernel is given by

$$K(z, \mathbf{\Omega}; z', \mathbf{\Omega}') = \frac{1}{u} \frac{\beta_{\text{scat}}(z')}{4\pi} P(z', \mathbf{\Omega}, \mathbf{\Omega}') \Theta(z - z') + \frac{A}{\pi} \Theta(-\mu') |\mu'| \delta(z) \tag{2.30}$$

for upward directions $\mu > 0$ and

$$K(z, \mathbf{\Omega}; z', \mathbf{\Omega}') \quad = \quad \frac{1}{u} \frac{\beta_{\text{scat}}(z')}{4\pi} P(z', \mathbf{\Omega}, \mathbf{\Omega}') \Theta(z' - z) \ , \tag{2.31}$$

for downward directions $\mu < 0$. Kernel K describes both scattering on air molecules from direction $\mathbf{\Omega}'$ into $\mathbf{\Omega}$ with a scattering phase function P and Lambertian reflection at the lower boundary of the model atmosphere with a surface albedo A. Here, Θ is the Heaviside step function and δ is the Dirac delta. The series may be initialized with the direct beam

$$I_0(z, \mathbf{\Omega}, \lambda) = \delta(\mathbf{\Omega} - \mathbf{\Omega}_\odot) F_\odot(\lambda) \ e^{-\Delta\tau(z, z_{\text{top}}, \lambda)/\mu_\odot} \ , \tag{2.32}$$

where $\Omega_\odot = (\mu_\odot, \varphi_\odot)$ represents the direction of the unidirectional solar beam entering the model atmosphere at a height z_{top} and $\delta(\mathbf{\Omega} - \mathbf{\Omega}_\odot) = \delta(\mu - \mu_\odot) \delta(\varphi - \varphi_\odot)$. $F_\odot$ is the solar flux. Repeated substitution of the lower order scattering solution in Eq. (2.29) provides the expression

$$I_n(z, \mathbf{\Omega}, \lambda) \quad = \quad F_\odot(\lambda) \int_o^{z_{\text{top}}} dz_n \cdots dz_1 \int_{4\pi} d\Omega_{n-1} \cdots d\Omega_1$$
$$\prod_{l=1}^{n} K(z_{l+1}, \mathbf{\Omega}_{l+1}; z_l, \mathbf{\Omega}_l) \prod_{l=0}^{n} e^{-\Delta\tau(z_{l+1}, z_l \lambda)/u_{l+1}} \ , \tag{2.33}$$

with $z_o \equiv z_{\text{top}}$, $\mathbf{\Omega_1} \equiv \mathbf{\Omega}_\odot$ and $z_{n+1} \equiv z$, $\mathbf{\Omega}_{n+1} \equiv \mathbf{\Omega}$. Here, the integrations over altitude and solid angle

$$\int d\Gamma^n \equiv \int_0^{z_{\text{top}}} dz_n \cdots dz_1 \int d\Omega_{n-1} \cdots d\Omega_1 \tag{2.34}$$

takes all possible light paths Γ^n with n scattering points into account (see figure 2.1). Substitution of (2.5) in (2.33) provides the compact notation

$$I_n(z, \mathbf{\Omega}, \lambda) = F_\odot(\lambda) \int d\Gamma^n \ T(\Gamma^n, \lambda) \ w(\Gamma^n) \ , \tag{2.35}$$

with

$$w(\Gamma^n) = \prod_{l=1}^{n} K(z_{l+1}, \mathbf{\Omega}_{l+1}; z_l, \mathbf{\Omega}_l) \ . \tag{2.36}$$

Thus, the part of the intensity scattered n times can be calculated as an integration of the transmittance T over all possible paths Γ^n, where $w(\Gamma^n)$ weights the contribution of the corresponding photon path with respect to the total intensity I.

Finally, we assume that the scattering properties and the solar flux $F_\odot$ are fairly constant within the spectral range of averaging. In this case, the wavelength averaged transmittance of diffuse light is given by

$$\bar{T}(z, \mathbf{\Omega}) = \sum_{n=0}^{\infty} \bar{T}_n(z, \mathbf{\Omega}) \tag{2.37}$$

(cf. Eqn. 2.28) taking all orders of scattering into account with

$$\bar{T}_n(z, \mathbf{\Omega}) = \frac{1}{\Delta\lambda} \int d\Gamma^n \ w(\Gamma^n) \int_{\lambda_1}^{\lambda_2} d\lambda \ T(\Gamma^n, \lambda) \ . \tag{2.38}$$

The wavelength integral over the path dependent transmittance $T(\Gamma^n, \lambda)$ can be calculated by applying the OCM representation (2.27),

$$\bar{T}_n^{\mathrm{OCM}}(z, \mathbf{\Omega}) = \frac{\delta\lambda}{\Delta\lambda} \int d\Gamma^n w(\Gamma^n) T^{\mathrm{scat}}(\Gamma^n) \sum_{i=1}^{B} \gamma_i(\Gamma^n) \ e^{-\zeta(\Gamma^n)} \tag{2.39}$$

with the transmission function $T^{\mathrm{scat}}(\Gamma^n)$ from equation (2.10) and the dpdf coefficients $\gamma_i(\Gamma^n)$ and $\zeta(\Gamma^n)$ from equation (2.22) and (2.19), respectively.

For example, for singly scattered light ($n = 1$) the path integrations can easily be worked out in more detail. For upward directions ($\mu > 0$) the transmittance at any altitude z is given by

$$\begin{aligned}
\bar{T}_{n=1}^{\mathrm{OCM}}(z, \mathbf{\Omega}) &= \frac{\delta\lambda}{\Delta\lambda} \left\{ \frac{1}{u} \int_0^z dz' \ \beta_{\mathrm{scat}}(z') P(z', \mathbf{\Omega}, \mathbf{\Omega}_\odot) T^{\mathrm{scat}}(z', z) \right. \\
&\qquad \left. \sum_{i=1}^{B} \gamma_i(z', z) e^{-\zeta_i(z', z)} + \frac{A}{\pi} \sum_{i=1}^{B} \gamma_i(0, z) e^{-\zeta_i(0, z)} \right\}
\end{aligned} \tag{2.40}$$

and for downward directions ($\mu < 0$) we get the corresponding expression

$$\begin{aligned}
\bar{T}_{n=1}^{\mathrm{OCM}}(z, \mathbf{\Omega}) &= \frac{\delta\lambda}{\Delta\lambda} \frac{1}{u} \int_0^z dz' \ \beta_{\mathrm{scat}}(z') P(z', \mathbf{\Omega}, \mathbf{\Omega}_\odot) T^{\mathrm{scat}}(z', z) \\
&\qquad \sum_i \gamma_i(z', z) e^{-\zeta_i(z', z)} \ .
\end{aligned} \tag{2.41}$$

Here, the path integrals in the transmittance function T^{scat} and the dpdf coefficients γ_i and ζ_i is given by

$$\int_{\Gamma^{n=1}} ds = \frac{1}{\mu_\odot} \int_{z'}^{z_{top}} d\tilde{z} + \frac{1}{\mu} \int_{z'}^{z} d\tilde{z} \tag{2.42}$$

Analogous, the wavelength averaged transmittance of the direct beam can be calculated by

$$\bar{T}_\odot^{OCM}(z, \mathbf{\Omega}) = \delta(\mathbf{\Omega} - \mathbf{\Omega}_\odot) \frac{\delta\lambda}{\Delta\lambda} T_\odot^{\text{scat}}(z) \sum_i \gamma_i(z)\, e^{-\zeta(z)} \qquad (2.43)$$

with corresponding path integrals

$$\int_{\Gamma^{n=0}} ds = \frac{1}{\mu_\odot} \int_z^{z_{top}} d\tilde{z} \qquad (2.44)$$

used in equations (2.10),(2.22) and (2.19).

In the case of a satellite nadir measurement geometry the backscattered transmittance for the direct beam component I_0 yields an averaged transmittance using equations (2.43),(2.22), and (2.19) of

$$\bar{T}_0^{OCM}(z_{\text{top}}, \Omega) = \frac{\delta\lambda}{\Delta\lambda} T_\odot^{\text{scat}}(z_{\text{top}}) \sum_{i=1}^B \frac{\int_0^{z_{\text{top}}} \alpha_i(s) n(s)\tilde{\mu}\, ds}{\int_0^{z_{\text{top}}} n(s)\tilde{\mu}\, ds} \exp\left[-\xi_i \int_0^{z_{\text{top}}} n(s)\tilde{\mu}\, ds\right], \qquad (2.45)$$

where $\tilde{\mu} = \frac{\mu_\odot + \mu}{\mu_\odot \mu}$ for solar zenith and satellite zenith angles $\mu_\odot$ and μ respectively. Here, we assume that scattering properties and the solar flux are fairly constant within the range of spectral averaging.

For the single scattering case ($n = 1$), we determine from equation (2.40) the averaged single-scattering contribution to the total transmittance as

$$\begin{aligned}
\bar{T}_{ss}^{OCM}(z_{\text{top}}, \Omega) &= \frac{1}{\mu} \frac{\delta\lambda}{\Delta\lambda} \int_0^{z_{\text{top}}} \bar{\beta}_{sca}(z) \bar{P}(z, \Omega, \Omega_o) \\
&\times \sum_i \frac{\int_z^{z_{\text{top}}} \alpha_i(s)\, n(s)\tilde{\mu}\, ds}{\int_z^{z_{\text{top}}} n(s)\tilde{\mu}\, ds} \exp\left[-\xi_i \int_z^{z_{\text{top}}} n(s)\tilde{\mu}\, ds\right] dz. \quad (2.46)
\end{aligned}$$

Both, the backscattered transmittance of the direct beam component and this single-scattering formulation of the OCM method is used for the retrieval of total water vapour columns from GOME in chapter 3 (cf. chapter 3, Eq. 3.20 and 3.21).

The discussion above shows two important aspects of the OCM sampling technique: The wavelength averaging of the transmittance can be efficiently calculated by use of Rieman summation. Furthermore, for photon paths of low scattering order the path integration does not provide any numerical difficulties. However, with increasing order of scattering the path integration becomes more complex and may result in high numerical effort. Thus, the OCM technique is very well suited for radiative transfer problems in the near infrared and the longwave part of the visible of the solar spectrum, when the effect of clouds on the radiation field can be neglected.

2.2.4 Nonhomogeneous Atmospheres

The primary aim behind developing new spectral methods such as OCM is to enhance accuracy without loss in computational efficiency. This is especially useful when repeated

calculations of the same spectral region need to be performed for different densities and for different pressure and temperature realizations of an absorption spectrum, as might be expected in atmospheric modeling or trace gas retrieval situations. OCM lends itself very easily to a determination of extinction in nonhomogeneous atmospheres. For instance, pure absorption may be modeled by discretizing the altitude integrals over a number of different altitude layers. In such a vertically-stratified radiative transfer model the required wavelength-average may be altitude-discretized in OCM form as follows. The basic exponential sum remains unchanged, regardless of the number of altitude levels involved,

$$T_{abs}^{OCM} = \frac{\delta\lambda}{\Delta\lambda} \sum_{i=1}^{B} \gamma_i' e^{-\zeta'}, \tag{2.47}$$

where the primes simply denote that these are soon to be calculated from discretized quantities. The altitude-discretization is introduced by changing the altitude integrals in equations (2.27) to summations over L atmospheric layers with partial column densities N_ℓ ($\ell = 1, \ldots, L$), viz,

$$\gamma_i' = \frac{\displaystyle\sum_{\ell=1}^{L} \bar{\alpha}_i^{(\ell)} N_\ell}{\displaystyle\sum_{\ell=1}^{L} N_\ell} \text{ and } \zeta_i' = \sum_{\ell=1}^{L} N_\ell \xi_i \ . \tag{2.48}$$

The alpha coefficients $\bar{\alpha}_i^{(\ell)}$ are easily calculated from a realization of the cross-section $\sigma(T(z_\ell), p(z_\ell), \lambda)$ for the ℓth layer, given the temperature and pressure at some mean altitude z_ℓ within the layer. Alternately it is sometimes useful to have access to a precalculated grid of $\alpha_i(T, p)$ values as a function of temperature and pressure for each bin index i. The required $\bar{\alpha}_i^{(\ell)}$, for which a realization of the cross-section does not exist, is then easily interpolated from nearest neighbor values in temperature and pressure for every binning index i via

$$\bar{\alpha}_i^{(\ell)} = \alpha_i(T(z_\ell), p(z_\ell)) \ , \tag{2.49}$$

Figure 2.3 shows contours of cross-section dpdf coefficients $\alpha_i(z)$ as a function of altitude and binning index. The smoothness of the contours over altitude facilitates the precalculation of an $\alpha_i(T, p)$ grid for each binning index i, over a wide range of temperatures and pressures.

2.3 Sampling Methods Comparison of OCM and k-distribution

At first glance, OCM appears to be equivalent to exponential sum methods used in fitting cross-section spectra such as the well-known k-distribution method. In this section, we compare the OCM and the k-distribution methods in order to gain some insight into their formal relationship as well as to evaluate the usefulness of OCM.
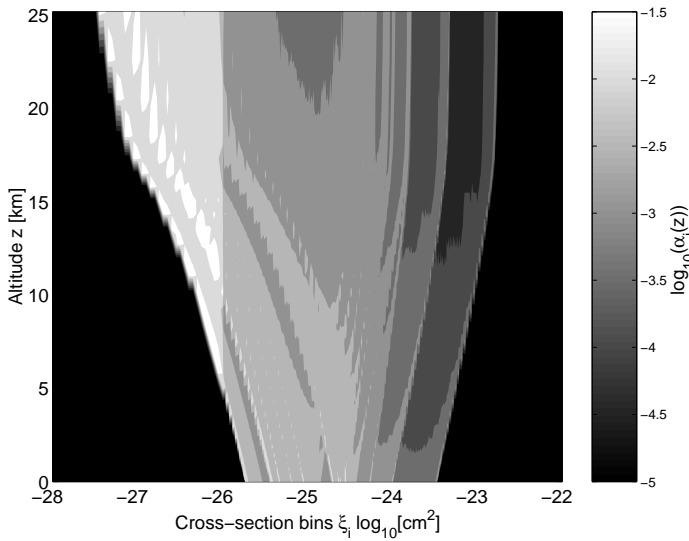
Figure 2.3: Typical contours of cross-section dpdf coefficients $\alpha_i(z)$ as a function of altitude and cross-section bins for a typical atmospheric forward modeling/retrieval situation. The dpdf's are calculated from water vapor cross-section realizations in the region around 17000 cm^{-1}. High pressures (low altitudes) result in broad absorption lines with relatively high trough and low peak cross-section values. For low pressures (high altitudes) the individual absorption lines narrow and the dpdfs are more spread out over cross-section range. For cross-sections higher than 10^{-26} narrower cross-section bins ξ_i are used resulting in relatively lower $\alpha_i(z)$ values. The higher binning resolution represents the peaks of the lines more accurately.

2.3.1   Analytical Comparison

We begin by reviewing the basic properties of the k-distribution. In this comparison we work in terms of Gauss-Legendre quadrature (*Kato et al.* [1999]) to express the average transmittance via

$$
\begin{aligned}
\bar{T}_{abs}^{k-dist} &= \int_0^\infty f(k)e^{-kN}\,dk \\
&\approx \sum_{j=1}^{G} a_j e^{-k(g_j)N} \ .
\end{aligned}
\tag{2.50}
$$

where $f(k)$ is the probability density function for a cross-section $k = \sigma(\lambda)$, N is the column density of absorber, G is the number of Gauss-Legendre quadrature points, a_j is the associated weight, and $g(k) = \int_0^k f(k')\,dk'$ is the cumulative probability density function. In fact, $f(k)$, in discretized form, is identical, up to a constant scaling, to the α coefficients in equation (2.14).

$$
f_j(k) \propto \alpha_j = \mathrm{dpdf}(k, \mathcal{R}) \ .
$$

However it is the inverse of the discretized cumulative density function, namely $k(g_j)$, which is used in an interpolation over quadrature points g_j

$$k(g_j) = g^{-1}(g_j(k)). \tag{2.51}$$

We note that the OCM σ and the k-distribution method k both represent cross-section and are thus identical in value. Equation (2.50) can be written in its general form as

$$\bar{T}_{abs}^{k-dist} = \int_0^1 e^{-k(g)N} dg, \tag{2.52}$$

using the inversion in equation (2.51). It is possible to use Gauss-Legendre quadrature in order to make the transformation from (2.52) to the sum in (2.50). Unfortunately the coefficients in equation (2.50) cannot be related to the original cross-section spectrum in a simple fashion because the coefficients are usually determined from the n zero points x_{j0} of Legendre polynomials $\mathcal{L}^{(n)}$ of order $n = 2G$ (where we make use of G zero points of the symmetric Legendre polynomials between 0 and 1 only). The corresponding weights, at quadrature points $g_j = x_{j0}$ are given by,

$$a_j = \int_{-1}^1 \mathcal{L}^{(n)}(x) dx = \frac{2(1 - x_{j0}^2)}{n^2 (\mathcal{L}^{(n-1)}(x_{j0}))^2} \ . \tag{2.53}$$

We note that there are other ways to get the most appropriate weights. For example, Lacis & Oinas *Lacis & Oinas* [1991] construct an explicit relationship between the weights and the average absorption coefficients to get the most appropriate sampling for $k(g)$. By comparison, the weights in the OCM exponential sum are taken directly from the dpdf. This approach lends itself directly to a simple relationship between the coefficients and the cross-sections which is not dependent on the absorber amount.

In our implementation of the k-distribution method, the quadrature points g_j and weights a_j are usually kept fixed for all altitude levels ℓ while the inverse cumulative density function $k(g_j, z)$ is left to vary with altitude. For each realization of the cross-sections $\sigma(z_\ell, \lambda)$ at level ℓ, corresponding to a set of $k(g_j, z_\ell)$ values with dimension j, one obtains

$$\bar{T}_{abs}^{ck} = \sum_{j=1}^G a_j \exp\left[-\sum_{\ell=1}^L k(g_j, z_\ell) N_\ell \right] \ , \tag{2.54}$$

from equation (2.50). Eq. (2.54) is frequently used as the basic formalism of the correlated k-distribution (ck) method for nonhomogeneous atmospheres *Fu & Liou* [1992].

Although both OCM and the ck-distribution method are exponential sum methods, they differ significantly in the way they parameterize cross-section space. As will be shown later, the accuracy-limiting parameter for OCM is the magnitude of $\delta\lambda$ and not the dimension of $\mathcal{Q}$. The opposite is true for the k-distribution method, for which the crucial parameter is the number of quadrature points. The size of $\delta\lambda$ is much less important although $\delta\lambda$ does determine the resolution of $k(g_j)$. In both cases an additional important parameter is also considered: the number of highly-structured absorption lines contained in the sampling width $\Delta\lambda$.

2.3.2   Wavelength Correlation in Nonhomogenous Atmospheres

The ck-distribution has been frequently used in order to model the nongrey nature of atmospheric absorptions in nonhomogeneous atmospheres *Goody & Yung* [1989]; *Lacis & Oinas* [1991]; *Bennartz & Fischer* [1999]; *Buchwitz et al.* [2000]. In the treatment of the ck-distribution thus far we have tacitly assumed that a fixed mapping is maintained between the position of each $\delta\lambda$ in the sampling width and the quadrature coefficients a$_j$ in the case of our ck-distribution implementation. A false mapping due to this assumption may occur due to the result of significant changes in pressure and temperature—the so-called *correlation problem* for light paths through nonhomogeneous atmospheres *Lacis & Oinas* [1991]; *Fu & Liou* [1992]. This false mapping occurs when weaker absorption lines (which are covered by the wings of stronger lines at low altitudes) become more distinct at higher altitudes as the line widths decrease with decreasing pressure. This adds additional maxima to the dpdf and therefore alters the monotonic dependence of $f_j(k)$ on altitude. From this it follows that the one-to-one mapping between the quadrature weights a_j and the corresponding sub-wavelength intervals $\delta\lambda$ breaks down. In contrast, OCM treats atmospheric inhomogeneity directly and is thus not based on an altitude correlation assumption.

Figure 2.4 shows calculations of the discretized probability density function $f_i(k)$ for artificial cross-sections, assuming a nonhomogeneous model atmosphere, as follows. The averaged transmittance is calculated over a 10 cm^{-1} wavenumber region covering a number of distinct absorption lines of two different line intensities. The artificial cross-sections consist of a series of alternately strong and weak absorption lines for 11 different altitudes levels with decreasing pressure from 1 to 10^{-2} atm and decreasing temperature from 300 to 200 K. A total column of 1×10^{23} molec/cm^2 is arbitrarily assumed. The upper panels of Figure 2.4 show two extreme situations: one in which the weak lines are always evident no matter how much the strong lines are pressure-broadened and one in which the weak lines emerge out of the wings of the strong lines almost as soon as pressure-broadening ceases to be significant. The effect on the dpdf's is shown as a function of altitude level in the corresponding lower panels of Figure 2.4 (c) and (d). The peaks in the dpdf correspond to both the peaks and the troughs in the spectrum. As one proceeds from lower atmospheric levels to higher ones, additional distinct peaks due to additional maxima and troughs in the spectrum are evident for all altitude levels in Figure 2.4(d) but occur only for levels higher then the fourth level in Figure 2.4(c). Figure 2.4(c) is therefore an example of a breakdown of the one-to-one mapping between $\delta\lambda$ and a_j.

To demonstrate what effect this has on the calculated transmittance we vary the separation between the line-center of the weak and strong lines over the range of 0.07 and 0.6 cm^{-1} (see Figure 2.5). Figure 2.5 shows a comparison with a line-by-line calculation of the average transmittance calculated using OCM and the ck-distribution methods. The error in the calculated transmittance using the correlated ck-distribution increases with respect to line separation between 0.07 and 0.2 cm^{-1} and decreases again at the largest separation of 0.6 cm^{-1}. In contrast, the OCM error stays constant for all cases, showing that OCM does not suffer from any correlation problem and is well suited to the modeling of average transmittances in nonhomogeneous atmospheres without the need for additional assumptions. Although the effect in this case is small, the effect for top-of-the-atmosphere fluxes can be as much as 0.2–1% *Fu & Liou* [1992]; *Buchwitz et al.* [2000].
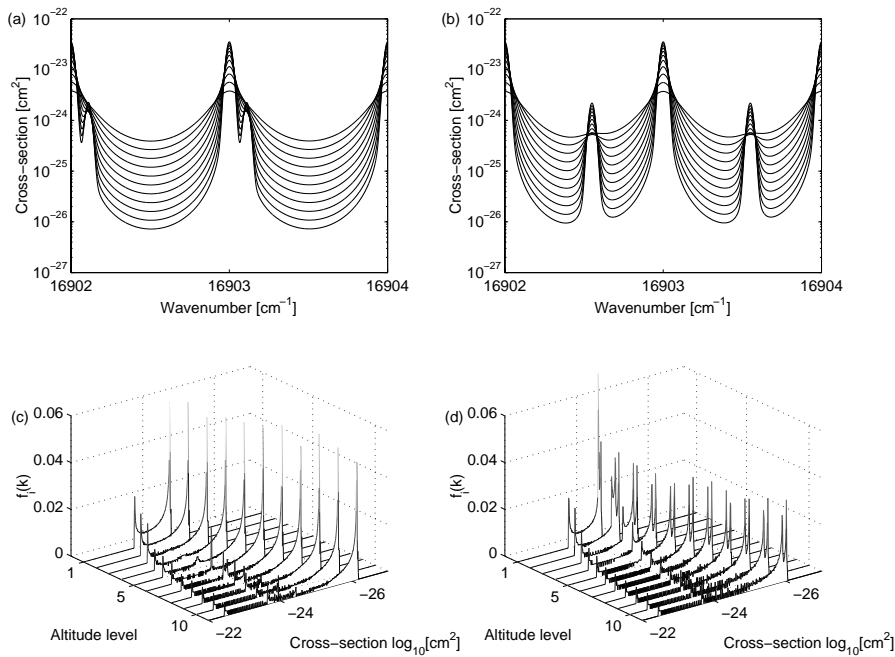
Figure 2.4: Synthetic cross-section spectra for two extremes of line overlap and their dpdf distributions as a function of altitude level for a band of highly-structured line absorptions. Altitude level 1 corresponds to the highest pressure. The line profiles correspond to 11 pressures and temperatures focusing on a 2 cm^{-1} wavenumber range out of a total range of 10 cm^{-1} used to calculate the dpdf's. The line intensities are 1.25×10^{-24} cm/molec for the stronger and 1.63×10^{-25} cm/molec for the weaker lines. The dpdfs show a marked difference according to the separation of the strong and weak line-centers.

for realistic scenarios of, for example, water vapor absorption in the far and near infrared regions.

For completeness we note that the error due to the correlation assumption may be reduced significantly in specific implementations of the ck-distribution method by fine-tuning the quadrature coefficients through exponential sum-fitting to lbl results *Lacis & Oinas* [1991]; *Buchwitz et al.* [2000] or by the use of explicit mapping functions retaining a fixed relation between $\delta\lambda$ and the cross-section $k_j(\delta\lambda)$ at each altitude *Bennartz & Fischer* [1999]. The line intensities used in this section are in fact extremes for water vapor absorption bands near 17000 cm^{-1}. The latter will be used as an example of highly-structured absorption in the remainder of this work.
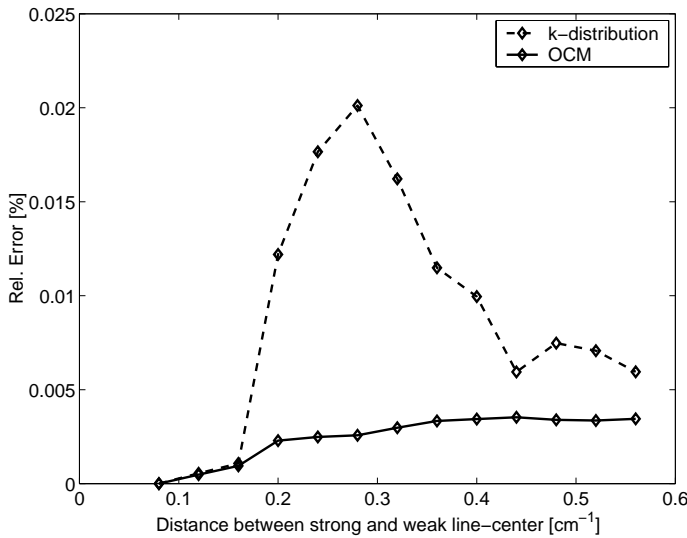
Figure 2.5: Differences between the averaged transmittance calculated using a lbl model and the averaged transmittance determined using OCM and the correlated ck-distribution methods, as a function of the strong/weak line-centers separation. The synthetic absorption spectra are shown in Figure 2.4 and described in detail in the text. The weak lines are submerged in the wings of the strong lines for separations of about 0.1 cm^{-1} and evolve distinct maxima in the corresponding dpdf $f_j(k)$ for low pressures at separations of about 0.2 cm^{-1}. At 0.6 cm^{-1} the weak and the strong absorption lines are as far apart as they can be and have distinct maxima for all pressure and temperatures.

2.3.3   Application: Water Vapor Radiative Transfer Forward Modeling

We consider the case of atmospheric water vapor absorption bands in the visible and shortwave infrared in order to determine the accuracy and limitations of OCM for radiative transfer forward modeling in the context of highly-structured absorption bands. Figure 2.6 displays five of a total of 31 pressure-temperature realizations of the absorption cross-section between 16660 and 17245 cm^{-1} using a resolution of $\delta\lambda$=0.0117 cm^{-1} for line data taken from HITRAN2000 *Giver et al.* [2000]; *Rothman et al.* [1998]. Such realizations correspond to a total number of sampled points $N_{\text{sampled}} = 5 \times 10^4$. Pressure and temperature data together with realistic water vapor density profiles is taken from the European Center for Mid-range Weather Forecasting (ECMWF) (Figure 2.6).

We evaluate the performance of OCM by comparing it with a ck-distribution implementation as laid out in section 2.3.1. The mean transmittance due to absorption $\bar{T}_{abs}(z, \lambda)$ is calculated using both OCM (equation 2.47) and the ck-distribution method (equation 2.54) for the cross-section realizations and water vapor profiles mentioned earlier in this section. The results are compared with each other and with a monochromatic (lbl) calculation of equation (2.1). The methods are compared in terms of number of
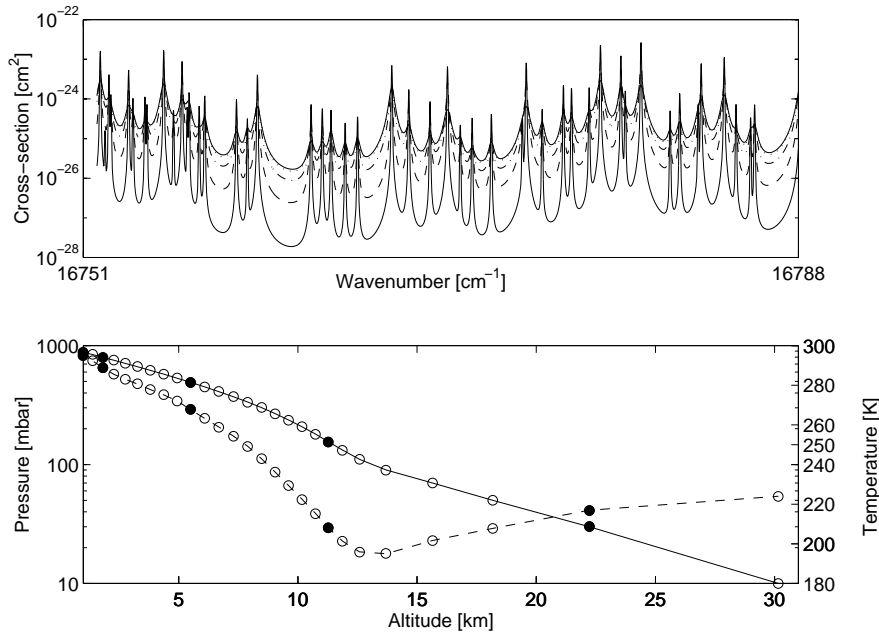
Figure 2.6: Upper panel: Five numerical realizations of the absorption cross-section for water vapor taken from various altitudes in a typical Earth atmosphere. The lowest curve corresponds to the lowest pressure. Lower panel: Atmospheric pressure (solid line) and temperature (dashed line) as a function of altitude for 31 pressure and temperature tuples $(T_\ell(z_\ell), p_\ell(z_\ell))$ taken from ECMWF data. The five filled circles indicate the five altitude levels at which the cross-sections in the upper panel have been calculated.

quadrature points (a term which we use synonymously with number of cross-section bins in the case of OCM) and in terms of sampling width. The number of quadrature points is $B = \dim(\mathcal{Q})$ in the case of OCM and G in the case of the ck-distribution method.

In principle one could distinguish between two cases for method comparison:

1. a *common basis* comparison, where the number of quadrature points is the same for both methods,

$$B = G \tag{2.55}$$

2. an *optimal* comparison, where each of the methods is configured so as to perform better than some required accuracy ϵ, i.e.

$$|\bar{T}_{abs} - \bar{T}_{abs}^{\mathrm{OCM}}| < \epsilon \, , \tag{2.56}$$

$$|\bar{T} - \bar{T}_{abs}^{\mathrm{k-dist}}| < \epsilon \, . \tag{2.57}$$

How does one determine optimality (case 2) for each of the methods? For the ck-distribution, the representation of $f_j(k) = \mathrm{dpdf}(k = \sigma, \mathcal{R})$ is optimal when it is possible
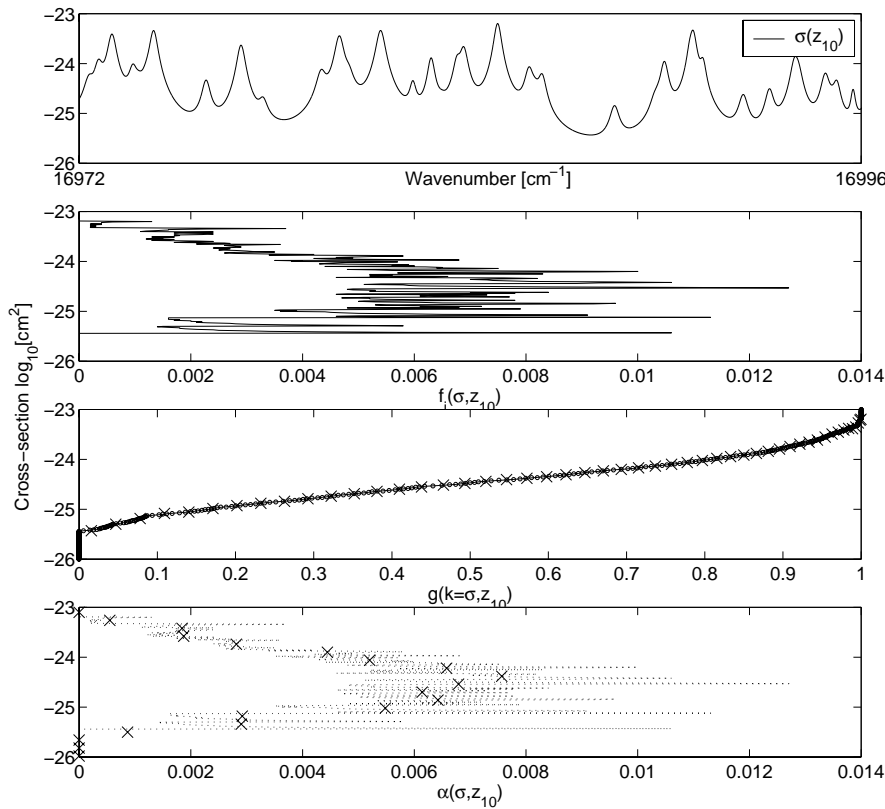
Figure 2.7: Comparison of ck-distribution and OCM implementations. Top panel: Water vapor cross-section of the 10th altitude level of Figure 2.6. Second panel from top: dpdf of the cross-section of the upper panel. Third panel from top: Cumulative density function (cdf) of the dpdf using each discrete point (dots) together with a 50-point quadrature representation (crosses) of the same dpdf. Bottom panel: The same dpdf as in the second panel (dots) together with the relevant part of the corresponding 50-point quadrature representation (crosses).

to obtain an inverse cumulative density function $g^{-1}(k, z_\ell)$ (cf. equation 2.51) and dotted solid line in panel three of Figure 2.7 using the zero point Gauss-Legendre polynomials (crosses in third panel Figure 2.7) such that equation (2.57) is satisfied. Such optimality depends on G, $\dim\{x_{j0}\}$ and $\delta\lambda$.

For OCM, the representation of $\alpha_i(\sigma)$ (see equation 2.14, where f is a log_{10} representation of the cross-section realizations with $f = log_{10}(\sigma(z,\lambda))$ and Eq. 2.13) may be termed optimal when equation (2.57) is satisfied for values B and $\delta\lambda$. Panel four in Figure 2.7 shows a representation of $\alpha_i(\sigma)$ for high B (dotted curve) and low B (crosses).

In some sense the common basis comparison (case 1) is the fairest one to make given that both methods will then have the same number of terms in the exponential sum and thus carry roughly the same computational burden. We note that $\delta\lambda = 0.0117$ cm^{-1} is

kept fixed for the remaining comparisons in this subsection since the accuracy of OCM can be improved arbitrarily by reducing the size of $\delta\lambda$, whereas the accuracy of the basic ck-distribution method is difficult to improve beyond a certain degree of quadrature as we show next.

Degree of Quadrature

The relative error in transmittance for both methods with respect to the results of line-by-line calculations is shown in the middle and lower panels of Figure 2.8, for a sampling width $\Delta\lambda = 25$ cm^{-1} and 31 altitude levels (cf. Figure 2.6) covering a wide range of atmospheric pressure, temperature and water vapor concentration. The number of quadrature points $B = G = \dim\{x_{j0}\}$ has been varied in a common basis comparison. Clearly the error of the ck-distribution method is much smaller than for the OCM method for low number of quadrature points. However the OCM error decreases as the number of quadrature points increases, whereas the error of the ck-distribution method stays constant above approximately 15 quadrature points.

The leveling-off of the ck-distribution error is primarily due to the numerical error introduced by the construction of the dpdf using a numerical binning method rather than using a smooth, analytical band-model representation (cf. Lacis & Oinas *Lacis & Oinas* [1991]). The numerical noise thus introduced cannot be compensated for by increasing the amount of quadrature points. In contrast, when using a smooth, analytical function for $k(g, z_\ell)$, the integral form of the correlated ck-distribution method (Eq. 2.50) may be represented to arbitrary accuracy by Eq. 2.54 by increasing the amount of quadrature points. However, analytical representation of the $k(g, z_\ell)$ functions using band models may result in less accurate results when compared to lbl-calculated transmittance without considerable fine-tuning of the quadrature as mentioned earlier *Lacis & Oinas* [1991] (for a detailed discussion of the usage of analytical analytical representation of the $k(g, z_\ell)$ functions see appendix C).

Sampling Width

We next consider the error introduced by both methods for different sampling widths $\Delta\lambda$. Again the comparison is made on a common basis but this time the degree of quadrature is kept fixed at a relatively high value of 50 points. The results are shown in figure 2.9. For a complex absorption spectrum like that due of the rovibrational band of water vapor discussed already, different widths and positions of the sampling width interval $\Delta\lambda$ may cover different amounts of structure, or more precisely, a different number of distinct lines. In order to accommodate this we performed 20 calculations with both methods for each of a number of sampling width intervals with centers located in a range from 16900–17000 cm^{-1}. The sampling width was allowed to take on a fixed value ranging from 50 to 0.2 cm^{-1} for each set of 20 calculations. The upper panel of Figure 2.9 shows the resulting number of distinct lines as a function of sampling width. Each errorbar shows the maximum spread around the mean values of 20 calculations for each $\Delta\lambda$. There is frequently only one or perhaps no line present in the case of the smaller sampling widths (< 2 cm^{-1}). For sampling widths larger than 25 cm^{-1} the middle and lower panels of Figure 2.9 show that the relative error averaged over 20 calculations per bin for
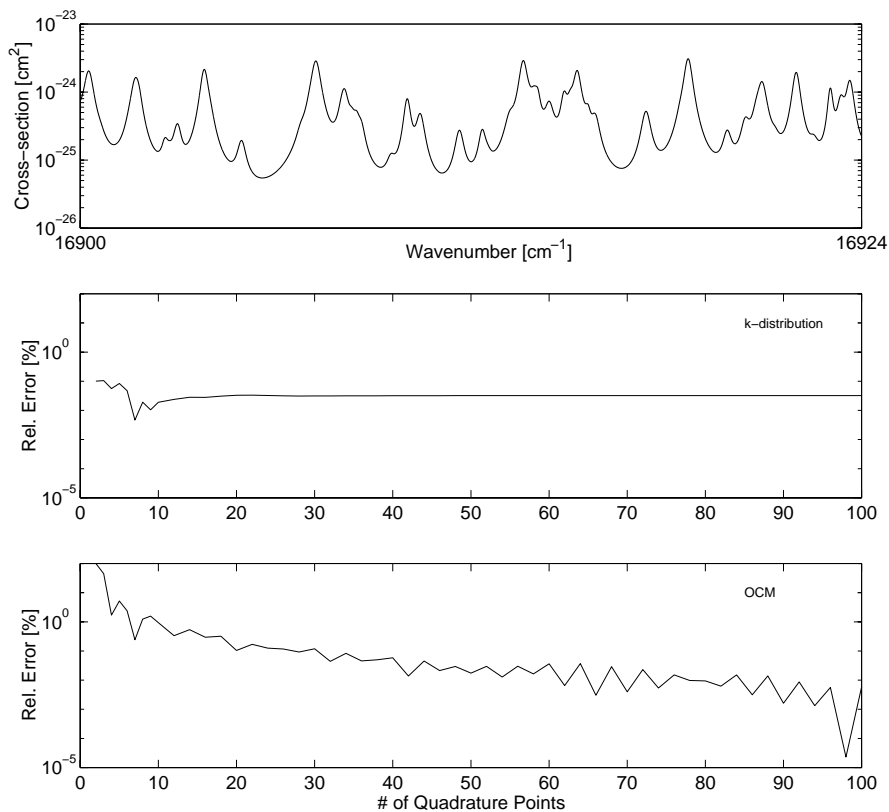
Figure 2.8: Effect of increasing the number of quadrature points. Top panel: same cross-section as in figure 2.7 (solid line). Middle panel: relative residuals between a lbl and ck-distribution calculation of average transmittance, as a function of the number of quadrature points. Bottom panel: Same as the second panel but for the OCM method.

both methods with respect to the line-by-line results is very small. However, for smaller sampling widths, the ck-distribution exhibits significantly more error, whereas the error remains more or less fixed (on average) and generally smaller in the case of the OCM method.

Apparently an accurate representation of $k(g, z_\ell)$ using the Gauss-Quadrature weights a_j is very difficult to achieve when $\Delta\lambda$ contains only a few distinct lines, as is shown in Figure 2.10a. In this case the $g(k, z_\ell)$-curve increases sharply at values very close to one (panel two and three in Figure 2.10a), reflecting that only very few points of the realization of the cross-section represent the highest cross-section values. Panel three of Figure 2.10a also shows that using as many as 50 quadrature points a_j was not sufficient to accurately interpolate the a_j-grid (crosses in Figure 2.10a). Here, even less sampling points would be more appropriate because the over sampling of the flat part of the $k(g, z_\ell)$ curve is increasing the method related error with respect to what is gained by higher sam-
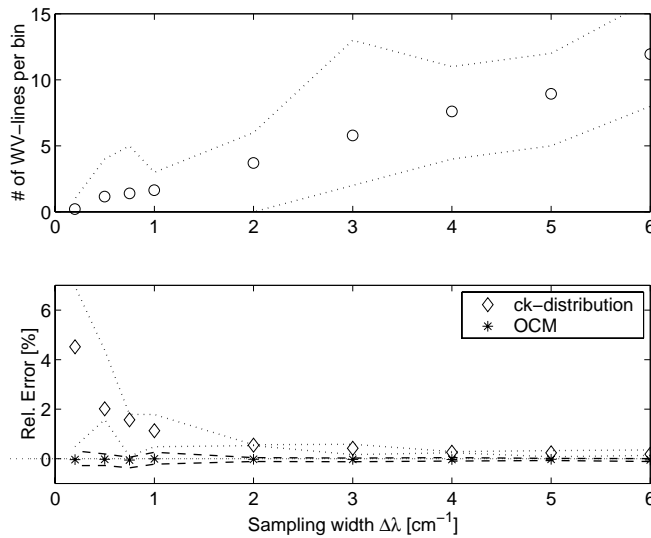
Figure 2.9: Relative Errors of the Methods. The top panel shows the mean number of absorption lines per sampling width used in an average transmittance lbl calculation. For each sampling width 20 calculations of the transmittance were performed within a 100 cm^{-1} region of the water vapor absorption band utilizing 50 quadrature points on a common basis comparison. The dotted line denotes the maximum spread in the number of lines per bin size. Lower panel: Mean relative error for the ck-distribution method (diamonds) and the OCM method (stars) out of 20 calculations with the same bin size for the lbl-calculated transmittance. The dotted and the dashed lines surrounding the error values for both methods show the maximum spread in the relative error. The dotted straight line denotes the zero error value.

pling resolution (section 2.3.3). Figure 2.10b shows the same plots but for a wavenumber region of 25 cm^{-1} (containing about 30 distinct lines). Here the increase of $g(k, z_\ell)$ is much smoother for the regions close to one. Consequently the curve can be accurately represented by Gauss-Legendre Quadrature. In general, sampling regions containing only a small number of different absorption lines with only a few different line intensities result in dpdfs with only a few maxima. This, in turn, results in $k(g, z_\ell)$ functions which exhibit strong changes with respect to g and Eq. (2.50) is consequently difficult to represent in its discretized form (Eq. 2.54).

Summary of Results

The contour plots of Figure 2.11 summarize the results of Figure 2.8 and Figure 2.9 by calculating the relative method-related error for both methods as a function of all possible values for $\Delta\lambda$ and degree of quadrature. For these calculations we simply use one (rather than 20 averaged) calculations per $\Delta\lambda$ interval. The results indicate that both methods give good results in the case of a high number of quadrature points and large sampling
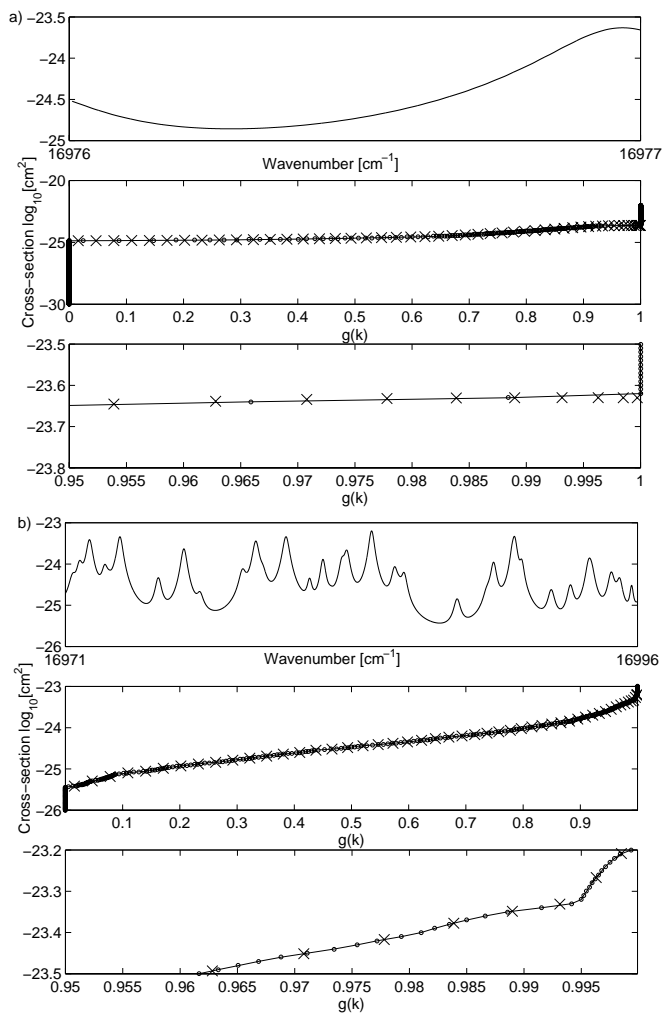
Figure 2.10: (a): The top panel shows a cross section of water vapor for a sampling width of 1 cm^{-1}. The second panel shows the cumulative density function of this cross-section (dots) and its representation by 50 Gauss-Legendre quadrature points (crosses). The third panel shows the same as the second panel but focused in on the region between 0.95 and 1. (b): Same as part (a) but for a larger sampling width (25 cm^{-1}) (top panel). Here, the region of the cumulative density function very close to 1 (lowest panel) can be represented much better by the Gauss-Legendre quadrature points than for the sampling width of part (a).

widths. Overall, OCM appears to be more accurate. However the ck-distribution gives better results for fewer quadrature points. The implication is that the accuracy of the ck-distribution method is limited by the sampling width whereas the accuracy of the OCM method is limited by computational time.
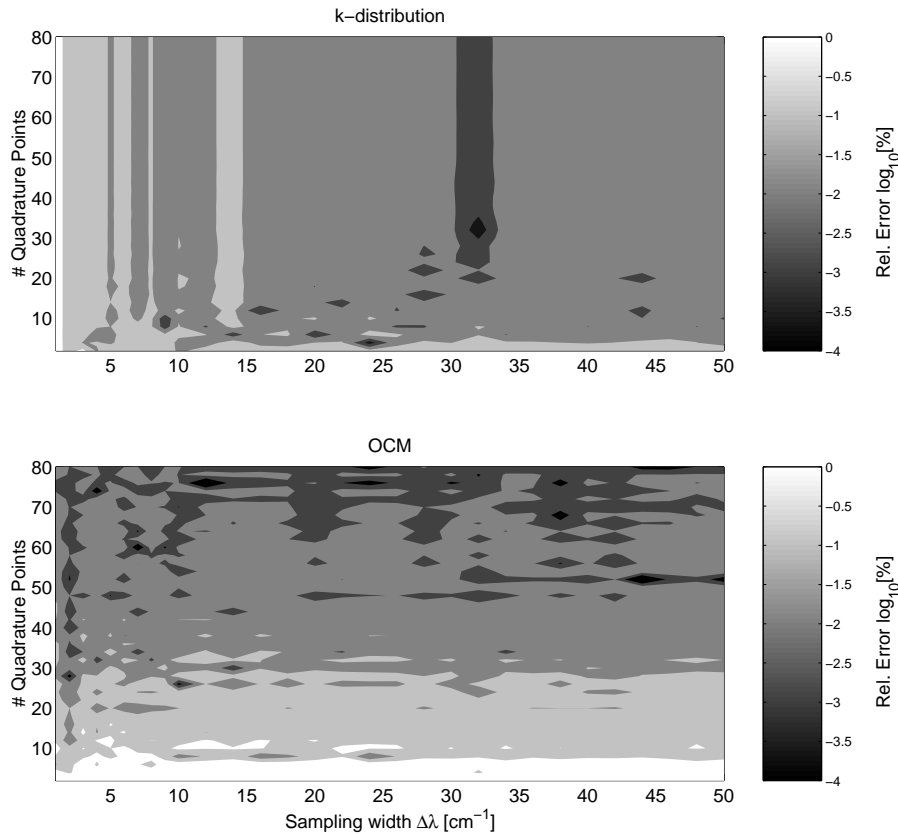
Figure 2.11: Summary of residuals (relative to lbl calculations) of Figure 2.8 and 2.9 for both methods. The top panel shows the relative residual between the average transmittances calculated from lbl and the ck-distribution method as a function of the sampling width and the number of quadrature points. The lower panel shows the same but for the case of OCM.

2.4   Summary

We have provided a method which accurately estimates reduced flux or transmittance due to highly-structured absorption bands. The method is applicable to arbitrary wavelength subsets of numerical realizations of altitude-dependent absorption cross-section profiles. OCM obviates the need for complex analytical formulations of line-by-line extinction. We have shown how it may be applied to radiative transfer forward modeling of absorption and scattering situations to arbitrary order. Perhaps most importantly, OCM formally includes the density profile so that there is no need to invoke correlation assumptions in order to model atmospheric inhomogeneity, as in the case of the ck-distribution method. This greatly simplifies numerical implementations in radiative transfer forward models. The OCM formalism lends itself naturally to profile retrieval from measurements of at-

mospheric upwelling radiation and should be considered as a serious alternative for future generations of retrieval algorithm development as well as for faster radiative transfer forward modeling (see chapter 6 of this thesis).

Acknowledgements

Bibliography

Banks, P. M., and G. Kockarts, Aeronomy, 109 pp., *Academic Press*, New York and London, Part B, 1973.

Bennartz, R., J. Fischer, A modified k-distribution approach applied to narrow band water vapor and oxygen absorption estimates in the near infrared, *J. Quant. Spect. & Rad. Transfer, 66*, 539-553, 1999.

Buchwitz, M., V. V. Rozanov, and J.P. Burrows, A correlated-k distribution scheme for overlapping gases suitable for retrieval of atmospheric constituents from moderate resolution radiance measurements in the visible/near-infrared spectral region, *J. Geophys. Res., 105*, 15,247-15,261, 2000.

Curtis, A. R., Discussion of "A Statistical Model for Water Vapor Absorption", *Q. J. R. Metereol. Soc., 78*, 638-640, 1952.

Fu, Q. and K. N. Liou, On the correlated k-distribution method for radiative transfer in nonhomogeneous atmospheres, *J. Atmos. Sci., 49*, 22, 2139-2156, 1992.

Giver L.P., C. Chackerian and P. Varanasi, Visible and near-infrared ($H_2^{16}O$) line intensity corrections for HITRAN-96, *J. Quant. Spect. & Rad. Transfer, 66*, 101-105, 2000.

Godson, W. L., The evaluation of infrared-radiative fluxes due to atmospheric water vapor, *Q. J. R. Metereol. Soc., 79*, 367-379, 1953.

Goody, R. M., and Y. L. Yung, Atmospheric Radiation: Theoretical Basis, *Oxford University Press*, Oxford, 1989.

Hasekamp, O., and J. Landgraf, Ozone profile retrieval from backscattered ultraviolet radiances: The inverse problem solved by regularization, *J. Geophys. Res., 106*, 8077-8088, 2001.

van der Hulst, H. C., Theory of absorption lines in the atmosphere of the earth, *Ann. Astrophys.,8*, 1-11, 1945.

Kato, S., T. P. Ackerman, J. H. Mather, and E. E. Clothiaux, The k-distribution method and correlated-k approximation for shortwave radiative transfer model, *J. Quant. Spect. & Rad. Transfer, 62*, 109-121, 1999.

Lacis, A. A., and V. Oinas, A description of the correlated k distribution method for modeling nongrey gaseous absorption, thermal emission, and mutlitple scattering in vertically inhomogeneous atmospheres, *J. Geophys. Res., 96*, D5, 9027-9063, 1991.

Lenoble, J., Atmospheric Radiative Transfer, *A. Deepak Publishing*, Hampton, Virginia, 1993.

Malkmus, W., Random Lorentz band model with exponential-tailed s^{-1} line-intensity distribution function, *J. Opt. Soc. Am., 57*, 323-329, 1967.

Maurellis, A. N., Non-Auroral Models of the Jovian Ionosphere, Ph.D. thesis, 75 pp., University of Kansas, June 1998.

O'Brien, D. M., and A.C. Dilley, Infrared Cooling of the Atmosphere: accuracy of correlated k-distributions *J. Quant. Spect. & Rad. Transfer, 64*, 483-497, 2000.

Rees, M. H., Physics and Chemistry of the Upper Atmosphere, *Cambridge University Press*, New York, 1989.

Rodgers, C. D., Inverse Methods for Atmospheric Sounding, *World Scientific*, Singapore, 2000.

Rothman, L.S., *et al.*, The HITRAN molecular spectroscopic database and HAWKS (HITRAN Atmospheric Workstation): 1996 edition, *J. Quant. Spect. & Rad. Transfer, 60*, 665-710, 1998.

Shapiro, D. A., R. Ciurylo, R. Jaworski, and A. D. May, Modeling the spectral line shapes with speed-dependent broadening and Dicke narrowing, *Can. J. Phys.*, 79, 1209-1222, 2001.

Thomas, G. E. and K. Stamnes, Radiative Transfer in the Atmosphere and Ocean, *Cambridge University Press*, United Kingdome, 1999.

Tikhonov, A., On the solution of incorrectly stated problems and a method of regularization, *J. Geophys. Res., 102*, 84-97, 1963.

Chapter 3

Forward Modeling and Retrieval of Water Vapor from GOME: Treatment of Narrow-Band Absorption Spectra

We present the algorithm and results for a new fast forward modeling technique applied to the retrieval of atmospheric water vapor from satellite measurements using a weak ro-vibrational overtone band in the visible. The algorithm uses an Optical Absorption Coefficient Spectroscopy (OACS) method which is well-suited to situations where line widths in the absorption spectrum are much narrower than the instrumental resolution and where efficient numerical solutions of the equation of radiative transfer are needed. We present examples of OACS forward-modeled reflectivity which include the differential contribution of singly-scattered photons and compare them with spectral measurements of the Global Ozone Monitoring Experiment (GOME). In particular, we apply OACS to the retrieval of water vapor column (WVC) densities from GOME spectral data between 585 and 600 nm. Method precisions are better than 0.7% for high and better than 3.4% for low WVC. The total accuracy of the retrieval method appears to be better than 0.8 and 4% for high and low WVC, respectively. The retrieval results are compared to WVC values given by ECMWF and SSM/I and allow us to conclude that the OACS retrieval method is reliable except in cloud-rich situations. In cloud free cases, an upper limit of 18% error on the retrieved WVC due to the impact of multiple and aerosol scattering as well as aerosol extinction is estimated. In addition, the accuracy of the retrieval is sufficient to permit the detection of systematic differential fit mismatches between modeled and real GOME spectra. The magnitude of such mismatches places an upper limit on the accuracy of HITRAN'96 water vapor line strength values of about 10–20%.

3.1   Introduction

Spectroscopic measurements from satellite-based instruments covering relatively broad wavelength regions may be used to affect column and vertical profile retrieval for many different atmospheric constituents. The Global Ozone Monitoring Experiment (GOME) spectrometer on the European Space Agency's ERS-2 satellite [*ESA*, 1995; *Burrows et al*, 1999] covers a wavelength region between 240 and 790 nm. In this wavelength region absorption bands of many constituents such as, for example, $O_2, NO_2, H_2O, O_3, (O_2)_2$, and OClO are measurable. Column concentration retrieval is routinely carried out for O_3 and NO_2 (level 2 products). Important information about OClO, volcanic SO_2, H_2CO from biomass burning and tropospheric BrO, has also been delivered [*Thomas et al*, 1998].

The SCanning Imaging Absorption spectroMeter for Atmospheric CartograpHY (SCIA-MACHY)
[*Bovensmann et al*, 1999] will be launched on ENVISAT in 2001 and will extend wavelength coverage into the near infrared up to 1750 nm while adding two additional channels in regions between 1.9 and 2.4 microns. Thus GOME's list of targeted species will be extended to include CO, CO_2, N_2O and CH_4. The absorption features of some of these gases are often contaminated by strong water vapor absorption bands [*Schrijver*, 1999; *Buchwitz et al*, 2000]. Retrieval of such species would thus require fast forward modeling of the water vapor using the results of a sensitive retrieval method retrieving water vapor column (WVC) concentrations, for example in the visible region of the instrument.

This paper focuses on the retrieval of WVC from GOME measurements in the visible between 585 and 600 nm. This relatively weak absorption window was first described in *Maurellis et al.*, [2000a]. It contains additional absorption features due to sodium, the ozone Chappuis band, the $(O_2)_2$ collision complex, which we account for in this work as well as a weak contribution of NO_2. In contrast, the most prominent water vapor absorption band covered by the GOME detectors is at 720 nm. This band contains, on average, features which are up to an order of magnitude more optically dense than the strongest features in the weak 590 nm band. Nevertheless, we expect that the reflectivity measured in the 720 nm region is less sensitive to changes in pressure and temperature over altitude. Due to the strong absorption in the line center and the strong overlap of the line wings in the lower troposphere, at high pressures and high water vapor content, the 720 nm region is less sensitive to changes in WVC. In this paper we present a new method called Optical Absorption Coefficient Spectroscopy (OACS) which allows both for fast and accurate forward modeling of GOME reflectivity measurements affected by water vapor absorption as well as relatively fast retrievals of WVC.

Until recently the retrieval of WVC from GOME measurements was not successful without the introduction of substantial modification [*Noël et al*, 1999; *Casadio et al*, 2000] to differential methods such as the Differential Optical Absorption Spectroscopy method (DOAS) [*Platt*, 1994; *Platt et al*, 1999] used for the retrieval of GOME level 2 products [*Burrows et al*, 1999]. In principle, DOAS operates by separating out the broadband absorption structure due to elastic scattering or broad-band absorption from the differential structure of the trace gas under study in order to fit Beer's Law to a measured reflectivity spectrum. DOAS offers a good compromise between speed, numerical accuracy and instrument performance and has repeatedly proven its usefulness for many molecular species. However it is frequently combined with a simple arithmetric wavelength-averaging

of optical densities for broad band absorbers in order to establish a linear dependence
between the logarithm of the measured reflectivity and the fit parameters [*Marquard et
al*, 2000; *Burrows et al*, 1999]. In this case, the retrieval of the atmospheric water vapor
concentrations would result in a systematic underestimation of the expected WVC due to
an inadequate sampling of highly-varying optical densities by a single detector pixel [*Maurellis et al*, 2000a,b]. In addition, discrepancies may also arise out of inadequate treatment
of air mass factors used to account for the contribution of atmospheric scattering [*Noël
et al*, 1999; *Casadio et al*, 2000].

It is important to make the distinction between *narrow-band* and *broad-band* absorbers
in the context of a spectral fitting window in order to separate the reflectivity contribution
of absorbers with strong differential structure from the relatively smooth background. In
addition to coping with intrinsic spectral complexity the retrieval of atmospheric trace
gas columns also requires accurate spectral information as well as spectrometers which
operate at sufficient spectral resolution. However, spectral coverage (i.e., the potential to
retrieve a wide variety of atmospheric constituents using a single instrument) usually has
to be compromised by a reduction in spectral resolution. For example, two linear array
detectors with 1024 detector pixels each are needed in order to cover the wavelength
range of the Ozone Chappuis band between 400 and 800 nm using the GOME instrument (channel three and four), where each detector pixel covers a wavelength range of
about 0.2 nm. The spectral sampling is sufficient to resolve spectral absorption features
of many species especially in the near ultraviolet where line-broadening by predissociation of excited molecular states causes the optical density to vary little within the span
of a single detector pixel (for example in the case of ozone). In contrast, many species
with absorption bands in the visible and near-infrared (for example, water vapor, NO_2,
methane, or atomic species like sodium) lack smoothing from line-broadening and may
contain a number of distinct absorption lines within the wavelength region covered by one
detector pixel. This also holds for wide parts of the solar irradiance spectrum over the
entire ultraviolet and visible regions which contains narrow-band Fraunhofer absorption
lines.

The fast forward modeling and retrieval method presented here focuses on the problem
of spectral sampling in cases of such narrow-band absorption spectra. This means that
the spectral width of the instrumental function and the sampling width of the detector is
much broader than the width of a single absorption line. In such cases a convolution and
sampling integral over the modeled highly structured reflectivity spectra has to be introduced when modeling the spectra measured by an instrument with insufficient sampling
capacity. The proposed Optical Absorption Coefficient Method (OACS) shows that this
problem can be solved accurately and with sufficient efficiency that, using operational
data from GOME in the visible, the water vapor column (WVC) retrieved is comparable
to other fundamental different satellite measurement techniques and data assimilation
models [*Vesperini et al*, 1998; *Chaboureau et al*, 1998].

The problem of the treatment has also been dealt with by a new Spectral Structure
Parameterization (SSP) method [*Maurellis et al*, 2000b]. In the latter work it was shown
that the complexity of spectra ranging from single line absorption to broad-band absorption may be characterized, to second order in accuracy, by a simple parameterization
scheme. In what follows we show that the OACS retrieval method permits both fast and
accurate forward modeling of reflectivities as well as relatively fast retrievals of trace gas

concentrations.

In principle, an OACS retrieval method could take advantage of the DOAS method in the sense that it could utilize a first-order polynomial in order to account for the unknown surface albedo as well as the non-structured background contribution of atmospheric scattering. However, in order to account for the contribution of single-scattered photons, we show that a more accurate representation can be obtained in the form of an additional OACS term derived from the solution of the equation of radiative transfer. However, the contribution of multiplescattering can be significant in the visible region covered by this instrument. Therfore a polynomial similar to the one used in standard DOAS methods is introduced to account for the broad-band contribution of multiple-scattered photons. The influence of the neglected differential contribution of the latter on the modeled reflectivities as well as fit residuals and retrieved WVCs has to be estimated and discussed in some detail. However, apart from these assumptions, OACS already displays the ability to retrieve WVCs for low cloud cover situations with an accuracy of state-of-the-art products like the ones from the European Center of Medium Range Weather Forecast (ECMWF) and the Special Sounder Microwave Imager (SSM/I). In addition, this first extensive study retrieving water vapor from GOME operational data in the visible shows the potential of OACS to be applied to WVC retrieval from the forthcoming SCIAMACHY instrument especially in the infrared.

In Section 3.2 we introduce the radiation transport scheme on which OACS is based together with the mathematical formulation of the method. Section 3.3 briefly describes the GOME instrument performance and how GOME-measured earth radiances and solar irradiances are handled for the purposes of WVC retrieval. The issue of undersampling and the specific definition of reflectivity used for retrievals from GOME data are also presented. In section 3.4 the HITRAN'96 water vapor line-strength values used in the OACS method are described in some detail since the method's sensitivity to changes in the reflectivity with respect to the cross-section of the trace gas under study requires an accurate knowledge of the line parameters and their dependence on the pressure and temperature for a specific geolocation. A retrieval of WVCs from an entire water vapor absorption band requires accurate modeling of all additional absorbers within this band in order to prevent the fit from confusing part of the instrumentally smoothed water vapor absorption spectrum with the background. An introduction in the modeling of this background together with a description of the required input data is also given in Section 3.4. Section 3.5 estimates the intrinsic OACS method-related error due to the specific sampling of the intensities. Section 3.6 describes the forward modeling of GOME spectral measurements using the OACS method. The results are compared to an independent solution of the equation of radiative transfer using a doubling-adding model (DAM) [*de Haan et al*, 1987]. In section 3.7 the effect on the retrieved WVC due to the differential contribution of photons scattered more than once in the atmosphere (multiplescattering) as well as aerosol scattering and absorption are discussed and quantified using results of the DAM model. In Section 3.8 we estimate the precision and the accuracy of the method by retrieving WVCs from artificial absorption spectra which are forward-modeled using a lbl calculation. Here we also present a study of the influence of multiplescattering and aerosol loading on the retrieved WVC. The results of WVC-retrieval from three different GOME tracks are presented in Section 3.9. In this section we also discuss the impact of differential fit mismatches on the residuals and the retrieved WVCs which we relate

predominantly to instrumental errors and to errors in the water vapor line-strength values
taken from the HITRAN'96 database. A preliminary validation of the OACS retrieval
results using ECMWF and SSM/I data is set out in section 3.10. The latter is discussed
in conjunction with the effect of clouds. Finally, in Section 3.11, we focus on potential
implementation of the OACS method in routine retrieval and its use for forward modeling
of water vapor absorption bands in spectral regions containing narrow-band absorption
features other than water vapor.

3.2   Optical Absorption Coefficient Spectroscopy

The transport equation of scalar radiative transfer in its plane parallel approximation is
given by

$$\mu \frac{dI_\lambda}{dz}(z, \Omega) = -\beta_{\text{ext}}(z)\{I_\lambda(z, \Omega) - J_\lambda(z, \Omega)\} \tag{3.1}$$

where I_λ is the specific intensity field for a given wavelength λ, J_λ is the corresponding
source function and β_{ext} is the extinction coefficient (see Table 1). Further, z represents
the altitude and Ω is the direction of the intensity field with $\Omega = (u, \varphi)$, where $\mu = |u|$ is
the cosine of the zenith angle. I_λ is subject to boundary conditions at the top and bottom
of the atmosphere ($z = 0$ and z_{top}), respectively, of the form

$$I_\lambda(z_{\text{top}}, \Omega_-) = 0 \tag{3.2}$$

$$I_\lambda(0, \Omega_+) = \frac{\Lambda}{\pi} F^\downarrow \tag{3.3}$$

for which we have assumed isotropic ground reflection by a Lambertian surface with an
albedo Λ. Here, Ω_+ and Ω_- indicate upward and downward directions, respectively, and
$F^\downarrow$ is the downward flux at the lower boundary of the atmosphere,

$$F^\downarrow = \int_{\Omega_-} I(0, \Omega)\, \mu\, d\Omega \,. \tag{3.4}$$

Neglecting multiplescattering in the visible part of the solar spectrum, the source function
is given by

$$J_\lambda(z, \Omega) = F_o \frac{\beta_{\text{sca}}(z)}{\beta_{\text{ext}}(z)}\, P(z, \Omega_o, \Omega)\, e^{-\tau(z)/\mu_o} \tag{3.5}$$

where β_{sca} is the scattering coefficient, F_o is the incoming solar flux, P is the scattering
phase function and Ω_o, μ_o describes the solar geometry. The optical depth τ is defined by

$$\tau(z) = \int_0^z \beta_{\text{ext}}(z')\, dz' \,. \tag{3.6}$$

Thus, in the singlescattering approximation, the radiative transfer equation (3.1) can
be integrated easily, which provides the reflected intensity field at the top of the atmo-
sphere as a function of the boundary condition (3.3),

$$I_\lambda(z_{\text{top}}, \Omega) = I_\lambda(0, \Omega)\, e^{-\tau(0)/\mu}$$

$$+ \quad \frac{F_o}{\mu} \int\limits_o^{z_{top}} \beta_{sca}(z) \, e^{-\tau(z)\frac{\mu_o+\mu}{\mu_o\mu}} P(z,\Omega,\Omega_o) dz \qquad (3.7)$$

If we further assume that the downward flux $F^\downarrow$ in (3.3) is dominated by its direct beam contribution

$$F^\downarrow \approx \mu_o \, F_o \, e^{-\tau(0)/\mu_o} \,, \qquad (3.8)$$

we can approximate the specific intensity in the viewing direction of the satellite with

$$I_\lambda(z_{\text{top}}, \Omega) = \frac{\Lambda}{\pi} \mu_o F_o \, e^{-\tau(0)\frac{\mu_o+\mu}{\mu_o\mu}}$$

$$+ \quad \frac{F_o}{\mu} \int\limits_o^{z_{top}} \beta_{sca}(z) \, e^{-\tau(z)\frac{\mu_o+\mu}{\mu_o\mu}} P(z,\Omega,\Omega_o) dz \qquad (3.9)$$

Let us now assume that Rayleigh scattering is the dominant form of single scattering. In this case we may write the scattering coefficient $\beta_{\text{sca}}(z,\lambda)$ as,

$$\beta_{sca}(z,\lambda) = \sigma_R(\lambda) \sum_{k=1}^{K} n_k(z). \qquad (3.10)$$

Here n_k denotes the density of the kth species and $\sigma_R(\lambda)$ is the Rayleigh scattering cross-section with a corresponding phase function of

$$P(\Omega_o \to \Omega) = p(\theta) = \frac{3}{4}(1 + \cos^2 \theta), \qquad (3.11)$$

satisfying

$$\frac{1}{4\pi} \int p'(\Omega \to \Omega') d\Omega = 1. \qquad (3.12)$$

We now consider a satellite instrument which spectrally redistributes incoming intensities because of the slit in the path of the optics. The result is, that the detectors sample a smoothed intensity. We assume that this may be accounted for by convolving the measured intensity using an instrumental response function $\mathcal{H}(\lambda, \lambda'; \Sigma)$ with a spectral σ-width Σ. After the convolution is performed the intensity is sampled by simply averaging over the wavelength region $\Delta\lambda$ covered by one detector pixel. In addition we assume that the differential contribution of Fraunhofer line absorption in the measured solar irradiance is negligible. By dividing $I \equiv I_\lambda(z_{\text{top}}, \Omega)$ from Eq. 3.9 with $\mu_o F_o$ we write the unitless normalized reflectivity R measured by a single detector pixel j as

$$R_j = \int_{\Delta\lambda_j} \int_{-\infty}^{+\infty} \frac{\pi I}{\mu_o F_o} \mathcal{H}(\lambda, \lambda'; \Sigma) d\lambda' \frac{d\lambda}{\Delta\lambda_j}. \qquad (3.13)$$

Here, the outermost wavelength integral takes place over detector pixel wavelength range $\Delta\lambda_j$. For convenience it is possible to separate Eq. 3.13 into a pure surface reflectance and an atmospheric single-scattering part, $R_j = R_{\text{surf,j}} + R_{\text{ss,j}}$, using Eq. 3.9 with $\tilde{\mu} \equiv (\frac{1}{\mu_o} + 1)$ in the case of a nadir viewing instrument ($\mu = 1$), such that

$$R_{\text{surf,j}} = \Lambda \int_{\Delta\lambda_j} \int_{-\infty}^{+\infty} e^{-\tau(z_0,\lambda')\tilde{\mu}} \mathcal{H}(\lambda,\lambda';\Sigma) \mathrm{d}\lambda' \frac{\mathrm{d}\lambda}{\Delta\lambda_j} \qquad (3.14)$$

accounts for the reduced intensity of the measured light reflected at the ground level
by absorption and scattering out of the light path and

$$
\begin{aligned}
R_{\text{ss,j}} &= \frac{p(\theta)}{4\mu_o} \int_{\Delta\lambda_j} \int_{-\infty}^{+\infty} \left[\int_0^\infty \beta_{\text{sca}}(z,\lambda') e^{-\tau(z,\lambda')\tilde{\mu}} dz \right] \\
&\times \ \mathcal{H}(\lambda,\lambda';\Sigma) \mathrm{d}\lambda' \frac{\mathrm{d}\lambda}{\Delta\lambda_j}
\end{aligned}
\qquad (3.15)
$$

accounts for light undergoing single scattering at each altitude z. We now separate
the various absorbers into constituents k, for which the change in cross-section within the
wavelength region $\Delta\lambda$ is very small (for example the Rayleigh scattering cross-section σ_R)
and constituents f with narrow-band cross-sections within $\Delta\lambda$. In the case of $\Delta\lambda \ll \Sigma$
we may exchange the position of the sampling and the convolution integral and write Eq.
3.14 and 3.15 as

$$
\begin{aligned}
R_{\text{surf,j}} &= \Lambda \int_{-\infty}^{+\infty} \left\{ e^{-\sum_{k=1}^K \int_{z_0}^\infty \bar{\sigma}_k(z') n_k(z') \tilde{\mu} dz'} \right. \\
&\times \ \left. \int_{\Delta\lambda_j} e^{-\sum_{f=1}^F \int_{z_0}^\infty \sigma_f(z',\lambda) n_f(z') \tilde{\mu} dz'} \frac{d\lambda}{\Delta\lambda_j} \right\} \\
&\times \ \mathcal{H}(\lambda,\lambda';\Sigma) \mathrm{d}\lambda' \ ,
\end{aligned}
\qquad (3.16)
$$

and

$$
\begin{aligned}
R_{\text{ss,j}} &= \frac{p(\theta)}{4\mu_o} \int_{-\infty}^{+\infty} \left\{ \int_0^\infty \left[\beta_{\text{sca}}(z,\lambda') \right. \right. \\
&\times \ e^{-\sum_{k=1}^K \int_z^\infty \bar{\sigma}_k(z') n_k(z') \tilde{\mu} dz'} \\
&\times \ \left. \left. \int_{\Delta\lambda_j} e^{-\sum_{f=1}^F \int_z^\infty \sigma_f(z',\lambda) n_f(z') \tilde{\mu} dz'} \frac{d\lambda}{\Delta\lambda_j} \right] dz \right\} \\
&\times \ \mathcal{H}(\lambda,\lambda';\Sigma) \mathrm{d}\lambda' \ .
\end{aligned}
\qquad (3.17)
$$

Here $\bar{\sigma}_k$ is the arithmetic mean cross-section of the kth absorber with a low-frequency
spectral structure within $\Delta\lambda$. The problem remains to formulate the innermost integral,
i.e. the sampling term over the high frequency components, in a way that is still suitable
for a relatively fast forward modeling and fitting.

3.2.1 Opacity Sampling Method

Recently a new opacity-sampling technique was proposed [*Maurellis*, 1998] which rapidly
evaluates the wavelength-averaged Lambert-Beer's Law transmittance due to any general

Table 3.1: Summary of Some of the Most Important Notations Used in This Paper

Sign	Description
k	A. c.[a] with broad-band X-s.[b]
f	A. c. with narrow-band X-s.
ℓ	Atmospheric layer
μ_o, μ	Incoming and outgoing angle cosine
j	Detector pixel number
i	Cross-section bin
$\bar{\alpha}_{ij}^{(\ell)}$	Alpha value interpolated in p, T
ξ_i	X-s. bin center value
Σ	Instrument slit-width
$\Delta\lambda$	Detector pixel width
γ	WV-line HWHM
$\delta\lambda$	Grid size reference spectra
I, I_0	Specific intensities
R	Reflectivity $(= (\pi/\mu_o)I/I_0)$
Λ	Surface albedo
$S_{\hat{\nu}}$	Line strength
$\Delta\phi$	Differential fit mismatch correction

[a] Atmospheric constituent
[b] Cross-section

line or continuum absorption spectrum in a nongray atmosphere. It utilizes numerical realizations of pressure- and temperature-dependent absorption cross-sections in order to compute the non-normalized discretized probability density function (pdf), denoted α_{ij}, of the cross-section at a value of ξ_i, over a wavelength range $\Delta\lambda$. The pdf thus carries the information of the detailed spectral structure as a function of absorption cross-section ξ_i within the wavelength range of a detector pixel j and satisfies

$$\int_{\Delta\lambda_j} \sigma(\lambda)\, d\lambda \approx \sum_{i \in \mathcal{R}} \alpha_{ij} \xi_i \delta\lambda.$$

$\mathcal{R}$ denotes an ordered, non-overlapping set of bin indices covering the full range of possible values of the absorption cross-section and with bin centers given by the values of ξ_i.

It has been shown [*Maurellis*, 1998] that the Beer's law component of an one-species form of Eq. (3.14) may be expressed without the convolution in the integral as

$$\int_{\Delta\lambda_j} \exp\left(-\int_{\infty}^{z} \sigma(\lambda, z')n(z')dz'\right) \frac{d\lambda}{\Delta\lambda_j} \approx$$

$$\sum_{i \in \mathcal{R}} \eta_{ij} \exp\left[-\xi_i \int_{\infty}^{z} n(z')\,dz'\right] \frac{\delta\lambda}{\Delta\lambda_j}, \qquad (3.18)$$

where

$$\eta_{ij} = \frac{\displaystyle\int_{\infty}^{z} \alpha_{ij}(z')\,n(z')\,dz'}{\displaystyle\int_{\infty}^{z} n(z')\,dz'}$$

The wavelength grid size, $\delta\lambda$, is the crucial parameter in the trade-off between computational speed and the accuracy of the representation in Eq. (3.18). We choose $\delta\lambda = 2 \times 10^{-3}\Delta\lambda$ in this work. Next, the integral over path $\mathcal{S}$ may be altitude-discretized by writing it as a summation over a series of atmospheric layers ℓ with column densities N_ℓ (see Fig. 3.1), viz.

$$\int_{\Delta\lambda_j} \exp\left(-\int_{\infty} \sigma(\lambda, z')n(z')dz'\right) \frac{d\lambda}{\Delta\lambda_j} \approx$$
$$\sum_{i} \bar{\eta}_{ij}^{\ell} \exp\left(-\xi_i \sum_{\ell=1}^{L} N_\ell\right) \frac{\delta\lambda}{\Delta\lambda_j}, \qquad (3.19)$$

where

$$\bar{\eta}_{ij}^{\ell} = \frac{\displaystyle\sum_{\ell=1}^{L} \bar{\alpha}_{ij}^{(\ell)} N_\ell}{\displaystyle\sum_{\ell=1}^{L} N_\ell},$$

and $\bar{\alpha}_{ij}^{(\ell)} = \alpha_{ij}(T_\ell(z_\ell), p_\ell(z_\ell))$. In this formulation N_ℓ contains an implicit multiplicative factor which accounts for the greater air mass traversed by non-zero solar zenith angle photons. In all calculations we assume that this air mass correction factor is determined simply by spherical geometry.

The use of Eq. (3.19) to replace the spectral sampling integral we call an Opacity Coefficient Method (OCM). The coefficients $\bar{\alpha}_{ij}^{(\ell)}$ represent the probability density function for cross-section averaged out over each atmospheric level ℓ. In practice they are determined from spectral realizations (see Section 3.4) for each detector pixel j which have been pre-calculated for a range of temperatures and pressures. These pre-calculations are used to compile an $\alpha_{ij}(p, T)$ table for every combination of i and j. Independently acquired temperature and pressure profiles (in terms of an altitude grid $\{z_0, z_\ell\}$, see Fig. 3.1) corresponding to a specific reflectivity measurement are then used to interpolate between entries in the $\alpha_{ij}(p, T)$ tables in order to obtain $\bar{\alpha}_{ij}^{(\ell)}$ appropriate to each atmospheric altitude level.

Substituting Eq. (3.19) back into Eq. (3.16) and (3.17) yields

$$\hat{R}_{\text{surf,j}} = \Lambda \int_{-\infty}^{+\infty} \left\{ e^{-\sum_{k=1}^{K} \int_{z_0}^{\infty} \bar{\sigma}_k(z')n_k(z')\tilde{\mu}dz'} \right.$$
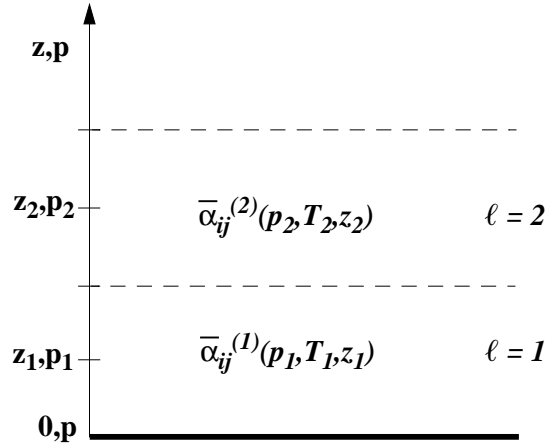
Figure 3.1: Each atmospheric layer ℓ is defined such that the values for pressure p_ℓ and temperature T_ℓ at altitude z_ℓ of a given profile are the mean values of each layer ℓ. In this way $\bar{\alpha}_{ij}^{(\ell)}(p_\ell, T_\ell)$ represents the mean coefficient values for each layer ℓ interpolated in pressure and temperature from the $\alpha_{ij}(p, T)$-table, where p and T are taken from a fixed grid of pressures and temperatures used for the construction of the table.

$$
\begin{aligned}
&\times \quad \sum_i \frac{\sum_\ell \bar{\alpha}_{ij}^{(\ell)} N_\ell \tilde{\mu}}{\sum_\ell N_\ell \tilde{\mu}} \, e^{\left(-\xi_i \sum_\ell N_\ell \tilde{\mu}\right)} \frac{\delta\lambda}{\Delta\lambda_j} \Bigg\} \\
&\times \quad \mathcal{H}(\lambda, \lambda'; \Sigma) \mathrm{d}\lambda' \qquad\qquad\qquad\qquad\qquad (3.20)
\end{aligned}
$$

$$
\begin{aligned}
\hat{R}_{\mathrm{ss,j}} = \quad &\frac{p(\theta)}{4\mu_o} \int_{-\infty}^{+\infty} \left\{ \int_0^\infty [\beta_{\mathrm{sca}}(z, \lambda') \right. \\
\times \quad & e^{-\sum_{k=1}^K \int_z^\infty \bar{\sigma}_k(z') n_k(z') \tilde{\mu} dz'} \\
\times \quad & \sum_i \frac{\sum_\ell \bar{\alpha}_{ij}^{(\ell)} N_\ell \tilde{\mu}}{\sum_\ell N_\ell \tilde{\mu}} \, e^{\left(-\xi_i \sum_\ell N_\ell \tilde{\mu}\right)} \frac{\delta\lambda}{\Delta\lambda_j} \Bigg] dz \Bigg\} \\
\times \quad & \mathcal{H}(\lambda, \lambda'; \Sigma) \mathrm{d}\lambda' \qquad\qquad\qquad\qquad\qquad (3.21)
\end{aligned}
$$

which is the basic form used in this work for verification against forward modeling of the Eq. (3.14) and (3.15) (cf. chapter 2, Eq. 2.45). We further include an additional first order polynomial term to account for the broad-band contribution of aerosol scattering and multiply scattered photons, both for forward model verification against results from other radiative transfer models as well as in the retrieval algorithm (see Section 3.6). The impact of the differential spectral contribution of this additional term is discussed in Section 3.7.
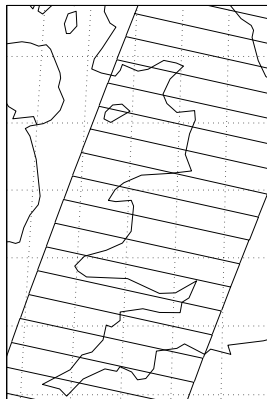
Figure 3.2: GOME ground surface pixel coverage (solid boxes) of about
$0.4° \times 4°$ shown along with the $1°$-grid size of the ECMWF assimilation
model (dotted grid).

3.3   GOME Measurements

3.3.1   Operation

The GOME instrument is a four-channel grating spectrometer covering a wavelength
range between 240 to 790 nm. The spectra are recorded simultaneously for each wave-
length. The instantaneous nadir field of view (IFOV) is $2.9° \times 0.14°$ (along $\times$ across the
track) and earth radiances are integrated for 1.5 seconds by scanning from east to west
which corresponds to an earth footprint of about 40×320 km^2 (Fig. 3.2). In the current
study only nadir radiances are used so that the mean angle between the satellite IFOV
and zenith is zero. However, we could easily account for other angles between the satel-
lites line-of-sight and the zenith. GOME solar irradiance measurements are performed
once a day. The detector pixel-to-pixel variability is smaller than 2% and is monitored by
LED's illuminating the detector arrays. The correction for the pixel-to-pixel variability,
the straylight and leakage fraction, and the noise produced by the cross-talk from the
Peltier coolers is part of the level 0 to 1 data processing [*DLR*, 1996, 1999]. The solar
irradiance and the earth radiance measurements are also corrected for the polarisation
sensitivity of the instrument. After applying these corrections the GOME level 1 data
product provides a calibrated earth radiance spectrum I in photons/(cm$^2 \cdot$ nm $\cdot$ sec $\cdot$ sr)
and a calibrated sun irradiance spectrum πF in photons/(cm$^2 \cdot$ nm $\cdot$ sec). Table 2 sum-
marizes some of the most important instrument characteristics of the GOME instrument.

3.3.2   Spectral Resolution and Undersampling

In a retrieval or in a study of forward-modeled reflectivity using high resolution reference
cross-sections, an instrumental response function with a σ-width Σ has to be applied to
the modeled reflectivity (Eq. 3.13). This function takes into account the photon energy

Table 3.2: The GOME Instrument Performance (585–600nm)

Number of used detector pixels	69
FWHM slit function (ch3)[a]	0.27 nm
Detector pixel width $\Delta\lambda$ (ch3)	0.2 nm
Instantaneous Field Of View	$2.9^o \times 0.14^o$
Ground pixel size (Fig. 3.2)	40×320 km^2
Pixel-to-pixel variability	$< 2\%$
Random noise value	0.1%
Accuracy of absolute radiances	1%

[a]Channel 3

redistribution due to the slit. In the case of the GOME instrument it may be represented by convolving the radiatively-transported absorption spectra with a Gaussian function which has a full-width-half-maximum (FWHM) of 0.27 nm. The detector pixel coverage is about 0.2 nm within channel 3, i.e. the convolved absorption spectrum is wavelength averaged over a wavelength region of 0.2 nm covered by each detector pixel. This means that in the case of GOME the spectral resolution (Σ) is close to the spectral sampling by the detector pixels ($\Delta\lambda$) and so the requirement that $\Delta\lambda$ be much less than Σ, as was assumed for Eq. 3.16 and 3.17, is not satisfied, i.e the instrument undersamples all absorption features with effective widths close to or smaller than the FWHM of the slit function.

3.3.3   Spectral Calibration and Rebinning

The in-flight spectral wavelength calibration of the radiance and the irradiance is done using an on-board Pt/Cr/Ne hollow cathode gas-discharge lamp. Temperature changes over the orbit are taken into account in the spectral calibration. The error on the calibration is known to be on the order of 0.004 nm [*Caspar & Chance*, 1997]. We note that the interpolation of radiances measured by an instrument with a low sampling rate onto a different grid may introduce significant errors [*Roscoe*, 1996]. Moreover different wavelength calibrations are used for the sun irradiance measurement and the earth radiance. Thus, in this study, both spectra are *rebinned* instead of interpolated on a standard wavelength grid defined for an OACS retrieval. The rebinning procedure is carried out as follows. For each measurement, the GOME-reported radiance and irradiance wavelengths are assumed to define the central wavelengths of two different sets of bins. After adjustment for Doppler shift (see following paragraph), a fraction of the intensity within each bin is redistributed to the nearest bin of the predefined standard grid according to their fractional overlap in wavelength. In this way, the intensity of a high resolution reference absorption spectra integrated over one bin of the standard grid with $\delta\lambda << \Delta\lambda$ can be correlated with the *rebinned* GOME detector pixel-averaged intensity on the same grid without introducing errors in the integrated reflectivity per detector pixel bin. Thus, rather then adjusting the alpha coefficients for a shift of the wavelength grid due to different calibrations we adjust the measured GOME spectra to the standard grid used by OACS. The alpha co-

efficients can therefore be taken from a look-up table interpolated only over pressure and
temperature (*and not over wavelength*).

   We correct the Doppler-shifted irradiance calibration with a knowledge of the relative
velocity of the spacecraft to the sun provided for each sun irradiance measurement. The
relative velocity is about 6 km/sec which results in a wavelength shift of about 0.01 nm
(about 5% with respect to a pixel). Hereafter, reflectivity always refers to a Doppler
shift-corrected measurement.

3.4   Molecular Absorption Spectra and Atmospheric Profiles

3.4.1   Water Vapor Absorption Spectra

We use the HITRAN'96 database to calculate a number of realizations of a water va-
por absorption spectrum covering the entire altitude range for which we have pressure
and temperature profiles available, for each given geolocation. The main spectral pa-
rameters provided by the HITRAN'96 database are the integrated cross-section values
(line strength) $S_{\hat{\nu}}$ in $cm^{-1}/(molec \cdot cm^{-2})$ and the pressure-dependent air-broadened line
halfwidth γ_{air} in cm^{-1}/atm. For a detailed description of the calculation of the temper-
ature correction of the integrated line intensity the reader is referred to *Rothman et al.*,
[1998].

   The pressure-broadened line half-width-half-maximum HWHM $\gamma(p, T)$ for a gas at
pressure p [atm], temperature T [K], and partial pressure p_{self} [atm] is calculated by

$$\gamma(p, T) = \left(\frac{T}{T_{ref}}\right)^n \left(\gamma_{air}(p_{ref}, T_{ref})p_{air}\right), \tag{3.22}$$

   where γ_{air} is the line-broadening contribution due to collisions with all other molecules,
mainly nitrogen and oxygen, and n is the coefficient for the temperature dependence of
the total line halfwidth [*Rothman et al*, 1998].

   The largest expected volume mixing ratio of water vapor is of the order of 10^{-2}.
Therefore the self-broadening contribution is neglected in the calculation of the full-
line halfwidth (cf. [*Liou*, 1980]). Using a Doppler halfwidth, in cm^{-1}, given by $\Delta v_D = \bar{\nu}/c(\sqrt{2kT/M})$, we calculate the wavenumber dependent cross-section in $cm^2/molec$ using
a Voigt line shape via

$$\sigma(\bar{\nu}, \bar{\nu}_0, p, T) = S_{\bar{\nu}}(T)\Upsilon(\bar{\nu}, \bar{\nu}_0, p, T), \tag{3.23}$$

   where Υ is the normalized Voigt function in units of centimeters. The Voigt profile is
numerically calculated using the algorithm by *Armstrong*, 1967.

   Fig. 3.3 shows an example of the change of the cross-section due to the change in
pressure and temperature over the dominant water vapor absorption altitude region from
0 to 16 km for one selected water vapor absorption line at 16804.04 cm^{-1}.

   The 590 nm water band is a ro-vibrational overtone band which is part of the 5ν-
polyad (see Table 3). The band spans weak absorptions from about 565–605 nm. Due
to an intensity mismatch of the GOME instrument resulting from spectral aliasing [P.
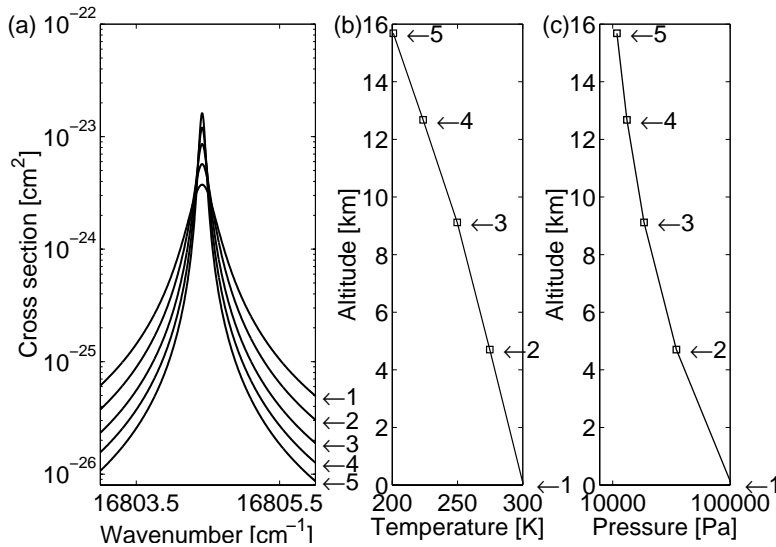
Figure 3.3: The effect on the shape of a water vapor absorption line at 16804.42 cm^{-1} in the earth's atmosphere due to the vertical change in temperature and pressure. The five line profiles in panel (a) correspond to five different altitudes taken from typical equatorial profiles of temperature (panel b) and pressure (panel c).

Stammes, Statistical analysis of channel-to-channel jumps in GOME spectra, *technical memo*, 2000] between channel 3 and 4 we do not make any use of absorption lines above 600 nm. The lines below 585 nm are considered to be too weak and modeling of the background is complicated by a strong $(O_2)_2$ absorption feature (see Section 3.4.2 and Fig. 3.5). The average lifetime of the excited ro-vibrational states is long enough for a collisional redistribution of the absorbed energy in the troposphere. Therefore the water vapor line shape is dominated by pressure broadening (Lorentz line shape) which introduces a significant change in the total transmitted light especially due to changes in the wings of the lines, where the cross-section may change over an order of magnitude over the first 16 km. Decreasing pressure and temperature gives rise to a significant decrease in the absorption. This effect may be different for two lines with overlapping wings, as is often the case for a typical water vapor spectrum.

Following recent measurements of the cross-section of water vapor in the visible and near infrared evidence is growing for systematic deviations in the line-strength values from those given by the HITRAN'96 database [*Carleer et al*, 1999; *Belmiloud et al*, 2000; *Learner et al*, 2000; *Giver et al*, 1999]. We will discuss systematic patterns in the residuals between the results of our fits and the measured GOME spectra which we relate predominantly to errors in the values of the line parameters. A sense of the magnitude of the differences between such line-strength values coming from the database and the ones "measured" by the satellite instrument may be estimated for a specific radiative transport scenario. This estimate is based on residuals between forward models

Table 3.3: Spectroscopic values relevant to the water vapor band under
study

WV-band (5ν-polyad) wavelength range	585 - 600 nm
Other atmospheric constituents within above range	$(O_2)_2, O_3, Na$
Number of WV-lines (HITRAN'96)	638
HWHM WV-line γ	0.09 [cm^{-1}]^a
Grid size of reference spectra $\delta\lambda$	0.0117 [cm^{-1}]

^{a}Average value within the WV-band at 1 atm

utilizing the HITRAN'96 line parameters and GOME measurements. The results are used
to correct for differential fit mismatches (see Section 3.9).

3.4.2   Other Sources of Extinction

In this section other sources of extinction are discussed, which modify the reflectivity be-
tween 585 and 600 nm. These sources are Rayleigh scattering and scattering from aerosol
loading as well as additional extinction by $(O_2)_2$, O_3, NO_2, sodium and the contribution
of Fraunhofer line absorption. The fraction of photons generated by thermal emission
is generally well below 1% and can therefore be neglected [*Buchwitz et al*, 2000]. The
Earth's surface is treated as a wavelength-independent Lambertian reflector with albedo
Λ diffusely reflecting a fraction of the light. Column density and cross-sections for the ad-
ditional absorbers come from various independent sources and are used to model the total
background correctly (Fig. 3.4). This is necessary because modeling of the background
using, for example, higher order polynomials may treat part of the low resolution water
vapor spectrum as background and result in a lower retrieved WVC.

Rayleigh and Mie Scattering

In order to calculate the total optical density, including the contribution of light scattered
out of the light path (Eq. 3.14) as well as the probability of scattering into the light path at
each altitude z (Eq. 3.15), we assume that Rayleigh scattering is the dominant scattering
process. The Rayleigh scattering cross-section (Eq. 3.10) in air is given by

$$\sigma_R \times 10^{24} = \frac{3.9993 \times 10^{-4}\nu^4}{1 - 1.069 \times 10^{-2}\nu^2 - 6.681 \times 10^{-5}\nu^4}, \tag{3.24}$$

where $\nu = 1/\lambda$ [μm^{-1}] and $\sigma_R \times 10^{24}$ is given in units of cm^2, using the formulation of
Chance and Spurr [1997]. The cross-sections are reproduced to better than 1% compared
to the Rayleigh scattering cross-sections tabulated by *Bates*, [1984]. No attempt is made
in this study to estimate the amount of scattering by large particles by means of Mie
scattering. In this study we treat the contribution of Mie scattering (for example in
clouds and from aerosols) to the total absorption as one of the major sources of error. We
quantify the error from the influence of aerosol loading using a doubling-adding model
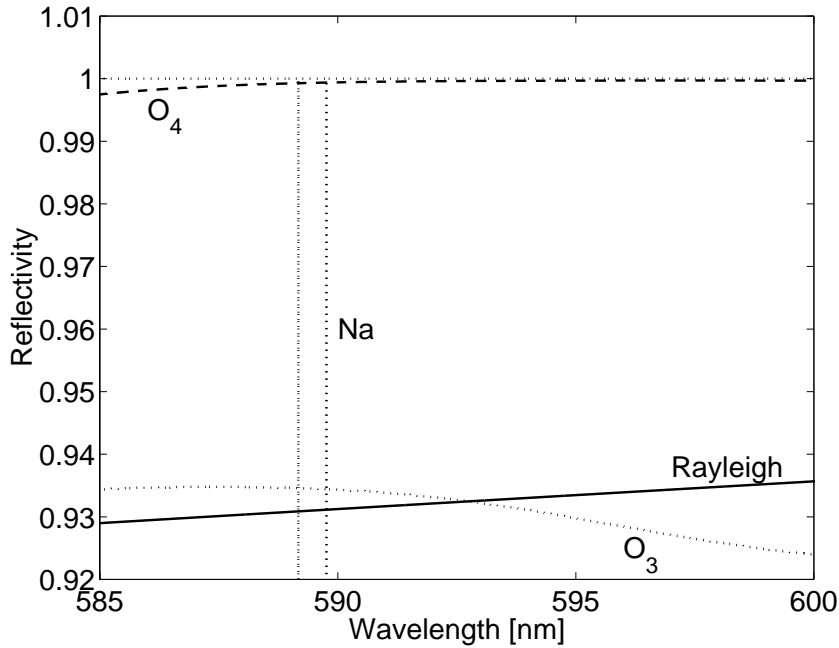
Figure 3.4: Construction of the background in the wavelength region between 585 and 600 nm. O_2 and sodium densities are taken from two empirical atmospheric models [*Hedin et al.*, 1991, *Plane et al.*, 1998]. The O_3-density is taken from GOME GDP level 2 data. Cross sections are taken from various sources described in the paper. The SZA is 23°.

which solves the equation of radiative transfer including all orders of scattering for both molecules and aerosols. The results are discussed in Section 3.7.

Fraunhofer line absorption

We estimated the effect of assuming an unstructured solar irradiance F_0 using a high resolution sun spectrum from Kitt Peak ($\Delta\nu = 0.02$ cm^{-1}) [*Wallace et al*, 1998] in the following way. We calculate the reflectivity including a sun spectra in Eq. (3.13) by

$$R_j = \frac{\pi}{\mu_o} \frac{\int_{\Delta\lambda_j} \int_{-\infty}^{+\infty} I(F_0)\mathcal{H}(\lambda, \lambda';\Sigma)d\lambda' \frac{d\lambda}{\Delta\lambda_j}}{\int_{\Delta\lambda_j} \int_{-\infty}^{+\infty} F_0\mathcal{H}(\lambda, \lambda';\Sigma)d\lambda' \frac{d\lambda}{\Delta\lambda_j}}, \tag{3.25}$$

and compare it with the results of Eq. (3.14) and (3.15), where F_0 in Eq. (3.25) is assumed to be constant and consequently divides out.

The differences in reflectivity between including and excluding F_0 have a maximum of 1% around the area of the Sodium lines and less than 0.3% over the remaining wavelength range using the Kitt-Peak sun-spectrum together with a high WVC of 1.44×10^{23} molec/cm^2. The assumption made for Eq. (3.14) and (3.15) therefore introduces a small,

nevertheless not negligible, error in the area of the sodium absorptions (see also section 3.10.4).

Ring Effect

The filling-in of Fraunhofer lines and atmospheric absorption structures due to inelastic rotational Raman scattering (Ring-effect) [*Grainger and Ring*, 1962; *Chance & Spurr*, 1997; *Vountas et al*, 1998] usually needs to be considered in large parts of the GOME wavelength range, particularly in the ultraviolet. As mentioned in the previous section the region close to the sodium absorption may contribute somewhat to this effect. However, even though the wavelength region between 575 and 585 nm of GOME sun irradiance spectra exhibits similar or stronger Fraunhofer line structure than the region of the water vapor absorption, GOME reflectivity spectra (Eq. 3.13) show only very weak structures within the former region. These structures can be related predominantly to the Ring effect because of the absence of other strong line absorbers between 575 and 585 nm. It is therefore expected that also the Ring structures in the water absorption wavelength region is relatively small. In addition, accurate modeling of the Ring effect including polarisation, which is needed for a polarisation sensitive instrument such as GOME [*Aben et al*, 2001], is very complicated and far beyond the scope of this paper. We therefore neglect he Ring effect for this study and discuss it as a possible source of error.

Sodium

In this work we model the contribution of the sodium background in the earth atmosphere at 588.9 and 589.5 nm to the total background absorption by calculating column concentrations for the non-sporadic atmospheric sodium layer at 90 km from a model by *Plane et al.*, [1998]. Its contribution to the total sodium absorption with respect to the sodium Fraunhofer lines is very weak. A typical mean sodium column in the earth atmosphere is about 6.9×10^9 molec/cm^2. Nevertheless, it was found that modeling the sodium earth background absorption reduces the fit residual and improves convergence time. Thus, it is used in both forward modeling and the retrieval.

The $(O_2)_2$ collision complex

The atmospheric absorption feature of the $(O_2)_2$-collision complex within the region of 560 and 600 nm was investigated by *Perner and Platt*, [1980]. Subsequently *Pfeilsticker et al.*, [1997] presented atmospheric measurements of $(O_2)_2$ in the wavelength range from about 450 to 650 nm and *Solomon et al.*, [1998] modeled and calculated the contribution of $(O_2)_2$ to the total absorption in this region. Cross-sections of $(O_2)_2$ have been measured by, for example, *Greenblatt et al.*, [1990] and *Newnham and Ballard*, [1998]. The cross-sections we use in this work are measured by means of Cavity Ring Down Spectroscopy by *Naus and Ubachs*, [1999] for pressures between 0 and 1 atmospheres at room temperature. The results of both *Greenblatt et al.* and *Naus and Ubachs* indicate that we may safely assume negligible temperature dependence for the cross-section. The optical density is calculated for each ground pixel using an O_2-density column from the Neutral Atmosphere Empirical Model MSISE90 [*Hedin et al*, 1991] for a given date, time, altitude-range and geolocation. Due to small variations in the O_2-density the difference in densities in the slant path of

the light with respect to the used vertical column densities from the *Hedin*-model is small and may affect the results only for very high SZA. There is a significant absorption due to $(O_2)_2$ visible in the GOME spectra on the blue side of our wavelength window for high SZA. Fig. 3.5 shows such an absorption peak in the GOME spectra for the region between 560 and 600 nm at 62° latitude and for a SZA of 73°. For comparison we show a monochromatic forward calculation based on Eq. 3.14 and 3.15 including absorptions from $(O_2)_2, O_3$, sodium and water vapor. The modeled spectrum is adjusted to the GOME measurement by fitting a first order polynomial to account for the unknown surface albedo Λ together with a first-order polynomial to account for the broad band contribution of aerosol loading and multiplescattering (Eq. 3.30 and 3.28). Apart from the water window described in this study another water absorption at the blue side of the spectrum between 565 and 580 nm superimposed on the $(O_2)_2$ absorption peak is clearly visible. The latter is reproduced well in the region between 565 and 575 nm, whereas the absorption features superimposed on the peak between 575 and 580 nm are poorly reproduced. This could be related to problems in the water vapor cross-section database.

NO_2

Within our wavelength region of interest, NO_2 has an optical density of a maximum of 1×10^{-3} [*Richter and Burrows*, 2000] which is two to three orders of magnitude smaller than water vapor and about two orders smaller than the optical density of ozone. For the purpose of this paper and within the wavelength region used we neglect the contribution of NO_2 which is below the sensitivity limit of our method. Nevertheless small contributions of NO_2 absorption for high NO_2 content, for example in the case of biomass burning, may contribute additional structure to our residuals.

Ozone

For the cross-section of the ozone Chappuis absorption band we use high-resolution reference spectra at atmospheric temperatures of 202, 221, 241, 273 and 293 K and pressures at 100 and 1000 mbar recorded using Fourier-Transform spectroscopy in the UV-visible-NIR spectral regions (240-850 nm) by *Voigt et al*, [2000]. The ozone slant column density (SCD) for a specific geolocation and SZA is taken from the GOME Data Processor (GDP) [*Balzer & Loyola*, 1996; *DLR*, 1999] level 2 data product [*Burrows et al*, 1999]. Its accuracy is known to be on the order of 5% for SZA less than 70°. The optical density is calculated by integrating over the altitudes corresponding to the five cross-section temperatures listed above assuming the local pressure and temperature profile.

3.4.3   Pressure and Temperature Profiles

The pressure and temperature profiles used in the retrieval are taken from ECMWF (c.f. Section 3.4.1). The ECMWF data assimilation model [Vesperini, 1998] provides us with 31, 50 or 60 altitude levels in pressure and temperature, according as the date is before March 1999, after March 1999 and after October 1999 respectively. Data is provided for the entire globe at 0h, 6h, 12h, and 18h UTC with a ground pixel resolution of 1° in latitude and longitude. The data is interpolated onto a 0.5° grid that matches the
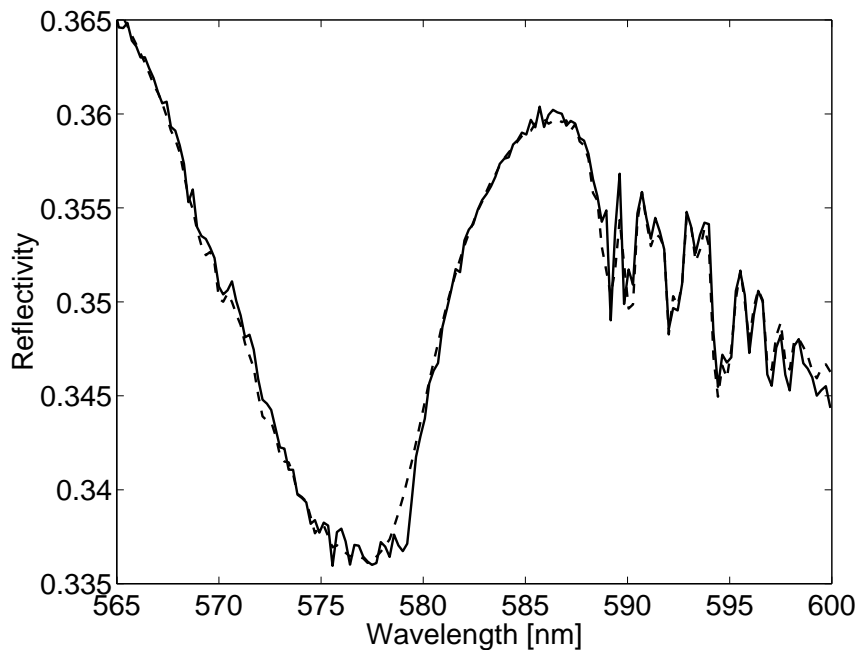
Figure 3.5: Comparison of a forward-modeled lbl calculation (dashed curve)
of the reflectivity using Eq. 3.14, 3.15 and 3.28 with a GOME measurement
(solid curve) taken at $62°N$ (SZA=$73°$). The background consists of $(O_2)_2$,
O_3 and Sodium. The stronger of the two $(O_2)_2$ absorption peaks is clearly
visible around 577 nm with another water vapor absorption band between
565 and 580 nm superimposed on it. In the case of the latter there are some
discrepancies between model and measurement in the region between 575
and 580 nm which could be related to problems in the water vapor cross-
section database.

resolution of SSM/I data and improves the overlap between ECMWF ground pixels and
GOME ground pixel. GOME level 1 geolocation data consists of 5 data-tuples in latitude
and longitude: 4 components for the edges and one for the center of a ground pixel.
They span an area of roughly $0.4° \times 2.5°$ in latitude and longitude (depending on the
geolocation, see Fig. 3.2). For each data-tuple the nearest ECMWF value is sorted out
and a mean pressure and temperature is calculated for each altitude layer ℓ. In this study
we use up to 31 pressure and temperature levels which cover an altitude range between
0 and 23 km. The atmospheric layers ℓ are defined as described in Section 3.2. For each
ground pixel a set of $\bar{\alpha}_j^{(\ell)}$ per detector pixel j for a given altitude layer ℓ is calculated by
interpolating alpha tables to the mean pressure and temperature (cf. Eq. 3.30 and Fig.
3.1) to be used in an OACS fast forward model or in an OACS fit to be described next.

3.5   Intrinsic OACS Accuracy

The intrinsic accuracy of the OACS method is limited by two method-related sources of error: 1) the discretization error due to the Opacity Coefficient Method (OCM) caused by replacing the integrals in Eq. 3.16 and Eq. 3.17 (Eq. 3.20 and 3.21); 2) exchange of the convolution with the sampling integral. This error is related to the fact that GOME detectors undersample the instrumental function of the instrument by $\Delta\lambda \not\ll \Sigma$ (Section 3.3.2). As mentioned in Section 3.2 the first error may be reduced arbitrarily by decreasing $\delta\lambda$ and thus increasing the number of realization points per absorption line of the high resolution reference spectrum. The second error, related to the basic transport equations (Eq. 3.14 and Eq. 3.15), is introduced by performing the sampling of the high resolution reflectivity spectrum before the convolution (*convolution problem*), as is done for both Eq. 3.16, 3.17 and for the basic OACS equation (Eq. 3.20 and 3.21). However, performing the sampling before the convolution makes the fitting much more efficient, because the convolution has to be performed only over 69 measurement points during each iteration step and not over the high-resolution absorption spectrum.

In order to quantify the intrinsic method-related error we will compare the reflectivity calculated using the OACS method (Eq. 3.20 and 3.21) with a lbl calculation based on Eq. 3.14 and 3.15. The density subcolumn profiles of water vapor per atmospheric level for two specific geolocations are taken from the ECMWF data assimilation model. Fig. 3.6 shows the comparison between both calculations for a typical equatorial scenario over the ocean with a high WVC of 1.34×10^{23} molec/cm^2 and a low WVC of 8.19×10^{21} molec/cm^2 over land at SZAs of 23.5^o and 73°, respectively. Both ground pixels are cloud free. The two figures also show the relative residuals between the lbl and the OACS forward model, which is defined as (lbl-OACS)/lbl, hereafter. From the residuals we conclude that, for $\delta\lambda = 2 \times 10^{-3}\Delta\lambda$, the relative spectral accuracy of the method in reflectivity is better than 2% for high WVC and better than 0.2% for low WVC. For a comparison of reflectivities between the results of the lbl and the OACS forward model *without* performing the convolution the accuracy of the method appears to be better than 0.4% for high and better than 0.2% for low WVC. We conclude that the residual is dominated by error source number (2) above, namely the *convolution problem*.

3.6   Forward Model

We use Eq. (3.20) and (3.21) to construct a basic fast forward model reflectivity spectrum which includes single scattering via

$$R_j = \hat{R}(N_\ell, \Lambda_j; \tilde{\mu}_\ell)_{\text{surf},j} + \hat{R}(N_\ell; \tilde{\mu}_\ell)_{\text{ss},j}, \tag{3.26}$$

where j is the jth detector pixel within the window of interest. The altitude-dependent path-length factor $\tilde{\mu}_\ell$ is calculated using a Chapman function [*Banks & Kockarts*, 1973] which takes the curvature of the atmosphere into account. We adjust the forward-modeled spectrum to the GOME measurement in the region between 585 and 600 nm by fitting a first-order polynomial for the unknown surface albedo Λ_j, assuming

$$\Lambda_j = A\lambda_j + B, \tag{3.27}$$
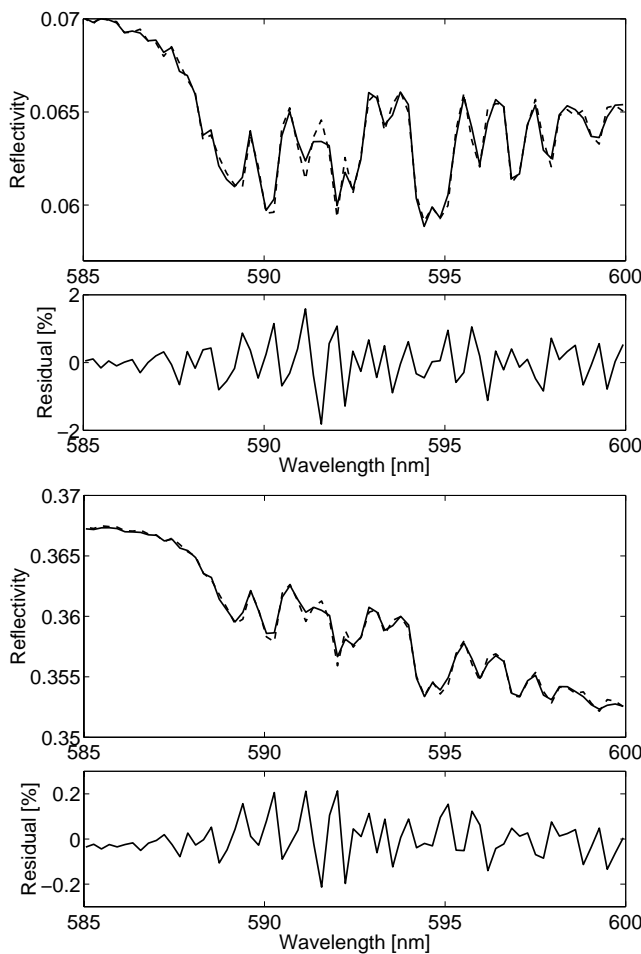
Figure 3.6: Comparison of modeled spectra for specific measurement scenes. The reflectivity plot shows a forward-modeled lbl calculation using Eq. 3.14 and 3.15 (solid line) and a forward-modeled reflectivity using the OACS method (Eq. 3.20 and 3.21; dashed line). The residual plot shows the relative method-related intrinsic error in reflectivity ([lbl-OACS]/lbl; used throughout the paper). Upper two panels: A high WVC of 1.34×10^{23} molec/cm^2 measurement over the Pacific at 23° latitude and 250° longitude for a SZA of 23.5°. Lower two panels: A low WVC of 8.19×10^{21} molec/cm^2 for a measurement over land at 62° latitude and 262.5° longitude for a SZA of 73°.

where A and B are free fit parameters. Since the differential contribution of multiplescattering and aerosol extinction appears to be lower than 2% in cases of cloud free ground pixels (see Section 3.7) within our spectral region of interest we include an additional

first-order polynomial,

$$R_{\mathrm{ms,j}} = C\lambda_j + D, \tag{3.28}$$

where C and D are additional free fit parameters in order to account for the broadband contribution of higher orders of scattering.

Thus, in its entirety, the forward model consists of three terms, viz.

$$R_j = \hat{R}(N_\ell, \Lambda_j; \tilde{\mu}_\ell)_{\mathrm{surf,j}} + \hat{R}(N_\ell; \tilde{\mu}_\ell)_{\mathrm{ss,j}} + R_{\mathrm{ms,j}}. \tag{3.29}$$

Figure 3.7 shows a comparison between a solution of the full scalar radiative transfer equation using an independent method and the OACS forward model described above (Eq. 3.29). For the full solution of the radiative transfer equation including the multi-plescattering source term we use a doubling-adding model (DAM) [*de Haan et al*, 1987] (see also following Section 3.7). The coefficients A to D used in Eq. 3.27 and Eq. 3.28 are retrieved by a fit to the solution of the DAM-model after the calculation of Eq. 3.20 and 3.21 is performed. We used a WV-subcolumn profile taken from the ECMWF assimilation model with a total WVC of 1.34×10^{23} molec/cm^2 under a SZA of 40°. For the DAM-model a maritime situation with a low surface albedo of 0.03 without aerosol loading is used. The comparison between the fast forward modeling using OACS and the full radiative transfer solution given by the DAM reveals a relative difference of less than 2% (Fig. 3.7, lower panel) which is comparable to the intrinsic method-related accuracy of the method (see previous section). Note how there appears to be some degree of freedom left in the absolute quantities and spectral dependence of the usually unknown surface albedo as well as the broad-band multiple-scattering contribution. This is due to the fitting of the OACS forward model to the reference model spectrum (which is, in this case, the result of the DAM but will be, in the remainder of the paper, a small set of GOME measurements). Nevertheless, the surface albedo of 3%, as used in the DAM, is derived for the above case study to better than 35% at 592 nm (see Table 4). In future studies, this could be improved by replacing the first-order polynomial R_{ms} in Eq. 3.29 by an OACS-modified term which accounts for the differential contribution of higher-order scattering. In addition the surface albedo could also be retrieved from a fit to the spectrum in a spectral region beyond the water vapor absorption which may improve the robustness of the fit (see also Section 3.10.5).

A detailed description of the influence of different aerosol loading and the relative contribution of singly- and multiply-scattered photons on the reflectivity will be presented in the next section in which we also discuss the impact of aerosols and multiple scattering on the relative residuals between OACS and DAM.

Figure 3.8 shows the results of a fast forward modeling of GOME spectra using Eq. 3.29 for a high and a low WVC. A total of 30 atmospheric layers ℓ is used to cover altitudes up to about 23 km, with temperature, pressure and water vapor subcolumn profiles taken from spatially- and temporally-collocated ECMWF data. The absorption due to other absorbers as well as the Rayleigh singlescattering contribution are included as described in the previous section. Again, both residuals are on the order of the intrinsic method-related error for high and low WVC as shown in Figure 3.6. One exception is the wavelength region between 589 and 590 nm where the the residual increases somewhat in the case of low water vapor content.

Table 3.4: Relative contribution of ground-reflected, singly-scattered and multiply-scattered photons to the total reflectivity calculated by the DAM model and for the scenario introduced in Fig. 3.7. DAM model calculations are performed assuming a SZA of 40° and a WVC of 1.44×10^{23} [molec/cm^2] for each case.

	Model Input		Model Output		
	AOD [a]	Λ	GR [b]	SS [c]	MS [d]
Maritime Clear Sky	0	0.03	43.8	48.2	8.0
Maritime Aerosol	0.21	0.03	20.0	53.2	26.8
Rural Clear Sky	0	0.10	69.1	22.8	8.1
Rural Aerosol	0.51	0.10	17.9	30.9	51.2
	OACS Retrieval Results				
	WVC 10^{23} [$\frac{molec}{cm^2}$]	Δ WVC [%]	Λ	$\Delta\Lambda$ [%]	
Maritime Clear Sky	1.33	-7.7	0.040	+33.3	
Maritime Aerosol	1.65	+14.8	0.042	+40.0	
Rural Clear Sky	1.42	-1.6	0.105	+5.0	
Rural Aerosol	1.69	+17.6	0.109	+9.0	

[a] Aerosol Optical Depth
[b] Percentage of ground reflected light at 592 nm
[c] Percentage of single scattering at 592 nm
[d] Percentage of multiple scattering at 592 nm

3.7   Narrow-Band Contribution of Aerosol Loading and Multiple Scattering

In the formulation of the basic transport equation (Eq. 3.9) we neglect the contribution of multiply-scattered photons to the total reflectivity. For the fast forward modeling as well as for the retrieval in the next sections we use a first order polynomial to account for the broad-band multiple-scattering contribution (Eq. 3.28). By this we neglect the narrow-band (differential) contribution of water vapor to the total reflectivity caused by multiply-scattered photons.

To account for the full effect of multiple scattering, we solve the full scalar radiative transfer equation including the multiple scattering source term by employing the DAM, which, for our purposes, has been reduced to the scalar representation of the radiation field. The reflectance $R(\lambda)$ is calculated in a line-by-line mode of a spectral resolution of 0.01 cm^{-1}. For the assessment of the effect of multiply-scattered light on the measurement, we investigate four atmospheric scenarios: two with maritime and rural boundary layer aerosol loading and two clear-sky scenarios (i.e. without aerosols). All scenarios include
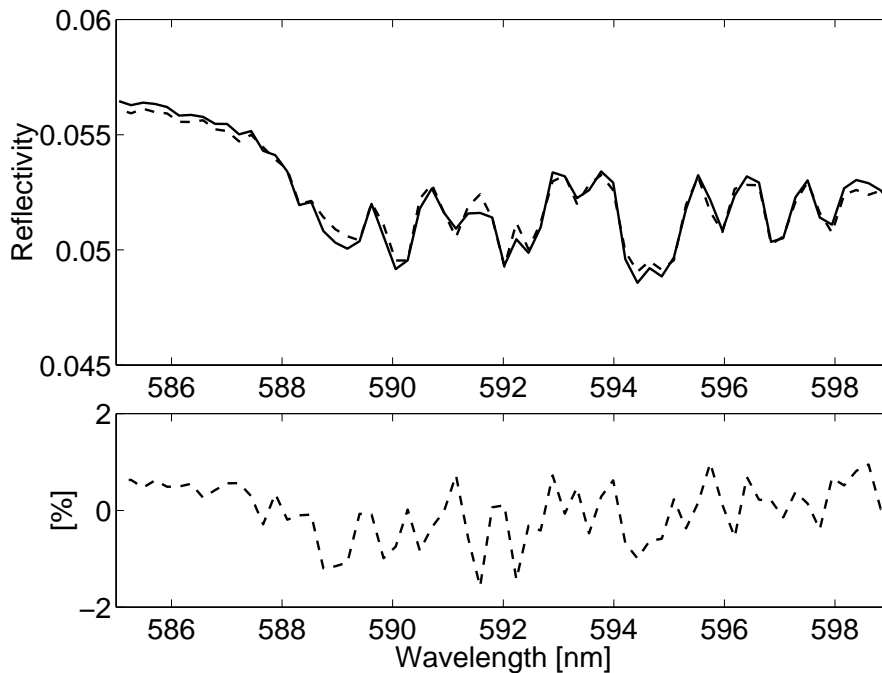
Figure 3.7: The upper panel shows a comparison between the results of OACS forward modeling (dashed line) and the doubling adding model (DAM, solid line) of *de Haan et al*, [1987]. A WVC of 1.34×10^{23} molec/cm^2 is assumed in the doubling adding code together with a SZA of 40°. The lower panel gives the relative residual.

the effects of Rayleigh scattering, ozone absorption and (maritime or rural) Lambertian ground-level reflection. In the case of the maritime scene we use a surface albedo of 3% whereas for the rural scene a surface albedo of 10% is used. For maritime aerosol loading a constant particle density of 4 000 particles per cm^3 is assumed. For the middle and upper troposphere, we assume a tropospheric background aerosol, for which the particle density decreases with the third power in pressure. The optical properties of the aerosols are taken from *Shettle and Fenn* [1979]. The total aerosol optical depth is 0.26 at $\lambda = 590$ nm. In the rural case we have chosen a constant but much higher particle density of 15 000 particles per cm^3 below 1 km and the total aerosol optical depth is then 0.51 at $\lambda = 590$ nm.

Table 4 lists the relative contribution of ground-reflected, singly- and multiply-scattered photons as a percentage of the total reflectivity using the DAM-model for four different aerosol loading cases as described above. Without aerosols the maximum contribution of multiply-scattered photons is below 10% in the wavelength range between 585 and 600 nm. Single scattering is the dominant source of reflectivity (50% effect) in the maritime aerosol scenario because of low surface albedo and the ground-reflected component is com-
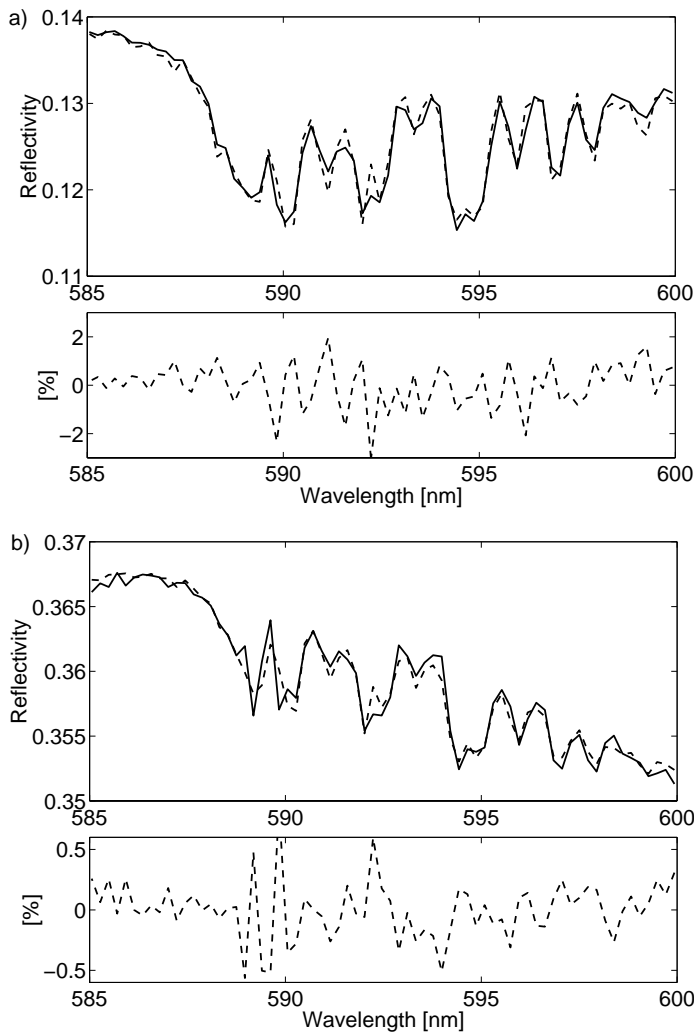
Figure 3.8: Forward modeling results from OACS (dashed lines) in comparison with GOME spectra (solid lines) taken at the same location. Temperature, pressure and water vapor concentration profiles have been taken from ECMWF. Upper two panels (a): Reflectivity spectra for a WVC of 1.75×10^{23} molec/cm^2 at a SZA of 27°. Lower panels (b): Same as upper panels but for a WVC of 8.19×10^{21} molec/cm^2 at a SZA of 73°. Both ground pixels are cloud free. In both cases the lower plots show the residual. For the low WVC case (lowest panels) sodium line absorption in the region of 589.5 nm increases the residual significantly above the intrinsic method-related error value (compare Fig. 3.6).

parable to that due to multiple scattering. This may be contrasted with the rural aerosol scenario in which multiple scattering is the dominant source of scattered light (50%) due to the high aerosol optical density. Aerosols reduce the ground-reflected component by up to 20–50%.

In addition to the evidently broadband aerosol effects just discussed it is also reasonable to expect that a significant differential contribution due to multiply-scattered photons may affect the retrieved WVC. Since the radiation transport model presented in this paper does not explicitly account for the latter we present a comparison in Fig. 3.9 between a lbl calculation based on Eq. (3.14), (3.15) and (3.28) and the results of the DAM forward model for the four scenarios discussed above. The parameters C and D needed for the lbl calculation are obtained by a fit to the DAM result. The differences in the residuals between Fig. 9 a,c and Fig. 9 b,d indicate that aerosol-loaded scenarios may give rise to significant differential structure. The latter is a 2% effect compared with a 20–25% broadband aerosol contribution. Even though this is comparable to or just below the 2% precision of the OACS method for high WVC it is a systematic effect. In section 3.8.4 we therefore perform OACS retrieval on all four spectra modeled by the DAM in order to estimate the effect of multiple scattering due to Rayleigh and aerosol scattering on the retrieved WVC together with the effect of aerosol extinction.

3.8   Sensitivity Analysis of the Retrieval Method

3.8.1   Retrieval Method

We fit Eq. 3.29 to GOME reflectivity spectra along with optical densities of O_3, $(O_2)_2$ and sodium as well as the Rayleigh scattering contribution as described in Section 3.4. The numerical method used is a robust, non-linear, large-scale trust-region method [*Byrd et al*, 1988] which solves the optimization problem

$$\min_{N_\ell, \Lambda_j, R_{\mathrm{ms},j}} \sum_j \left[R_j \quad - \quad \left(\hat{R}(N_\ell, \Lambda_j; \tilde{\mu}_\ell)_{\mathrm{surf},j} \hat{R}(N_\ell; \tilde{\mu}_\ell)_{\mathrm{ss},j} + R_{\mathrm{ms},j} \right) \right]^2. \qquad (3.30)$$

The fit parameters are the vertical water vapor column densities N_ℓ of ℓ atmospheric layers and the surface albedo and multiple scattering parameters (see Section 3.6). All 69 measurement points j within our region of interest are fitted simultaneously together with the four parameters A to D.

For each OACS fit we start with a flat water vapor subcolumn profile $N_{\ell,0} = 10^{16}$, where the N_ℓ are given in units of the water vapor vertical column density per atmospheric layer (c.f. Eq. 3.19). Each fit is constrained by an upper limit $N_{\ell,max}$ in the form of a step function with high values over the first atmospheric layers and lower values for the higher levels. The lower profile constraint is set to $N_{\ell,lower} = 0$. The constraints prevent the fit from giving too much weight to the higher altitude levels which otherwise would increase the relative contribution of the single scattered photons and, in so doing, decrease the total mean free path length. The latter would lead to a reduced total WVC. The effect of introducing this constraint is to reproduce the relative single-scattering contribution
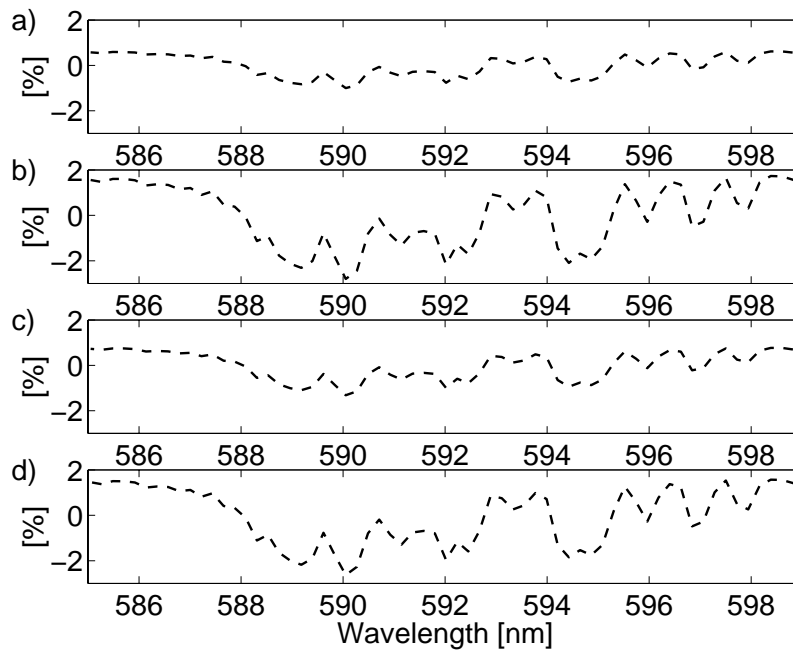
Figure 3.9: Relative differences between the monochromatic model pre-
sented in this paper based on Eq. 3.14, 3.15 and 3.28 and the result of the
DAM for the specific scenario presented in Fig. 3.7. The upper two panels
show the results for a maritime case with a surface albedo of 3% under (a)
clear sky conditions and (b) with maritime aerosol loading. The lower two
panels show the results for a rural case with surface albedo of 10% for (c)
clear sky conditions and (d) with rural aerosol loading.

to the total reflectivity to better than 1% when compared to the results given by the lbl
forward model.

3.8.2 Precision and Accuracy of the Fitting Method

We henceforth adopt the term *precision* to describe measurement-related random errors
and the term *accuracy* to describe the absolute difference between the true and the re-
trieved value due to systematic errors. These differencies are caused by the response of
the result due to the intrinsic method-related error as well as the robustness of the result
to errors in the main input quantities: the accuracy of the measurement and the altitudes
profiles of atmospheric temperature and pressure. The random noise of a typical satellite
measurement is dependent on photon shot noise, detector shot noise and digitization ef-
fects and is quantified to be about 0.1% of the absolute radiance in the case of GOME
[*DLR*, 1999]. The GOME instrument is also sensitive to the polarization of the light which
is measured for each channel. In what follows we adopt a total system error for GOME
measurements of about 1%. This is derived from a full error calculation including random

noise errors, the error of the fractional polarization values, the polarization correction factor and the error on the instrument response function known from pre-flight calibration studies. As mentioned in Section 3.3.3 the error on the spectral calibration is known to be on the order of 0.001 nm within our wavelength region [*Caspar & Chance*, 1997]. For the temperature and pressure profiles taken from the ECMWF data assimilation model an uncertainty of 0.3% [*Filiberti et al*, 1998] in pressure and 0.1% in temperature [*Francis et al*, 2000] is assumed.

We estimate precisions and accuracies for the retrieval of WVCs using OACS (Eq. 3.30) from the monochromatically forward-modeled spectrum used before to estimate the intrinsic method-related error (Section 3.5, Fig. 3.6) as follows. One hundred simulated reflectivity spectra are produced by adding random noise errors normally distributed around one third of the reflectivity values, randomly chosen, where the 2σ range is given by their random noise values provided with the measurement. The noise values are taken from level 1 data for both solar irradiance and earth radiance. At the same time and for each modified spectrum the wavelength grid is shifted randomly within the calibration error range in order to simulate calibration errors. In a separate calculation we shift the temperature and pressure profiles used in the fit to their expected maximum and minimum values due to potential systematic errors in the ECMWF database. In the same simulations we similarly increase and decrease the reflectivity by 1% in order to explore the effects of the systematic uncertainties in the measured intensities. This permits a check of the precision (standard deviation for the mean retrieved WVC from artificial spectra with random noise added), the accuracy (mean retrieved WVC for the random noise modified spectra) and the robustness or total accuracy (response to shifted input profiles and known systematic errors in the measurements) of the method.

3.8.3   Sensitivity Study Results

Fig. 3.10 shows two representative examples of OACS WVC fit results for two artificial modified spectra utilizing different altitude ranges for a fixed density subcolumn profile with a relatively high WVC of 1.34×10^{23} molec/cm^2. Each fit covers a range of atmospheric levels between 0 and the value denoted on the x-axis. Each atmospheric level is defined as described in section 3.2.1 and shown in Fig. 3.1. In general, best results are obtained with an altitude range covering 18 atmospheric levels (corresponding to a range of about 10 km above the earth surface) with the full range of WVCs agreeing to better than 2%. This altitude range is sufficient to cover the bulk of the water vapor at any geolocation while still keeping the number of fit parameters as small as possible (the water density drops by more than two orders of magnitude over the first 10 km, see WV-subcolumn profile in Fig. 3.11). For higher altitude ranges there is not sufficient information to restrict the fit. These findings are supported by the calculation of mean weighting functions $\partial R^{(\ell)}/\partial n_{VC}^{(\ell)}\big]_j$ per atmospheric layer and per detector pixel j (Fig. 3.11), where R is the OACS formulation of the reflectivity based on Eq. 3.29. Up to the 18th altitude level the weighting functions show similar changes in the reflectivity per altitude level with respect to changes in the water vapor density n (Fig. 3.1). Above about the 20th level small changes in the water vapor density induce large unsystematic changes in the reflectivity for different wavelengths. This results in additional local fit
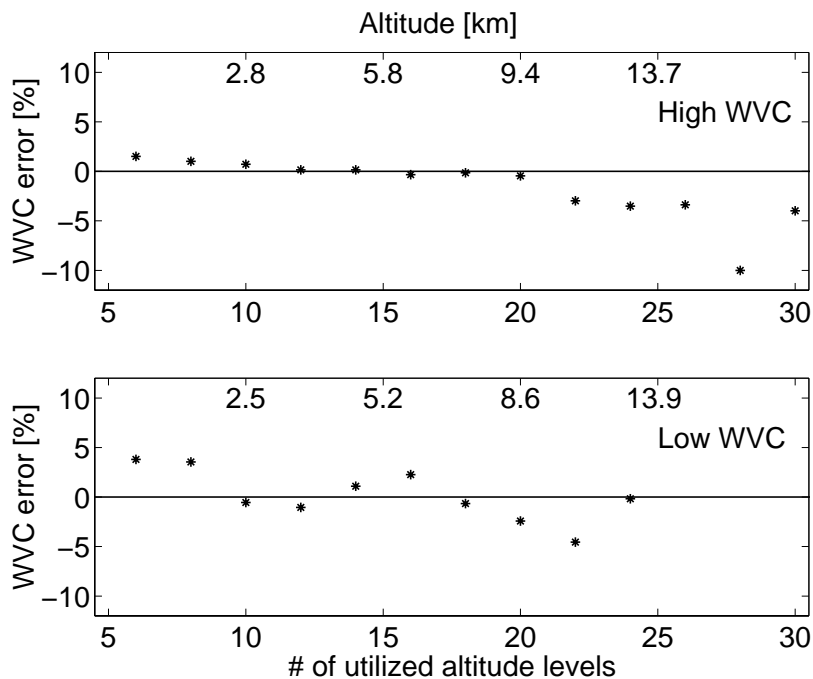
Figure 3.10: Relative residuals of the retrieved WVC (dots) from monochro-
matically forward-modeled spectra using the OACS method. Typical exam-
ples are given for a high WVC (upper panel) of 1.34×10^{23} molec/cm^2 and a
low WVC (lower panel) of 8.19×10^{21} molec/cm^2 covering different altitude
ranges as follows. Each value x on the abscissa represents the utilization of
$\ell = 1$ to x atmospheric layers in the retrieval. Best results were achieved
when using about 18 altitude levels (covering the range of 0 to 10 km). For
the low WVC the fit fails to converge within the given limits when utilizing
more than 24 levels.

minima which makes the fit unstable and increases the uncertainties in the fit results
(see retrieved WVC results in Fig. 3.10 using more than 20 atmospheric layers). For the
retrieval of WVCs presented in this paper we therefore utilize 18 atmospheric levels to
achieve best results for the full range of very high and very low WVCs.

Fig. 3.12 shows retrieved WVCs from 100 forward-modeled, random noise-modified
spectra. Two extreme cases are considered: a high WVC (1.34×10^{23} molec/cm^2) and a
low WVC (8.19×10^{21} molec/cm^2). First, we performed 100 OACS fits to the modified
spectra using exactly the same pressure and temperature profiles as used in the forward
model. The precision of the method is given by the 1σ-distribution of the resulting values
around their mean value. In the case of high WVC the precision is 0.66% and for low WVC
it is 3.4%. The difference between the mean value and the WVC value used as an input in
the model provides the accuracy of the method which is 0.05% for high and 1.35% for low
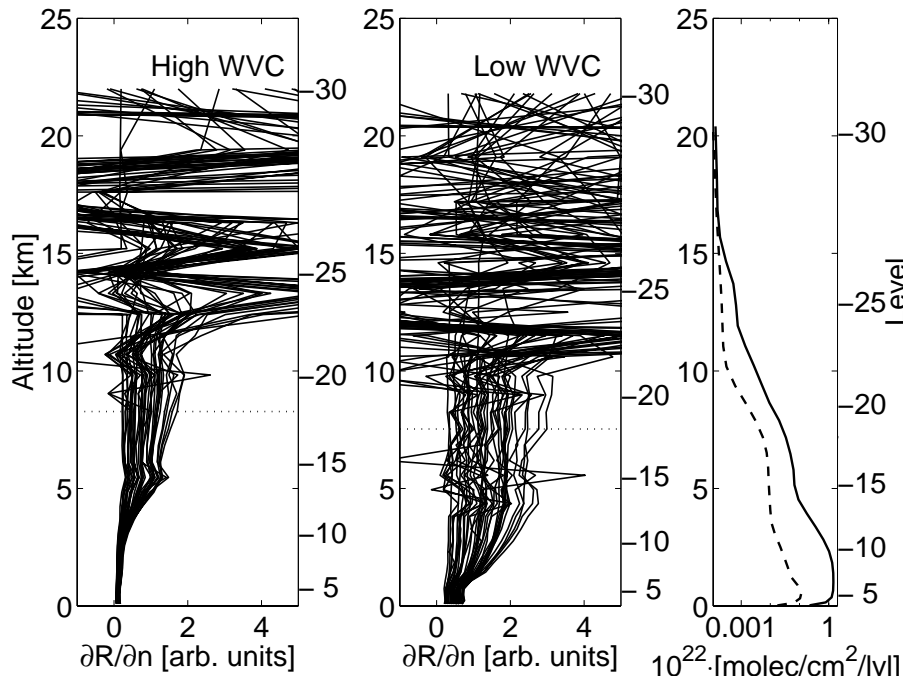
Figure 3.11: Change in reflectivity due to change in water vapor density over altitude (weighting functions $\partial R/\partial n$) for the forward-modeled reflectivity over altitude using OACS. The left panel shows the result for the high WVC and the middle panel for the low WVC used in Fig. 3.10. Each plot consists of 69 weighting functions, one for each GOME detector pixel in the wavelength range between 585 and 600 nm. The dotted line denotes the maximum (18th) atmospheric level (right axes) used in the retrieval. For comparison the panel on the right shows the corresponding water vapor subcolumn profile for the low (dashed line) and the high WVC (solid line). Above the 18th level small changes in the water vapor density introduce large changes in the reflectivity value.

WVCs. In both cases OACS underestimates the WVC used in the lbl model. Second, 100 fits to the random noise modified spectra are performed with shifted input profiles and spectral intensities. All possible combinations in the shifted inputs (shifted to the lowest and highest expected values within their range of uncertainty) are taken into account. The maximum impact on the WVC for all the possible cases reveals a total accuracy of the method due to changes in the input profiles of at most 0.8 and 4% for high and low columns, respectively, which we interpret as the robustness of the method to systematic errors in the input quantities.
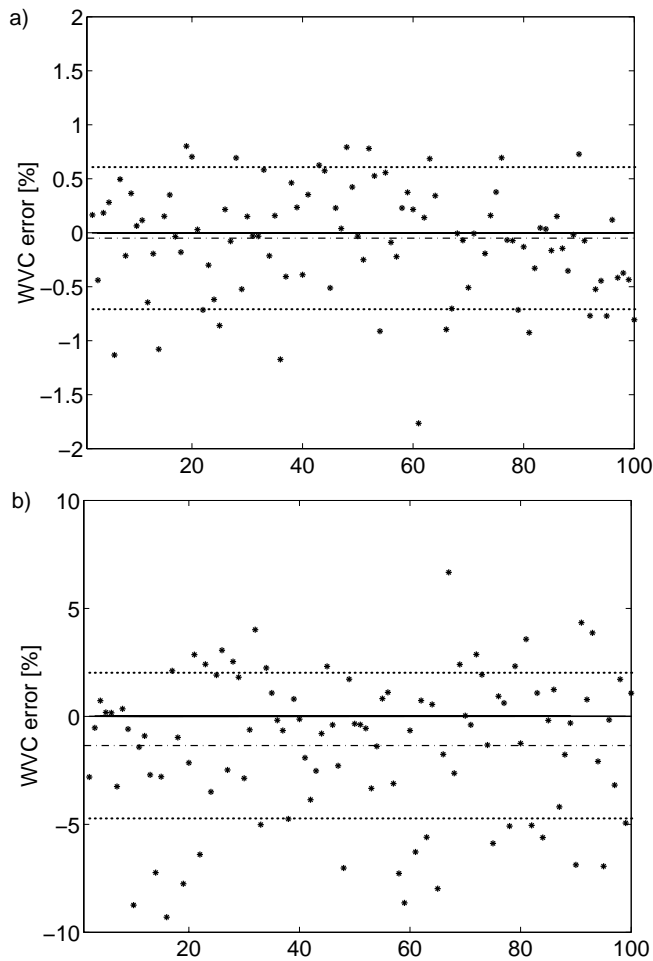
Figure 3.12: Relative differences (dots) between the OACS-retrieved WVC
and the WVC used for 100 monochromatically forward-modeled spectra.
The forward-modeled spectra are modified by expected instrument random
noise and calibration errors for the high and low WVC cases used in Fig.
3.10 (upper panel (a) and lower panel (b), respectively). The 1σ standard
deviation (dotted lines) is 0.66% for high WVC and 3.4% for low WVC. The
difference between the mean of the 100 retrieved WVCs and the input WVC
is given by the dotted-dashed line. From this we estimate an accuracy for
the method of 0.05% for high WVC (a) and 1.35% for low WVC (b).

3.8.4   Impact of Multiple Scattering and Aerosol Loading on the Retrieved WVC

We performed OACS retrieval on all four spectra modeled by the DAM and described
in detail in section 3.7. The results listed in Table 4 reveal a very small error for cases

with no aerosol loading and surface albedo of 10% and an error of at most 18% for high aerosol loading with an optical depth of 0.51. We get an error of -7% in the case of a maritime situation without aerosol loading, where the contribution of multiple scattering is relatively weak (8%). This is because the retrieval of such a small surface albedo (+30% error) is difficult to achieve in conjunction with the fit parameters of a broad-band multiple scattering contribution. An overestimated surface albedo leads to an overestimation of the ground reflected light contribution and therefore to an underestimation of the WVC. The maritime retrieval results in Table 4 show that the effect of multiple Rayleigh scattering and surface albedo retrieval (-7% error on the WVC) together with aerosol loading (+14% error) may often cancel out for intermediate aerosol loading. This cancellation may not occur for rural cases where significant aerosol loading and increased multiple scattering may lead to an overestimation of the WVC in all the cases. In general, an increased aerosol loading leads to an enhanced multiple scattering contribution and therefore to longer light paths than expected by the model. The latter results consequently in an overestimation of the WVC.

In summary we conclude that the inclusion of an additional polynomial (Eq. 3.29) seems to be an adequate approach to treat the broad-band multiple scattering and aerosol contribution to the reflectivity. We thus expect an error of at most 18% on the retrieved WVC due to differential contributions of multiple scattering and aerosol loading in extreme cases. The systematic errors due to the differential contribution especially in cases of high aerosol loading remains a subject for future study.

3.9   Retrieval From GOME Data

We performed OACS fits for a single GOME track on October 23, 1998, between $-80°$ and $80°$ in latitude for a series of longitudes between 117° and 279° for 470 measurements. As mentioned earlier, a step function is used to constrain the fit by an upper limit for each value N_ℓ (Section 3.8.2). The shape of the step function is scaled with respect to an expected WVC such as can be taken from climatology. In our case we scale the upper profile constraint differently for geolocations with high ($> 1 \times 10^{23}$ molec/cm^2), medium (between 1×10^{23} molec/cm^2 and 1×10^{22} molec/cm^2) and low ($< 1 \times 10^{22}$ molec/cm^2) expected WVC. The climatology is derived from ECMWF. The convergence tolerance limits are set to 1×10^{11} molec/cm^2 for the WVC value and 1×10^{-11} for the optimization function values. The fit has converged when one of the tolerance limits is reached.

3.9.1   Differential Fit Mismatches

The upper panel of Fig. 3.13 shows the mean value of 250 residuals of OACS fits for cloud-free ground pixels over the described GOME track. All these residuals display similar spectral patterns which are related to the spectral pattern of the intrinsic method error residual shown in Fig. 3.6. This high frequency pattern has a rate of 0.8 nm^{-1} which corresponds to a half-cycle of 4 detector pixels each of which covers a region of 0.2 nm. The second panel shows a moving average of the mean residual values over 8 detector pixels, i.e over two cycles of the intrinsic error residual. The result is a clear averaging out of the high frequency structure. However in the region between 591 and 597 nm a
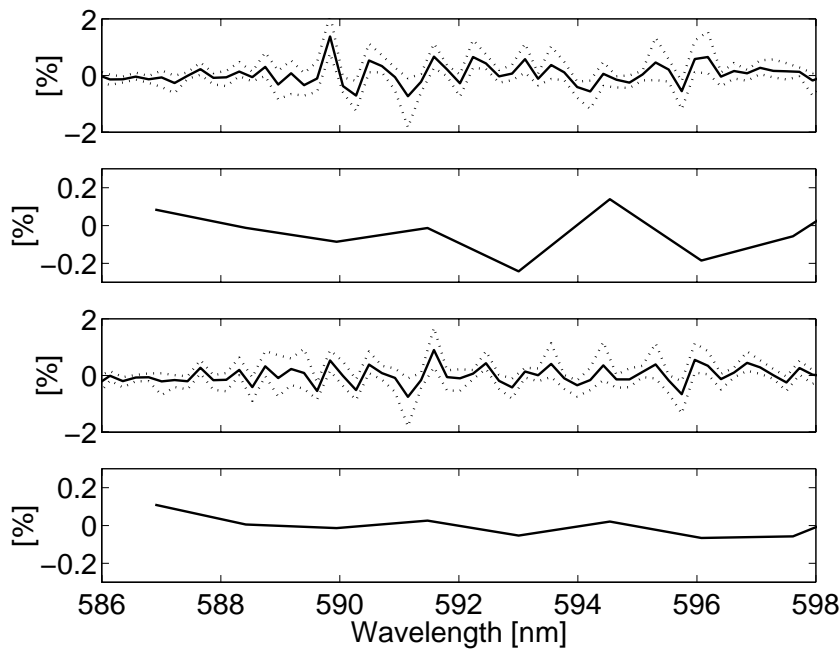
Figure 3.13: A cumulative plot of 250 OACS fit residuals of cloud-free
ground pixels for a GOME track on October 23, 2000 between $-80°0$ and
$+80°$ in latitude. The upper panel shows the mean value and outer limits
of all residuals for OACS fits without any correction applied. The second
panel shows the mean value of a moving average applied over 8 detector
pixels. Note the different scale with respect to the first panel. The third
panel shows the residuals in the corrected cases applying Eq. 3.33. We use
only *one* calculation of $\Delta\phi$, i.e. from one geolocation, for all fits. The lowest
panel shows the moving average over 8 pixels applied to the residuals after
corrected fitting.

lower frequency structure contained within the residuals does not vanish. We relate this
low frequency differential fit mismatch predominantly to instrumental errors as well as
systematic deviations in the line strength values given by the HITRAN'96 database used
in this study. However, other systematic errors introduced by the measurement or the
modeling of the background may also contribute to this effect (see end of next section
and discussion in section 3.10.4).

In November 1999 new measurements of the water vapor absorption lines lying both
within the 590 nm band as well as in other bands were published [*Giver et al*, 1999]
which showed relative differences in the integrated line intensities with respect to the
values given by HITRAN'96 of up to 17%. However measurements of water vapor absorp-
tion bands other than the one used in this study [*Learner et al*, 2000] recently showed

discrepancies ranging from about 100% for small lines to about 20% for strong lines for the main water vapor absorption bands in the region between 1110 and 685 nm. They also found systematic differences in various bands ranging from 6% to 33%. Even though measurements by *Learner et al* in the wavelength range between 585 and 600 nm have not intensively been studied yet large differences in some of the water absorption bands between 1110 and 685 nm suggest the presence of potentially large uncertainties in the reference cross-sections of the HITRAN'96 database used in this study. In addition, the measurements by *Giver et al* correct the line intensities in many cases to lower values whereas in the measurements of *Learner et al* predominantly higher values where found [*Belmiloud et al*, 2000]. Measurements of the water vapor absorption bands by [*Carleer et al*, 1999] and results of Cavity Ring Down measurements performed by [*Naus*, 2000] also show significant differences from HITRAN'96 in the absorption line strengths within the 590 nm band. This suggests that systematic database errors may contribute significantly to the observed differential fit mismatch.

3.9.2   Adjustment for Errors in Input Quantities

In order to describe a mismatch in the jth pixel between the model and the measurement we define a parameter ϕ as follows. Assume that $R_{mod}(\phi_0)]_j$ is the top-of-the-atmosphere reflectivity calculated by a lbl forward model using the values from a specific spectral database, i.e. $R_{mod}(\phi_0)]_j$ is the modeled reflectivity before applying any spectral database correction. The modeled reflectivity should properly include all physical effects such as background scattering or other absorptions as well as a convolution integral and pixel-binning to simulate the instrument sampling. It is further assumed that there exists some $\Delta\phi$, i.e. a small correction to the parameter ϕ, which may be applied to the modeled reflectivity $R_{mod}(\phi_0)]_j$ in order to reproduce the measured satellite reflectivity $R_{sat}]_j$,

$$\phi_0 \quad \rightarrow \quad \phi_0 + \Delta\phi = \phi \qquad\qquad (3.31)$$

$$R_{mod}(\phi_0)]_j \quad \rightarrow \quad R_{mod}(\phi)]_j = R_{sat}]_j. \qquad\qquad (3.32)$$

Without loss of generality it is possible to represent the general model reflectivity $R_{mod}(\phi)]_j$ as an exponent of a function f containing ϕ, so that

$$R_{sat}(\phi)]_j = e^{f(\phi)} \approx R_{mod}(\phi_0)]_j \exp\left(\left.\frac{\partial f}{\partial\phi}\right]_{\phi=\phi_0} \Delta\phi\right), \qquad\qquad (3.33)$$

Here f has been expanded in a Taylor series to first order assuming a linear response to errors in ϕ. Thus Eq. (3.33) allows direct estimation of $\Delta\phi$ directly from measurements and models of those measurements, assuming that the models are correct. Eq. (3.33) is also used in the retrieval presented in this paper to correct for the systematic differential fit mismatches showed in Fig. 3.13.

It is possible to show empirically that $\Delta\phi$ is a robust quantity with respect to the geometry of the measurement (i.e. it is independent of the geolocation) when $\partial f/\partial\phi]_{\phi=\phi_0}$ is identified with effective optical density of a pixel $\hat{\tau}$. In order to do so, we calculate $\Delta\phi$ using Eq. 3.33 for three different GOME measurements R_{sat} in the equatorial, the sub tropics and polar region, i.e. for a high, mean and low water column (Fig. 3.14). In each

case a lbl forward model R_M was used based on Eq. 3.14 and 3.15 including a fit to the
surface albedo Λ and the broad-band multiple scattering contribution using Eq. 3.27 and
3.28 respectively. For the forward modeling we use water vapor subcolumn profiles from
the ECMWF database where the total column densities differ less than 5% from the SSM/I
value. Two important error sources have to be taken into account: (1), the assumption
on the water subcolumn profile made by using the ECMWF water vapor values and (2),
the contribution of differential residual pattern due to narrow-band multiple scattering
effects which may both affect the spectral shape of the curves. However, the effect of both
of these errors should be seen in the spectral dependence of the derived $\Delta\phi$ (Fig. 3.14)
as they both would display the characteristic absorption pattern of the water vapor lines.
In contrast to this the derived $\Delta\phi$ in Fig. 3.14 does not show this characteristic pattern
for all three scenarios. The figure also shows that the spectral dependence of $\Delta\phi$ exhibits
a similar shape in all cases in the region of strong water absorption between 587 and 598
nm which is independent of the geometry of the light path.

Uncertainty in spectral database information might be summed up as arising either out
of missing line data or errors in existing line parameters. *Belmiloud et al.*, [2000] showed
that for water vapor the effect of erroneous line intensities was probably greater than the
effect of missing lines, at least in the case of HITRAN'96 which is the database used for
our retrieval. Thus in what follows we assume that the relative error in the cross-section
of a pixel is dominated by the relative error in the pixel-averaged line intensity,

$$\frac{\Delta\hat{\sigma}}{\hat{\sigma}} = \frac{\Delta\hat{S}_{\bar{\nu}}}{\hat{S}_{\bar{\nu}}}, \tag{3.34}$$

where $\hat{S}_{\bar{\nu}}$ represents a pixel-averaged line intensity (cf. Eq. 3.23). It is also assumed that
the effect on the line intensity of different temperatures for different light paths is small.

In order to link the $\Delta\phi$ correction, which we relate to the differential fit mismatch, to
uncertainties in line intensities of the gas in question we consider the following. Assume
that effective cross-sections $\hat{\sigma}_{sat,j}(s)$ and $\hat{\sigma}_{mod,j}(s)$ exist which satisfy

$$R_{sat}]_j = \exp\left(-\int_s \hat{\sigma}_{sat,j}(s)n(s)ds\right), \tag{3.35}$$

$$R_{mod}]_j = \exp\left(-\int_s \hat{\sigma}_{mod,j}(s)n(s)ds\right). \tag{3.36}$$

Then setting $\hat{\sigma}_{sat,j}(s) - \hat{\sigma}_{mod,j}(s) = \Delta\hat{\sigma}$ and $\hat{\sigma}_{mod,j} = \hat{\sigma}$ in Eq. (3.34) we obtain

$$
\begin{aligned}
R_{sat}]_j &= R_{mod}]_j \\
&\times \exp\left(-\int_s [\hat{\sigma}_{sat,j}(s) - \hat{\sigma}_{mod,j}(s)]\, n(s)ds\right), \\
&= R_{mod}]_j \\
&\times \exp\left(-\frac{\Delta\hat{S}_{\bar{\nu},j}}{\hat{S}_{\bar{\nu},j}}\int_s \hat{\sigma}_{mod,j}(s)n(s)ds\right).
\end{aligned}
\tag{3.37}
$$

If $\partial f/\partial\phi]_{\phi=\phi_0}$ from Eq. (3.33) is identified with the optical density in Eq. (3.37) then
$\Delta\phi_j = -\Delta\hat{S}_{\bar{\nu},j}/\hat{S}_{\bar{\nu},j}$ is a quantity which depends purely on errors in pixel-averaged line
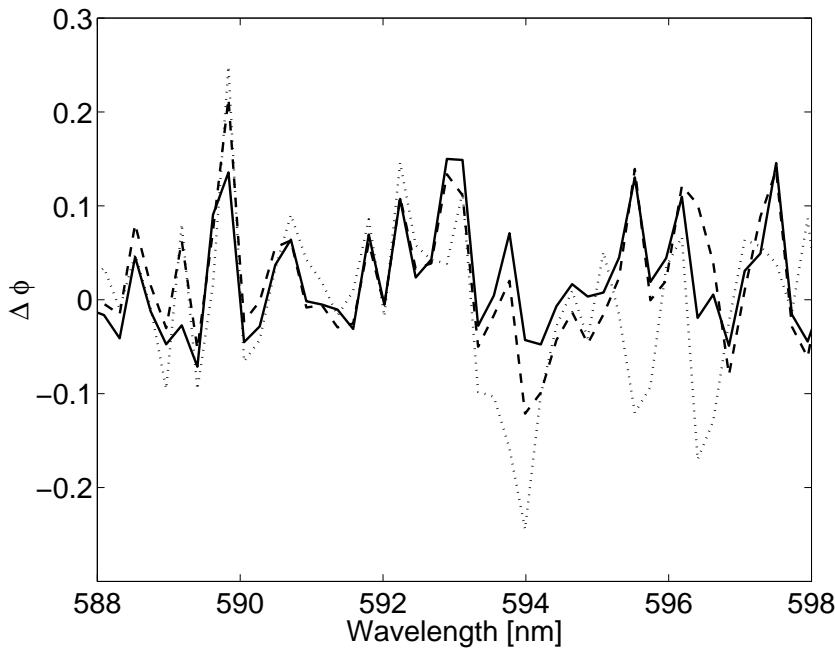
Figure 3.14: Pixel-to-pixel variation of $\Delta\phi$ calculated for three different GOME measurements. In each case the GOME measurement is used together with the corresponding lbl forward model result to calculate $\Delta\phi$ from Eq. 3.33. Values of $\Delta\phi$ for a high (solid), medium (dashed) and a low WVC (dotted line) are shown. The measurements were taken at significantly different geolocations with SZAs of $37°, 23°, 73°$, respectively. The three curves show similar spectral patterns which are quite different from the absorption signature of water vapor (c.f. figure 3.13). Below 588 and above 598 nm the differences between the modeled and measured spectra are small and the results are dominated by the noise of the measurement.

strength. It represents the correction required to bring the cross-section using the line strength values of the spectral database into agreement with what the real cross-section should be, given the correct atmospheric profile and the assumptions listed above.

The third panel in Fig. 3.13 shows the same mean residual as in the upper most panel but now for fits where the correction (Eq. 3.33) is applied using only *one* calculation of the differential fit mismatch $\Delta\phi$ for a single geolocation. For these fits the low frequency pattern in the region between 591 and 597 nm vanishes when applying the moving average over eight detector pixels (lowest panel). The derived WVCs are changing by applying the correction to values which are on average 17% higher than the values received from the uncorrected fits. Based on the assumption of a non-scattering atmosphere and relating the differential fit mismatch $\Delta\phi_j$ solely to systematic errors in the cross-section, we estimate the error in the pixel-averaged line strength $\Delta\hat{S}_{\bar{\nu}}/\hat{S}_{\bar{\nu}}$ (Eq. 3.37) to be on the order of

10 to 20%. Apart from these errors in the line strength values of the spectral database,
additional systematic contributions to the differential fit mismatch can be instrumental
errors or the structures in the sun irradiance spectrum due to Fraunhofer line absorption.
The latter is estimated to contribute less than 15% to the value of the differential fit
mismatch in the region of the Sodium lines and less than 5% to the remaining wavelength
region based on the calculations explained under 3.4.2 using Eq. (3.25) with and without
a constant F_0 together with Eq. (3.33).

3.9.3 Corrected Retrieval Results

Fig. 3.15 shows OACS WVC fit results which include the line-strength correction for the
same track as described in Section 3.9.2. For comparison we show the WVC values as given
by the ECMWF data assimilation model and the SSM/I microwave sounder which forms
part of the Defense Meteorological Satellite Program (DMSP) F14 satellite platform.
SSM/I global swath data are averaged on a 0.5×0.5 degree global grid. Data from
descending swathes are used in order to reach maximum overlap with the corresponding
GOME track. We average the data from each GOME ground pixel within a range of, on
average, $4°$ in longitude and $0.4°$ in latitude for each of the GOME geolocation 5-tuples of
the GOME ground pixel (see also Section 3.4.3 and Fig. 3.2). SSM/I data is not available
over land. The percentage cloud cover, also shown in the figure, is reported by GDP level-2
data. OACS fits give good results for GOME ground pixels with low cloud cover using the
first 18 pressure and temperature levels from the corresponding ECMWF pressure and
temperature profiles. In addition, the dynamic range in the WVC densities ranging from
values of 8×10^{20}molec/cm^2 in the polar regions to values of about 1.5×10^{23}molec/cm^2
at the equator is well reproduced and the variation between successive ground pixels is
very low.

The response of the retrieval method to the presence of high cloud cover does not
always result in a drop in WVC as might be expected for clouds that block the light from
traveling through the lower troposphere where the bulk of the water vapor is located. The
latter is the case, for example, in the region around $-18°$, where the retrieved columns
are significantly smaller than the values given by ECMWF and SSM/I. This also applies
to the narrow feature with strong cloud cover at $8°$ latitude for which OACS retrieves
lower WVC than is retrieved from the surrounding ground pixels. The same is the case
for the somewhat broader cloud cover at around $-42°$. even though the drop over about
six ground pixels is surrounded by higher WVC.

There are no regions to be found where OACS systematically under- or overestimates
the values given by ECMWF or SSM/I over a large area. Most of the systematic differences
over broader latitudinal regions are related to the presence of clouds.

OACS retrievals of WVCs including the line-strength correction were performed on
two additional GOME tracks. One track occurred on February 25, 1997 from 11:26 to
12:01 UTC at longitudes ranging from 322°E to 322°E and another on September 30,
1999 from 0:09 to 1:05 UTC covering longitudes from 82°E to 213°E. ECMWF data
is given for 12:00 UTC and 00:00 UTC respectively. These GOME tracks were chosen
predominantly for their good temporal and spatial overlap with SSM/I data and their
relatively low cloud content. Fig. 3.17 shows a scatter plot comparing OACS-retrieved
and ECMWF WVCs for all ground pixels (upper panel) and separately for cloud-free
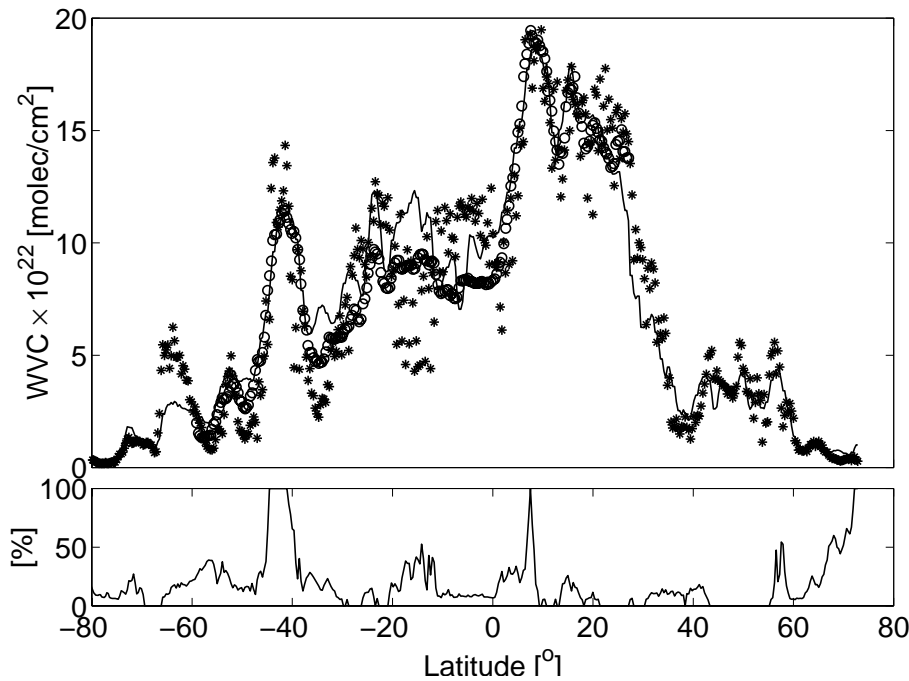
Figure 3.15: OACS WVC fit results over latitude (upper panel, stars) for
a GOME track on October 23, 1998 covering longitudes from 117°E at 73°
latitude to 279°E at −80° latitude. By way of a preliminary validation we
also show the values given by ECMWF at 18:00 UTC (solid curve) and the
SSM/I Microwave Sounder between 15:49 UTC and 16:39 UTC (circles).
SSM/I data is not available over land (> 30° latitude). The cloud coverage
in percentage per ground pixel is taken from GOME GDP level-2 data and
is indicated by the solid curve in the lower panel. OACS-retrieved WVCs
decrease in the case of strong cloud coverage e.g. at 8° and −18° in latitude.

pixels where the percentage cloud coverage is less than 10% (lower panel) including all
three GOME tracks. The scatter between OACS WVC values and values of ECMWF for
all three tracks is smaller than 50% and the systematic deviation is small. The gradient
of the linear fit through the results is 1.06 in the cloud free case (lower panel, Fig. 3.17).
The average effect on the retrieved column due to the presence of cloud is a drop in the
WVC, which results in a gradiant of 0.96 for all examined ground pixels (upper panel,
Fig. 3.17). Fig. 3.18 shows four scatter plots for cloud-free pixels for three different ranges
of SZAs as well as for pixels over the ocean (low surface albedo) only. The results show
that OACS is stable to changes in the surface albedo as well as to the geometry of the
measurement.

Fig. 3.16 shows two typical line strength-corrected OACS fits for geolocations with high
and low water vapor content together with their residuals. Both residuals are comparable
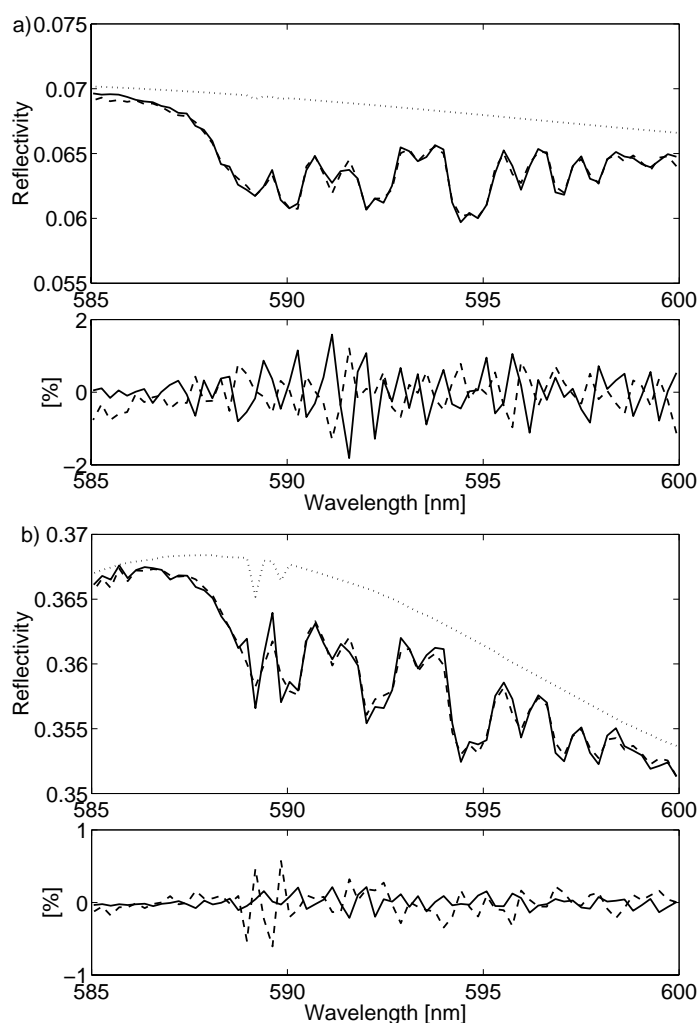
Figure 3.16: Results and residuals of typical OACS fits to two cloud-free
GOME measurements for the case of high WVC (panels a) and low WVC
(panels b). The solid lines in the both of the upper panels represent the
GOME reflectivity. Dashed lines in the upper panels represent the OACS
fit. The background (all absorbers other than water vapor) is shown by the
dotted lines. The residuals (dashed lines) are compared, in both of the lower
panels, with the intrinsic method related error (solid lines; c.f. Fig. 3.6).

to or smaller than the intrinsic method-related error and show essentially random scatter
except for the region of strong sodium absorption in cases where the water vapor content
is low (Fig. 3.16b).
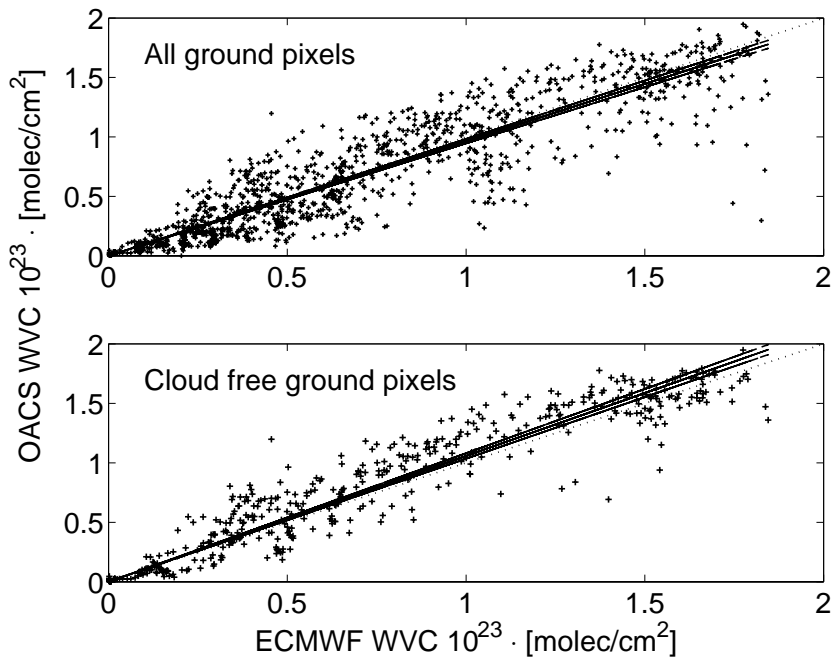
Figure 3.17: The two panels show scatter plots for WVCs retrieved by OACS in comparison with those given by ECMWF for all retrieved ground pixels (upper panel) and for ground pixels where the percentage cloud coverage is less than 10% (lower panel). OACS WVCs are retrieved for three different GOME tracks between $-80°$ and $+80°$ in latitude: on February 25, 1997 from 11:26 to 12:01 UTC at longitudes ranging from $322°E$ to $322°E$, on September 30, 1999 from 0:09 to 1:05 UTC between $82°E$ and $213°E$ longitude and on october 23, 1998 from 17:52 to 18:32 UTC between $117.16°E$ and $278.82°E$ longitude. ECMWF data is given for 12:00 UTC and 00:00 UTC and 18:00 UTC respectively. The solid lines in both panels denotes the best fit of a linear polynomial through the OACS WVC values with the 99% confidence interval for each residual surrounding it. The gradients are 0.96 for all pixels and 1.06 for the cloud free pixels

.

3.10   Discussion of Results

Thus far a number of assumptions have been made with respect to the treatment of the radiative transfer problem, the modeling of the background absorption and the quality of the input and reference data. The aim of this section is to discuss the preliminary validation of the OACS WVC results in light of known systematic differences between ECMWF and SSM/I and the influence of clouds and surface albedo.
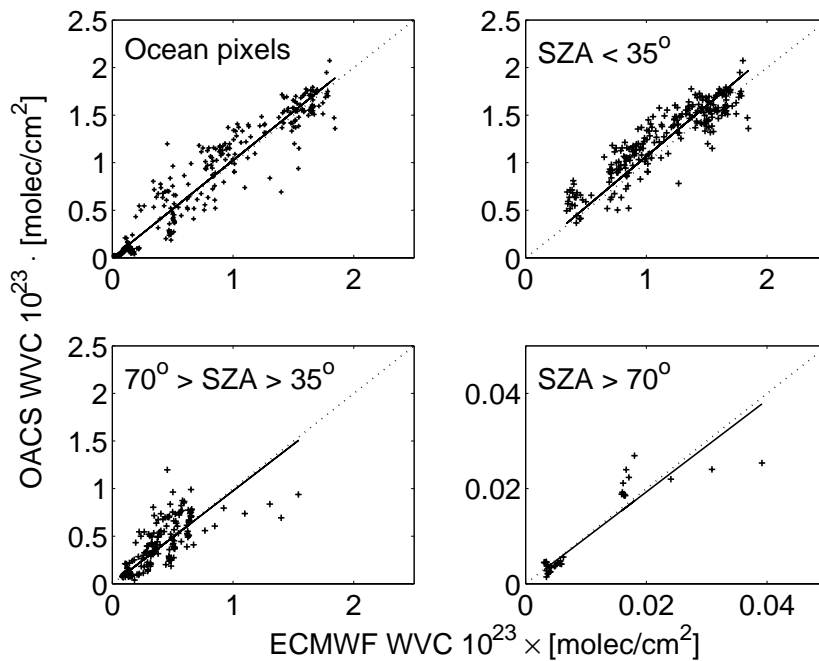
Figure 3.18: The four panels show scatter plots of WVCs retrieved by
OACS from GOME measurements of *cloud-free* ground pixels in comparison
with the values given by the ECMWF data-assimilation model. All studied
GOME tracks described in Fig. 3.17 are included. The upper left panel gives
results for measurements over the ocean only, i.e. with a low surface albedo.
The other panels give results for different SZA ranging between 20° and 85°.

3.10.1 Summary of Results

The results presented in section 3.9.3 and displayed in Fig. 3.17 show that the the cor-
relation between the OACS-GOME results and the reference ECMWF/SSMI values is
very good. The absolute differences between ECMWF data and OACS retrieved WVC
can be bigger than 50% for some cases, whereas the mean scatter is better than 11% for
ground pixels with no cloud cover and better than 30% for all retrieved ground pixels.
The method-related sensitivity and accuracy is of course significantly better.

3.10.2 Validation Datasets

In general, comparisons between WVCs given by ECMWF and SSM/I show significant
discrepancies. ECMWF is known to underestimate WVC values given by SSM/I by 30–
50% in the tropics and to overestimate in the sub-tropics by as much as 60% depending on
season and geolocation [*Vesperini et al*, 1998]. ECMWF WVC values over the ocean are
predominantly based on data from the TIROS N operational vertical sounder (TOVS).
The standard deviation between TOVS WVC and radiosonde data in the 1000-850 hPa

layer is known to be on the order of 20% and less than 40% in the layer between 500 and 300 hPa [*Chaboureau et al*, 1998].

The temporal and spatial collocation of GOME data with validation data is a significant challenge in its own right. All GOME measurements may be temporally collocated to within one hour of ECMWF values. Nevertheless, changes in the water vapor densities within this time window are possible. Such changes may contribute to both the scattering and the systematic effects in a comparison between the two data sets. As is shown in Fig. 3.2 the spatial overlap between the GOME ground pixel size and the smoothed ECMWF data gives rise to a higher spatial sensitivity of the OACS results in the latitudinal direction, whereas in longitudinal direction the spatial resolution of ECMWF data is significantly better. However, the change in water vapor column density over longitude is expected to be much lower than in the latitudinal direction [*Randel et al*, 1996; *Vesperini et al*, 1998].

It was noted before that OACS-retrieved WVCs do not show any significant systematic differences from the values given by ECMWF. Small overestimations of the OACS WVCs with respect to ECMWF values can be examined for SZA smaller than 35° including the tropical region (Fig. 3.18; (upper right panel). A small fraction of WVCs retrieved for cloud-free pixels and SZA between 35° and 70° (including the sub-tropical region) exhibit smaller values than given by ECMWF (Fig. 3.18; (lower left panel). From this we conclude that OACS-retrieved WVCs from the GOME tracks used in this study are consistent with the trends observed from an intercomparison between ECMWF and SSM/I. For higher SZA above 70° (lower right panel) there is no clear effect on the retrieved column of an enhanced contribution of multiply-scattered photons. However, the number of retrieved pixels is too small for good statistics.

3.10.3   Clouds

Systematic deviations of the WVCs from the values of ECMWF appear to be related predominantly to the presence of clouds. Clouds may affect the retrieved WVC in two ways. On the one hand, light may be blocked by clouds from traveling through the lower troposphere where the bulk of the water vapor column is situated. This would cause a drop in the retrieved WVC. On the other hand, an enhanced path length due to multiple scattering in the clouds might yield an increase in the retrieved WVC. Therefore the result of the net effect will depend on cloud top height, the cloud character and the thickness of the cloud layer. As described in Section 3.9.3 we found that strong cloud cover often causes a decrease in the retrieved WVC (Fig. 3.17). However, in some cases the opposite effect occurs. In general, the good correlation between ECMWF and OACS as well as the relatively small response to the presence of clouds suggests that the effect of the blocking of the light and the effect of enhanced path length may often compensate each other.

The cloud cover fraction is reported by GDP level-2 data. This fraction is derived by the initial cloud fitting algorithm (ICFA) and cloud top pressure is taken from the International Satellite Cloud Climatology project (ISCCP)[*Koelemeijer et al*, 1999]. Differences in the retrieved cloud fractions with respect to the collocated Along Track Scanning Radiometer-2 (ATSR-2) can be as much as 0.18[*Koelemeijer et al*, 1999]. We call a GOME ground pixel cloud free when the ICFA algorithm reports a cloud fraction of lower than 0.1. Therefore, large parts of the scattering in the case we call cloud-free (Fig.

3.17) may be attributed to ground pixels partially covered by clouds or errors in the cloud
fraction values given by GDP level-2 data.

3.10.4 Differential Fit Mismatch

For the calculation of the error $\Delta\phi$ of the model input parameter ϕ we assumed that
the water vapor subcolumn profile concentrations used in the calculation of R_M given
by ECMWF are close to reality. We further assumed that the differential contribution
of multiple scattered photons are weak. The signatures of both of these errors, not to
mention some contribution of the Ring effect and the Fraunhofer line effect discussed in
section 3.4.2 and 3.9.2 especially in the two pixels covering the sodium lines, should also
contribute to the differential spectral structure of the calculated cross-section correction
$\Delta\phi$. We quantified the contribution of the Fraunhofer line effect to be less than 15% of
$\Delta\phi$ in the aerea around the sodium lines and less than 5% in the remaining wavelength
region. The signature of neglecting the differential impact of multiple scattering in the
calculation of $\Delta\phi$ should be visible as asystematic effect (c.f. section 3.7 and Fig. 3.9)
displaying the differential structure of the water vapor absorption. This effect is extremely
small. Consequently, we relate the differential fit mismatch predominantly to instrumental
pixel-to-pixel variations which are not corrected for by the level 1 data processing together
with errors in the line strength databases. This places an upper limit of accuracy on the
latter of about 10 to 20%.

3.10.5 Surface Albedo

For each OACS fit we retrieve a surface albedo Λ (Eq. 3.27) assuming that the surface
may be modeled as a Lambertian reflector. Fig. 3.19 shows the retrieved albedo at 590
nm together with the cloud cover for the same GOME track shown and described in Fig.
3.15. The cloud-free results are comparable with those of *Koelemeijer et al,* [1997] using
GOME measurements with an atmospheric correction scheme. However, the wavelength
dependence of the albedo (Eq. 3.27) within our spectral window might be influenced by
the simultaneously fitted multiple scattering term (Eq. 3.28). A fit to the solution of the
DAM revealed an albedo accuracy of about 30% at 592 nm for a ocean type surface
albedo of 0.03 (Table 4). For higher albedo over land (around 0.1) the accuracy is better
than 10% due to the model calculations and retrievals. The impact of multiple scattering
and aerosol extinction can introduce errors in the retrieved albedo value of up to 40% for
maritime cases. The response to clouds is also clearly visible in Fig. 3.19. In the case of
strong cloud cover the retrieved albedo can easily reach 0.5.

3.11 Overview and Outlook

3.11.1 Summary

We have shown that OACS is able to forward-model upwelling reflectivity with accuracies
better than 2%, when compared to results from a lbl calculation. In column retrieval terms,
the precision of OACS (which depends on instrumental characteristics) is 0.66% for high
WVC and 3.4% for low WVC. The accuracy of the method is better than 0.05% and
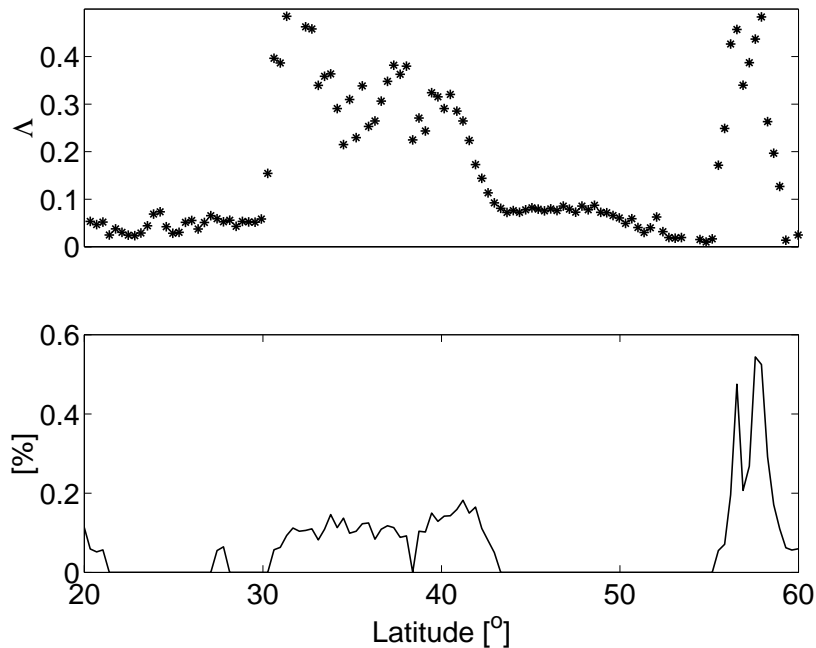
Figure 3.19: Surface albedo Λ at 590 nm retrieved with the OACS method
for the GOME track described in Fig 3.15 (upper panel). The first part of
the track (which covers 40° to 60° latitude at about 260° in longitude) starts
over the Canadian Shield which is dominated by water in the form of lakes
and by vegetation. OACS retrieved albedos between 0.03 and 0.1 for cloud
free pixels (the percentage cloud cover is shown in the lower panel). The
other part, from the Rocky Mountains over the Gulf of California and the
Pacific (40° to 20° latitude at about 255° in longitude), frequently yielded
albedos below 0.05.

1.4% for high and low WVC, respectively. Besides calibrated radiances, the only necessary
inputs from an operational perspective are specific temperature and pressure profiles for
a given geolocation and SCDs of ozone. Method inputs which are pre-calculated and
stored in lookup tables include pdfs of water vapor cross-section realizations taken from
the HITRAN'96 database and cross-sections of $(O_2)_2$ and O_3. The robustness or total
accuracy of the method due to errors in the input pressure and temperature profile was
found to between 0.8% and 4% for high and low WVC, respectively. The obtained WVCs
for cloud-free ground pixel situations correlate very well to WVCs given by ECMWF and
SSM/I. The ground pixel-to-pixel variation of the retrieved column densities are low and
the method is robust to changes in surface albedo as well as changes in the SZA.

3.11.2   Implementation and Routine Retrieval

We have introduced, tested and presented a preliminary validation of a novel, fast forward
modeling and retrieval method. The intention was to develop a relatively fast method for
modeling spectral measurements for which the instrumental resolution is much broader
than the absorption features of the trace gas under study. OACS uses a pdf coefficient
method for the calculation of reflectivities containing the full altitude-dependent structure
of the spectrum which can be stored in a look-up table. OACS forward modeling is
very fast with respect to line-by-line methods and a retrieval of trace gas column from
constituents with narrow-band absorption spectra can be done on reasonable time scales.
A retrieval of WVCs as described in this paper utilizing 18 altitude levels takes about 20
minutes per measurement on a Pentium II, 450 MHz, using an uncompiled MatLab code.
Although this is still slow with respect to recent other DOAS methods [*Buchwitz et al*,
2000; *Noël et al*, 1999] fitting time can be improved significantly by porting the algorithm
to a compiled language and using improved computer power. For the purpose of faster
but less comprehensive on-line retrieval preliminary testing indicates that accuracies in
the total retrieved WVC comparable to OACS can be obtained by replacing the basic
exponential sums with a spectral structure parameterization-modified DOAS formulation
(DOAS-SSP) [*Maurellis et al*, 2000b] which is approximately twenty times faster than
OACS and considerably easier to implement in a routine retrieval context.

3.11.3   Future developments

Improvements in the accuracy of the results and the stability of the fit may be gained
by using additional information about surface albedo, cloud cover and cloud height. For
example, surface albedo may be obtained by inspection of the region beyond the edges
of the water vapor absorption band. Using such additional inputs would reduce the pa-
rameter space in the fitting of WV-subcolumn profiles and thus reduce the freedom of
the fit in giving too much weight to the atmospheric scattering contribution by reducing
the surface albedo or vice versa. The current OACS modified solution of the radiative
transfer equation is best applied only to ground reflected and single scattered photons.
We have shown that this is sufficient for retrieval of WVC from operational GOME data,
utilizing the spectral water vapor window between 585 and 600 nm, within an accuracy of
18%, which is comparable to or better than available operational data products. In future
studies the first-order polynomial accounting for the broad-band absorption contribution
of multiple-scattered photons in the fast forward modeling as well as in the retrieval
might be replaced by a full OACS-modified solution for higher orders of scattering. This
could also serve as a starting point for implementing aerosol scattering and absorption
parameters. However, OACS could be easily applied in its current form to measurements
of the water vapor absorption in the infrared regions around 2 μm of the forthcoming
SCIAMACHY instrument on the ENVISAT platform, where the contribution of multiple
scattering is much smaller than in the visible region.

3.11.4 Conclusions

Apart from the application to routine trace gas retrieval OACS provides an efficient tool for studying physical processes from remote-sensing spectral measurement. This is because OACS is based on a fundamental, physical model. Consequently, it may be used to validate laboratory measurements of trace gas absorption cross-sections with measurements from satellites. For example, we have shown that there is some evidence for inaccuracies in the HITRAN'96 database as proposed by recent measurements of the water vapor absorption line parameters. Additionally, the fast forward modeling capabilities of OACS can be used to model and study atmospheric absorption features other than water vapor, as we demonstrated in the case of the $(O_2)_2$ absorption feature around 575 nm even for high SZA. A future application of OACS in the near infrared will be to forward-model water vapor absorption bands in spectral regions containing absorption features of atmospheric species other than water vapor.

Bibliography

Aben, I., D. M. Stam, and F. Helderman, The Ring effect in skylight polarisation, *Geophys. Res. Lett., 28*, 3, 519-522, 2001.

Armstrong, B. H., Spectrum Line Profiles: The Voigt Function, *J. Quant. Spect. & Rad. Transfer, 7,* 61-88, 1967.

Balzer, W. and D. Loyola, Product Specification Document of the GOME Data Processor, *Technical Document ER-PS-DLR-60-0016*, Deutsche Forschungsanstalt für Luft- und Raumfahrt, 21 pp., 1996.

Banks, P. M., and G. Kockarts, Aeronomy, 109 pp., *Academic Press*, New York and London, Part B, 1973.

Bates, D. R., Rayleigh scattering by air, *Planet. Space Sci., 32,* 785-790, 1984.

Belmiloud, D., R. Schermaul, K. Smith, N. F. Zobov, F. Nikolai, J. W. Brault, R. C. M. Learner, D. A. Newnham, and J. Tennyson, New Studies of the Visible and Near-Infrared Absorption by Water Vapour and Some Problems with the HITRAN Database, *Geophys. Res. Lett., 27*, 3703-3707, 2000.

Bovensmann, H., J. P. Burrows, M. Buchwitz, J. Frerick, S. Noëll, V. V. Rozanov, K. V. Chance, and A. Goede, SCIAMACHY - Mission Objectives and Measurement Modes, *J. Atmos. Sci., 56*, 127-150, 1999.

Buchwitz, M., V. V. Rozanov, and J. P. Burrows, A near-infrared optimized DOAS method for the fast global retrieval of atmospheric CH_4, CO, CO_2, H_2O, and N_2O total column amounts from SCIAMACHY Envisat-1 nadir radiances, *J. Geophys. Res., 105,* 15,231-15,245, 2000.

Burrows, J. P., M. Weber, M. Buchwitz, V. Rozanov, A. Ladstttter-Weienmayer, A. Richter, R. deBeek, R. Hoogen, K. Bramstedt, K.-U. Eichmann, and M. Eisinger, The Global Ozone Monitoring Experiment (GOME): Mission Concept and First Scientific Results, *J. Atmos. Sci., 56,* 151-175, 1999.

Byrd, R. H., R. B. Schnabel and G. A. Shultz, Approximate Solution of the Trust Region Problem by Minimization over Two-Dimensional Subspaces, *Mathematical Programming, 40,* 247-263, 1988.

Carleer, M., A. Jenouvrier, A.-C. Vandaele, P. F. Bernath, M. F. Mérienne, R. Colin, N. F. Zobov, O. L. Polyansky, J. Tennyson, and V. A. Sarin, The Near Infrared, Visible and Near Ultraviolet Overtone Spectrum of Water, *J. Chem. Phys., 111,* 2444-2450, 1999.

Casadio S., C. Zehner, G. Piscane, and E. Putz, Empirical Retrieval of Atmospheric Air Mass Factor (ERA) for the Measurement of Water Vapor Vertical Content using GOME Data, *Geophys. Res. Lett., 27,* 1483-1486, 2000.

Chaboureau, J.-P., A. Chédin, and N. A. Scott, Remote Sensing of the vertical distribution of atmospheric water vapor from the TOVS observations: Method and validation, *J. Geophys. Res., 103,* 8743-8752, 1998.

Chance, K., and R. J. D. Spurr, Ring Effect Studies: Rayleigh Scattering, Including Molecular Parameters for Rotational Raman Scattering, and the Fraunhofer Spectrum, *Applied Optics, 36,* 5224-5230, 1997.

Chance, K., Analysis of BrO Measurements from the Global Ozone Monitoring Experiment, *Geophys. Res. Lett., 25,* 3335-3338, 1998.

Caspar, C., and K. Chance, GOME Wavelength Calibration Using Solar and Atmospheric Spectra, *Proc. 3rd ERS Symposium* at Florence, Italy, Mar. 17 to 21, ESA SP-414, 1997.

DLR, GOME data Processor Extraction Software Users Manual, *Doc.No.: ER-SUM-DLR-GO-0045, DLR/DFD, Oberpfaffenhofen, Germany*, 1999.

DLR, GOME Level 0 to 1 Algorithm Description, *Technical Note ER-TN-DLR-GO-0025, DLR/DFD, Oberpfaffenhofen, Germany*, 1996.

The Global Ozone Monitoring Experiment Users Manual, *Ed. F. Bednarz*, ESA Publication SP-1182, ESA Publication Division, ESTEC, Noordwijk, The Netherlands, 1995.

Filiberti, M.-A., F. Rabier, J.N. Thépaut, L. Eymard, and P. Courtier, Four-dimensional variational assimilation of SSM/I precipitable water content data, *Q. J. R. Meteorol. Soc, 124,* 1743-1770, 1998.

Francis, J. A., and A. J. Schweiger, A New Window Opens On The Arctic, *EOS, 81,* 2000

Giver, L.P., J. C. Chackerian, and P. Varanasi, Visible and Near-infrared $H_2^{16}O$ Line Intensity Corrections for HITRAN-96, *J. Quant. Spect. & Rad. Transfer, 66,* 101-105, 1999.

Grainger, J. F., and J. Ring, Anomalous Fraunhofer line profiles, *Nature, 193,* 1962.

Greenblatt, G. D., J. J. Orlando, J. B. Burkholder, and A. R. Ravishankara, Absorption Measurements of Oxygen Between 330 and 1140 nm, *J. Geophys. Res., 95,* 18577-18582, 1990.

de Haan, J., P. Bosma, and J. Hovenier, The adding method for multiple scattering calculations of polarized light, *Astron. Astrophys., 181,* 371-391, 1987.

Hedin, A. E., Extension of the MSIS Thermosphere Model into the Middle and Lower Atmosphere, *J. Geophys. Res., 96,* 1159-1172, 1991.

Koelemeijer, R. B. A., P. Stammes, and D. Stam, Spectral Surface Albedo Derived From GOME Data, *Proc. 3rd ERS Symp. on* Space at the service of our Enviroment, *Florence, Italy, 17-21 March 1997*, ESA SP-414, 3 Vols, 1997.

Koelemeijer, R. B. A., and P. Stammes, Validation of GOME cloud cover fraction relevant for accurate ozone column retrieval, *J. Geophys. Res., 104,* 18,801-18,814, 1999.

Learner, R., R. Schermaul, J. Tennyson, N. Zobov, J. Ballard, D. Newnham, and M. Wickett, Measurement of H_2O Absorption Cross-Sections for the Exploitation of GOME data, *ESTEC Contract No 13312/9/NL/SF*, Final Presentation, 2000.

Liou, K.-N., An Introduction to Atmospheric Radiation, *Academic Press*, 1980.

Marquard, L. C., T. Wagner, and U. Platt, Improved air mass factor concepts for scattered radiation differential optical absorption spectroscopy of atmospheric species, *J. Geophys. Res., 105*, 1315-1327, 2000.

Maurellis, A. N., Non-Auroral Models of the Jovian Ionosphere, Ph.D. thesis, 75 pp., University of Kansas, June 1998.

Maurellis, A. N., R. Lang, W. J. v. d. Zande, U. Ubachs, and I. Aben, Precipitable Water Column Retrieval from GOME Data, *Geophys. Res. Lett., 27*, 903-906, 2000a.

Maurellis, A. N., R. Lang, and W. J. van der Zande, A New DOAS Parameterization for Retrieval of Trace Gases with Highly-Structured Absorption Spectra, *Geophys. Res. Lett., 27*, 4069-4072, 2000b.

Naus H., and W. Ubachs, Visible absorption bands of the $(O_2)_2$-collision complex at pressures below 760 Torr, *Applied Optics, 38*, 3423-3428, 1999.

Naus, H., W. Ubachs, P.F. Levelt, O.L. Polyansky, N.F. Zobov, and J. Tennyson, Cayity-Ring-Down Spectroscopy on Water Vapor in the Range 555-604 nm, *J. Molec. Spec., 205*, 117-121, 2001.

Newnham, D. A., and J. Ballard, Visible absorption cross sections and integrated absorption intensities of molecular oxygen (O_2 and O_4), *J. Geophys. Res., 104,*, 28,801-28,816, 1998.

Noël, S., M. Buchwitz, H. Bovensmann, R. Hoogen, and J. P. Burrows, Atmospheric Water Vapor Amounts Retrieved from GOME Satellite Data, *Geophys. Res. Lett., 26*, 1841-1844, 1999.

Perliski, L. M., and S. Solomon, On the Evaluation of Air Mass Factors for Atmospheric Near-Ultraviolet and Visible Absorption, *J. Geophys. Res, 98,* 10,363-10,374, 1993.

Perner, D., and U. Platt, Absorption of light in the atmosphere by collision pairs of oxygen $(O_2)_2$, *Geophys. Res. Lett., 7,* 1053-1056, 1980.

Pfeilsticker, K., F. Erle, and U. Platt, Absorption of solar radiation by atmospheric O_4, *J. Atmos. Sci., 54,* 933-939, 1997.

Platt, U., Modern Methods of the Measurement of Atmospheric Trace Gases, *Physical Chemistry Chemical Physics, 1,* 5409-5415, 1999.

Platt, U., Differential Absorption Spectroscopy (DOAS), *Air Monitoring by Spectroscopic Techniques*, M.W.Sigwist(Ed.), pp.27-84, Wiley, New York, 1994.

Plane, J. M. C., R. M. Cox, J. Qian, W. M. Pfenninger, G. C. Papen, C. S. Gardner, and P. J. Espy, Mesospheric Na layer at extreme high latitudes in summer, *J. Geophys. Res., 103,* 6381-6389, 1998.

Randel, D. L., T. H. Vonder Haar, M. A. Ringerud, G. L. Stephens, T. J. Greenwald, and C. L. Combs, A New Global Water Vapor Dataset, *Bulletin of the AMS, 77, 6*, 1996.

Richter, A., and J. P. Burrows, A multi wavelength approach for the retrieval of tropospheric NO2 from GOME measurements,*Proceedings of the ERS-ENVISAT symposium, Gothenburg October 2000*, ESA SP-461, 2000.

Roscoe, H. K., D. J. Fish, and R. L. Jones, Interpolation errors in UV-visible spectroscopy for stratospheric sensing: implications for sensitivity, spectral resolution, and spectral range, *Applied Optics, 35,* 427-432, 1996.

Rothman, L. S., C. P. Rinsland, A. Goldman, S. T. Massie, D. P. Edwards, J.-M. Flaud, A. Perrin, C. Camy-Peyret, V. Dana, J.-Y. Mandin, J. Schroeder, A. McCann, R. R. Gamache, R. B. Wattson, K. Yoshino, K. V. Chance, K. W. Jucks, L. R. Brown,

V. Nemtchino, and P. Varanasi, The HITRAN Molecular Spectroscopic Database and
HAWKS (HITRAN Atmospheric Workstation): 1996 Edition, *J. Quant. Spect. & Rad.
Transfer, 60,* 665-710, 1998.

Schrijver, H., Retrieval of carbon Monoxide, Methane and Nitrous Oxide from SCIA-
MACHY Measurements, *ESAMS'99 - European Symposium on Atmospheric Measure-
ments from Space, ESTEC, Noordwijk, the Netherlands, 1*, ESA WPP-161, 285-294,
1999

Shettle, E. P., and R. W. Fenn, 1979: Models for aerosols of the lower atmosphere and the
effects of the humidity variations on their optical properties, Air Force Geophys. Lab.
(OP), Envir. Res. Pap. 676, AFGL-TR-79-0214, Hanscom, Massachusetts (technical
report).

Solomon, S., R. W. Portmann, R. W. Sanders, and J. S. Daniel, Absorption of Solar Radi-
ation by Water Vapor, Oxygen, and Related Collision Pairs in the Earth's Atmosphere,
J. Geophys. Res., 103, 3847-3858, 1998.

Thomas W., E. Hegels, S. Slijkhuis, R. Spurr, and K. Chance, Detection of Biomass
Burning Combustion Products in Southeast Asia from Backscatter Data Taken by the
GOME Spectrometer, *Geophys. Res. Lett., 25*, 1317-1320, 1998.

Vesperini, M., Humidity in the ECMWF model: Monitoring of operational analyses and
forecasts using SSM/I observations, *Q. J. R. Meteorol. Soc., 124,* pp.1313-1327, 1998.

Voigt, S., J. Orphal, and J. P. Burrows, Absorption cross-sections of O_3 at atmospheric
temperatures (203-293 K) and pressures (100-1000 mbar) in the 12500-40000 cm-1
spectral range measured using FTS, *Chem. Phys. Lett.*, submitted, 2000.

Vountas, M., V. V. Rozanov, J. P. Burrows, Ring effect: Impact of Rotational Raman Scat-
tering on Radiative Transfer in Earth's Atmosphere, *J. Quant. Spect. & Rad. Transfer,
60*, 943-961, 1998.

Wallace, L., K. Hinkle, and W. Livingston, An Atlas of the Spectrum of the Solar Pho-
tosphere from 13,500 to 28,000 cm-1, *N.S.O. Technical Report #98-001*, NSF/NOAO,
June 1998, (technical report).

Chapter 4

A New DOAS Parameterization for Retrieval of Trace Gases with Highly-Structured Spectra

Differential Optical Absorption Spectroscopy (DOAS) has proven to be an extremely useful technique for retrieving trace gas columns from atmospheric measurements of reflected solar irradiance. We show that the use of DOAS is strongly constrained by the complexity of the absorption spectral structure (for eg., the vibration-rotation bands of many species in the visible and infrared) that may be sampled by individual pixels in a detector array. To this end we introduce a Spectral Structure Parameterization (SSP) which is dependent primarily on the cross-section and to a lesser extent on the concentration of the atmospheric species intended for retrieval. We show that SSP may be used to determine under which conditions DOAS will be sufficiently accurate for retrieval purposes. SSP also offers a new alternative for trace gas column retrieval, especially in cases when the spectra involved exhibit complex absorption structure.

4.1   Introduction

Retrieval of atmospheric trace gas columns demands both accurate spectral information
as well as spectrometers which operate at sufficient spectral resolution. The radiative
transfer problem is usually complicated by more than simple absorption, i.e. there may
also be multiple scattering both into and out of the detected beam as well as scattering
from clouds and aerosols. However retrieval situations do exist in which either absorption
is the dominant process or in which atmospheric scattering may be accounted for by a
wavelength-dependent *a priori* air mass factor derived from a full radiative transfer treat-
ment. Such situations are frequently successfully exploited by assuming that Beer's law
operates, and applying one form of it, the Differential Optical Absorption Spectroscopy
(DOAS) method [*Platt*, 1999], to the retrieval. DOAS operates by separating out the
broad-band structure (due to elastic scattering or broad-band absorptions) from the dif-
ferential structure (due to the trace gas under study) in order to fit Beer's Law to a
measured transmittance spectrum. In many cases DOAS offers a good compromise be-
tween speed, numerical accuracy and instrument performance and has proven its retrieval
reliability for many molecular species, especially in the near ultraviolet where predissocia-
tion of excited molecular states leads to sufficient line-broadening for the spectra to appear
smooth at detector resolution (for example, in the case of ozone columns from GOME
data [*Burrows et al.*, 1999]). (In this context we use *smooth* to imply that the absorption
strength varies little within the wavelength range of a detector pixel.) In contrast, many
species with absorption bands in the visible and the near infrared involve vibrational and
vibrational-overtone spectra (e.g. water vapor and methane) lack the smoothing from
line-broadening that allows Beer's Law to be formulated in terms of averaged optical
depth, as is the case in DOAS. In this work, we show that the success of DOAS retrieval
depends considerably on the degree of absorption spectrum structure, which can range
from single line (highly-structured) to broad-band (smooth) absorption. This dependence
may be characterized using a Spectral Structure Parameterization (hereafter SSP) which,
in the context of a particular detection scheme, is sufficient to decide *a priori* whether
or not DOAS may be used for trace gas retrieval. In addition, SSP provides a highly
accurate, new formulation of the optically-thin retrieval problem which may be used as a
practical replacement for DOAS.

4.2   Calculation of Atmospheric Transmittances

Spectrometers used in the measurement of atmospheric radiance usually operate across a
large spectral range and at a resolution which, on the wavenumber scale, may be ten to
a hundred times worse than the spectral structure resolved in laboratory measurements.
For example, retrieval from the GOME instrument on the ERS-2 satellite [*Burrows et al.*,
1999] covers a range of some 11 000–42 000 cm^{-1} with individual detector pixels which
each span about 6 cm^{-1}. Structure in laboratory spectral data is frequently resolved at
0.01 cm^{-1} or better. In order to facilitate retrieval the laboratory spectrum must be
sampled at the resolution of a single unit of detection, for example, a pixel of a grating
spectrometer detection array. Such a pixel may measure the solar photon irradiance at the
top of the atmosphere (I_{j0}) and the photon flux after attenuation by the atmosphere (I_{j0})

over a certain wavenumber range. The resulting transmittance spectrum $\frac{I_j}{I_{j0}}$ is usually
fitted by a *modeled* atmospheric transmittance, denoted by $\frac{I_j}{I_{j0}}\Big]_{\mathcal{M}}$, using a non-linear
least-squares method. The implicit fit parameter in the modeled transmittance is the
desired trace gas column density N. The subscript j tags a detector pixel wavenumber
region (of width Δk_j). The pixels are usually fitted simultaneously, often with equal weight
for all pixels, and the modeled transmittance may be convolved with a slit function in
order to account for the optics of the instrument. In order to focus solely on intrinsic,
method-related error in this letter we do not adopt any kind of slit function, consider only
one pixel ($j = 1$), and simulate retrievals assuming a gray atmosphere, i.e. $\int n(z)dz = N$.
However, all these simplifications may be generalized in the case of a real retrieval.

We first consider two alternative general forms of the modeled transmittance used in
a retrieval: either a pixel-averaged cross-section is used to obtain the transmittance, viz.

$$\frac{I}{I_0}\Big]_{\mathcal{D}} = \exp\left(-\int \langle \sigma(z,k) \rangle_k \, n(z) \, dz\right) \ , \tag{4.1}$$

or a pixel-averaged transmittance is calculated via

$$\frac{I}{I_0}\Big]_{\mathcal{R}} = \left\langle \exp\left(-\int \sigma(z,k) n(z) \, dz\right) \right\rangle_k \ . \tag{4.2}$$

Here $\langle \ldots \rangle_k$ denotes an average over wavenumbers sampled by the detector pixel, i.e.,

$$\langle \ldots \rangle_k \equiv \int \ldots \frac{dk}{\Delta k} \ .$$

Equation (4.1) describes an approximation often made in DOAS retrievals (hence the
model subscript $\mathcal{D}$). Equation (4.2) represents the real or reference transmittance (hence
subscript $\mathcal{R}$), i.e. a proper wavenumber-average of the transmittance [*Lenoble*, 1983] which
is usually calculated using a line-by-line method. In both cases absorption is assumed to
be the dominant process. Thus both are based on Beer's law. However, their use in re-
trieval clearly differs in that the wavenumber integration is executed at different positions
in the calculation. In what follows we show that this difference has very important conse-
quences for retrieval accuracy and provide a quantitative method for deciding when the
DOAS approximation (equation 4.1) works. In addition, we provide a retrieval alternative
based on equation (4.2) and show that this offers a greater sensitivity to the cross-section
spectral structure sampled by each detector pixel and thus significant improvements in
both retrieval accuracy and applicability.

4.3   Spectral Structure Parameterization

Consider only one detector pixel (spanning a range in wavenumber of size Δk) and assume
that the net absorption may be covered by absorption over an effective width $w\Delta k$ at
some average intensity S satisfying $\langle \sigma(k) \rangle_k = wS$ and $0 < w \leq 1$ (see figure 1). Then the
pixel-averaged optical depth (i.e. the mean optical depth per pixel) may be expressed in
terms of w and S as

$$\langle \tau \rangle_k = \langle \sigma(k) \rangle_k N = wSN \ , \tag{4.3}$$
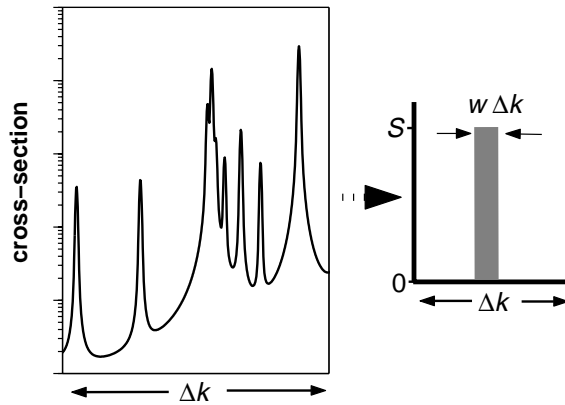
Figure 4.1: Schematic of the construction of an effective width parameter w
and an average absorption cross-section intensity S (right hand panel) from
a typical absorption spectrum which has been sampled over a wavenumber
range Δk by a single detector pixel (left hand panel).

as can the modeled transmittance, on evaluation of the integrals in equations (4.1) and
(4.2), viz.

$$\left. \frac{I}{I_0} \right]_{\mathcal{D}'} = \exp(-wSN) , \tag{4.4}$$

$$\left. \frac{I}{I_0} \right]_{\mathcal{R}'} = 1 + w \exp(-SN) - w . \tag{4.5}$$

Here a primed subscript denotes the SSP form of the transmittance. The parameters w
and S are uniquely defined by simultaneous solution of equations (4.3) and (4.5) for a
range of mean optical depths and transmittances. (The latter can always be determined
from a line-by-line model in advance, say, of a retrieval). The parameterization depends,
in general, on the mean optical depth and thus on the column density. This is because
the effective width of a line profile increases as N increases. That this is a third or higher
order effect follows from a Taylor expansion to second order of the exponents in equations
(4.2) and (4.5) which further reveals that

$$w \approx \frac{\langle \sigma \rangle_k^2}{\langle \sigma^2 \rangle_k} \text{ and } S \approx \frac{\langle \sigma^2 \rangle_k}{\langle \sigma \rangle_k} , \tag{4.6}$$

assuming optical thinness. As anticipated,

$$\left. \frac{I}{I_0} \right]_{\mathcal{R}'} \rightarrow \left. \frac{I}{I_0} \right]_{\mathcal{D}'} \text{ as } w \rightarrow 1 ,$$

which follows from the observation that DOAS underestimates the pixel-averaged trans-
mittance unless $w = 1$. Figure 2 shows the result of plotting this transmittance underes-

timation normalized to the reference transmittance, viz.

$$\Delta T_{\mathcal{D}}(w; \langle \tau \rangle_k) \equiv \left(\frac{I}{I_0} \Bigg]_{\mathcal{R}'} - \frac{I}{I_0} \Bigg]_{\mathcal{D}'} \right) / \frac{I}{I_0} \Bigg]_{\mathcal{R}'} \tag{4.7}$$

as a function of effective width for different mean optical depths. In retrieval, the transmittance error due to DOAS will be acceptable when

$$\Delta T_{\mathcal{D}} \leq \Delta T \;,$$

where ΔT represents the uncertainty in the measured transmittance (for eg. due to detector shot noise). The contours in figure 2 correspond to different mean optical depths which, in turn, depend on expected atmospheric columns. The vertical dot-dash line indicates a typical GOME value of $\Delta T \approx 3 \times 10^{-4}$ [*Chance*, 1998]. A range of values for w (calculated using equations 4.2, 4.3 and 4.5 or estimated using equations 4.6) coupled with the expected range in mean optical depths (which depend on atmospheric quantities) may be used to define a region of potential applicability of DOAS. If the region lies completely to the left of ΔT in figure 2, then the error in transmittance estimates due to the DOAS approximation is negligible.

For instance, in the retrieval of atmospheric bromine monoxide near 350 nm with GOME, $w \approx 0.8$ and mean optical depths range from 1×10^{-3} to 5×10^{-3}. Figure 2 shows that the transmittance error resulting from the DOAS assumption is quite acceptable. On the one hand, spectra displaying broad-band structure comparable to detector pixel wavelength range (such as ozone dissociation near 340 nm) correspond to values of $w \approx 1$ and DOAS is often applicable. At the other extreme, the spectra of atomic gases possessing isolated resonances (such as the sodium lines near 590 nm) would be described by $w \approx 0.01$. In this case DOAS will not accurately model the transmittance except for low optical depths (in which case the change in transmittance will already be almost negligible). An intermediate situation exists in the case of the vibrational bands of water (580–605 nm), for which $w \approx .05$–0.2 for optical depths of greater than 3×10^{-4}. These and further predictions are summarized in table 1.

4.4   Retrieval Simulations

We simulate column retrieval from synthetic transmittance spectra in order to determine the degree to which the error in transmittance discussed above translates into an intrinsic, method-related error. The transmittance spectra are calculated using line-by-line methods on synthetic absorption spectra for a range of optical depths. The different curves in figure 3a are constructed with the same absorption lines positioned at the same arbitrary wavenumbers and assuming the same integrated line intensities but computed for a range of different line widths. This range of line widths gives rise to a range of spectral structure, from narrow-line to broad-band absorption. The simulated cross-sections are normalized so that $\langle \tau \rangle_k = N$ (equivalently so that $wS = 1$). Figure 3b shows the range of values for w obtained from simultaneously solving equations (4.3) and (4.5) with pre-calculated transmittances (equation 4.2) for each of the spectra in figure 3a over a range of optical depths (solid curves). Clearly w depends strongly on spectral structure. Equations (4.6)
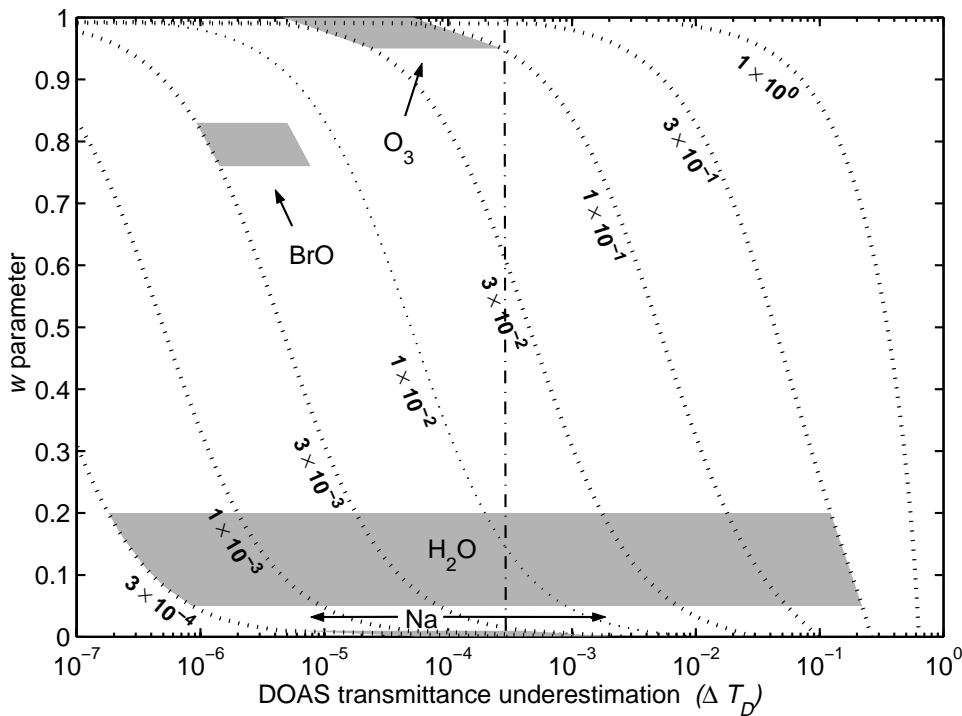
Figure 4.2: Heuristic for determining the range of applicability of the DOAS approximation to spectral fitting of measured transmittances. DOAS transmittance underestimation as a fraction of the correct transmittance is plotted as a function of w and mean optical depth (dotted curves). Also shown are regions of the plot relevant to GOME retrievals of sodium, bromine monoxide and ozone as well as water vapor in the visible (see table 1). The dash-dot line shows a GOME detector-related uncertainty of 2.7×10^{-4}. Regions which lie completely to the left of this line would always yield acceptable DOAS retrieval error.

also appear to yield a reasonable estimate of w (dotted lines in figure 3b) when $\langle \tau \rangle_k < 0.1$. We conclude that w is a robust indicator of detector pixel-averaged spectral structure.

Equations (4.4) and (4.5) may be used in a least squares procedure in order to simulate column retrieval for each of the spectra in figure 3a (see figure 3c). Retrievals which use the DOAS approximation consistently underestimate the column because DOAS always underestimates the transmittance ($\Delta T_D > 0$). DOAS retrieval accuracy improves as $w \to 1$, i.e. in the progression from blue to yellow solid curves in figure 3c. In contrast, SSP (dashed curves) retrieves columns at no worse than 0.02% error and this only for very low mean optical depths. This is largely because the source of the error is numerical and can, in principle, be reduced even further. It is important to note that the results shown here are for retrieval *based on a single detector pixel and a single atmospheric column*, i.e.

Table 4.1: DOAS applicability for GOME- or SCIAMACHY-retrievable
species

Species	Spectral Range[a] (nm)	Mean Optical Depth[b]	Pixel Range[c] (nm)
H_2O	580–605	3×10^{-4}–1×10^{0}	0.21
O_3	335–345	3×10^{-2}–1×10^{-1}	0.12
BrO	344–360	3×10^{-3}–5×10^{-3}	0.11
Na	590,591	3×10^{-4}–3×10^{-2}	0.21
SO_2	240–330	3×10^{-3}–6×10^{-2}	0.33
H_2O	2260–2380	$\approx 10^{-6}$–2×10^{1}	0.27
N_2O	2310–2380	$\approx 10^{-8}$–9×10^{-3}	0.27
CO	2260–2336	$\approx 10^{-8}$–2×10^{-2}	0.27
CH_4	2260–2380	$\approx 10^{-8}$–6×10^{-2}	0.27

	w parameter	DOAS?[d]	Retrieval Error[e]
H_2O	0.05–0.2	No	$> 10\%$
O_3	0.96–1	Yes	$< 0.1\%$
BrO	0.75–0.85	Yes	$< 0.05\%$
Na	0.005–0.01	No	$> 10\%$
SO_2	0.96–1	Yes	$< 0.02\%$
H_2O	0.3–1.0	No	$> 10\%$
N_2O	0.3–1.0	Yes	$< 0.1\%$
CO	0.3–1.0	Yes	$< 1\%$
CH_4	0.3–1.0	No	$> 10\%$

[a]Indicates the portion of a detector's spectral range available for or currently used in
retrieval of this species.

[b]Mean optical depth per detector pixel depends both on the species' column density and
its absorption spectrum.

[c]Wavelength range spanned by a representative detector pixel.

[d]Applicability of DOAS formulation assuming detector-related error of about 0.03% (see
also figure 2).

[e]Single-pixel DOAS retrieval error estimates based on the results of simulations in figure
3.

our simulations do not take into account the many additional errors incurred in actual
retrieval due to pixels with wavenumber-dependent uncertainties and modeling of the
background reflectance. Preliminary testing of multi-pixel simulations (not shown) with
realistic atmospheric profiles confirm that for trace gases with highly-structured spectra
at atmospheric optical depths and for a range of w values, SSP retrieval yields results
with better than 0.1% method-related accuracy. We conclude that simply substituting
the right hand side of equation (4.5) in place of the $\exp(-\langle\tau\rangle_k)$ term in a DOAS retrieval,
in conjunction with a pre-calculated $w(\langle\tau\rangle_k)$ curve, will generally yield a much improved
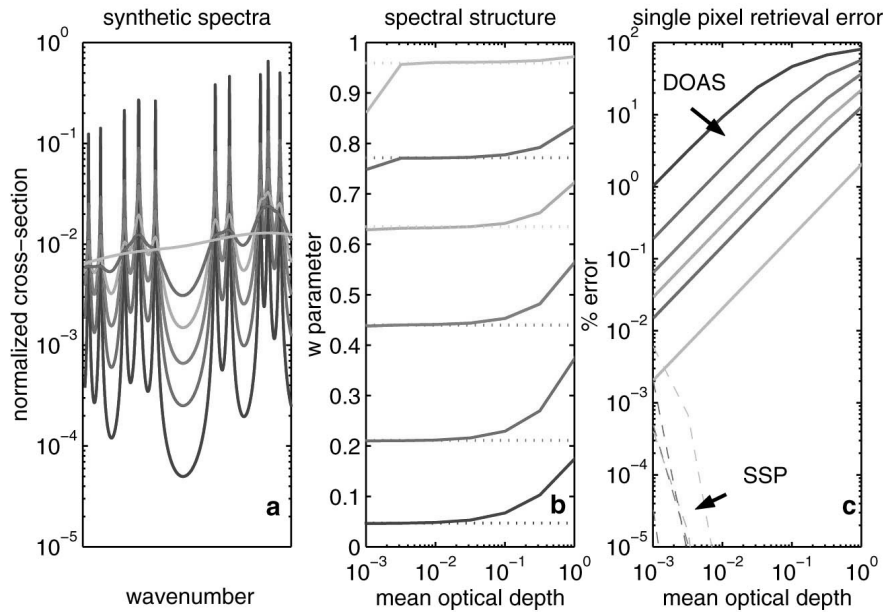
Figure 4.3: **Panel a.** Synthetic absorption cross-sections ranging from narrow-line to broad-band absorption (from dark to bright). **Panel b.** Spectral structure parameter w as a function of mean optical depth, calculated from simultaneous solution of equations (4.3) and (4.5) (solid curves) and also estimated using equations (4.6) (dotted lines). Colours correspond to the profiles in panel (a). Clearly w is weakly dependent on mean optical depth but strongly dependent on spectral structure. **Panel c.** Fractional column retrieval error, $(N_{\text{retrieved}} - N)/N$, using DOAS (solid curves) and SSP (dashed curves) retrieval methods on transmittances determined by line-by-line integration of the cross-sections shown in panel (a) for known columns $N = \langle \tau \rangle_k$. The dependence of w on mean optical depth in panel (b) is interpolated in the fitting procedure. DOAS retrieval error becomes comparable with SSP retrieval error as $w \to 1$ (bright curves).

fit accuracy for the retrieved column.

4.5   Summary

Since DOAS is computationally very simple to implement it is usually an ideal first choice for trace gas column retrieval. We have presented a heuristic for determining the intrinsic limiting accuracy of DOAS in terms of a simple spectral structure parameterization which, in the optically-thin case, may be estimated directly from the absorption cross-section spectrum (see equations 4.6). A lower limit to the accuracy of a potential DOAS implementation may be determined from figure 2 which may be used to decide whether

or not DOAS should be implemented. We have also presented retrieval simulations which
may be used to determine the magnitude of DOAS and SSP retrieval errors. It is now
clear why DOAS retrievals consistently underestimate precipitable water vapor columns
by up to a factor of three using absorption measurements in the visible [*Maurellis et al.*,
2000] and why DOAS generally cannot be used to directly infer water vapor column from
GOME data without considerable modification [*Noël et al.*, 1999]. Perhaps most impor-
tantly, the SSP formalism is a substantial modification to differential optical absorption
retrieval methods which offers a much greater range of applicability than DOAS as well
as significant improvements in retrieval accuracy for a very small additional investment
in computational complexity.

Bibliography

Burrows, J. P., M. Weber, M. Buchwitz, V. Rozanov, A. Ladstatter-Weissenmayer, A.
   Richter, R. DeBeek, R. Hoogen, K. Bramstedt, K. U. Eichmann and M. Eisinger, The
   global ozone monitoring experiment (GOME): Mission concept and first scientific re-
   sults, *Journ. Atmos. Sci., 56,* 151-175, 1999.
Chance, K., Analysis of BrO Measurements from the Global Ozone Monitoring Experi-
   ment, *Geophys. Res. Lett., 25,* 3335-3338, 1998.
Lenoble, J., *Atmospheric Radiative Transfer*, 111 pp., A. Deepak Publishing, Hampton,
   Virginia, 1983.
Maurellis, A. N., R. Lang, W. J. van der Zande, I. Aben and W. Ubachs, Precipitable
   Water Column Retrieval from GOME Data, *Geophys. Res. Lett., 27,* 903-906, 2000.
Noël, S., M. Buchwitz, H. Bovensmann, R. Hoogen and J. P. Burrows, Atmospheric Water
   Vapor Amounts Retrieved from GOME Satellite Data, *Geophys. Res. Lett., 26,* 1841-
   1844, 1999.
Platt, U., Modern Methods of the Measurement of Atmospheric Trace Gases, *Physical
   Chemistry Chemical Physics, 1,* 5409-5415, 1999.

Chapter 5

Application of the Spectral Structure Parameterization Technique: Retrieval of Total Water Vapor Columns from GOME

We use a recently proposed spectral sampling technique for measurements of atmospheric transmissions called the Spectral Structure Parameterization (SSP) in order to retrieve total water vapor columns (WVC) from reflectivity spectra measured by the Global Ozone Monitoring Experiment (GOME). SSP provides a good compromise between efficiency and speed when performing retrievals on highly structured spectra of narrow-band absorbers like water vapor. We show that SSP can be implemented in a radiative transfer scheme which treats both direct-path absorption and absorption by singly scattered light directly. For the retrieval we exploit a ro-vibrational overtone band of water vapor located in the visible around 590 nm. We compare our results to independent values given by the data assimilation model of ECMWF. In addition, results are compared to those obtained from the more accurate, but slower, Optical Absorption Coefficient Spectroscopy (OACS).

5.1   Introduction

The retrieval of concentrations of narrow-band line absorbers, such as water vapor (WV), from space-borne spectral instruments is often complicated by the relatively low resolution of the detector with respect to the width of an individual absorption line. For example, GOME spectral sampling in the visible region (channel 3) is 0.2 nm which covers up to 12 individual absorption lines of WV in the spectral region around 580 nm [*ESA*, 1995]. To allow accurate modeling of such absorption spectra requires a large number of spectral realization points in order to resolve the narrowest lines, especially at high altitudes where pressure broadening is absent. In principle, band models, exponential sum fitting methods or other opacity sampling techniques, like the well known k-distribution method [*Lacis & Oinas*, 1991; *Kato et al.*, 1999], and the more recently proposed Optical Absorption Coefficient Spectroscopy technique (OACS) [*Maurellis et al.*, 2000a; *Lang et al.*, 2002] (cf. chapter 2 for basic OCM formulation and chapter 3 for specific OCM application called OACS) can be used to solve this problem. In practice, both of the latter two methods use opacity sampling probability functions to represent the effective absorption within a specific spectral sampling interval. These probabilities are then used either directly (OACS), or indirectly, via a transformation from wavelength into cross-section space (k-distribution), as weighting functions of a set of opacity basis functions, whose summation replaces a computationally expensive spectral sampling integral. Both of these methods have demonstrated their ability to solve the problem of spectral sampling in an accurate and efficient way for atmospheric water vapor absorption, in case of OACS utilizing GOME measurements in the absorption region around 590 nm [*Lang et al.*, 2002] and, in case of the k-distribution method, on synthetic spectra in the IR regions of the SCanning Imaging Absorption CartograpHY (SCIAMACHY) instrument on ESA's Environmental satellite ENVISAT [*Buchwitz et al.*, 2000].

In contrast, in the Spectral Structure Parameterization (SSP) recently proposed by *Maurellis et al.* [2000b] (chapter 4), and applied here for the first time to retrievals from reflectivity measurements, the number of opacity functions and their weights are reduced to only one basis function with one weighting parameter, called the spectral structure parameter w, which characterizes the spectral structure of the absorber within a specific wavelength range and at a specific altitude. SSP lends itself therefore more to the basic concept of band models, where the average absorption over a specific wavelength interval is represented by averaged line parameter values. Different to band models, SSP is well suited for relatively small sampling regions containing only a small number of distinct absorption lines, such as those found in the regions covered by the detector pixels of both GOME and SCIAMACHY (both instruments work at relatively high spectral resolution across a wide wavelength region). In addition, the implementation of SSP in a radiative transfer scheme including direct path absorption, as well as the contribution of single scattering to the measured reflectivities, is relatively simple and requires only a small amount of computational effort. Consequently, SSP retrieval of WVC is fast and may be performed on a global scale in a reasonable time, as demonstrated in this paper .

Retrieval of WVC from GOME has also been demonstrated by *Noël et al.*, [1999], and *Casadio et al.*, [2000], utilizing absorption bands in the region around 700 and 740 nm, respectively. We are focussing on a ro-vibrational overtone band of WV in the visible between 580 and 605 nm covered by the GOME instrument. This band was first exploited

for the retrieval of WVC by *Maurellis et al.*, [2000a], using the OACS sampling technique. SSP is a retrieval method, which is easy to implement, fast, self-contained and based on first principles. The only inputs needed for the retrieval of WVC by SSP are pressure and temperature profiles, which are, for global retrievals, taken from a climatology model and calculated on-line. No *a priori* knowledge about the water vapor profile is required and SSP retrieves subcolumn profile from which a total column is calculated. The only constraints applied to the fits are three standard upper profile constraints for tropical, mid-latitude and high-latitude cases.

In the following section we briefly summarize the basic concept of SSP for homogeneous atmospheres. Then we show how SSP can be applied to nadir satellite reflectivity measurements probing nonhomogeneous atmospheres, including light paths where photons undergo a single-scattering event. Thereafter, we present results of SSP forward-modeled reflectivity spectra, which we compare to both line-by-line (lbl) forward-modeled spectra, as well as GOME measurements. SSP retrieval results from monochromatically forward-modeled spectra are used to assess the method related bias and to introduce a retrieval correction term for high WVC values. The impact of multiple scattering and aerosol loading on the retrieval values will also be discussed in some detail. We then expand our retrievals to both a single GOME track and a global coverage (i.e. three days of continuous GOME measurements). The results are compared and discussed with respect to co-located WVC given by the European Center of Medium Range Weather Forecast (ECMWF) data assimilation model, after which we present our conclusions.

5.2   Sampling of Homogeneous Absorption

For homogeneous absorption over a direct path in the absence of any scattering events, the spectrally sampled transmittance may be defined as

$$\langle T \rangle_{\Delta\lambda} = \int_{\Delta\lambda} \exp(-\sigma(\lambda)N)\frac{d\lambda}{\Delta\lambda}, \tag{5.1}$$

where $\sigma(\lambda)$ is the absorption cross-section, N is the total column density and $\Delta\lambda$ is the sampling width. The transmittance $\langle T \rangle_{\Delta\lambda}$ may also be expressed as:

$$\langle T \rangle_{\Delta\lambda} = 1 + w\exp(-SN) - w. \tag{5.2}$$

Here, S has units of cross-section, therefore, determines the height of a box with width w ($0 < w \leq 1$) in units of $\Delta\lambda^{-1}$, which covers the area of absorption equivalent to the area covered by the individual lines of the absorber within the spectral region $\Delta\lambda$ (see Figure 5.1) with

$$\langle \sigma(\lambda) \rangle_{\Delta\lambda} = wS, \tag{5.3}$$

and the pixel-averaged optical depth $\langle \tau \rangle_{\Delta\lambda} = wSN$.

w and S are now defined by the simultaneous solution of equations (5.2) and (5.3) with the result that they are implicitly dependent on N. A Taylor expansion to second order of the exponents in Eq. (5.1) and (5.2) reveals that
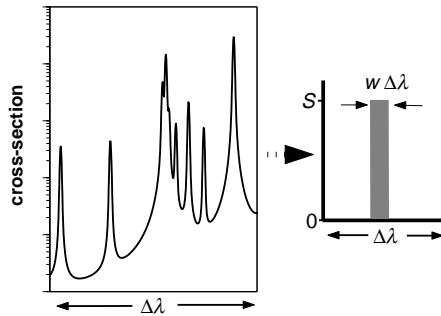
Figure 5.1: Schematic of the construction of an effective pixel coverage parameter w and effective mean value for the absorption cross-section S (right hand panel) from a typical absorption spectrum which has been sampled over a wavelength range $\Delta\lambda$ by a single detector pixel (left hand panel).

$$w \approx \frac{\langle\sigma\rangle^2_{\Delta\lambda}}{\langle\sigma^2\rangle_{\Delta\lambda}} \text{ and } S \approx \frac{\langle\sigma^2\rangle_{\Delta\lambda}}{\langle\sigma\rangle_{\Delta\lambda}} \; . \tag{5.4}$$

The latter is a good approximation of w and S in cases of a wavelength-averaged optical depth of lower than 0.1 [*Maurellis et al.*, 2000b] (cf. equations in chapter 4 and Figure 3 in the same chapter).

5.3 Application to Nadir Measurements in Nonhomogeneous Atmospheres

For the specific scenario of modeling the WV absorption from a nadir viewing geometry, we subdivide the atmosphere into 18 levels ℓ, containing WV subcolumn densities N_ℓ. For real measurements, pressure and temperature profiles, as well as oxygen and nitrogen profiles for the calculation of Rayleigh scattering albedo, are taken from the Neutral Atmosphere Empirical Model MSISE90 [*Hedin et al.*, 1991] for a given date, time, and geolocation at fixed altitude levels. We use 18 atmospheric layers ℓ to cover altitudes from the ground up to 9 km and, therefore, more than 99% of the atmospheric water vapor. The WV density drops generally by more than 2 orders of magnitude over the first 10 km (see also *Lang et al.*, 2002). In general, the w width parameter or, respectively, the structure of the spectrum, changes with pressure and temperature over altitude due to the pressure and temperature dependent width of the lines. The same holds for the pixel-averaged line strength S. For the treatment of nonhomogeneous paths traversed by photons undergoing higher orders of scattering we now assume that the absorption over the different light paths throughout the atmosphere is dominated by the level with the maximum absorption, as is the shape of the measured absorption line. Consequently, the choice of a dominant absorbing layer is dependent on the shape of the profile of the absorber of interest. Note, that due to the strong exponential decrease of the WV profile

with respect to altitude, we may assume that the maximum impact on the absorption
over a specific light path will occur at the lowest point of the path. A solution of the
transport equation of scalar radiative transfer in its plane parallel approximation [*Lang
et al.*, 2002] reveals that the measured reflectivity R of a nadir viewing instrument may
be separated into three distinctive parts, viz.,

$$R_j = \Lambda \langle R_{surf} \rangle_j + \langle R_{ss} \rangle_j + \langle R_{ms} \rangle_j, \tag{5.5}$$

where j is a specific spectral interval with width $\Delta\lambda$, Λ is the surface-albedo of a
Lambertian surface, $R_{surf,j}$ is the reflectivity of the direct light path reflected at the earth
surface, $R_{ss,j}$ is the reflectivity of singly scattered and $R_{ms,j}$ of multiply scattered light.
Using the assumption above on the dominant w-parameter we define $w_{max} = w(N(\bar{\ell}))$,
where $N(\bar{\ell})$ is the maximum subcolumn density for a specific path at level $\bar{\ell}$. Now, we
may write the reflected light coming from the surface, utilizing equation (5.2), as

$$\langle R_{surf} \rangle_j = 1 + w(\bar{\ell}_{surf})_j \exp\left[-\sum_{\ell} \tilde{\mu} S(\ell)_j N(\ell) \right] - w(\bar{\ell}_{surf})_j, \tag{5.6}$$

where $\tilde{\mu}$ is the geometric path-length factor for a nadir viewing instrument, with $\tilde{\mu} \equiv
(\frac{1}{\mu_o} + 1)$, μ_o is the cosine of the solar zenith angle (SZA) and $w(\bar{\ell}_{surf})_j$ is the dominant
w-parameter w_{max} for the specific case of the direct, surface reflected path. Because, in
the case of WV absorption, we expect the maximum optical density at the surface layer
we may set $\bar{\ell}_{surf} = 1$. Using the same reasoning for the single-scattering contribution we
can then write, by again utilizing Eq. (5.2),

$$
\begin{aligned}
\langle R_{ss} \rangle_j \;=\;& \frac{p(\Theta)}{4\mu_0} \int_0^\infty \langle \beta(\ell(z))_{sca} \rangle_j \\
\times\;& \left\{ 1 + w(\bar{\ell}_{ss})_j \exp\left[-\sum_{\ell=\ell(z)}^{\ell_{top}} \tilde{\mu} S(\ell)_j N(\ell) \right] - w(\bar{\ell}_{ss})_j \right\} dz,
\end{aligned}
\tag{5.7}
$$

where $\bar{\ell}_{ss} = \ell(z)$, because $\ell(z)$ is the lowest altitude point for each single-scattering path
and, therefore, in the case of WV, the point with most impact on the absorption (for a
detailed discussion of the dominant layer assumption see appendix D). In addition, we
assume that Rayleigh scattering is the dominant form of single scattering and $\langle \beta(\ell(z))_{sca} \rangle_j$
is the mean Rayleigh scattering coefficient within $\Delta\lambda_j$ at altitude z, with a corresponding
phase function of $p(\Theta) = \frac{3}{4}(1 + cos^2(\Theta))$, where Θ denotes the SZA.

The multiple-scattering contribution $\langle R_{ms} \rangle_j$ to the reflected light is represented by a
first order polynomial with free parameters C and D, which accounts for the broad-band
effect of multiple scattering. In the previous study by *Lang et al.* 2002, it was shown that
the error on the retrieved WVC using this kind of treatment for the multiple-scattering
contribution is lower than 20% in cloud-free situations for a worst-case scenario of high
WVC of 1.4×10^{23} molec/cm^2, low surface albedo of 0.03 and 0.1 and high aerosol loading
for maritime and rural scenarios, respectively, utilizing the OACS retrieval technique (see
also section 5.7 for the impact of aerosol loading and multiple scattering on the SSP
retrieval). Similarly, the unknown surface albedo is represented by a first order polynomial

with free parameters A and B. The parameters A to D have to be adjusted to the real measurement when comparing SSP forward model results to the measurements, as well as during the retrieval and fitting of WVC values.

For details concerning the different contributions to the total reflectivity, as well as a detailed discussion about the impact of multiple scattering within this wavelength region, the reader is referred to the afore mentioned study by *Lang et al.*, 2002 and, for the specific case of SSP, to section 5.7 of this work.

5.4   Construction of Look-Up-Tables for w and S

In this study we utilize Equations (5.4) in order to construct a look-up-table for each of the parameters w and S. For a range of 22 temperatures T and 31 pressure values p, covering all p and T values thought relevant for our altitude region of interest for all possible geolocations, we then calculate realizations of the cross-section σ utilizing line-parameters from the HITRAN '96 database and Voigt absorption line shapes [*Armstrong*, 1967]. For those realizations we use 50000 numerical grid points over the whole spectral region between 585 and 600 nm in order to resolve the narrowest lines with at least 5 points. We use a sampling width $\Delta\lambda$, which is three times smaller than the sampling width of a GOME detector pixel and more than 4 times smaller than the full-width-half-maximum (FWHM) of the instrumental response function, which satisfies the Nyquist criterion (see also following section) and results in a total of 207 spectral bins. By doing so we create for each parameter w and S, a 22 by 31 by 207 look-up-table matrix which we can interpolate over p and T for a specific measurement scenario at each altitude level ℓ. Figure 5.2 shows w and S for one wavelength bin j in dependence of the p and T reference profiles. From this we see that w and S vary smoothly with respect to p and T, meaning that interpolation on intermediate p, T-tuples leads to reasonable results [*Maurellis et al.*, 2000b] (chapter 4). As the pressure decreases the w parameter also decreases (upper panel Figure 5.2), i.e. the spectrum becomes more structured due to the pressure-related narrowing of the lines. The line width is only weakly dependent on the temperature [*Rothman et al.*, 1998] which can also be seen from the w contour plot. The S parameter (lower panel Figure 5.2) changes significantly only for the lowest pressures. For low pressures, when the w parameter decreases, the S parameter increases, because the area of absorption or the averaged line intensity within a certain wavelength bin has to be conserved. Due to the temperature dependence of the line-intensity value of individual absorption lines [*Rothman et al.*, 1998], the variation in temperature for the S parameter is stronger than that for the w parameter.

In general, the w,S-tables are smaller than the usual tables used for the k-distribution method, and significantly smaller than the look-up-tables used for the OACS method, because the extra dimension for the summation over cross-section probability, or cross-section bin space, necessary in the latter two methods, is not required for SSP. Therefore, the interpolation on the look-up-tables can be performed very rapidly even for small $\Delta\lambda$, and thus, for high wavelength resolution.
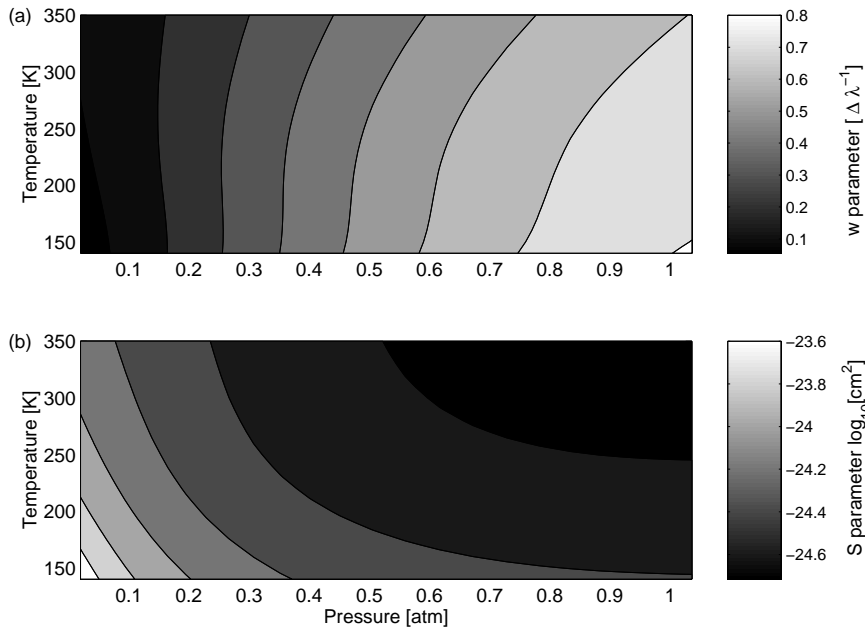
Figure 5.2: Contour plot of the w- (a) and the S-parameter (b) look-up-table
for one spectral sampling bin j in dependence of temperature and pressure.
A standard pressure and temperature grid is used for the construction of the
look up tables, covering all possible pressure and temperature ranges within
the altitude region of interest.

5.5 Forward Modeling and Retrieval

The spectral region between 585 and 600 nm is covered by 69 detector pixels of the
GOME instrument. Within this region absorptions of the additional absorbers $(O_2)_2$, O_3,
NO_2 and Sodium have to be taken into account, together with the loss of light scattered
out of the light path by means of Rayleigh scattering. Apart from Sodium and NO_2,
which contributes very little to the total absorption in this spectral region, all of these
remaining absorbers contribute to a smooth background absorption. The contribution of
the Fraunhofer line absorption to the so called I_0 effect and the contribution of the Ring
effect, from rotational Raman-scattering, to the total reflectivity is also assumed to be
rather small within this spectral region (for a detailed discussion the reader is referred to
Lang et al., 2002).

GOME measures the earth radiance I in nadir viewing geometry for a footprint of
40 by 320 km. The solar irradiance F_0 is measured once for every orbit (for a detailed
description of the instrument see *ESA*, 1995 or *Burrows*, 1999). The instrumental function
$\mathcal{H}(\lambda, \lambda'; \Sigma)$ of channel 3 is represented here by a Gaussian function with a FWHM Σ. The
reflectivity measured by the kth detector pixel is then defined as

$$R_k^{\mathrm{GOME}} = \int_{\Delta\lambda_k} \int_{-\infty}^{+\infty} \frac{\pi I(\lambda)}{\mu_o F_o} \mathcal{H}(\lambda, \lambda'; \Sigma) \mathrm{d}\lambda' \frac{\mathrm{d}\lambda}{\Delta\lambda_{\mathrm{k}}}, \tag{5.8}$$

where $\Delta\lambda_k$ is the sampling width of a GOME detector pixel of about 0.21 nm in the case of channel 3. The modeled reflectivity R_k is represented by

$$R_k = \int_{\Delta\lambda_k} \int_{-\infty}^{+\infty} R(\lambda_j) \mathcal{H}(\lambda_{\mathrm{j}}, \lambda'; \Sigma) \mathrm{d}\lambda' \frac{\mathrm{d}\lambda_{\mathrm{j}}}{\Delta\lambda_{\mathrm{k}}}, \tag{5.9}$$

where

$$R_j = (A\lambda_j + B)\langle R_{surf}\rangle_j + \langle R_{ss}\rangle_j + (C\lambda_j + D). \tag{5.10}$$

Here, it must be noted that Eq. 5.9 is only a good representation of Eq. 5.8 when $\Delta\lambda << \Sigma$, satisfying the Nyquist criterion. In our case $\Delta\lambda$ (around 0.07 nm) is a third of the spectral width covered by a single GOME detector pixel, whilst Σ is about 0.29 nm.

In Figure 5.3 we present a direct comparison between sample GOME measurements and forward calculations using Eq. (5.9) for two representative measurement geometries and geolocations with both high and low WVC. Realistic WV profiles used for the forward calculations are taken from the ECMWF database, with the resulting fit residuals being smaller than 1%, except for the region near the solar sodium Fraunhofer lines which is not explicitly modeled here.

For the SSP retrievals we fit Eq. 5.9 to GOME reflectivity spectra utilizing a robust, non-linear, large-scale trust-region method [*Byrd et al.*, 1988], which solves the optimization problem

$$\min_{N_\ell, (A...D)} \sum_k \left[R_k^{\mathrm{GOME}} - R_k\left(N_\ell, (A...D)\right) \right]^2. \tag{5.11}$$

Each SSP fit is initialized with a flat WV subcolumn profile $N_{\ell,0} = 10^{16}$, where the N_ℓ are given in units of subcolumn density. Each fit is constrained by an upper limit $N < N_{\ell,max}$ in the form of a step function. $N_{\ell,max}$ consists out of three steps over the total number of levels with high values over the first three kilometers, medium values between 3 and 5 km, and low values for the higher levels. The lower profile constraint is set to $N_{\ell,lower} = 0$. The constraints prevent the fit from giving too much weight to the higher altitude levels, which otherwise would increase the relative contribution of the singly scattered photons to unrealistic values by setting the surface albedo to zero and, in doing so, decrease the total mean free path length. We scale the upper profile constraint differently for geolocations between 30° and -30° latitude, between $\pm 30^o$ and $\pm 60^o$ latitude and latitudes above or below $\pm 60^o$.

5.6   Method Accuracy and Bias Adjustment

Two important assumptions were made in the derivation of Eq. 5.6 and 5.7: (i) the analytical derivation of the w and S parameter (Eq. 5.4) which is only accurate for optical densities lower than 0.1 (Figure 3 in chapter 4) and (ii) the assumption on the dominant spectral structure parameter w_{max} for individual light path of single-scattered
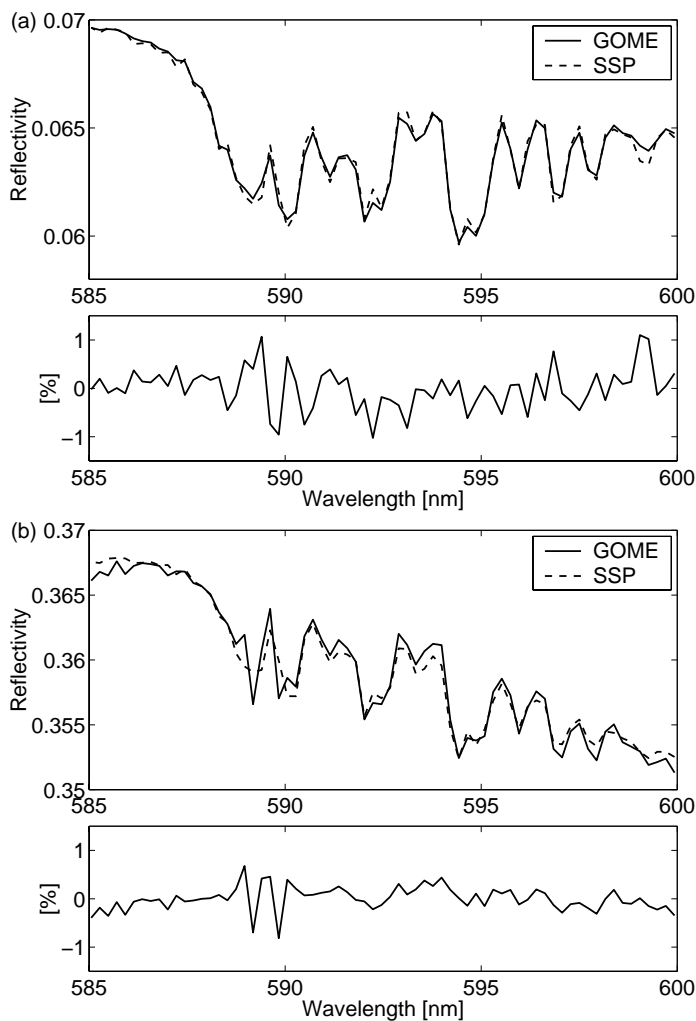
Figure 5.3: The upper panels (a) show a GOME measurement (solid line)
at 34° latitude and 110^oW longitude over the pacific with a SZA of 23°
together with the result of a SSP forward model (dashed line) and their
residual ((GOME-SSP)/GOME). The albedo was adjusted using a first order
polynomial, resulting in a value of 0.04 at 590 nm. The WV density profile
was taken from ECMWF with a high WVC of 1.34×10^{23} [molec/cm^2]. The
lower panels show the same but than for a rural GOME measurement at 62°
latitude and 100^oW longitude with a high SZA of 73° and a low WVC of
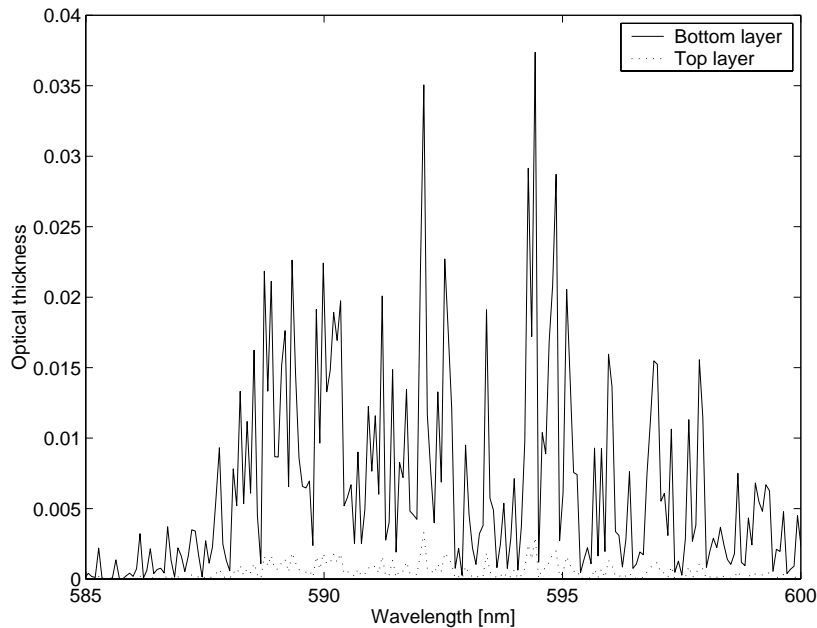8.9×10^{21}. For this pixel the albedo was adjusted resulting in a value of 0.32
at 590 nm.

Figure 5.4: Spectral averaged optical thickness for the bottom and top atmospheric layer used in the retrieval with subcolumn densities of 1.8×10^{22} and 1.3×10^{21} molec/cm^2, respectively. Here, we selected a high total WVC of 1.83×10^{23} molec/cm^2.

photons (section 5.3; cf. appendix D). The bias introduced due to these assumptions we call the method-related bias of SSP.

In principle, by reducing the thickness of the individual layers (i.e. utilizing more altitude layers) the optical thickness per layer may be always reduced below the 0.1 limit, where analytical derivation for w and S are a good approximation of the real value and the non-linear nature of the absorption of individual lines per layer becomes weakened. However, increasing the number of altitude layers increases the number of fit parameters and makes the optimization procedure computationally more expensive without gaining much additional information about the profile. Figure 5.4 shows that, by using 18 altitude layers, the spectrally averaged optical density per layer is significantly below the 0.1 using a high WVC of 1.84×10^{23} molec/cm^2. Therefore, in our case, the analytical derivation of w and S is a good assumption and does not contribute to the method-related bias. Consequently, our assumption of the dominant spectral structure parameter w_{max}, which is equal to the w value for the layer with the highest optical density in the path, creats a bias. The fixed w_{max} is usually higher with respect to what the real w parameter per layer would be. From Eq. 5.2, an underestimation follows for high WVC.

In order to quantify this bias and to correct for it, we perform SSP retrievals of 26 monochromatically forward-modeled reflectivity spectra on the basis of Eq. 5.10 from a range of WV profiles, with the total WVC ranging between 8×10^{21} and 1.8×10^{23}
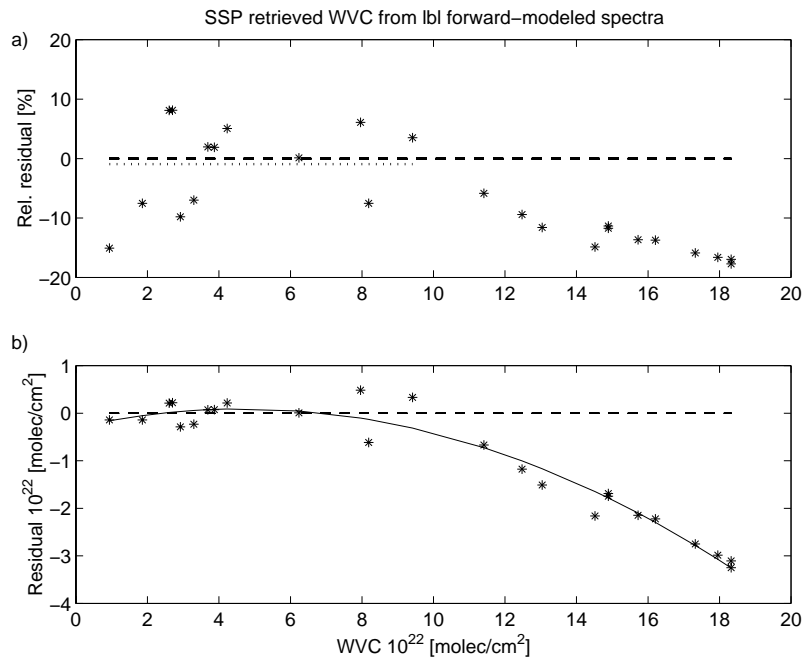
Figure 5.5: Relative (a) and absolute (b) differences between the retrieved
WVC by SSP and the WVC utilized in the monochromatically forward
model. The solid line in the lower panel (b) shows a third order polyno-
mial fit through the absolute difference values. The polynomial is used to
adjust for the systematic method related bias of the SSP retrieval. The up-
per panel (a) also shows the accuracy of the method (dotted line) for low
and mid-range WVC up to 1×10^{23} molec/cm^2.

molec/cm^2. These profiles were taken from the ECMWF database and chosen to be
representative of a wide range of significantly different geolocations. The contributions
by the additional background absorbers were also accounted for. In order to make a
direct comparison, realistic values for the variables A to D were obtained from the best
fit of the forward-lbl modeling results to GOME measurements taken at corresponding
geolocations.

The results are summarized in Figure 5.5, which shows the relative and absolute dif-
ferences between WVCs retrieved using SSP and that used for the forward-lbl modeling,
respectively. For low- and mid-range columns ($\leq 1 \times 10^{23}$ molec/cm^2) the maximal differ-
ences between the retrieved and the true values is about 10%. For instances of very low
WVC ($< 1 \times 10^{22}$ molec/cm^2) which occur predominantly at high latitudes, the differences
are larger due to the high SZA which are usually associated with such GOME measure-
ments. Note that together with the lowest WVC (i.e. 8×10^{21} molec/cm^2) utilized in the
forward-lbl calculations, a SZA of 61° was used, which corresponds roughly to latitudes
>70°. The accuracy (dotted line Figure 5.5a) for low and mid columns up to 1×10^{23}

molec/cm^2, calculated from the mean relative differences, is -1.1%.

For instances of high WVC ($>1\times 10^{23}$ molec/cm^2) the systematic retrieval bias increases up to a maximum of -20%, which is referred to the underestimation of the WVC by the dominant layer assumption. An empirical correction term was found by fitting a second-order polynomial (solid line in Figure 5.5b) to the absolute differences, which results in

$$WVC_{corr} = -0.018 * (WVC - 0.096)^2 + 0.164 * (WVC - 0.096) - 0.283, \qquad (5.12)$$

where the WVC is in units of 10^{22} molec/cm^2 (Figure 5.5).

5.7   Aerosol Loading and Multiple Scattering

Even in the absence of clouds, the background aerosol may cause a significant error in the retrieved WVC value. Aerosols may affect the net absorption, as well as the path length of the scattered light and, therefore, affect the assumptions made with respect to scattering and surface albedo.

The full effect of multiple scattering and aerosols on the retrieved WVC has been estimated by solving the full scalar radiative transfer equation, including the multiple scattering source term, by employing a doubling-adding model (DAM) [*de Haan et al.*, 1987], which has been reduced to the scalar representation of the radiation field. The reflectance $R(\lambda)$ is calculated in a line-by-line mode for a spectral resolution of 0.01 cm^{-1}.

We investigate four atmospheric scenarios: a maritime case and a rural boundary layer case both with and without aerosol loading (clear-sky scenario). The clear sky scenario solely quantifies the contribution of multiple Rayleigh scattering and its impact on the retrieved WVC. All scenarios include the effects of Rayleigh scattering, ozone absorption and Lambertian surface reflection. In the case of the maritime scene we use a surface albedo of 0.03, whereas for the rural scene a surface albedo of 0.1 is used. For maritime aerosol loading a constant particle density of 4 000 particles per cm^3 is assumed. For the middle and upper troposphere, we assume a tropospheric background aerosol, for which the particle density decreases with the third power in pressure with the optical properties of the aerosols being taken from *Shettle and Fenn* [1979]. In the rural case we have chosen a constant, but much higher, particle density of 15 000 particles per cm^3.

Table 5.1 lists the relative contribution of ground-reflected, single and multiple-scattered photons as a percentage of the total reflectivity using the DAM-model for the four different aerosol loading cases described above and with a medium WVC of 7.72×10^{22} molec/cm^2, for which the systematic method related bias may be neglected. Without aerosols, the maximum contribution of multiply-scattered photons is about 8% at 590 nm. Singlescattering is the dominant source of reflectivity for the maritime aerosol scenario (47%) because of low surface albedo, with the ground-reflected component being comparable or lower than the contribution due to multiple scattering. This may be contrasted with the rural aerosol scenario, in which multiple scattering is the dominant source of scattered light (51%) due to the high aerosol optical density. Aerosols reduce the ground-reflected component down to 13%.

Table 5.1: Relative contribution of ground-reflected, singly-scattered and multiply-scattered photons to the total reflectivity calculated by the DAM model assuming a SZA of 40° and a WVC of 7.72×10^{22} [molec/cm^2] for each case.

	Model Input		Model Output		
	AOD[a]	Λ	GR[b]	SS [c]	MS [d]
Maritime Clear Sky	0	0.03	42.2	49.6	8.2
Maritime Aerosol	0.30	0.03	17.9	46.9	35.2
Rural Clear Sky	0	0.10	67.8	23.9	8.3
Rural Aerosol	0.63	0.10	13.0	25.1	61.9

	SSP Retrieval Results			
	WVC[e]	Δ WVC [%]	Λ	$\Delta\Lambda$ [%]
Maritime Clear Sky	7.68	-0.33	0.036	+20.0
Maritime Aerosol	6.76	-12.3	0.052	+73.3
Rural Clear Sky	7.69	-0.26	0.110	+10.0
Rural Aerosol	9.14	+18.6	0.121	+21.0

[a]Aerosol Optical Depth
[b]Percentage of ground reflected light at 592 nm
[c]Percentage of single scattering at 592 nm
[d]Percentage of multiple scattering at 592 nm
[e]10^{22} molec/cm^2

The first-order polynomial utilized in this retrieval to implement multiple scattering (Eq. 5.5) does not account for a differential contribution reflecting the absorption by water vapor, but only for the broad-band effect. The retrieval of parameters C and D may, therefore, influence the retrieval of the surface albedo (parameters A and B) and the WVC.

Table 5.1 also includes the SSP retrieved WVC and surface albedo values from the DAM forward-modeled reflectivity spectra for the four scenarios. The results show that SSP retrieves accurate values for both of the clear sky situations. It underestimates the WVC by 12%, in the case of maritime aerosol loading, and overestimates it by 18% in the case of rural aerosol loading. The error in the retrieved albedo is generally of the order of 20%, except for the maritime case, where the aerosol layer above the surface alters the retrieved surface albedo value significantly resulting in a decrease in the retrieved WVC.

For high WVC, the retrieval using SSP is affected by the method-related bias (see previous section). After application of the empirical correction (Table 5.2), the error due to multiple scattering for the maritime and rural case is less than 6 and 2%, respectively (clear sky cases). The impact due to maritime and rural aerosol loading on the retrieved column is less than 9 and 14%, respectively, after correction for the method-related bias.

Table 5.2: Same as Table 5.1 but for a high WVC of 1.43×10^{23} molec/cm^2. The relative difference Δ WVC is calculated between the model value and the corrected retrieved WVC

	Model Input		Model Output		
	AOD[a]	Λ	GR[b]	SS[c]	MS [d]
Maritime Clear Sky	0	0.03	43.8	48.2	8.0
Maritime Aerosol	0.21	0.03	20.0	53.2	26.8
Rural Clear Sky	0	0.10	69.1	22.8	8.1
Rural Aerosol	0.51	0.10	17.9	30.9	51.2

	SSP Retrieval Results				
	WVC[e]	corr. WVC	Δ WVC [%]	Λ	$\Delta\Lambda$ [%]
Maritime Clear Sky	12.5	13.5	-5.2	0.039	+30.0
Maritime Aerosol	14.0	15.5	+8.5	0.038	+26.6
Rural Clear Sky	13.3	14.5	+1.6	0.102	+2.0
Rural Aerosol	14.6	16.3	+14.1	0.112	+12.0

[a]Aerosol Optical Depth
[b]Percentage of ground reflected light at 592 nm
[c]Percentage of single scattering at 592 nm
[d]Percentage of multiple scattering at 592 nm
[e]10^{22} molec/cm^2

5.8 Results for Single GOME Pass

Figure 5.6a shows uncorrected WVC results (stars) using SSP for the GOME pass on October 23, 1998, between $-80°$ and $80°$ in latitude and longitudes between 90^oW and 150^oW, which contains a total of 476 ground-pixel nadir measurements. For comparison, we show values from the OACS method utilizing the same GOME measurements (solid line) and exploiting the same spectral region, together with co-located values from ECMWF (solid line with dots).

In general, the SSP values compare well with the ECMWF values, except in situations where the percentage cloud cover significantly exceeds 10%. This may be explained by an enhanced photon path length as is modeled by SSP due to an enhanced contribution of multiple-scattered photons in the case of the presence of thick clouds. Moreover, the presence of a significant cloud cover will reduce the transmission of light to the lower layers of the atmosphere where most of the water vapor is located. These two effects occasionally tend to cancel each other, as for the first the SSP model underestimates the absorption resulting in an overestimation of the WVC by the fitting procedure, whilst for the second SSP overestimates the absorption resulting in an underestimation of the WVC.

In comparison to the similarly implemented but more accurate OACS sampling method, the uncorrected SSP results systematically underestimate the higher columns, as could be
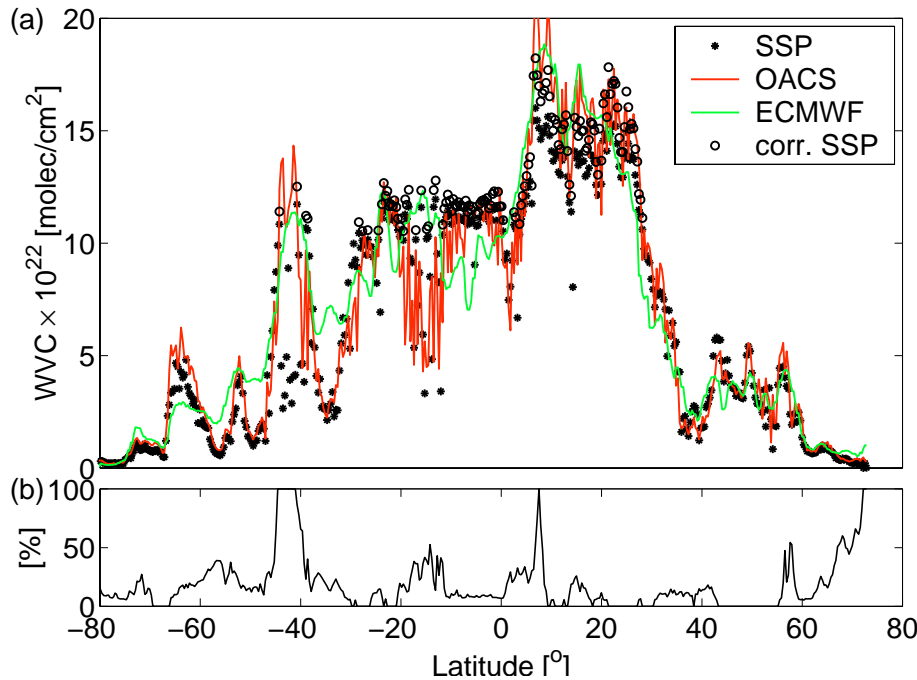
Figure 5.6: SSP uncorrected WVC fit results over latitude ((a), filled cir-
cles) for a GOME pass on October 23, 1998, covering longitudes from 90°W
at 73° latitude to 150°W at -80° latitude. For validation, the WVC val-
ues from OACS using GOME measurements (red curve) and from ECMWF
given at 18:00 UTC are shown (green curve). The open circels denote SSP
corrected values for WVC higher than 1×10^{23} molec/cm^2. The cloud cover-
age in percentage per GOME observation is taken from GOME GDP level-2
data and is indicated by the solid curve in the lower panel.

expected considering the method related bias of SSP (see Section 5.6). The highest WVC
in the tropics are systematically about 15 to 20% lower than those of the other datasets.
The circles in Figure 5.6 show SSP retrieved WVC after the bias-correction (Eq. 5.12) for
values $>1 \times 10^{23}$ molec/cm^2 were applied.

A critical parameter which governs the accurate retrieval of WVC is the shape of the
resulting subcolumn profile retrieved by SSP. Due to the effect of the altitude dependence
of both p and T on the spectral structure of WV, the effective absorption is governed
by the specific atmospheric paths through which the photons travel. The retrieval of
an unrealistic shape of the retrieved subcolumn profile may, therefore, unrealistically
alter the weights of various atmospheric paths, i.e. the relative contribution between
ground-reflected, singly and multiply scattered light. This yields an error in the retrieved
surface albedo, which weights the direct, ground-reflected, light path contribution (Eq.
5.5) or an error in the retrieved broad-band multiplescattering contribution. This error
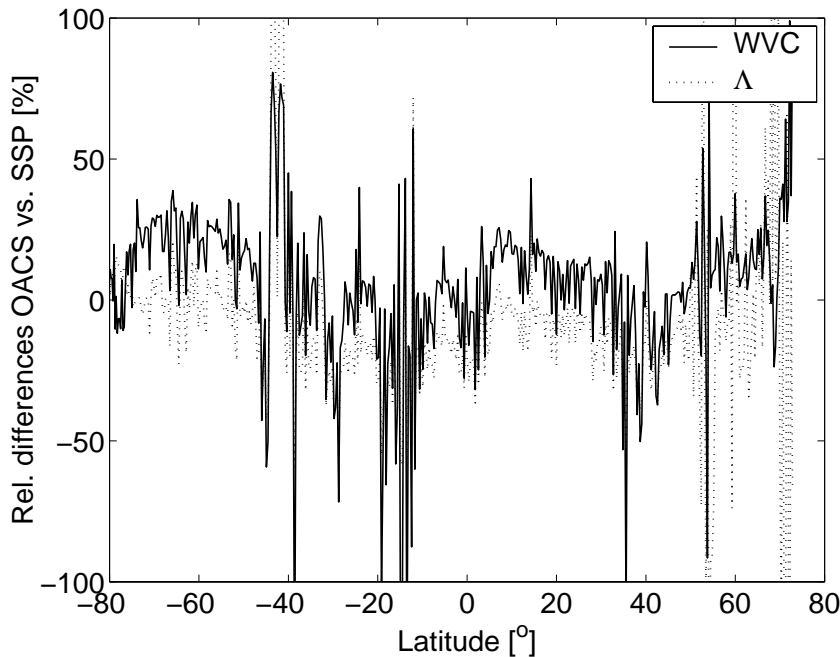propagates into the final retrieved column. From Figure 5.7 we can see that the differences

Figure 5.7: Relative differences between SSP and OACS for retrieved values of WVC ([OACS-SSP]/OACS; solid line) and surface albedo Λ ([SSP-OACS]/OACS; dotted line). An underestimation of the surface albedo leads to an overestimation in the retrieved WVC. The relative differences result form the same GOME track as shown in Figure 5.6 including all ground pixel.

between the WVC values retrieved by OACS and SSP and the differences between the surface albedo values retrieved by both methods are very well correlated. Introducing upper fit constraints assists both methods in finding the accurate profile shapes but the OACS method is, due to its more accurate treatment of the representation of the spectral structure at each altitude level, superior to the SSP method, resulting in higher sensitivity and better agreement with the independent data-set from ECMWF, especially for high WVC. However, a big benefit of SSP is that it is about 4 to 5 times faster than the OACS method even though it uses a higher sampling resolution then the one used for OACS in *Lang et al.*, [2002].

5.9   Global Retrieval Results

Finally we present the results of a global WVC retrieval of 47000 ground pixel from GOME measurements between -70° and 70° latitude on the 22nd to the 24th of October, 1998 using the SSP method. The globally corrected results (Eq. 5.12) are shown in the global plot in Figure 5.8a. For comparison we show the global WVC, as given by ECMWF, on

the 23rd of October, 1998, 18:00 UTC (Figure 5.8b). Figure 5.8c shows the global WVC as
retrieved by SSP for cloud-free pixels, i.e. where the cloud-fraction is reported to be lower
than 10%. The cloud cover fraction was taken as reported by the GOME Data Processor
(GDP) level 2 data [*Balzer & Loyola*, 1996; *DLR*, 1999]. This fraction is derived by the
initial cloud fitting algorithm (ICFA) with the cloud top pressure being taken from the
International Satellite Cloud Climatology project (ISCCP) [*Koelemeijer et al.*, 1999].

The general latitudinal dependence of WV concentration, with high WVC in the
equatorial regions and low WVC towards the poles is well represented by the SSP retrieval
results. Individual features common to both the ECMWF model results and the SSP
results may also be identified as, for example, the low WVC above north-west China and
the Gobi desert as well as in the United States at this time above North-west Carolina. A
similar transition from low to high WVC can be observed from the southern part of the
United States to Mexico and the Caribbean Sea. However, GOME-SSP WVC results show
significantly lower values compared to ECMWF above the Sahara, Saudi Arabia and the
Andes around -40° latitude. SSP retrieves high WVC above the Philippine Sea north of
New Guinea where the ECMWF model reports only medium water vapor concentrations.

Figure 5.9 shows a scatter plot between SSP retrieved WVC from GOME and collo-
cated WVC data reported by ECMWF, where the GOME measurements coincide with
ECMWF data within a 1 hour time window at the 23rd of October, 1998. We compare
420 GOME measurements with a GDP level 2 data reported cloud fraction of less than
10%. The gradient of the scatter data is 0.98 with a maximum scatter of 50%.

5.10   Discussion

Differences in the surface albedo retrieved by the OACS sampling technique and SSP, both
exploiting the same WV absorption band, lead to overall differences between the retrieved
WVC. The difficulties in the retrieval of the correct surface albedo is a general problem for
nadir remote-sensing techniques, especially during instances of high aerosol optical depth.
This is due to the uncertain contribution to the backscattered light introduced by aerosol
layers, with the aerosol profile being a critical parameter. Moreover, surface albedo is also
dependent on wavelength, geolocations and season. In our wavelength region of interest,
the utilized first-order polynomial is a good approach for the wavelength dependence of the
albedo for most cases [*Koelemeijer et al.*, 1997]. We find, that the accuracy of the retrieved
values and the gradients of the surface albedo are correlated with the shape of the retrieved
WVC profile and the retrieved contribution of multiply scattered photons, which is also
accounted for by a first order polynomial. For this reason, we introduced three different
step functions, depending on geolocation, as upper constraints for the retrieved profile, in
order to prevent the optimization method occasionally finding a local fit minima by setting
the ground albedo to zero and unrealistically increasing the scattering components.

An additional concern for any WV retrieval approach is the accuracy and completeness
of the cross-section database used for the construction of the w-S look-up table. From
recent measurement studies of water vapor absorption bands other than the one used
in this study, *Learner et al.*, [2000], recently showed discrepancies ranging from about
100% for small lines to about 20% for strong lines for the main water vapor absorption
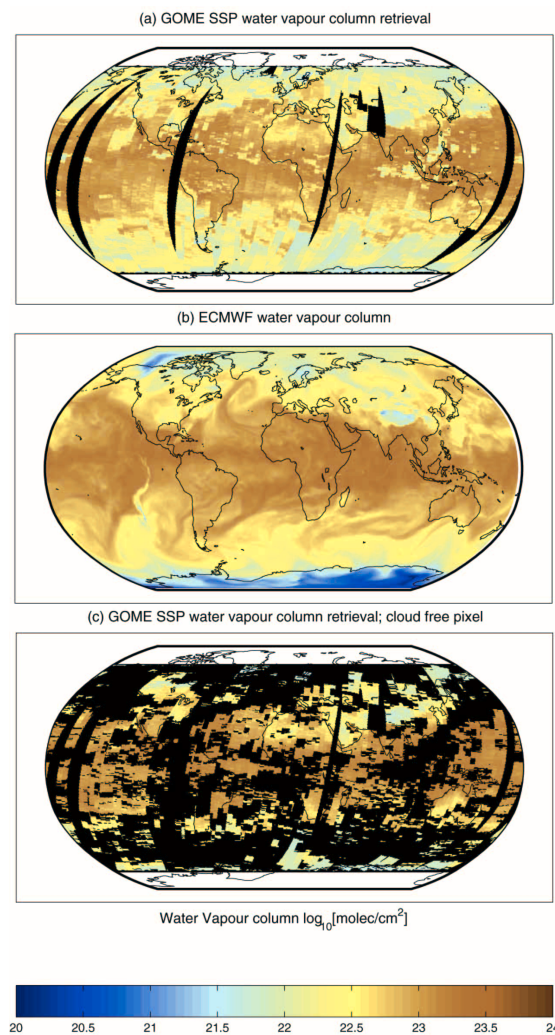bands in the region between 1110 and 685 nm. They also found systematic differences in

Figure 5.8: Global total water vapor column plots for all retrieved GOME ground pixel using SSP (a). The measurements were performed from the 22nd to the 24th of October, 1998. The middle panel (b) shows global WVC as given by ECMWF at the 23rd of October, 1998, 18:00 UTC. The lower panel (c) shows SSP columns for GOME observations where the cloud fraction reported by GOME level-2 data is lower than 10%. Data gaps for GOME retrievals are due to calibration periods or data processing failures. At 24th of October from 14:00 UTC GOME was in Narrow Swath Mode until 11:00 UTC the next day. For these tracks the data was interpolated to the standard swath width.
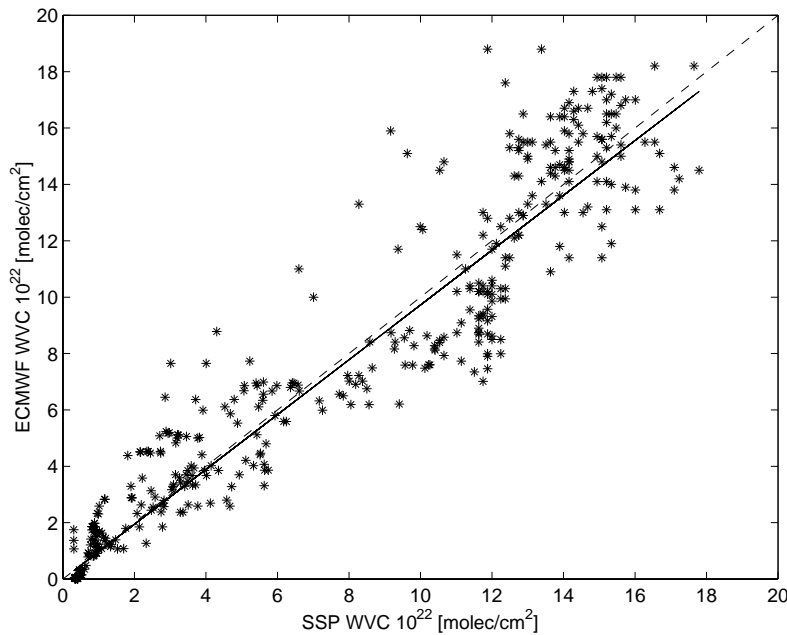
Figure 5.9: Scatter plot between ECMWF total WVC and SSP retrievals
for GOME measurements with a GDP level-2 data reported cloud fraction
lower than 10%. The GOME measurements are performed between $-70°$
and $+70°$ in latitude: on September 30, 1999 from 0:09 to 1:05 UTC between
120E and 180E longitude and on october 23, 1998 from 17:52 to 18:32 UTC
between $90°$W and $150°$W longitude. Co-located ECMWF data is given for
00:00 UTC and 18:00 UTC respectively. The solid line denotes the best fit
of a linear polynomial to the retrieved columns.

various bands ranging from 6% to 33%. Even though measurements by *Learner et al.*, in
the wavelength range between 585 and 600 nm have not been studied, large differences
in some of the water absorption bands between 1110 and 685 nm suggest the presence of
potentially large uncertainties in the reference cross-sections of the HITRAN'96 database
used in this study. In addition, the presence of many weak absorption lines, not accounted
for in the HITRAN'96 database, may contribute to an additional background absorption,
which may affect the retrieval of both surface albedo and broad-band multiple-scattering
contribution and, therefore, also the retrieval of WVC.

The contribution of aerosols and clouds to the error in the retrieved column, as given
in section 5.7, can only be estimated. In the case of aerosols, this is due to their high
variability in optical depth, concentration profile and scattering probabilities, all of which
depend on geolocation and season. In the case of clouds, the uncertainties arise from the
high variability with respect to cloud-top heights, form and density of clouds. Furthermore,
the scatter between SSP-retrieved WVC values and those given by ECMWF may also be
affected by systematic errors for cases, where the cloud-fraction is reported to be less

than 10%. Differences in the reported cloud-fraction by GDP level 2 data with respect to the co-located Along Track Scanning Radiometer-2 (ATSR-2) can be as much as 18% [*Koelemeijer et al.*, 1999].

5.11   Conclusion

In this study the spectral structure parameterization technique has been implemented and tested for retrieval of total WVC from GOME measurements utilizing a radiative transfer scheme, which includes molecular clear-sky direct-path absorption as well as molecular clear-sky single scattering, together with a broadband approximation of higher orders of scattering. The radiative transfer scheme was previously used for retrieval of total WVC using the Optical Absorption Coefficient Spectroscopy. SSP is less accurate and less sensitive than the OACS retrieval method but significantly faster and easier to implement. Retrieval of WVC using SSP for one ground pixel takes less than 30 seconds on a Pentium III, 800 MHz, using an uncompiled MATLAB retrieval code, and requires less than 128 MB internal memory.

Whereas OACS utilizes a spectral sampling technique based on cross-section probability density distribution functions, SSP utilizes average line parameters within the sampling region, and is, therefore, conceptually closer to band models. From retrieval studies of synthetic spectra we conclude that the sensitivity of SSP is better than 10% and the accuracy is about 1% for WVC lower than 1×10^{23} molec/cm^2. For WVC above this limit, a systematic offset of up to 20% is introduced by using an analytical second-order approach for the determination of the average line parameters w and S (Eq. 5.4). Moreover, the assumption of a dominant absorbing layer applied to the modeling of nonhomogeneous paths (Section 5.3 and Eq. 5.7) also introduces a bias. This bias has been corrected for in the current study by applying an empirical second-order polynomial (section 5.6).

We studied the impact of aerosols and the differential contribution of multiple scattering for four different scenarios utilizing synthetic spectra from a doubling adding radiative transfer method. For medium WVC for which no correction is needed the multiple-scattering impact on the SSP retrieved WVC is below 1%. Neglecting maritime aerosols and rural aerosols results in a retrieval error of less than 13 and 19% respectively. For corrected high WVC (Table 5.2) the error due to multiple scattering for maritime and rural scenario is less than 6 and 2%, respectively (clear sky cases). Here, the impact due to maritime and rural aerosols on the retrieved column is less than -9 and +14%, respectively, after correction for the method-related bias.

A global comparison between SSP retrieved WVC and data from ECMWF shows good general agreement in the latitudinal dependence of the water vapor concentration. However, significant regional differences, for example, over the Sahara and the Philippine Sea are found. The higher spatial resolution of the GOME measurements over sea and land with respect to ECMWF, where the density of ground measurements is low, is clearly an advantage of this kind of SSP retrievals from GOME. However, ECMWF data is provided for a specific time and day, whereas global GOME retrieval results, as shown in Figure 5.8, are collected over three days. Wide parts of the differences in the global data set may, therefore, also be related to changes in the global water vapor distribution over the three

days. The scatter plot comparison between SSP and ECMWF (Figure 5.9), as well as
the single GOME path comparison (Figure 5.6), are correlated in time and geolocation.
The scatter plot shows good correlation between the two data-sets of correlated cloud-free
ocean pixel with a gradient of 0.98. However, in some cases, the scatter can be as high as
50%, which points to local differences between the two data products.

5.12   Outlook

In general, SSP is well suited for fast clear-sky retrieval of narrowband absorbers from
nadir satellite instruments like GOME. The accuracy in the retrieval of the surface
albedo and the impact of aerosols and multiple scattering limits the accuracy of the
retrieved WVC. The latter may be improved by introducing surface albedo from global
databases once available and tested. The current implementation of SSP in a direct path
and single-scattering radiative transfer scheme provides the possibility for implementa-
tion of specific aerosol optical properties. The treatment of clouds for such nadir-viewing
measurements in the visible is a yet unsolved problem. SSP provides WVC (and po-
tentially profile) retrieval form instruments like GOME and SCIAMACHY, which are
not originally intended for WV retrieval. SSP of WV may be used to refine other re-
trievals from those satellite data because WV "contaminates" the entire spectrum. In
addition, SSP is, in principle, also suitable for the retrieval of spectrally overlapping
narrowband absorptions from different species. This situation occurs in the IR regions
around 2 μm covered by the SCIAMACHY instrument. Multi-species retrieval may be
performed by introducing an additional averaged line parameter, which accounts for the
degree of overlap between the different absorbers within a specific spectral sampling width.

Bibliography

Armstrong, B. H., Spectrum Line Profiles: The Voigt Function, *J. Quant. Spect. & Rad.
    Transfer, 7,* 61-88, 1967.

Balzer, W. and D. Loyola, Product Specification Document of the GOME Data Processor,
    Technical Document ER-PS-DLR-60-0016, Deutsche Forschungsanstalt für Luft- und
    Raumfahrt, 21 pp., 1996.

Burrows, J. P., M. Weber, M. Buchwitz, V. Rozanov, A. Ladstätter-Weißenmayer, A.
    Richter, R. deBeek, R. Hoogen, K. Bramstedt, K.-U. Eichmann, and M. Eisinger, The

Global Ozone Monitoring Experiment (GOME): Mission Concept and First Scientific Results, *J. Atmos. Sci., 56,* 151-175, 1999.

Buchwitz, M., V. V. Rozanov, and J. P. Burrows, A near-infrared optimized DOAS method for the fast global retrieval of atmospheric CH_4, CO, CO_2, H_2O, and N_2O total column amounts from SCIAMACHY Envisat-1 nadir radiances, *J. Geophys. Res., 105,* 15,231-15,245, 2000.

Byrd, R. H., R. B. Schnabel and G. A. Shultz, Approximate Solution of the Trust Region Problem by Minimization over Two-Dimensional Subspaces, *Mathematical Programming, 40,* 247-263, 1988.

Casadio S., C. Zehner, G. Piscane, and E. Putz, Empirical Retrieval of Atmospheric Air Mass Factor (ERA) for the Measurement of Water Vapor Vertical Content using GOME Data, *Geophys. Res. Lett., 27,* 1483-1486, 2000.

DLR, GOME data Processor Extraction Software User's Manual, *Doc.No.: ER-SUM-DLR-GO-0045, DLR/DFD, Oberpfaffenhofen, Germany,* 1999.

The Global Ozone Monitoring Experiment Users Manual, *Ed. F. Bednarz,* ESA Publication SP-1182, ESA Publication Division, ESTEC, Noordwijk, The Netherlands, 1995.

de Haan, J., P. Bosma, and J. Hovenier, The adding method for multiple scattering calculations of polarized light, *Astron. Astrophys., 181,* 371-391, 1987.

Hedin, A. E., Extension of the MSIS Thermosphere Model into the Middle and Lower Atmosphere, *J. Geophys. Res., 96,* 1159-1172, 1991.

Koelemeijer, R. B. A., P. Stammes, and D. Stam, Spectral Surface Albedo Derived From GOME Data, *Proc. 3rd ERS Symp. on* Space at the service of our Enviroment, *Florence, Italy, 17-21 March 1997,* ESA SP-414, 3 Vols, 1997.

Koelemeijer, R. B. A., and P. Stammes, Validation of GOME cloud cover fraction relevant for accurate ozone column retrieval, *J. Geophys. Res., 104,* 18,801-18,814, 1999.

Kato, S., T. P. Ackerman, J. H. Mather, and E. E. Clothiaux, The k-distribution method and correlated-k approximation for shortwave radiative transfer model, *J. Quant. Spect. & Rad. Transfer, 62,* 109-121, 1999.

Lacis, A. A., and V. Oinas, A description of the correlated k distribution method for modeling nongray gaseous absorption, thermal emission, and mutlitple scattering in vertically inhomogeneous atmospheres, *J. Geophys. Res., 96,* D5, 9027-9063, 1991.

Lang, R., A. N. Maurellis, W. J. van der Zande, I. Aben, J. Landgraf, and W. Ubachs, Forward Modeling and Retrieval of Water Vapor from GOME: Treatment of Narrow Band Absorption Spectra, *J. Geophys. Res.,* in press, 2002.

Learner, R., R. Schermaul, J. Tennyson, N. Zobov, J. Ballard, D. Newnham, and M. Wickett, Measurement of H_2O Absorption Cross-Sections for the Exploitation of GOME data, *ESTEC Contract No 13312/9/NL/SF,* Final Presentation, 2000.

Maurellis, A. N., R. Lang, W. J. v. d. Zande, U. Ubachs, and I. Aben, Precipitable Water Column Retrieval from GOME Data, *Geophys. Res. Lett., 27,* 903-906, 2000a.

Maurellis, A. N., R. Lang, W. J. van der Zande, A New DOAS Parameterization for Retrievalof Trace Gases with Highly-Structure Absorption Spectra, *Geophys. Res. Lett., 27,* 4069-4072, 2000b.

Noël, S., M. Buchwitz, H. Bovensmann, R. Hoogen, and J. P. Burrows, Atmospheric Water Vapor Amounts Retrieved from GOME Satellite Data, *Geophys. Res. Lett., 26,* 1841-1844, 1999.

Rothman, L. S., C. P. Rinsland, A. Goldman, S. T. Massie, D. P. Edwards, J.-M. Flaud,

A. Perrin, C. Camy-Peyret, V. Dana, J.-Y. Mandin, J. Schroeder, A. McCann, R. R. Gamache, R. B. Wattson, K. Yoshino, K. V. Chance, K. W. Jucks, L. R. Brown, V. Nemtchino, and P. Varanasi, The HITRAN Molecular Spectroscopic Database and HAWKS (HITRAN Atmospheric Workstation): 1996 Edition, *J. Quant. Spect. & Rad. Transfer, 60,* 665-710, 1998.

Shettle, E. P., and R. W. Fenn, 1979: Models for aerosols of the lower atmosphere and the effects of the humidity variations on their optical properties, Air Force Geophys. Lab. (OP), Envir. Res. Pap. 676, AFGL-TR-79-0214, Hanscom, Massachusetts (technical report).

Chapter 6

Toward Profile Retrieval of Narrow-Band Absorbers like Water Vapor from Nadir Satellite Measurements

The well known correlated k-distribution (ck) method and the Opacity Coefficient Method (OCM) described in this thesis, are well-suited to efficiently model mean transmittances and reflectivities for narrow-band absorption spectra such as those measured by satellite spectrometers. Profile retrieval of trace gases requires a combination of the maximum amount of spectroscopic information (related to pressure and temperature change and scattering height) with retrieval efficiency. Profile retrieval therefore serves as an excellent test of the OCM method. Profile retrieval is tested on artificial spectra simulating water vapor absorptions measured by the Global Ozone Monitoring Experiment (GOME). Here, two important questions concerning such retrievals are addressed. Firstly, how much profile information is contained within the absorption bands of interest in dependence of the number of utilized instrument detector pixels and what is the impact of the usage of different line-parameter databases on the retrieval. Secondly, how well can this profile information be retrieved using both the OCM method and, for comparison, the ck-distribution. Preliminary studies on profile retrieval from real GOME measurements have been performed using simultaneously the 590 nm and the 640 nm absorption bands of water vapor and comparing the results to a co-located radiosonde profile measurement.

6.1   Introduction

The problem of determining trace gas columns in Earth's atmosphere from nadir measurements of reflected sunlight is of particular interest to those working on the generation of high-level climatological data products from satellite measurements. In particular, the knowledge of concentration distribution over altitude is an important input for climate modeling and for chemical transport models. For example, in terms of climate modeling, the knowledge of the water vapor (WV) profile might be used for weather predictions as well as modeling the planetary energy balance, i.e. changes in local temperature (*climate forcing*), which may give rise to changes in the global mean temperature (*climate change*). In terms of chemical transport modeling, the knowledge of vertical WV distribution is of crucial importance for modeling the production of atmospheric OH, which is considered to be the most important free-radical oxidant in the troposphere. The OH radical is produced via the photolysis of ozone (for which also a good knowledge of its profile is required) and the successive reaction of singlet oxygen with water vapor, viz,

$$
\begin{aligned}
O_3 + h\nu &\rightarrow O_2 + O(^1D) \\
H_2O + O(^1D) &\rightarrow OH + OH.
\end{aligned}
$$
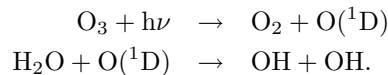
Moreover, water vapor profiles may also be used to refine retrievals of other trace gases from spectral remote-sensing measurements, because WV absorptions "contaminate" the entire spectrum from the visible to the far infrared and microwave region.

Profile retrieval of trace gases requires optimal use of spectral information content and the retrievals have to be conducted with computationally efficient radiative-transfer forward models. This chapter will show how the OCM method, introduced in this thesis (chapter 2 and 3) may be used to retrieve water vapor profile information from nadir satellite measurements like the ones from GOME and SCIAMACHY. In contrast to a number of retrieval methods already applied to those measurements retrieving total WVC and using *one-parameter* retrievals [*Noël et al.*, 1999; *Buchwitz et al.*, 2000; *Casadio et al.*, 2000], both OCM as well as the SSP method (chapter 4 and 5) retrieve subcolumn profiles (*multi-parameter* retrieval) from which a total WVC is calculated. Both methods establish a direct link between an average cross-section per layer and its subcolumn density. Part of the profile information is carried by the shape of the absorption profiles of the individual lines per atmospheric layer and, consequently, the average cross-section quantity $\alpha(z)$ (OCM) and w (SSP), which, for both methods, carry the information about the altitude-dependent spectral structure within a specific sampling region. Note, that other profile retrieval methods from nadir measurements, like, for example, ozone profile retrieval from GOME [*Hasekamp & Landgraf*, 2001], rely on profile information contained in differences in scattering height for different wavelengths. Those differences are significant especially in the UV, because of the relatively high single-scattering albedo in comparison to, for example, the near and far infrared. In the visible, both effects, altitude-dependent cross-sections as well as scattering heights, may contribute to the profile information content and their relative contribution is dependent on the inhomogeneity of the path and depend on the spectral width of the explored absorption band, respectively.

The following section will give a general introduction on how a singular value decomposition of weighting functions (or the Jacobian of the optimization problem) can be used

to evaluate the number of independent pieces of profile information contained within a
retrieved profile. It is possible to evaluate this number of independent pieces during the
optimization procedure by filtering out the effective null-space of the problem, which are
the contributions to the retrieved profile by the noise of the measurement or the bias of
the retrieval method. The role of the null-space in profile retrieval is also discussed in this
section.

As an example for profile retrievals where the null-space is not effectively filtered
out, section 6.2.1 will show subcolumns retrieved for some of the total WVC retrievals
discussed in previous chapters of this thesis, utilizing both spectral sampling methods,
OCM (chapter 3) and SSP (chapter 5). The retrieved profiles are compared to profiles
given by ECMWF corresponding in time and place. These retrievals use a constraint
non-linear, large-scale trust-region method [*Byrd et al.*, 1988] which already filters out
part of the error and noise contributions by the constraints applied. However, from the
comparisons with ECMWF profiles, remaining significant contributions of the null-space
to the retrieved profiles are still evident. From these retrievals the question arises how
much profile information is contained within such nadir measurements of water vapor
absorption considering the noise and systematic errors of the measurement, the bias of
the retrieval method and the spectroscopic information, providing an effective filtering of
the null-space of the problem is applied during the optimization process. Such an effective
filtering is made possible by using the so-called Phillips-Tikhonov regularization [*Phillips*,
1962] introduced in section 6.3.

In order to quantify the water vapor profile-information content solely in relation
to the retrieval method-related error, the explored WV absorption bands accessible by
GOME and the line-parameter databases, section 6.4 focuses on a synthetic retrieval of
the WV profile by OCM using a typical WV profile measured during a radiosonde takeoff.
For the synthetic retrieval only direct light paths are considered and the impact off differ-
ences in scattering heights on the retrieved profile information has not been considered.
OCM is compared to retrieval results using the correlated k-distribution (ck-distribution)
method as introduced in chapter 2, because both of these methods potentially offer a good
compromise between efficiency and accuracy. For the synthetic retrievals, three water va-
por absorption bands accessible to the Global Ozone Monitoring Experiment (GOME)
instrument are considered. The bands are located at wavelengths of approximately 590,
640 and 720 nm (Figure 6.2, upper panel). The three bands are covered by a total of
404 GOME detector pixels (sampling widths). For each of the used retrieval methods
the maximum amount of profile information contained within the three GOME-accessible
water vapor bands is determined as a function of the number of utilized detector pixels.
(Alternately this may be viewed as determining the minimum number of spectroscopic
information required to perform the best possible retrieval). In this way the performance
of the methods in the context of profile retrieval is illustrated along with the problem of
the optimal use of the spectroscopic information. The impact of using different absorption
line parameters from different databases on the profile information content is studied in
section 6.5.

In a final outlook section first studies on water vapor profile retrieval from real GOME
measurements are shown and discussed. These retrievals consequently also include the
impact of measurement noise and errors, as well as the impact of the instrumental slit
function and difference in scattering heights on the profile retrieval, which have not been

considered for the synthetic retrieval study.

6.2 The Linearized Forward Model

In this section the basic formalism of the inversion problem and some key retrieval diagnostics is set up. A singular value decomposition (SVD) of the Jacobian is used to access different contributions to the solution and the measurement (or model) space of the retrieval problem. Parts of this contributions may be identified as contributions from the model bias or the measurement noise (the null-space) and their relative weights (or significance) can be determined from the singular values obtained from the SVD. Starting with a SVD of the Jacobian a formalism can be developed, which filters the components of the null-space during the optimization process (see section 6.3) and is called the regularization of the inversion problem.

The inversion by regularization requires the Jacobian of the forward model which governs both the atmospheric radiative transfer as well as the effects of the instrument measuring the radiation, also known as the kernel K, given by

$$\mathbf{K} = \frac{\mathbf{d\bar{T}}}{\mathbf{dN}} \ , \tag{6.1}$$

which is a measure of the response of the method to changes in the subcolumn density for any given model $\mathbf{\bar{T}} = \mathbf{T}^{k-dist}$ or $\mathbf{\bar{T}} = \mathbf{T}^{OCM}$.

The models used in the retrieval are non linear and of the form

$$\mathbf{T}^{lbl,GOME} = \mathbf{\bar{T}}(\mathbf{N_i}) + \epsilon_\mathbf{T}. \tag{6.2}$$

Here, $\mathbf{N}$ is a vector of density profile values with dimension L and $\epsilon_\mathbf{T}$ is the measurement noise and model bias having the same dimension M as the measured transmittance vector $\mathbf{T}^{lbl,GOME}$ (in this chapter M corresponds to the number of used detector pixel). In the remainder of the paper we will either use measured GOME transmittance spectra $\mathbf{T}^{GOME}$ (following section and section 6.6) or synthetic lbl realizations for $\mathbf{T}^{lbl}$ (section 6.4) from which the density profile values $\mathbf{N}$ are retrieved using either OCM or the ck-distribution method. Normally such problems are solved iteratively using a Taylor expansion. After some iterations i the linear model equation can be written as

$$\mathbf{y} = \mathbf{KN_{i+1}} + \epsilon_\mathbf{T}, \tag{6.3}$$

where the measurement $\mathbf{y}$ is defined by

$$\mathbf{y} = \mathbf{T}^{lbl,GOME} - \mathbf{\bar{T}}(\mathbf{N_i}) + \mathbf{KN_i}. \tag{6.4}$$

Then, a least squares optimization can be used to find $\mathbf{N}$ (in the remainder of the chapter the iteration index i is omitted) directly via

$$\mathbf{N} = \min_\mathbf{N} ||(\mathbf{KN} - \mathbf{y})||^\mathbf{2}. \tag{6.5}$$

Rather than solving the least squares directly, it is also possible to use the singular value decomposition of $\mathbf{K}$, given by

$$\mathbf{K} = \mathbf{U\Sigma V}^\dagger, \tag{6.6}$$

providing $\mathbf{K}$ has been calculated for $\mathbf{N}$ close to the optimal solution. Here $\mathbf{U}$ is a matrix with orthonormal columns $(\mathbf{u_1}, ..., \mathbf{u_L})$ forming a basis of the measurement space describing $\mathbf{y}$ (so $\dim(\mathbf{u_k}) = \mathbf{M}$). The matrix $\mathbf{V}$ has columns $(\mathbf{v_1}, ..., \mathbf{v_L})$ which form an orthonormal basis of the solution space containing $\mathbf{N}$. (The dagger denotes a simple transpose.) Column vectors i of $\mathbf{V}$ spanning the space of the null-solution of $\mathbf{KN}$, with $\mathbf{KN} = \mathbf{0}$, form the null-space of the problem. For all such solution vectors the signal $\mathbf{y}$ in Eq. 6.3 is similar to the signal of the noise or the bias of the retrieval method $\epsilon_{\mathbf{T}}$.

Finally, $\mathbf{\Sigma}$ is a diagonal matrix containing the singular values $(\rho_1, ..., \rho_L)$ in descending order. The singular values weight the basis vectors according to how well they represent the measurement and the solution space (cf. [*Hansen*, 1994; *Hasekamp & Landgraf*, 2001]). This is made clearer on substitution of (6.6) into (6.3), viz,

$$\mathbf{y} = \sum_{\mathbf{f=1}}^{\mathbf{L}} \rho_{\mathbf{f}}(\mathbf{v_f^\dagger N})\mathbf{u_f} + \epsilon_{\mathbf{T}}. \qquad (6.7)$$

Thus the contribution to the measurement of the mth partial sum $\mathbf{y^{(m)}} = \sum_{\mathbf{f=1}}^{\mathbf{m}} \rho_{\mathbf{f}}(\mathbf{v_f^\dagger N})\mathbf{u_f}$ in Eq. (6.7) can be determined by evaluating the residual $||\mathbf{KN} - \mathbf{y^{(m)}}||$ for successive $m = 2, \dots, L$. In fact, adding additional terms beyond a certain value of m does not reduce the norm beyond the measurement error ϵ_T. The implication is that additional $(f > m)$ components $\mathbf{v_f^\dagger N}$ of the profile will be dominated by the measurement noise $\epsilon_{\mathbf{T}}$ (the contributions of the null-space) and will not add any additional information to the spectrum.

6.2.1 Water Vapor Subcolumn Profiles

In this section we want to discuss the results of WV subcolumn retrievals, previously performed in chapter 3 and 5, under the aspect of profile information content and contribution of measurement noise and model bias to the retrieval results. The subcolum profiles retrieved from GOME measurements in chapter 3 and 5 were used for the purpose of the retrieval of total water vapor column utilizing both, the OCM method and the SSP method (chapter 3 and chapter 5, respectively). For these retrievals the 590 nm WV absorption band accessible by GOME is used (Figure 6.2). There, the modeled transmittance $\mathbf{T_i^{SSP,OCM}}$ is fitted to GOME transmittance spectra $\mathbf{T_i^{GOME}}$, where i denotes the ith detector pixel, utilizing a robust, non-linear, large-scale trust-region method [*Byrd et al.*, 1988], which solves the optimization problem given by Eq. 6.5, where $\mathbf{N}=N_\ell$ are the WV subcolumns of ℓ atmospheric layer each at a mean layer-altitude z_ℓ. Each fit is initialized with a flat WV subcolumn profile $N_{\ell,0} = 10^{16}$ molec/cm^2 and constrained by an upper limit $N_{\ell,max}$ in the form of a step function with high values over the first atmospheric layers and lower values for the higher levels. The lower profile constraint is set to $N_{\ell,lower} = 0$. The constraints prevent the fit from giving too much weight to the higher altitude levels, which otherwise would increase the relative contribution of the singly scattered photons to unrealistic values by setting the surface albedo to zero and, in doing so, decrease the total mean free path length. The upper profile constraint are scaled differently for geolocations between 30° and -30° latitude, between $\pm30^o$ and $\pm60^o$ latitude and latitudes above or below $\pm60^o$ (for a detailed discussion see chapter 3, section 3.9 and chapter 5, section 5.5 and 5.8). Note, that the constraints contribute to a

regularization of the problem by constraining the amount of scattering in the retrieved profile and therefore regularizing the contribution of the measurement noise.

Figure 6.1 shows OCM and SSP retrieved WV subcolumn profiles for fits in cloud-free situations at significantly different geolocations and for a mean, high and low WVC. OCM profiles show generally good agreement with the given ECMWF profiles. It appears that OCM slightly underestimates the WV content above the bulk of the water vapor column which is usually situated in the lower part of the atmosphere. SSP retrieved subcolumn profiles show more scatter and, especially at higher altitudes, significant systematic deviations from the ECMWF. This is referred to the less accurate treatment of the spectral structure of the absorption by SSP with respect to altitude (see chapter 5, section 5.3 and 5.6). In addition, the dominant layer assumption of SSP results in an overestimation of the weight of single-scattering paths with high scattering heights (see Appendix C). Nevertheless, considering the simplicity of the method, also SSP retrievals mirror the ECMWF profile shapes to some extent. The good results are referred to the fact that both methods are self-contained retrieval methods based on first principles with a direct relation between the averaged cross-sections and the subcolumn parameters.

However, as laid out before, parts of the retrieved subcolumn profiles do not necessarily reflect the real profile (and, therefore, do not reflect fully the real profile information contained in the spectra and accessible by the measurement and the retrieval model) but have to be referred to the influence of the instrument noise and the biases in the retrieval methods. The scatter in the retrieved subcolumn profiles shown in Figure 6.1 may, therefore, be predominantly caused by contributions of the null-space of the problem to the retrieved profile. From this follows that the problem is ill-posed, meaning that not enough profile information is contained in the measurement in order to fully retrieve the real structure of the profile. From this also follows that the regularization of the problem by introducing the constraints was not sufficient to filter the contribution of the null-space and to identify the full amount of profile information contained in the measurements and accessible by the retrieval methods.

6.3 Phillips-Tikhonov Regularization

Profile inversion problems in atmospheric retrieval situations are frequently ill-posed problems. This means that the least squares solution, given by

$$\mathbf{N} = \sum_{\mathbf{f}=1}^{\mathbf{L}} \frac{(\mathbf{u_f^\dagger T})}{\rho_\mathbf{f}} \mathbf{v_f}, \tag{6.8}$$

is nonunique and requires regularization (or filtering of the null-space of the problem) in order to locate the most suitable solution. A variety of reqularization methods exist, including so-called statistical regularization [*Rodgers*, 2000] and the Phillips-Tikhonov regularization methods [*Phillips*, 1962; *Tikhonov*, 1963]. The latter method is employed in what follows.

A Phillips-Tikhonov Regularization (PTR) may be used to find an optimal solution vector from a constrained least squares

$$\mathbf{N}_{(\gamma)} = \min_{\mathbf{N}} \left(||(\mathbf{KN} - \mathbf{y})||^\mathbf{2} + \gamma^\mathbf{2} ||\mathbf{N}||^\mathbf{2} \right). \tag{6.9}$$
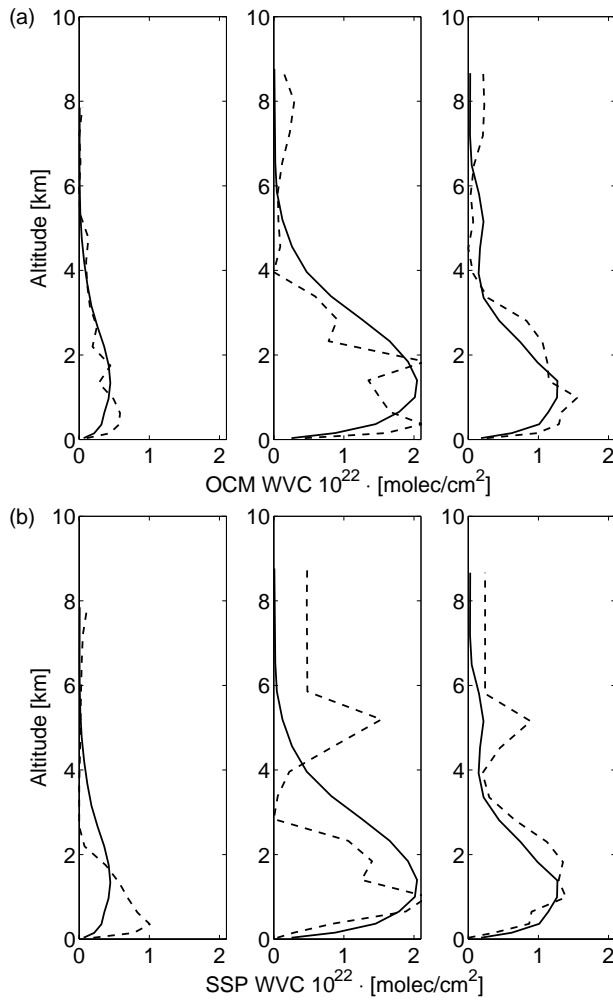
Figure 6.1: Three examples of water vapor profiles retrieved by OCM (a)
and SSP (b) (dashed lines). The thickness of the layers varies between 100
(close to surface) and 800 m (highest layers), depending on altitude and
geolocation. The left panels show the retrieved profiles for a low total WVC
of 2.85×10^{22} molec/cm^2 (for a measurement over the northern part of the
United States), the middle panels show a high WVC of 1.50×10^{23} molec/cm^2
(taken over the Pacific close to the equator) and the right panels show a mid-
range total WVC of 7.21×10^{22} molec/cm^2 (measured also over the Pacific
at 21° south). Each retrieved profile is compared with ECMWF data (solid
line).

Here γ denotes a value for which $||\mathbf{KN} - \mathbf{y}||$ cannot be reduced without increasing the norm
of the solution vector, $||\mathbf{N}||$. So $\gamma^2 ||\mathbf{N}||^2$ my be seen as a minimization of the contribution

of random scatter (noise contribution) over the solution vector $\mathbf{N}$. The optimal value of γ can be determined using the so-called parametric L-curve scheme ([*Hansen*, 1994]). The L-curve is a parametric plot of $||\mathbf{N}||$ and $||\mathbf{KN} - \mathbf{y}||$ parameterized by γ (Figure 6.4). There exists a value of γ beyond which all singular values $\rho_f > \gamma$ in the ordered sequence of singular values effect the norm less than the model error ϵ_T. The PTR solution (cf. Eq. (6.8)) is then given by

$$\mathbf{N}_{(\gamma)} = \sum_{\mathbf{f=1}}^{\mathbf{L}} \phi_{\mathbf{f}} \frac{(\mathbf{u}_{\mathbf{f}}^{\dagger} \mathbf{y})}{\rho_{\mathbf{f}}} \mathbf{v}_{\mathbf{f}}, \tag{6.10}$$

for which

$$\phi_f = \frac{\rho_f^2}{\rho_f^2 + \gamma^2}, \tag{6.11}$$

is often called the filter factor, as it filters out terms for which $\rho_f < \gamma$ and leaves the terms for $\rho_f > \gamma$ intact.

6.3.1   Profile Comparison and Information Content

As a consequence of the regularization, it is important to note that the regularized retrieved profile will, in general, be smoother than the true profile since a considerable amount of small-scale information is dominated by the noise of the instrument and therefore not contained in the measurement and cannot be retrieved. This loss of small-scale information due to instrument noise and method bias (smoothing of the profile) is generally characterized by the *averaging kernel*,

$$\mathbf{A} = \frac{\partial \mathbf{N}_{(\gamma)\text{retr}}}{\partial \mathbf{N}_{(\gamma)\text{true}}}, \tag{6.12}$$

which can also be used to obtain an averaged-true profile from the true profile via

$$\mathbf{N}_{(\gamma)\text{ave-true}} = \mathbf{A}\mathbf{N}_{(\gamma)\text{true}} + \epsilon_{\mathbf{T}}. \tag{6.13}$$

Thus in order to compare the retrieved and the true profile it is necessary to compare $\mathbf{N}_{(\gamma)\text{ave-true}}$ with $\mathbf{N}_{(\gamma)\text{retr}}$. Substituting $\mathbf{T} = \mathbf{KN}_{(\gamma)\text{true}}$ into Eq. (6.10) yields the following form for the averaging kernel

$$\mathbf{A} = \mathbf{V}\mathbf{\Phi}\mathbf{V}^{\dagger}, \tag{6.14}$$

with $\mathbf{\Phi} = \text{diag}(\phi_f)$ (cf. *Hasekamp & Landgraf*, 2001).

The number of independent pieces of information which can be retrieved from $\mathbf{N}_{\text{true}}$ for a given M independent equations (essentially the resolution of the retrieved profile) is called the number of *degrees of freedom for signal* (DFS) (cf. *Rodgers*, 2000) and can be written in terms of the singular value decomposition as

$$DFS = \sum_{f=1}^{L} \phi_f. \tag{6.15}$$

In principle, the DFS can be increased by adding more spectral intervals (detector pixels
or measurements; and thus increasing M). Beyond a certain point, however, the additional
signal does not effect the information about the retrieved profile above the instrumental
noise level and the retrieval method related bias and the DFS stays constant or may
even decrease in practice. In the next section the above analysis is applied to synthetic
retrievals from a typical radiosonde water vapor profile in order to find out how well the
retrievals fare using the ck-distribution method and OCM forward models.

6.4 Synthetic Profile Retrieval using OCM and the Correlated k-distribution Method

We first want to focus solely on the differences in the retrieved water vapor profile by using
two different sampling methods for different absorption bands which contain different
number of absorption lines, spanning different spectral regions and differ significantly in
strength of absorption. Two of the four GOME channels cover the three water vapor
absorption bands already mentioned above and shown in Figure 6.2. The lower panel of
Figure 6.2 shows a lbl calculation of the water vapor absorption using a simple direct-path
calculation with

$$T_i^{\text{lbl}} = \frac{1}{\Delta\lambda_{\text{i}}} \int_{\Delta\lambda_{\text{i}}} \exp\left(-\sum_{\ell}^{\text{L}^{\text{sonde}}} \sigma(\lambda, \text{z}_\ell)\text{N}_\ell^{\text{sonde}}\right) d\lambda, \qquad (6.16)$$

where $\Delta\lambda_i$ is the spectral sampling width (for example, 0.21 nm in channel 3 of GOME)
of the ith detector pixel and the cross-sections $\sigma(\lambda, z)$ are calculated from line parameters
taken from the HITRAN 96 database [$Rothman\ et\ al.$, 1998]. The lbl calculation uses
a typical radiosonde water vapor density profile, with $L^{\text{Sonde}} = 91$ subcolumn densities
N_ℓ^{sonde}, which has been measured, along with background pressure and temperature, up
to an altitude of 9 km on June 25, 1995 at de Bilt, The Netherlands, by the Koninklijk
Nederlands Meteorologisch Instituut (KNMI). The model does not include absorption
by additional absorbers apart from water vapor, scattering out of the light path, single-
and multiple scattering effects and does also not include a reduction of the light due to
the surface albedo. Effects, such as the influence of the instrumental response function,
have not been included in the calculation. Nevertheless, when comparing the monochro-
matically calculated transmittance (lower panel of Figure 6.2) to a real measurement of
GOME taken in coincidence with the radiosonde takeoff (upper panel of Figure 6.2) the
similar absorption features for the three absorption bands are evident.

The synthetic retrievals are performed using Eq. 6.9 and Eq. 6.16, where the minimal-
ization is performed simultaneously for all i spectral intervals (detector pixel) using both
the ck-distribution method (chapter 2, Eq. 2.50) and the OCM method (chapter 2, Eq.
2.29), respectively. The fit parameters are vertical water vapor subcolumn densities N_ℓ of
$L = 31$ atmospheric layers defined as such that the subcolum density profile taken by the
radiosonde is monotonically decreasing. No $a\ priori$ knowledge about the water vapor pro-
file and no constraints are applied during the fitting procedure. The discrete probability
density functions are calculated directly from the radiosonde pressure and temperature

information. An optimal number of quadrature points G for the ck-distribution and B for the OCM method is used (see also chapter 2, section 2.33). Figure 2.11 in chapter 2 shows that the forward modeling error in the case of the ck-distribution method will never be much smaller than about 10^{-2} % (which is about a factor of ten smaller than the instrumental noise value of the GOME instrument) for an instrumental sampling width of smaller than 7 cm^{-1} and more than 15 quadrature points. Therefore $G = 15$ quadrature are chosen for the ck-distribution method. In the case of OCM a quadrature of $B = 80$ is chosen.

6.4.1   Results

Figure 6.3 shows the monochromatically calculated transmittance using Eq. 6.16 along with the fit residuals using both the ck-distribution method and OCM (middle and lower panel) for all 404 GOME detector pixels covering all the three absorption bands. From this fit result it is concluded that the residuals increase significantly for stronger absorptions. The error for OCM increases by less than a factor of ten going from the weaker to the strong band, whereas the error for the ck-distribution method increases by more than a factor of 20. This is due to an amplification of the method bias for both methods (quadrature sampling, section 2.3.3) together with the error caused by the correlation assumption and by utilizing relatively small sampling widths (chapter 2, section 2.3.3) in the case of the ck-distribution method.

For the optimal solution of Eq. 6.9 an optimal γ-value is derived using the parametric L-curve scheme (cf. Eq. 6.10) for each method (Figure 6.4, upper panel). In addition, a number of fits are performed as a function of the number of detector pixels used (i.e. changing the spectroscopic information content) starting from including the first 40 pixels of the 590 nm band (see figure 6.2 for pixel numbering) and increasing in number of included pixel until all 404 pixels are utilized in the retrieval. For each fit the DFS is calculated from the filter-function ϕ (Eq. 6.11 and 6.15). Figure 6.5 shows the DFS values as a function of the number of detector pixels used. The increase in number of used detector pixels corresponds to an increase in wavenumber range from 17245 cm^{-1} (pixel number 404) to smaller wavenumbers (i.e. from smaller to higher fit-residuals, cf. Figure 6.3). As can be seen from Figure 6.5 the DFS sharply increases for the OCM method at around 80 utilized detector pixels after which it stays constant until about 230 pixels. In the case of the ck-distribution method the DFS increases in a less pronounced fashion at around 140 and stays constant until about 230 pixels. The increase of the DFS corresponds roughly to the inclusion of the 640 nm band. The subsequent decrease corresponds to the inclusion of the strongly absorbing part of the 720 nm band and can be related to the significant increase in the retrieval bias for stronger absorptions (Figure 6.3). In general the DFS values, or the number of independent pieces of information that can be retrieved, are systematically lower for the ck-distribution method than for the OCM method. Thus one can infer that a retrieval from synthetic spectra without measurement noise contribution which uses the first 230 detector pixels (including the complete two weaker absorption bands and the weaker part of the first strong absorption band) will contain more than five fully-independent pieces of profile information in the case of the OCS method and four fully-independent pieces of profile information in the case of the ck-distribution method.

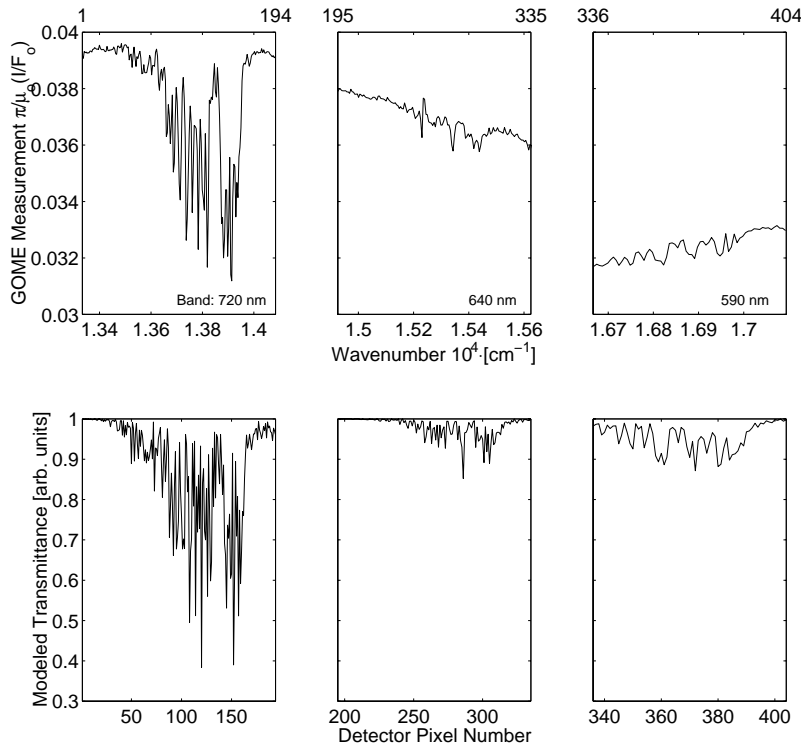Figure 6.4 shows retrieval diagnostics for the synthetic retrieval, assuming maximum

Figure 6.2: GOME measurements and monochromatically forward modeled
synthetic spectra of all three water vapor absorption bands accessible by the
GOME instrument. The three panels in the upper row show a GOME mea-
surement of the upwelling radiance I divided by a direct sun measurement
F_o. The three lower panels show a simple lbl calculation of the transmittance
for the same water vapor absorption bands using Eq. (6.16) and applying
the same sampling widths as for the GOME detectors. The lbl calculation
uses concurrent pressure, temperature and water vapor density profiles mea-
sured by a radiosonde balloon measurement at the Bilt, The Netherlands,
on the same day and within the ground pixel of the GOME measurement.
The detector pixel number i is shown on the upper horizontal axis of the
upper panels (start and end detector pixel of each absorption band) as well
as on the lower horizontal axes of the lower panels.

DSF for both methods. The diagnostics include the L-curve, γ-corner-values (upper panel)
and filter factors (lower panel) for 230 independent equations with maximum DSF for
both methods. The corner value of the L-curve is the optimal value for γ found during
the optimalization process (Eq. 6.9) for which both the norm of the solution vector $||\mathbf{N}_{(\gamma)}||$
(vertical axis) and the residual norm $||\mathbf{KN}_{(\gamma)} - \mathbf{y}||$ (horizontal axes) are minimal, i.e. the
best solution with respect to the measurement together with a minimal scatter (retrieval
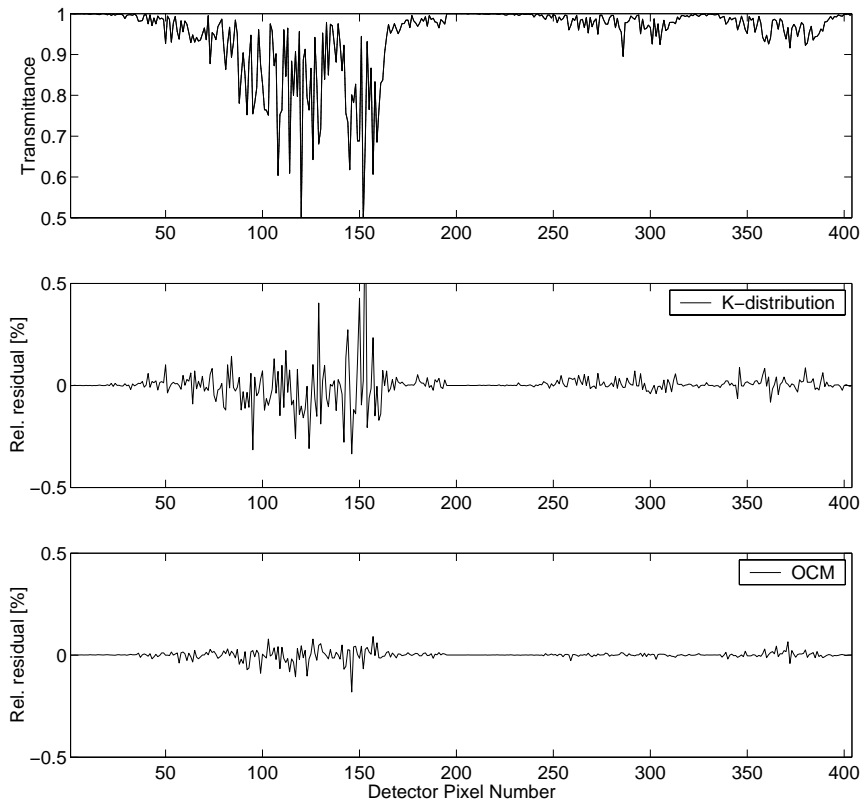
Figure 6.3: Comparison of transmittance calculations for the synthetic re-
trieval. The top panel shows the lbl calculation of the transmittance over
detector pixel number as is shown in the lower row of Figure 6.2. The mid-
dle and the lower panel show the fit residual for both the ck-distribution and
OCM, respectively

bias contribution) of the retrieved profile. For the parametric plot γ increases from right to
left on the horizontal axis (decreasing residual norm). The more values lie on the horizontal
part of the curve the more independent pieces of profile information are accessible from
the measurement. For the ck-distribution method γ is smaller and the corner lies more
to the right of the horizontal axis reflecting a larger method related bias with respect to
the OCM method (cf. Figure 6.3).

   The results of the synthetic retrieval are shown in Figure 6.6 and 6.7 which includes
averaging kernels together with the true (radiosonde) profile consisting of 91 layers, the
averaged-true profile and the retrieved profile (right panel) each consisting of 31 altitude
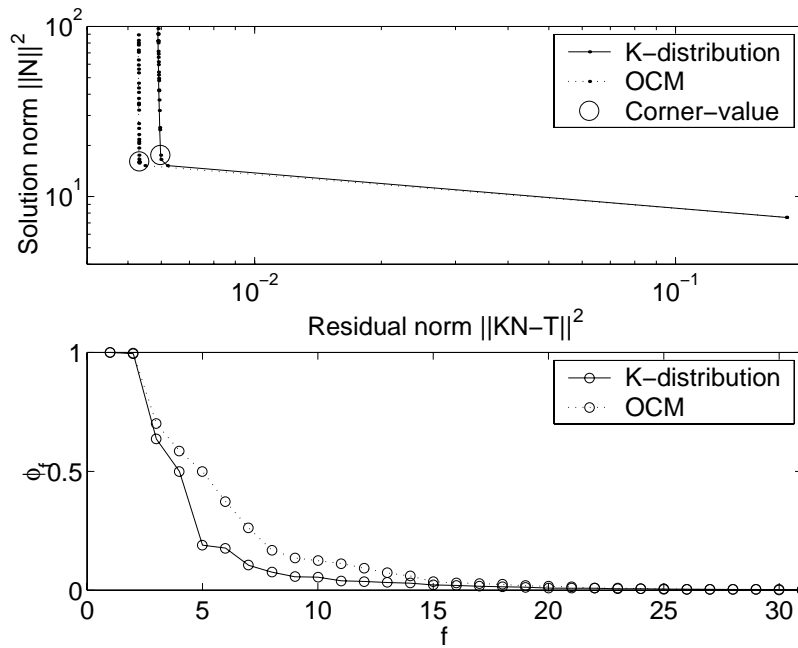layers.

Figure 6.4: Retrieval diagnostics for the synthetic retrieval assuming maximum DSF for both methods. This involves the use of 230 independent fit equations, i.e radiances taken from detector pixel number 174 to 404. Top panel: the L-curves for both methods (upper panel), which are parametric plots of the solution and the residual norm dependent on the γ parameter with $[||K\mathbf{N}_{(\gamma)} - \mathbf{y}||, ||\mathbf{N}_{(\gamma)}||]$. The corner values (circles) correspond to a specific γ value and are calculated analytically using the method discussed in the text and the methods of Hansen [*Hansen*, 1994]. Bottom panel: the filter functions of both methods for the γ-values shown in the upper panel. The γ values are equal to the fifth and the fourth singular values for the OCM and *ck*-distribution method, respectively, corresponding to five and four fully-independent pieces of profile information.

6.4.2 Discussion of Profile Retrieval Results

Figure 6.6 and 6.7 shows averaging kernels, retrieved profiles and profile residuals for the *ck*-distribution and the OCM method, respectively. Averaging kernel matrices are M by M matrices. The left panel of both figures therefore show 31 column vectors each peaked at different altitude heights reflecting how the profile information at each individual peak height is distributed over the neighboring altitudes (by the width of the peaks). The averaging kernels in the left panels of Figure 6.6 and 6.7 look very different for the two methods. Both the widths and the location of the peaks differ (see Figure 6.6 and 6.7, left hand panels). The peaks are broader in the case of the *ck*-distribution than in the case of OCM reflecting the lower DFS value of the *ck*-distribution method. In other words,
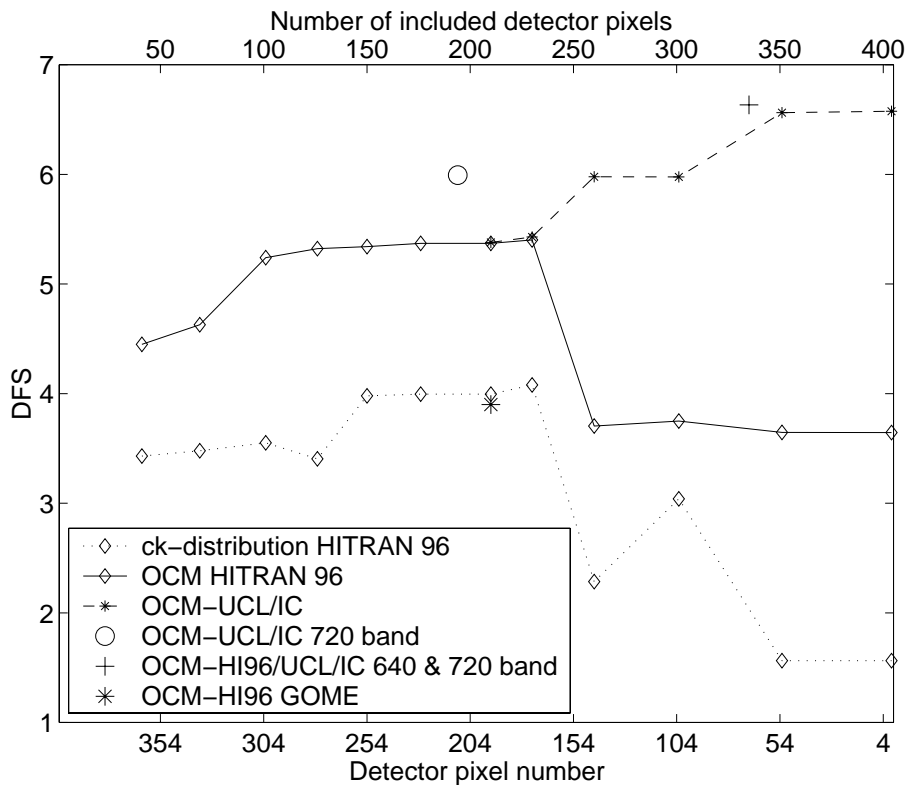
Figure 6.5: The Degrees of Freedom for Signal (DFS) for different spectral ranges. The lower axis shows the detector pixel number lower limit for the range of pixels included in the diagnostic, i.e. starting always from pixel number 404 and ending on the pixel number given on the axis. The upper axis denotes the total number of pixels included per calculation. The 720 nm band is covered by detector pixels 1 to 194, the 640 nm band by detector pixels 195 to 335 and the 590 band by detector pixels 336 to 404. Apart from the OCM and *ck*-distribution results utilizing the HITRAN 96 database (solid and dotted line, respectively) results for OCM retrieval utilizing the UCL/IC database (dashed line; for details see text). In addition individual results for retrievals including the 720 nm band (open circle) and the combined 640 nm and 720 nm band (plus) are shown. Finally the DFS value for OCM retrievals from GOME utilizing the combined 590 nm and 640 nm band is also displayed (star).

the information about the water vapour density at a specific altitude is interwoven with more information of the densities at other layers in the *ck*-distribution method than in the OCM method. In addition the amplitudes of the peaks at higher altitudes are higher in the case of the *ck*-distribution method than for the peaks at lower altitudes where

the bulk of the water vapor is situated. The OCM averaging kernel peak amplitudes also appear to be more even over the whole altitude range which means that each altitude is more fairly weighted in the retrieval. The width of the individual peaks (the resolution of the retrieval method) can be calculated by dividing the number of retrieval points by the DFS value scaled with altitude. The resolution is better than 1.6 km for the OCS and 2.1 km for the ck-distribution method.

The resolution of the two methods is reflected in the averaged true profile (Eq. 6.13) displayed in the middle panels of Figure 6.6 and 6.7 (dotted line). The averaged true profile is the optimal profile that can be retrieved from the true radiosonde profile (solid line) with the two methods using the assumptions discussed in this chapter. We further conclude that subkilometer variations in the true profile on the order of 100% for the layers below 4 km and of more than 100% for the layers above 4 km with respect to the averaged true profile (dotted line, right panel) cannot be resolved by either method.

The middle panels also show the retrieved profiles (dashed line) and the right panels the relative residuals between the averaged-true profile and the retrieved profile. From this it is concluded that the OCM and ck-distribution method retrieved profiles differ from the the averaged true profiles on the order of 100% and 50–100% for the layers below 4 km and up to 100% and more than 100% for the layers above 4 km, respectively. OCM clearly performs better than ck-distribution over the whole altitude range (the mean difference of 0.7% in the case of OCM is significantly better than the value for the ck-distribution method of 7.1%).

It may appear, for the comparison above, that the choice of sampling width biases the comparison somewhat against the ck-distribution method since a very small sampling width of the detector (corresponding to few sampled absorption lines per sampling width) is somewhat less favorable for the ck-distribution method. This is because the relatively small sampling width (around 6 cm^{-1}) used for a realistic GOME retrieval scenario results in a relatively high method-related error for the ck-distribution method (compared to sampling widths larger than 10 cm^{-1}, cf. Figure 2.11 and the discussion in chapter 2, section 2.3.3.2). For optimum return, a retrieval must involve an adequately high number of measurement data. This can be achieved either by improving the instrument (by increasing its wavelength range or by improving its spectral resolution), which is seldom practical, or by improving the wavelength resolution of the forward model. In the case of GOME measurements, the FWHM of the instrument function is close to the sampling width of the detector pixels, which has been used as the basis for the calculations. Improving the wavelength resolution of the forward model would mean that sampling widths have to be reduced below the width required by the Nyquist criterium for the instrumental response function. However, smaller sampling widths lead to a further increase in the method-related error in the case of the ck-distribution method. Furthermore, including a proper instrumental response function for the GOME instrument would make it even more difficult to achieve accurate values in the case of the ck-distribution method without substantial modification to the method (cf. *Buchwitz et al.*, 2000). Therefore it is concluded that, at least for relatively high-resolution measurements over nonhomogeneous paths of nongray atmospheres, OCM performs more accurately as a profile retrieval method than the ck-distribution method described in chapter 2 of this work.
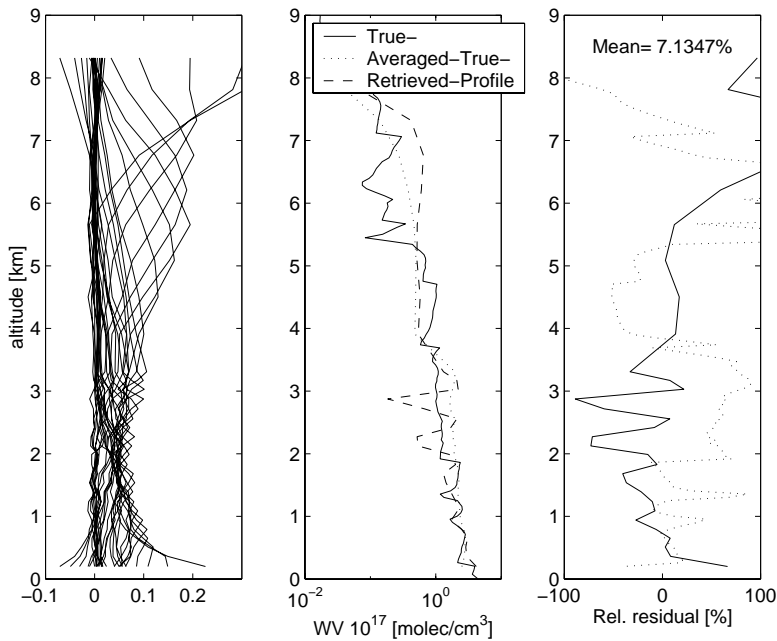
Figure 6.6: Profile retrieval result using the ck-distribution method. The left panel shows the 31 averaging kernel column vectors as a function of altitude for the 31 fit parameters (subcolumns). The middle panel shows the true (radiosonde) profile (solid line), the averaged-true profile (dotted line) and the retrieved profile. The right panel shows the relative difference between the averaged-true profile and the retrieved profile (solid line) together with their mean value for all altitudes. The right panel also shows the relative difference between the averaged-true profile and the true profile (dotted line), where the averaged-true profile is interpolated on the altitude-level grid of the true profile.

6.5 Impact of Absorption Line Parameter from Different Databases on Profile Retrieval

The impact of different water vapor absorption line parameters from different databases (and therefore also from different laboratory measurements) on the retrieval of both total WVC and WV profiles is currently under extensive study [*Belmiloud et al.*, 2000; *Learner et al.*, 2000; *Lang et al.*, 2002; *Veihelmann et al.*, 2002]. There are discrepancies between the databases reported ranging from about 100% for weak lines to about 20% for strong lines for the main water vapor absorption bands in the region between 1110 and 685 nm. *Coheur et al.*, [2002], report differences of only 5% in the line intensity between their own measurements and HITRAN 96 in the region between 400 and 800 nm but doubled the amount of assigned lines with respect to HITRAN 96. *Veihelmann et al.*, [2002], report
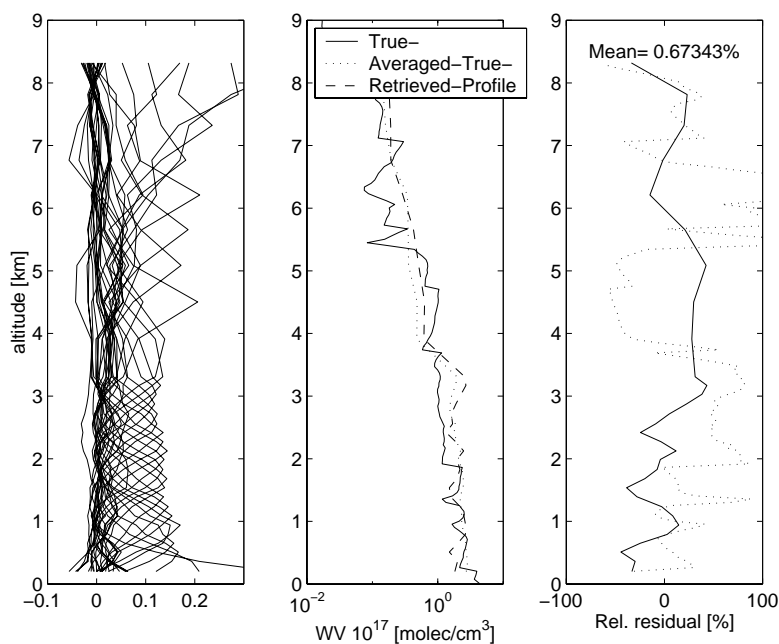
Figure 6.7: Same as Figure 6.6 but for a retrieval result using OCM.

differences of up to 30% in line intensities in the region between 585 and 600 nm between
monochromatically forward-modeled spectra using HITRAN 1999 [*Giver et al.*, 1999] and
ground-based direct sunlight measurements by means of a high resolution Fourier trans-
form spectrometer. In this chapter, so far, the HITRAN 96 database has been used for
calculations of monochromatically forward-modeled spectra, as well as for construction
of averaged cross-section parameters for both applied retrieval methods. A new database
due to a collaboration between University College London and Imperial College (hereafter
UCL/IC), and based on new laboratory measurements at Rutherford Appleton Laborato-
ries has been used recently by *Maurellis et al.*, [2002], in order to estimate the amount of
DFS using SSP (chapter 4 and 5) profile retrievals from synthetic spectra including effects
of the instrumental function and measurement noise. These simulations were performed
on various individual absorption bands (i.e. not combining spectral information from dif-
ferent absorption bands in order to utilize a maximum of spectroscopic information, like
is done in this chapter) of WV from the visible to the near infrared. The new UCL/IC
data is currently only available for the 720 nm band in the GOME accessible wavelength
region. The new line-parameter data increases the amount of lines within this spectral
region from 1552 (HITRAN 96) to 2428 in the region between 13300 and 14100 cm^{-1}.
Synthetic retrieval results by *Maurellis et al.*, [2002], show that the DFS value increases
by about 7 pieces of information going from 3–4 pieces in the case of using HITRAN 96
to 7 to more than 10 independent pieces when using UCL/IC. The effect of an increasing
DFS value is due to the additional lines contained in the UCL/IC database, because the
differences in line intensity with respect to HITRAN 96 appears to be small, as stated

above.

Figure 6.5 (dashed line) shows the DFS value when we perform the same kind of OCM retrievals as in the previous section but now using the UCL/IC instead of the HITRAN 96 database for the 720 nm band (i.e. from including detector pixel 194 to pixel number 1). Clearly the implementation of the new data bases adds additional pieces of profile information to the retrieval result. A maximum of 6.5 for the DFS value is reached when including the whole band, which relates to an increase of about 3 pieces of information due to the additional spectroscopic information. However, the increase is not as big as expected from the studies by *Maurellis et al.*, [2002], The latter is due to the fact that, here, also the significant impact of the retrieval bias caused by the high optical densities in the 720 nm band is taken into account, which counter-effects a potentially higher increase of the DFS value by adding additional spectral information. Utilizing simultaneously the 650 nm band (HITRAN 96) and the 720 nm band (UCL/IC) results in more than 6.5 DFS (Figure 6.5, plus sign at 335 independent equations used). Excluding the weak 590 nm band improves the maximum value for DFS by only a small amount, which is referred to the fact that at some point a principal maximum of accessible profile information is reached reflecting a trade off between spectroscopic information and the contribution of the retrieval bias. Finally, as a reference, the DFS value for OCM retrievals using only the 720 nm band with line-parameter data from the UCL/IC database is shown as an open circle in the same figure and for 195 detector pixel i. With about 6 independent pieces of information the latter is, as expected, smaller than the DFS for the retrievals combining a number of different bands.

In summary, a combination of the 650 nm and the 720 nm absorption band accessible by GOME give best results for retrievals from synthetic spectra without measurement noise added concerning the degrees of freedom for signal, providing that, for the 720 nm band, a database is used which contains significantly more absorption lines than HITRAN 96. In the case of using the HITRAN 96 database only, best results are achieved by combining the 590 nm and the 640 nm absorption bands. This is referred to the fact that the increase in the retrieval method related error, due to the high optical densities of the 720 nm band, counter-effects the additional spectroscopic information.

6.6   Outlook: Water Vapor Profile Retrieval from GOME Measurements

In a first attempt to use real GOME measurement data for WV profile retrieval we utilize the GOME measurement displayed in the upper panels of Figure 6.2. The measurement coincides with the radiosonde profile measurement utilized in the previous chapter in time and place (Figure 6.8; note, that the GOME measurement covers a surface area of 40 by 320 km, where part of the pixel is above the Netherlands and part above the North Sea). The total WVC measured by the radiosonde is 8.51×10^{22} molec/cm^2. Eq. 3.30 is used in the way as described in section 6.2.1 using an OCM retrieval (details on how OCM is implemented in a single-scattering radiative transfer scheme for WVC retrievals from GOME data see chapter 3) and utilizing the two absorption bands around 590 and 640 nm simultaneously. The decision on utilizing these bands is made because the OCM retrievals uses line parameters from the HITRAN 96 database and best results
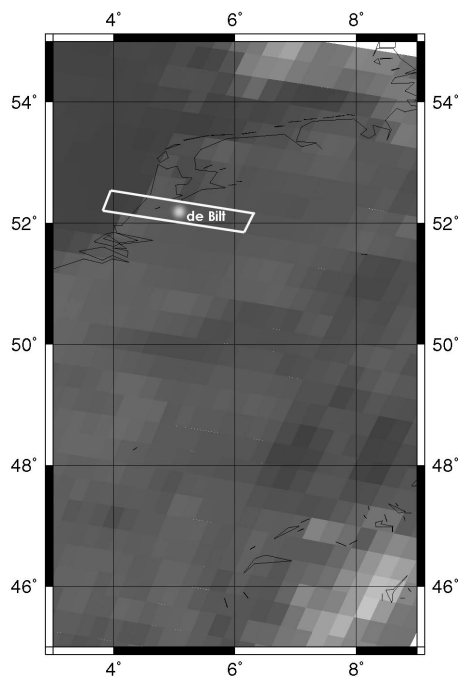
Figure 6.8: RGB plot of a number of broad band GOME Polarization Measurement Device (PMD) measurements encoded in red, green, blue (RGB) state vectors translating here to dark, grey and bright pixels. From such measurements land can be distinguished from ocean (here dark) and clouds result in white pixels. The GOME ground pixel used for WV profile retrieval in this section is framed in white and is cloud-free. The place of the radiosonde takeoff at de Bilt, The Netherlands, is also indicated.

are expected for combining the 590 nm and the 640 nm band (see DFS results in previous section). In total 210 GOME detector pixel are used (see Figure 6.2) covering the two absorption bands.

Figure 6.9 shows the results of a profile retrieval using 26 altitude layers covering a range up to 8 km. For the retrieval the same regularization scheme is applied as used in the previous sections for the synthetic retrieval study. From this a number of 3.9 independent pieces of information (DFS) are derived (Figure 6.15; star), which corresponds to an altitude resolution of about 2 km. This means that, by going from the specific synthetic retrievals of the previous sections to real retrievals from GOME measurements, the DFS value decreases by more than one degree of freedom for signal. This is not surprising because, in addition to the impact of the retrieval method related error, the amount of spectroscopic data and the quality of the database, here also the smoothing of the instrument slit function as well as the instrument noise and errors play a role. The latter

two are indeed expected to decrease the amount of accessible profile information. In contrast, the profile information included in the spectral differences of mean scattering heights is added for this kind of retrievals due to the usage of a radiative transport scheme, which includes a correct treatment of singly scattered photons (chapter 3). The left panel of Figure 6.9 shows the radiosonde profile consisting of 91 altitude layers (solid line) together with its averaged version using the derived averaging kernel matrix (Eq. 6.14) and the regularized retrieved profile. Systematic differences between the smoothed and the retrieved profile (right panel) occur predominantly above 6 km, corresponding to where the WV profile measured by the radiosonde drops by nearly one order of magnitude. It should be noted that the total WVC retrieved from the GOME measurement by simply adding the subcolumn WV values is 8.41×10^{22} molec/cm^2, thus very close to the value measured by the radiosonde of 8.51×10^{22} molec/cm^2. This means that the overestimation of the profile at higher altitudes (above 5 km) is compensated by an underestimation of the lower altitudes (below 5 km), where the bottom part contains nearly three and the top part more than one independent pieces of profile information.

6.7   Conclusion and Summary

Both retrieval methods SSP and OCM introduced in this thesis, establish a direct link between averaged absorption line parameters of a specific atmospheric layer and its corresponding subcolumn density. Both methods, as well as the *ck*-distribution retrieval method (chapter 2), showed their principal ability to retrieve subcolumn WV profile from synthetic absorption spectra of WV. In addition, OCM profile retrieval has been demonstrated from real GOME measurement. It has been shown in this chapter that a singular value decomposition of the kernel matrix of the retrieval problem in conjunction with a Phillips-Tikhonov-Twomey regularization can be used in order to calculate the amount of independent pieces of profile information (or degrees of freedom for signal DFS). Using such retrieval techniques, the influence on the DFS values with respect to the retrieval method related error, and the amount of spectroscopic information has been studied from synthetic spectra of three GOME accessible absorption bands between 580 and 800 nm. The synthetic spectra were calculated monochromatically using the HITRAN 96 database, which was also used to calculate averaged line parameters for all relevant retrieval methods.

In conclusion, OCM retrievals result in systematically higher DFS values than retrievals using the *ck*-distribution method introduced in chapter 2 of this thesis, which we relate to the higher method related error of the latter for cases with relatively small spectral sampling width (like is the case for the GOME instrument) containing only a few individual absorption lines (see also chapter 2, section 2.3.3.2). Including more and more spectral information by utilizing more and more detector pixels together with combining various absorption bands increases the DFS values until about 5.5 independent pieces of information for a combination of the complete 590 and 640 nm bands. Including also the 720 nm band leads either to a decrease of the DFS value due to an increase of the method related error because of this much more optically dense band, or to a further increase of the DFS values when simultaneously utilizing more spectroscopic information for this band. From this it is concluded that using different databases containing more line param-
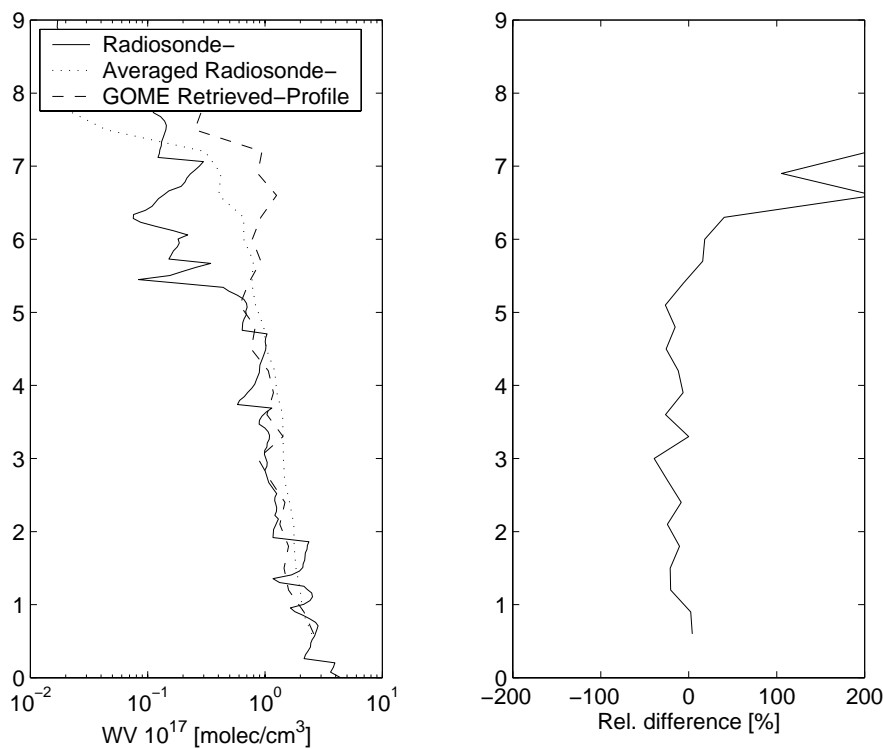
Figure 6.9: Results of a WV profile retrieval from GOME using the OCM
method (chapter 3). In total 210 GOME detector pixel are used including
the 590 nm as well as the 640 nm band. The applied regularization scheme
results in 3.9 independent pieces of profile information (2 km altitude reso-
lution). The regularized retrieval result (left panel, dashed line) is compared
to a co-located radiosonde measurement of the WV profile consisting of 91
altitude levels (left panel, solid line). The smoothed radiosonde profile using
the averaging Kernel of the retrieval is also shown in the left panel (dotted
line). The right panel shows the relative difference between the retrieved
profile and the smoothed radiosonde profile.

eters than HITRAN 96 (here, a new database from a collaboration between University
College London and Imperial College using new laboratory measurements at Rutherford
Appleton Laboratories has been used, called UCL/IC) improves the DFS values. This
new database is, so far, available only for the 720 nm WV-band of the GOME accessible
region and contains 50% more, predominantly weak, lines. The DFS value improves by at
least 3 points using the new database, which is still counter-effected by a relatively high
contribution of the retrieval method bias due to the high optical thickness of the band.
From this it is shown that new databases can affect profile retrieval of water vapor from
nadir satellite measurements significantly by simply adding additional absorption lines.

From this also the question on the lower limit of line intensities with any significance to such retrievals arises and may, therefore, well be the subject of future studies.

Finally, a preliminary OCM retrieval from a real GOME measurement has been performed from which 3.9 independent pieces of profile information have been retrieved. The result has been compared to a co-located radiosonde WV profile measurement and shows good agreement with the regularized radiosonde profile up to about 5 km. For higher altitudes the error increases significantly, which is referred to a significant decrease of the WV density at this altitude. A similar effect, even though less pronounced, has been found for the synthetic retrievals utilizing the same radiosonde profile. Here, especially the scatter between retrieved and regularized profile increases above 5 km together with the width of the peaks of the averaging kernel functions over altitude. For the retrieval from real GOME measurements the 590 nm band has been exploited simultaneously with the 640 nm band using line parameters from the HITRAN 96 database. Future studies may improve on this including also the 720 nm band, as well as more spectroscopic information from new WV absorption line-parameter databases.

Bibliography

Belmiloud, D., R. Schermaul, K. Smith, N. F. Zobov, F. Nikolai, J. W. Brault, R. C. M. Learner, D. A. Newnham, and J. Tennyson, New Studies of the Visible and Near-Infrared Absorption by Water Vapour and Some Problems with the HITRAN Database, *Geophys. Res. Lett., 27*, 3703-3707, 2000.

Buchwitz, M., V. V. Rozanov, and J.P. Burrows, A correlated-k distribution scheme for overlapping gases suitable for retrieval of atmospheric constituents from moderate resolution radiance measurements in the visible/near-infrared spectral region, *J. Geophys. Res., 105*, 15,247-15,261, 2000.

Buchwitz, M., V. V. Rozanov, and J. P. Burrows, A near-infrared optimized DOAS method for the fast global retrieval of atmospheric CH_4, CO, CO_2, H_2O, and N_2O total column amounts from SCIAMACHY Envisat-1 nadir radiances, *J. Geophys. Res., 105,* 15,231-15,245, 2000.

Byrd, R. H., R. B. Schnabel and G. A. Shultz, Approximate Solution of the Trust Region Problem by Minimization over Two-Dimensional Subspaces, *Mathematical Programming, 40,* 247-263, 1988.

Casadio S., C. Zehner, G. Piscane, and E. Putz, Empirical Retrieval of Atmospheric Air Mass Factor (ERA) for the Measurement of Water Vapor Vertical Content using GOME Data, *Geophys. Res. Lett., 27,* 1483-1486, 2000.

Giver, L.P., J. C. Chackerian, and P. Varanasi, Visible and Near-infrared $H_2^{16}O$ Line Intensity Corrections for HITRAN-96, *J. Quant. Spect. & Rad. Transfer, 66,* 101-105, 1999.

Hansen, P,. Regularization tools - A Matlab package for analysis and solution of discrete ill posed problems, *Numer. Algorithms, 6*, 1-35, 1994.

Hasekamp, O., and J. Landgraf, Ozone profile retrieval from backscattered ultraviolet radiances: The inverse problem solved by regularization, *J. Geophys. Res., 106*, 8077-8088, 2001.

Lang, R., A. N. Maurellis, W. J. van der Zande, I. Aben, J. Landgraf, and W. Ubachs,

Forward Modeling and Retrieval of Water Vapor from GOME: Treatment of Narrow Band Absorption Spectra, *J. Geophys. Res.*, in press, 2002.

Learner, R., R. Schermaul, J. Tennyson, N. Zobov, J. Ballard, D. Newnham, and M. Wickett, Measurement of H_2O Absorption Cross-Sections for the Exploitation of GOME data, *ESTEC Contract No 13312/9/NL/SF*, Final Presentation, 2000.

Maurellis, A. N., J. Tennyson, R. Lang, J. E. Williams, R. N. Tolchenov, and O. L. Polyanski, Impact of New Water Vapour Spectroscopy on Radiative Transfer Modeling and Retrieval, *NATO-ARW Meeting*, Fontevraud, France, April 2002.

Noël, S., M. Buchwitz, H. Bovensmann, R. Hoogen, and J. P. Burrows, Atmospheric Water Vapor Amounts Retrieved from GOME Satellite Data, *Geophys. Res. Lett., 26*, 1841-1844, 1999.

Phillips, P., A technique for the numerical solution of certain integral equations of the first kind, *J. Assoc. Comput. Mach., 9*, 84-97, 1962

Rodgers, C. D., Inverse Methods for Atmospheric Sounding, *World Scientific*, Singapore, 2000.

Rothman, L. S., C. P. Rinsland, A. Goldman, S. T. Massie, D. P. Edwards, J.-M. Flaud, A. Perrin, C. Camy-Peyret, V. Dana, J.-Y. Mandin, J. Schroeder, A. McCann, R. R. Gamache, R. B. Wattson, K. Yoshino, K. V. Chance, K. W. Jucks, L. R. Brown, V. Nemtchino, and P. Varanasi, The HITRAN Molecular Spectroscopic Database and HAWKS (HITRAN Atmospheric Workstation): 1996 Edition, *J. Quant. Spect. & Rad. Transfer, 60,* 665-710, 1998.

Tikhonov, A., On the solution of incorrectly stated problems and a method of regularization, *J. Geophys. Res., 102*, 84-97, 1963.

Veihelmann, B., R. Lang, K. M. Smith, D. A. Newnham, and W. J. van der Zande, *Geophys. Res. Lett.,* in press, 2002.

Appendix A

Line Parameters

A.1 Cross-Section, Line Intensity, Line Strength and f-values

This appendix introduces some of the most important quantities and relationships needed when dealing with atmospheric absorption phenomena. Problems with the definitions of terms like, cross-section, line intensity, line strength, f-values and Einstein coefficient often arise in conjunction with a specific definition of the irradiated energy field and, subsequently, the units of the spectral line parameters. The definition of the irradiated energy field effect the proportionality constants of the relations often to such an extent that some quantities may even become unidentifiable after a unit conversion. This appendix will partly follow the line of a revised version (2000) of a paper, previously published by *Hilborn*, [1982].'

A.1.1 Absorption Coefficient and Absorption Cross-Section

The absorption coefficient α is a phenomenological quantity. It is defined by a beam of light with specific intensity $i(\omega)$ at angular frequency ω propagating in direction x via,

$$\alpha(\omega) = -\frac{1}{i(\omega)} \frac{di(\omega)}{dx}, \tag{A.1}$$

where $i(\omega)$ is in units of power per unit area, per unit angular frequency interval $d\omega$. $i(\omega)$ can be translated to specific intensity with photons per second per wavenumber interval $d\nu$ and per sterad by,

$$i(\omega) \left[\frac{W}{cm^2 s^{-1}}\right] \rightarrow \frac{1}{2h\nu} i(\omega) \rightarrow i(\nu) \left[\frac{photons}{cm^2 \ s \ sr \ cm^{-1}}\right], \tag{A.2}$$

where the speed of light c has units of cm/s. For the remainder of this appendix energy units of angular frequency are used.

The angular frequency dependence can be described by a normalized **line-shape function** $g(\omega)$ in units of seconds (i.e. inverse energy; for a list of the units of the most important quantities used here see table A.1) with

$$\int_{-\infty}^{\infty} g(\omega)d\omega = 1. \tag{A.3}$$

Later on, in section A.1.5, an analogy between the emission and absorption rates of an atom and the classical oscillater and its oscillator strength (f-value) will be established.

We then may identify $g(\omega)$ with the normalized Lorentz profile of a stationary, classical oscillator with a Half-Width at Half Maximum (HWHM) determined by the classical radiative decay rate of a single-electron oscillator. However, if collisions are involved in the classical picture, the picture changes to a breaking of an infinite wave-train, which introduces a phase shift and results in a shifted Lorentzian with a collisional broadening parameter determining its HWHM (see A.3). If no collisions are involved Doppler broadening of the specific transition frequency ω_{12} may become the dominant effect and $g(\omega)$ is better described by a Gauss-profile. In the atmosphere both effects may play a role and the convolution of both of the latter profiles, leading to the so-called Voigt-profile, becomes the most appropriate line-shape to be used for $g(\omega)$.

One expects $\alpha(\omega)$ to be proportional to the number n_1 of atoms in level 1 (per unit volume) that the beam intercepts. The absorption cross-section $\sigma_a(\omega) \equiv \sigma(\omega)$ is then defined as

$$\alpha(\omega) = n_1 \sigma(\omega). \tag{A.4}$$

As long as there occurs no saturation of the populations of the energy levels and no saturation of the light beam (i. e. as long as the light is not too intense and the atomic density not too large), $\sigma(\omega)$ will be proportional to $g(\omega)$:

$$\sigma(\omega) = \sigma_0 g(\omega). \tag{A.5}$$

Here, σ_0 is a very important frequency-integrated quantity which fully characterizes the transition and is therefore the ideal quantity to be stored in molecular databases. We will come back to this aspect in section A.3. We call

$$\sigma_0 = \int_{-\infty}^{\infty} \sigma(\omega) d\omega, \tag{A.6}$$

the **line intensity** with units of area $\times$ angular frequency.

A.1.2   Einstein Coefficients

The total rate of spontaneous emission W_{21}^s from an upper level 2 to a lower level 1 and for N_2 atoms in the upper level is defined in terms of

$$W_{21}^s = A_{21} N_2, \tag{A.7}$$

where A is Einstein coefficient for spontaneous emission. A_{21} must be the reciprocal of the spontaneous radiative lifetime τ^s of level 2, with

$$\tau_{21}^s = 1 / \sum_i A_{2i}, \tag{A.8}$$

if level 2 can decay by radiative emission only, where level 1 may consist out of i sublevels.

The Einstein B coefficients are defined by

$$W_{12}^i = B_{12}^\omega \rho_\omega N_1 \tag{A.9}$$

$$W_{21}^i = B_{21}^\omega \rho_\omega N_2, \tag{A.10}$$

where ρ_ω is the energy density per unit angular frequency interval in a region containing N_2 atoms in the upper level and N_1 in the lower and W are the transition rates for induced absorption W_{12}^i and induced emission W_{21}^i.

Here it is important to note that ρ_ω is assumed to be constant over the region of significant absorption indicated by the sub- and superscripts ω.

In general one can show, that

$$B_{21}^\omega = \frac{\pi^2 c^3}{\hbar \omega_{21}^3} A_{21} \tag{A.11}$$

and

$$B_{12}^\omega = \frac{g_2}{g_1} B_{21}^\omega, \tag{A.12}$$

where ω_{21} is again the resonance frequency of the transition and g_1 and g_2 are the degeneracy factors of the levels. It is very important to realize that a different relation between A and B coefficients is found if some other measure of the radiation energy (for example, per wavenumber or per frequency f) is used (see *Hilborn*, [1982], for some examples). For example, for the HITRAN 96 molecular parameter database [*Rothman et al.*, 1998], the energy field is given in units of wavenumber.

A.1.3   Relationship Between the Einstein Coefficients and the Absorption Cross-Section

The problem to relate the Einstein B coefficients to cross-sections lies in the analysis of the behavior of nearly monochromatic, directed light beams. Both, the directional and the monochromatic character of the energy field, previously assumed to be constant over the region of significant absorption, have to be explicitly taken into account.

The monochromatic energy field

Hilborn, [2000], considers first the case of a monochromatic but still isotropic field with an induced absorption rate of

$$w_{12}^i(\omega)d\omega = b_{12}(\omega)N_1\rho(\omega)d\omega, \tag{A.13}$$

where $\rho(\omega)$ is the energy per unit volume and unit angular frequency in the range between ω and $\omega + d\omega$. We then find a connection between $b_{12}(\omega)$ and B_{12}^ω by

$$
\begin{aligned}
W_{12}^i &= \int_{-\infty}^{\infty} w_{12}^i(\omega)d\omega = \int_{-\infty}^{\infty} b_{12}(\omega)N_1\rho(\omega)d\omega \\
&= \rho_\omega N_1 \int_{-\infty}^{\infty} b_{12}(\omega)d\omega = \rho_\omega N_1 B_{12}^\omega,
\end{aligned} \tag{A.14}
$$

where ρ_ω is the integrated field over frequency range and the atomic frequency response may be written explicitly by

$$b_{12}(\omega) = B_{12}^\omega g(\omega). \tag{A.15}$$

The directional case

We now consider the directional light transmission case. The transition rate will be the same as long as the directional field produces the same energy density at the location of the atom as does the isotropic field. For a nearly monochromatic beam, the specific intensity $i(\omega)$ can be expressed in terms of the energy density by

$$i(\omega) = c\rho(\omega). \tag{A.16}$$

Within the angular frequency range ω to $\omega + d\omega$ we may then define the absorption rate due to radiation by

$$w^i_{12}(\omega)d\omega = N_1 b_{12}(\omega)i(\omega)d\omega/c. \tag{A.17}$$

For a beam $\rho(\omega)$ with cross-sectional area F the power absorbed within ω to $\omega + d\omega$ is

$$P = F\hbar\omega_{12} \times w^i_{12}(\omega)d\omega = \hbar\omega_{12}\rho(\omega)B^\omega_{12}g(\omega)N_1 F d\omega, \tag{A.18}$$

and the power loss from a beam over the distance Δx is

$$\Delta P = -\hbar\omega_{12}\rho(\omega)B^\omega_{12}g(\omega)n_1 F d\omega \Delta x, \tag{A.19}$$

where n_1 is the number of atoms per unit volume in level 1. By making the transition of

$$\frac{\Delta P}{F d\omega \Delta x} \rightarrow \frac{di}{dx}, \tag{A.20}$$

we find, utilizing the previous equations and Eq. (A.16), that

$$\frac{1}{i(\omega)}\frac{di(\omega)}{dx} = -\hbar\omega_{12}n_1 B^\omega_{12}g(\omega)/c. \tag{A.21}$$

Now, we may establish a relation between the Einstein B coefficient and the absorption cross-section (A.1 and A.4) by

$$\sigma(\omega) = \hbar\omega B^\omega_{12}g(\omega)/c. \tag{A.22}$$

Finally we may write the cross-section in terms of the A coefficient using the relation in (A.11) by

$$\sigma(\omega) = \frac{g_2}{g_1}\frac{\pi^2 c^2}{\omega^2}g(\omega)A_{21}. \tag{A.23}$$

It is very important to note that we get a relation between line intensity σ_o and Einstein coefficients only if we assume that $g(\omega)$ is sharply peaked at ω_{12} and therefore may replace ω by ω_{21} when carrying out the integration over angular frequency. (Note, that here the width of $g(\omega)$ is solely determined by the radiative lifetime of the state (A.8) and not by other effects like pre-dissociation or collisions as will be discussed in section A.3.) Under this assumption we get

$$\sigma_0 \quad = \quad \hbar\omega_{12}B_{12}^{\omega}/c \tag{A.24}$$

$$\sigma_0 \quad = \quad \frac{\pi^2 c^2}{\omega_{21}^2}\frac{g_2}{g_1}A_{21}. \tag{A.25}$$

A.1.4   Line Strength and Transition Dipole Moment

The quantum electrodynamic treatment of spontaneous emission shows that,

$$A_{21} = \frac{2e^2\omega_{21}^3}{3\varepsilon_0 hc^3}\sum_{m_1}|\langle lm_1|\vec{r}|2m_2\rangle|^2. \tag{A.26}$$

Here, A_{21} defines a transition from the sublevel m_2 of the upper level 2 to all possible m_1 sublevels of the lower level 1, where $\vec{r}$ is the sum of the electrons' position. The square of the transition moment μ_{21} is now defined as

$$\mu_{21}^2 \equiv e^2 r_{21}^2 \equiv e^2 \sum_{m_1}|\langle lm_1|\vec{r}|2m_2\rangle|^2. \tag{A.27}$$

From this we find the relation

$$\mu_{21}^2 = A_{21}\frac{3\varepsilon_0 hc^3}{2\omega_{21}^3}. \tag{A.28}$$

The **line strength** of a specific transition is defined by the following expression, which is symmetric in the upper and lower state labels:

$$S_{21} = S_{12} \equiv e^2 \sum_{m_2}\sum_{m_1}|\langle lm_1|\vec{r}|2m_2\rangle|^2 = g_2\mu_{21}^2. \tag{A.29}$$

With this definition, finally, we may write the relation between A and S as

$$S_{21} = g_2\frac{3\varepsilon_0 hc^3}{2\omega_{21}^3}A_{21}. \tag{A.30}$$

The same definition of line strength can be used for ro-vibrational transitions (like for example those relevant for water vapor in the atmosphere), where the dipole moment is not the moment of the electronic transition but related to the permanent dipole moment of the charge distribution over the nuclei. From Eq. A.30 and Eq. A.24 we may write the relation between the **line strength** and the **line intensity** as

$$\sigma_o = \frac{2\pi^2\omega_{21}}{3\varepsilon_0 hcg_1}S_{21}. \tag{A.31}$$

A.1.5 f-values

The analogy between a two level atomic transition and the emission or absorption rate of a classical, single-electron oscillator with oscillation angular frequency ω_{21}, defines a **oscillator strength**, which is called the f-**value** of the transition. The emission oscillator strength is defined as

$$f_{21} = -\frac{1}{3}A_{21}/\gamma_{cl}, \tag{A.32}$$

where

$$\gamma_{cl} = \frac{e^2\omega_{21}^2}{6\pi\varepsilon_0 mc^3}, \tag{A.33}$$

is the classical, radiative decay rate of the single-electron oscillator. Here, m is the mass of the electron. The absorption oscillator strength f_{12} is defined as

$$f_{12} = -\frac{g_2}{g_1}f_{21}. \tag{A.34}$$

Tabulated f values are usually given for specific degeneracy cases, where the angular momentum J_2 of the upper state is 1 and therefore $g_2=3$ and for the lower state $J=0$ and $g_1=1$. In addition, when the Einstein coefficient A_{21} equals the classical decay rate $(A_{21} = \gamma_{cl})$ f_g values are tabulated with

$$f_g \equiv f_{12} \equiv -3f_{21}. \tag{A.35}$$

Using Eq. (A.32) and (A.33) we obtain

$$f_{12} = \frac{g_2}{g_1}\frac{2\pi\varepsilon_0 mc^3}{\omega_{21}^2 e^2}A_{21}, \tag{A.36}$$

which we then can compare to Eq. (A.23) resulting in a relation between the f_g value and the cross-section for the specific case of tabulated $f_g = f_{12}$:

$$\sigma_{cl} = \frac{\pi e^2}{2\varepsilon_0 mc}f_g g(\omega). \tag{A.37}$$

For $f_g=1$ we arrive at the absorption cross-section of a stationary, classical oscillator.

A.2   Line Intensity and Line Shapes for Radiative Transfer and HITRAN '96 Definitions

A.2.1   Line Intensity and Temperature Dependence

Assuming local thermodynamic equilibrium (LTE) the relative population between individual states N_1, N_2 of a molecule at the ambient temperature T is governed by Boltzmann statistics, viz,

Table A.1: Units for some of the most important quantities used in this appendix

Quantity	Unit
A_{21}	s^{-1}
B_{21}, B_{12}	cm^2
Line intensity σ_o	$cm^2 s^{-1}$
Line intensity $S(T)$	$cm^2 s^{-1} molec^{-1}$
Line strength S_{21}, S_{12}	$C^2 cm^2$
Line-shape function $g(\omega)$	s

$$\frac{g_1 N_2}{g_2 N_1} = \exp\left(-\frac{\hbar \omega_{12}}{k_B T}\right) \tag{A.38}$$

and

$$\frac{N_1}{N} = \frac{g_1 \exp\left(-\frac{E_1}{k_B T}\right)}{Q(T)}, \tag{A.39}$$

where N is the total molecular density, E_1 is the energy of the lower state and $Q(T)$ is the total internal partition sum over all states i of the molecule, or over all degenerated states m with g_m being the degeneracy of state m:

$$Q(T) = \sum_i \exp\left(-\frac{E_i}{k_B T}\right) = g_m \sum_m \exp\left(-\frac{E_m}{k_B T}\right). \tag{A.40}$$

Let us now define a spectral line intensity S in units cm^2/molec $\times$ angular frequency at a specific reference temperature $S(T_{ref})$ relevant for usage in radiative transfer theory [*Penner*, 1959], which takes the total molecular density N and the population difference between the lower and the upper state of a ro-vibrational system into account. The latter statistically weights the contribution of the single-transition line intensity σ_o of an single molecule to the spectral line intensity of all N molecules by

$$S_{12}(T_{ref}) = \sigma_o \frac{1}{N}\left(N_1(T_{ref}) - \frac{g_1}{g_2} N_2(T_{ref})\right) \equiv \sigma_o \Omega(T_{ref}), \tag{A.41}$$

where $\Omega(T)$ is the weighted difference in the population, and, therefore, at all temperatures T,

$$S_{12}(T) = \sigma_o \Omega(T) = S(T_{ref}) \frac{\Omega(T)}{\Omega(T_{ref})}. \tag{A.42}$$

Finally, using Eq. A.38 and A.39, we get

$$S_{12}(T) = S_{12}(T_{ref}) \frac{Q(T_{ref})}{Q(T)} \frac{\exp\left(-\frac{E_i}{k_B T}\right)}{\exp\left(-\frac{E_i}{k_B T_{ref}}\right)} \frac{\left[1 - \exp\left(-\frac{\hbar \omega_{12}}{k_B T}\right)\right]}{\left[1 - \exp\left(-\frac{\hbar \omega_{12}}{k_B T_{ref}}\right)\right]}, \tag{A.43}$$

for which $S_{12}(T_{ref})$ is tabulated in the HITRAN database [*Rothman et al.*, 1998] (but, there, in units cm^{-1}/molec $\times\ cm^2$) together with the lower state energy E_1 of the individual transitions. One problematic point in calculating S_{12} for a specific temperature T from the database values is the calculation of the total internal partition sum Q, because, often, not all internal energy states are known. In addition, also the values for the lower state energy are not known for all the transitions tabulated in HITRAN, because, in contrast to $S_{12}(T_{ref})$, which can be derived from measurements, the lower state energy has to be derived from theory by identifying the measured transitions with specific ro-vibrational quantum states. *Rothman et al.*, [1998], therefore suggest the usage of a parameterization by *Gamache et al.*, [1990], with

$$Q(T) = a + bT + cT^2 + dT^3, \tag{A.44}$$

where the parameters a to d are tabulated and have been obtained from exponential sum fitting between this third order polynomial and all known lower state energy values. Errors for most of the HITRAN tabulated molecules, including water vapor, are reported to be smaller than 1% for temperature ranges between 70 and 3000K [*Rothman et al.*, 1998]. Up to now we defined the relationship between the phenomenological absorption cross-section $\sigma(\omega)$, the line intensity of a two-states transition σ_o and a temperature dependent line intensity relevant for atmospheric absorptions $S(T)$ with the basic quantum electrodynamic parameters, as there are the dipole-moment, the line strength and the f values. To close the picture, and in order to calculate a realization of the cross-section as defined in Eq. A.5 for a specific atmospheric situation, i. e. for a specific pressure and temperature, the usage of an adequate line-shape function $g(\omega, p, T)$ is discussed briefly in the next section.

A.3   Lorentz Line Shapes and Collisional Broadening

Generally, the subject of line shapes and collisional broadening of atomic and molecular spectral lines is a complex field. It has been comprehensively reviewed by *Allard & Kielkopf*, [1982].

As mentioned at the beginning of the last section, one has to separate the effect of

(I) the natural HWHM γ of a line, which is classically given by the decay rate of the single-electron oscillator at angular frequency ω_{21} by Eq. (A.33) and is more generally given by the Einstein A coefficients (Eq. A.8) (with FWHM=2γ=A_{21}).

(II) the effect of pre-dissociation, where crossing of a repulsive state with the excited state causes the molecule to dissociate at a specific rate, once excited, and which, therefore, causes the broadening of the width of the transition.

(III) the collision introduced shortening of the lifetime of the excited state and a frequency shift σ_c caused by the breaking of an infinite wave-train and the introduction of a phase shift due to the latter [*Lenz*, 1924; *Weisskopf*, 1933]. All three effects contribute to the width γ of the transition, which line-shape can be described using a Lorentzian function [*Allard & Kielkopf*, 1982], with

$$g(\omega) = \frac{1}{2\pi^2} \frac{\gamma}{(\omega - \omega_0 - \sigma_c)^2 + (\gamma)^2}. \tag{A.45}$$

Note, that the normalization here is $1/(2\pi^2)$ and becomes the, maybe more familiar, $1/\pi$ when we change units from angular frequency to frequency or wavenumbers.

In the remainder of this section we want focus on the effect of line broadening by collision, which is the dominant line broadening effect in the atmosphere. It is an effect entirely due to elastic collisions, because the effect of inelastic collisions would appear usually at frequencies far from the line center [*Omont*, 1972].

The collisional line broadening coefficient γ can be seen as the inverse of the mean time between two collision events [*Lenz*, 1924; *Weisskopf*, 1933]. It is generally proportional to the density of the molecules or atoms, their mean velocity and therefore to the pressure. Further is it dependent on an impact parameter, which is related to the smallest distance between collisional partner and emitter gained during the collision, and to the perturbation potential [*Allard & Kielkopf*, 1982] between the collisional partners. The detailed analytical formulae are quite complex and, usually, the values for the collisional partners of the molecule or atom are tabulated. For example, the HITRAN '96 database gives a relation between the tabulated collision parameter values in HITRAN '96 and γ for collisions in air and for collisions with the same species of molecules by

$$\gamma = \left(\frac{T_0}{T}\right)^{\tilde{n}} (\gamma_{air}(p - p_s) + \gamma_{self}p_s), \tag{A.46}$$

where γ_{air} and γ_{self} are the collisional parameters for air- and self-broadening in units of angular frequency per reference pressure, respectively, T_0 is a reference temperature, p and p_s are atmospheric and partial pressure, respectively, and $\tilde{n}$ is the temperature scaling parameter. All of the latter, except for the pressure values, are tabulated in the HITRAN database [*Rothman et al.*, 1998]. Usually the database values for γ_{air}, γ_{self} and $\tilde{n}$ are a mixture of experimental and theoretical values. For example, for water vapor, a small database of measured parameters was established and sorted as a function of the rotational transition quantum numbers, where the vibrational dependence was ignored. For the same rotational transitions with different measurement results, averaged values are calculated and finally scaled to transitions for which no measurements are taken (for details see *Rothman et al.*, [1998], and references therein). Note, that for atmospheric situations the self-broadening parameter is only relevant for N_2 and O_2. For water vapor being the fourth most abundant gas in the atmosphere the self-broadening contribution is already below 1% for the highest total water vapor columns and may therefore be neglected. This is important for retrievals, because otherwise the cross-section would become implicitly density dependent.

Bibliography

Allard, N., and J. Kielkopf, The effect of neutral nonresonant collisions on atomic spectral lines, *Rev. Modern Phys., 54*, 4, 1103-1182, 1982.

Gamache, R. R., R. L. Hawkins, and L. S. Rothman, Total internal partition sums in the temperature range 70-3000K: atmospheric linear molecules, *J. Mol. Spectrosc., 142*, 205-219, 1990.

Hilborn, R. C., Einstein coefficients, cross-sections, f-values, dipole moments and all that, *Am. J. Phys., 50*, 982-986, 1982.

Lenz, W., Einige korrespondenzmäßige Betrachtungen, *Z. Phys., 25*, 299-311, 1924.

Omont, A., E. W. Smith, and J. Cooper, 1973, Redistribution of resonance radiation. I. The effect of collisions, *Astrophys. J., 175*, 1, 185-199, 1972.

Penner, S. S., Quantitative Molecular Spectroscopy and Gas Emissivities, *Addison-Wesley*, Reading, MA, 1959.

Rothman, L. S., C. P. Rinsland, A. Goldman, S. T. Massie, D. P. Edwards, J.-M. Flaud, A. Perrin, C. Camy-Peyret, V. Dana, J.-Y. Mandin, J. Schroeder, A. McCann, R. R. Gamache, R. B. Wattson, K. Yoshino, K. V. Chance, K. W. Jucks, L. R. Brown, V. Nemtchino, and P. Varanasi, The HITRAN Molecular Spectroscopic Database and HAWKS (HITRAN Atmospheric Workstation): 1996 Edition, *J. Quant. Spect. & Rad. Transfer, 60,* 665-710, 1998.

Weisskopf, V., Die Breite der Spektrallinien in Gasen, *Z. Phys., 34*, 1-23, 1933.

Appendix B

Riemann Sum and Discretized Probability Density Function

A general smooth function f may be integrated over a range $x_i < x < x_f$

$$I = \int_{x_i}^{x_f} f(x)dx \tag{B.1}$$

Here the values of f cover the domain $y_i < f(x) < y_f$ for all $x \in [x_i, x_f]$. First, we split the integral (B.3) into M subintervals

$$\int_{x_i}^{x_f} f(x)dx = \sum_{j=1}^{M} \int_{x_j}^{x_j+1} f(x)dx \tag{B.2}$$

so that f is monotonic within the intervals $[x_j, x_{j+1}]$. Here, $x_1 = x_i$ and $x_M = x_f$. Per interval the inverse f^{-1} exists and the interval may transform to

$$\int_{x_j}^{x_j+1} f(x)dx = \int_{y_j}^{y_j+1} yg'(y)dy \tag{B.3}$$

with $g'(y) = df^{-1}/dy$. With the 'window' function W_j with

$$W_j(y) = \begin{cases} 1 & \text{for } y_j < y < y_{j+1} \\ 0 & \text{else} \end{cases} \tag{B.4}$$

we can rewrite the integral (B.3) in the form

$$I = \int_{y_i}^{y_f} y\alpha(y)dy \tag{B.5}$$

with the probability density function (pdf)

$$\alpha(y) = \sum_{j=1}^{M} g'(y)W_j(y) \tag{B.6}$$

which describes the frequency distribution of values of f in the domain $[y_i, y_f]$. Here, the pdf is normalized to

$$\int_{y_i}^{y_f} \alpha(y)dy = x_f - x_i . \tag{B.7}$$

The OCM formalism lends itself to the following special properties of ordered sums:

Lemma 1:

For a function $f(x, y)$ integrated over x the coefficients α_i of the Riemann sum (2.12) are itself function of y,

$$\int_{x_1}^{x_2} f(x, y)dx \approx \sum_{i=1}^{B} \alpha_i(y)f_i\delta x \tag{B.8}$$

where we neglect the residuum ϵ of the Riemann sum. Furthermore, for the integral mapping of $f(x, y)$ to a function $I_f(x)$ by

$$I_f(x) = \int_{y_1}^{y_2} k(y)f(x, y)dy \ , \tag{B.9}$$

where the integral kernel k can be any integrable function, a corresponding integration of $I_f(x)$ may be approximated by

$$\int_{x_1}^{x_2} I_f(x)dx \approx \sum_{i=1}^{B} I_{\alpha_i}f_i\delta x \tag{B.10}$$

with

$$I_{\alpha_i} = \int_{y_1}^{y_2} k(y)\alpha_i(y)dy \ . \tag{B.11}$$

Thus, the Riemann sum of the integral function f can be mapped in a straight forward manner to the Riemann sum of function $I_f(x)$ regarding the same binning set $\mathcal{R}_f$.

Lemma 2:

For a function f, binned in terms of an ordered set $\mathcal{R}$, and a monotonic, single-valued function h, the Riemann sum of the integral of $h \circ f$ has the same coefficients as (2.12), providing that $h \circ f$ is binned in terms of the ordered set

$$\mathcal{H} = \{h(f_i), i = 1, \ldots, B\} \ . \tag{B.12}$$

In other words,

$$\mathrm{dpdf}[f, \mathcal{R}] = \mathrm{dpdf}[h \circ f, \mathcal{H}] \ . \tag{B.13}$$

Appendix C

Analytical Malkmus Band Model Representations of "Pseudo-Absorption" Functions

This appendix shows examples of the usage of band models for the calculation of analytical "pseudo-absorption" functions. These functions are used to calculate average transmittances with the correlated k-distribution method. It will be shown that such analytically described "pseudo-absorption" functions (paf) can be discretized very accurately but give worse results for the calculation of average transmittance when compared to the usage of numerical realizations of paf. However, numerical realizations of paf carry the numerical errors of the cross-section histogram sampling. Improving the discretization, i.e. increasing the number of quadrature points, can not compensate for these numerical errors (c.f. chapter 2, Figure 2.8, mid panel) as will be shown in this appendix. As a consequence, the usage of more than 15 quadrature points for the ck-distribution method using Gauss-Legendre quadrature does not improve the accuracy of the spectral sampled transmittance with respect to lbl calculations.

Lacis & Oinas, [1991], use an inverse Laplace transformation [*Domoto*, 1974] of the Malkmus band model [*Malkmus*, 1967] representation of the transmittance $T(n)$ (chapter 1, Eq. 1.7), which is sometimes referred to as the inverse transmission, in order to represent the probability density function (pdf) $f(\sigma \equiv k)$ (chapter 1, Eq. 1.16 and 1.20; appendix B) by

$$\bar{f}(k) = \frac{1}{2} k^{-\frac{3}{2}} (BS)^{\frac{1}{2}} \exp\left[\frac{\pi B}{4}\left(2 - \frac{S}{k} - \frac{k}{S}\right)\right], \tag{C.1}$$

where $\bar{f}(k)$ is the normalized pdf, B is the effective line halfwidth, and S is the effective line strength as defined for chapter 1, Eq. 1.7. Calculating the cumulative density distribution function $g(k)$ (chapter 1, Eq. 1.17) via

$$g(k) = \int_0^k \bar{f}(k) dk, \tag{C.2}$$

using Eq. C.1, results in

$$g(k)_{\text{Malk}} = \frac{1}{2}\left[1 - \text{erf}\left(\frac{a}{\sqrt{k}} - b\sqrt{k}\right)\right] + \frac{1}{2}\left[1 - \text{erf}\left(\frac{a}{\sqrt{k}} + b\sqrt{k}\right)\right] e^{\pi B}, \tag{C.3}$$

where $a = \frac{1}{2}(\pi BS)^{\frac{1}{2}}, b = \frac{1}{2}(\pi B/S)^{\frac{1}{2}}$, and where $\text{erf}(z)$ is the error function

$$\mathrm{erf(z)} = \frac{2}{\sqrt{\pi}} \int_0^{\mathrm{z}} \mathrm{e}^{-\mathrm{t}^2} \mathrm{dt}. \tag{C.4}$$

Finally, the inverse of Eq.C.3

$$k^{\mathrm{Malk}}(g) = g_{\mathrm{Malk}}^{-1}(k), \tag{C.5}$$

may be used in the basic equation of the (correlated) k-distribution method (chapter 1, Eq. 1.19 and 1.20; chapter 2, Eq. 2.50).

In the remainder we want to answer the question how well the following approximations represent the lbl calculated transmittance $T(n)$ and how well the discretized models represent their integral form. In order to do so we use once an analytical Malkmus band-model representation of the paf $k(g, z)$ (Eq. C.3) and once its numerical histogram representation (chapter 1, Eq. 1.22 and appendix B):

$$T(n) = \int_{\Delta\lambda} \exp\left[-\int_z k(z)n(z)dz\right] \frac{d\lambda}{\Delta\lambda} \tag{C.6}$$

$$\approx \int_0^1 \exp\left[-\int_z k^{\mathrm{Malk,num}}(g, z)n(z)dz\right] dg \tag{C.7}$$

$$\approx \sum_{j=1}^G a_j \exp\left[-\int_z k^{\mathrm{Malk,num}}(g_j, z)n(z)\right]. \tag{C.8}$$

Calculations of the three terms have been performed for the same high-resolution cross-section realizations as shown in Figure 6, chapter 2. Figure C.1a shows $k(g, z)$ paf for all five altitude levels using the Malkmus band-model representation and the numerical representation. The results show that the overall shape of the numerical representations is resembled well by the Malkmus functions. However, Malkmus representation of $k(g, z)$ systematically underestimate the numerical representation of $k(g, z)$. Because of the direct usage of high-resolution realizations of cross-sections at different altitude levels z, $k^{\mathrm{num}}(g, z)$ is supposed to give a more realistic representation of $k(g, z)$ within $\Delta\lambda$. Note, that $k^{\mathrm{num}}(g, z)$ exhibits some fine structure not present for $k^{\mathrm{Malk}}(g, z)$ around 0.8 and increases very sharply very close to 1 (not visible in Figure C.1a; cf. Figure 2.9, chapter 2). Both of the latter give rise to difficulties in the discretization of $k^{\mathrm{num}}(g, z)$ (chapter 1, section 1.5.1, chapter 2, section 2.3). In contrast, $k^{\mathrm{Malk}}(g, z)$ is smooth over the whole range between 0 and 1 (Figure C.1b) and, thus, easier to discretize.

Figure C.2 shows results for a comparison of the three terms C.6, C.7, C.8 for both $k(g, z)$ representations in dependence of the amount of quadrature points used. Panel (a) shows a direct comparison between the discretized ck-distribution representations (C.7) using both $k^{\mathrm{Malk,num}}(g, z)$ representations and the lbl result (C.6). The relative differences are shown in panel (b). Clearly, The Malkmus band-model representation systematically underestimates the real transmittance by about 0.1 % for nearly all numbers of quadrature values. *Lacis & Oinas*, [1991], also report worse result for the calculated transmittance when using the Malkmus representation compared to using the numerical representation of $k(g, z)$. They report accuracies of 10 to 20% with respect to lbl calculations using an
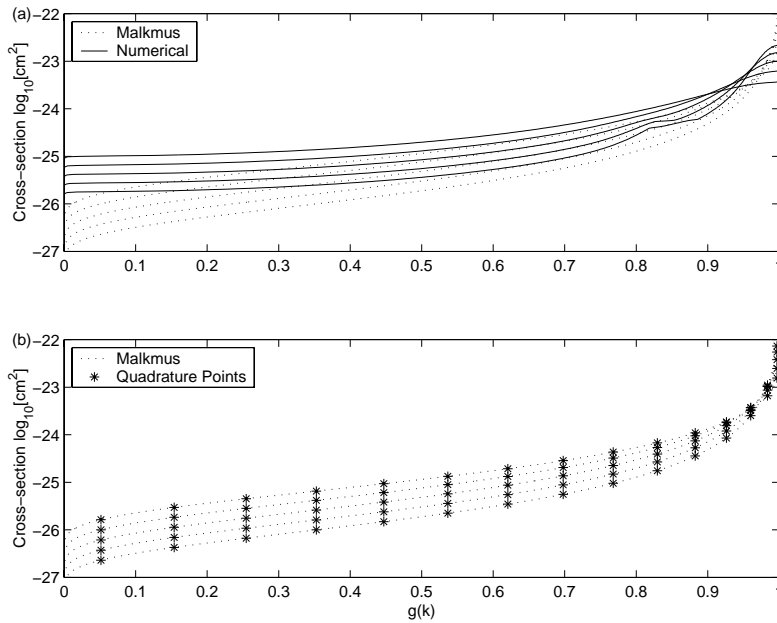
Figure C.1: (a) Analytical Malkmus band model (dotted lines) and numerical histogram (solid lines) representation of $k(g, z)$, for five altitude level z, where the used high resolution cross-section realizations are the same as shown in Figure 6 in chapter 2. (b) $k^{\text{Malk}}(g, z)$ is discretized (filled circles) at 15 zero point values of Legendre polynomials (chapter 2, section 2.3.1) with corresponding weights a_j (chapter 2, Eq. 2.49).

uncorrected Malkmus band-model approach for spectral regions broader than 5 cm^{-1} and tropospheric nongray absorptions (cf. chapter 2, section 2.3.3.2). Panel (c) shows the relative difference between the transmittances calculated for the integral and the discretized representation of the ck-distribution method (C.7 and C.8) using, again, both representations $k^{\text{Malk,num}}(g, z)$. Whereas the relative differences monotonically decreases for the Malkmus representations, the relative difference stays constant in case of the numerical representations above about 15 quadrature points. We refer the latter to the fact that the numerical noise introduced using a window function as given by Eq. 1.22 in chapter 1 and Eq. B.4 in appendix B followed by an inversion of the corresponding, smooth cumulative density function, can not be compensated for by increasing the amount of quadrature points. This is the reason why the results of ck-distribution sampling of transmittances using numerical realizations of paf can not be improved much by increasing the amount of quadrature points above a certain level.
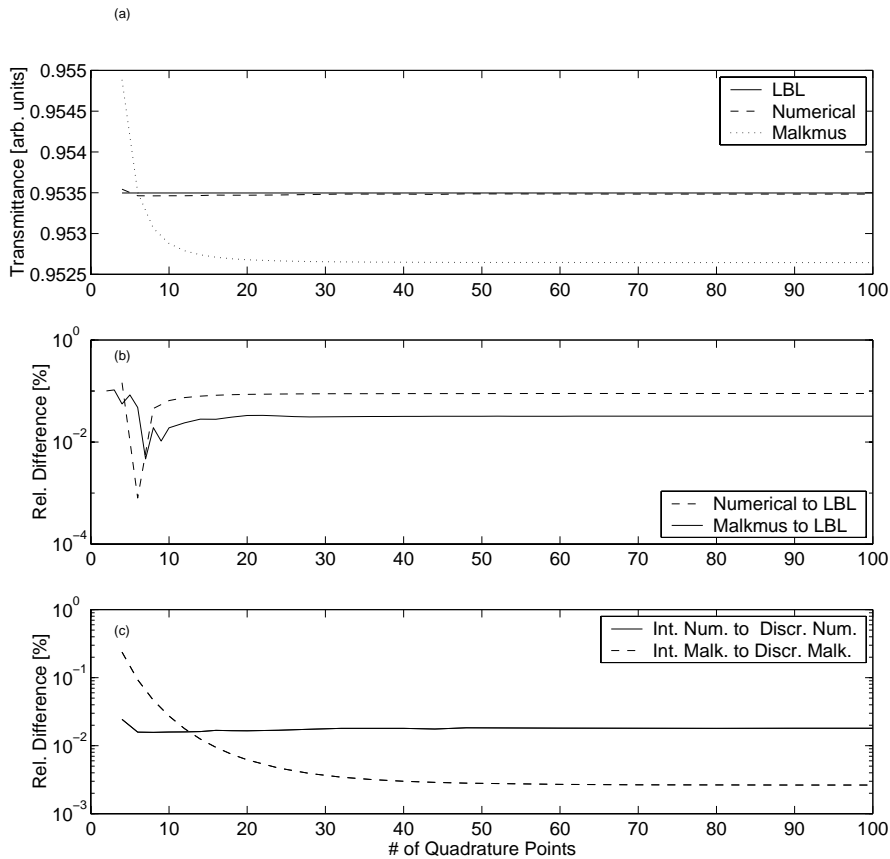
Figure C.2: Panel (a) shows results of two calculations of the discretized *ck*-distribution expression C.8 once using the Malkmus band-model approach and once using the numerical histogram approach. The results are compared to the lbl result calculated using C.6. Panel (b) shows the relative difference between the results for the *ck*-distribution expression and the lbl results. Panel (c) shows the relative difference between C.7 and C.8.

Bibliography

Domoto, G. A., Frequency integration for radiative transfer problems involving homogeneous non-gray cases: The inverse transmission function, *J. Quant. Spect. & Rad. Transfer, 14*, 935-942, 1974.

Lacis, A. A., and V. Oinas, A description of the correlated *k* distribution method for modeling nongray gaseous absorption, thermal emission, and mutlitple scattering in vertically inhomogeneous atmospheres, *J. Geophys. Res., 96*, D5, 9027-9063, 1991.

Malkmus, W., Random Lorentz band model with exponential-tailed s^{-1} line-intensity distribution function, *J. Opt. Soc. Am., 57*, 323-329, 1967.

Appendix D

SSP Retrieval for Nonhomogeneous Atmospheres

Assumptions have been made for applying the basic SSP equations (chapter 4, Eq 4.3 and 4.5) to the retrieval over nonhomogeneous paths, where the density of the absorbers as well as the shape of the absorption lines changes over the path s. The basic idea behind SSP is that the absorbing fraction of a spectral sampling region may be represented by a block characterized by two parameters w and S (chapter 4, section 4.3). Within SSP always a fraction 1-w of the light coming through the spectral region with width $\Delta\lambda$ independent on the absorber amount. Due to the nature of atomic and molecular transitions SSP breaks down in the limit of very strong absorptions, for which, using realistic absorption line shapes, the averaged transmittance always goes to zero. For the reminder of this appendix this principal assumption of SSP is assumed to be valid.

Both parameters, w and S, as introduced in chapter 4, depend on pressure and temperature and, therefore, on the specific light path s. An integration over the path s for all photon-energies lying within the absorbing spectral region $\Delta\lambda$ may be used to represent the optical density over the path s, by utilizing the side constraint $\langle\sigma(\lambda,s)\rangle_{\Delta\lambda} = wS(s)$, with

$$\langle\tau(\lambda)\rangle_{\Delta\lambda} = w\int_s S(s)n(s)ds, \tag{D.1}$$

where w is kept fixed over the whole path and only S varies in order to fulfill the side constraint (from here on $\langle\sigma(\lambda,s)\rangle_{\Delta\lambda} \equiv \langle\sigma(s)\rangle_{\Delta\lambda}$ and $\langle\tau(\lambda)\rangle_{\Delta\lambda} \equiv \langle\tau\rangle_{\Delta\lambda}$ is used for simplification).

Under the principal SSP assumption of the block representation of the absorption within $\Delta\lambda$ the transmission may then be written as

$$\langle T\rangle_{\Delta\lambda} = 1 + w\exp\left(-\int_s S(s)n(s)ds\right) - w, \tag{D.2}$$

where w is the width of the block and $S(s)$ its height.

Note that, so far, for this derivation of the transmittance for nonhomogeneous paths, we have not attached any explicit physical properties to the parameters $S(s)$ and w. In order to do so the question arises, what is the best choice of w and $S(s)$ considering the physical nature of the problem, while still satisfying all constraints.

D.1   Dominant Layer Assumption

In most atmospheric cases the pressure monotonically decreases with altitude and the impact of temperature changes on the line parameters may considered to be weak with respect to the impact of changes in pressure (which is a reasonable assumption for absorbers which are not very well mixed, i.e. absorb only over a limited altitude region, up to the ionosphere, where very high temperature differences over small altitude regions start to have significant impact). A natural choice of the physical property of $w \equiv w(s)$ is $w(s)$ being the averaged line-width of all lines contained within the spectral sampling region. In this case, $w(s)$ decreases *monotonically* over altitude and $S(s)$ consequently increases *monotonically* as is shown in Figure D.1 for some typical values of atmospheric water vapor absorption (cf. chapter 5, Figure 5.2). This is because the average cross-section $\langle \sigma(s) \rangle_{\Delta\lambda}$ stays the same for all s when only pressure broadening effects are considered and the contribution of lines which are not fully contained within the spectral sampling region (basic SSP assumption) is also neglected. This physical behavior of $w(s)$ and $S(s)$ is also reflected in the analytical equations derived for $w(s)$ and $S(s)$ from a Taylor expansion to second order of the exponents in Eq. (5.1) and (5.2) in chapter 4, which reveals that

$$w(s) \approx \frac{\langle \sigma(s) \rangle_{\Delta\lambda}^2}{\langle \sigma(s)^2 \rangle_{\Delta\lambda}} \text{ and } S(s) \approx \frac{\langle \sigma(s)^2 \rangle_{\Delta\lambda}}{\langle \sigma(s) \rangle_{\Delta\lambda}} \ . \tag{D.3}$$

Under the assumption that pressure has the dominant impact on the cross-section, $\langle \sigma(s)^2 \rangle_{\Delta\lambda}$ monotonically increases with altitude, whereas $\langle \sigma(s) \rangle_{\Delta\lambda}^2$ stays constant, from which the monotonic decrease of the w-parameter follows. However, in this case, Eq. D.2 for nonhomogeneous atmospheres is not valid anymore, because, there, it was assumed that $w(s) \equiv w$ stays constant over all altitude. Now, the final question is, what is the best choice of a specific point $\bar{s}$ over the path s for which, due to reasons of efficiency, $w(s)$ can be calculated using Eq. D.3, but for which the transmittance can be calculated as in Eq. D.2 with $w \equiv w(\bar{s})$.

To answer this question the absorbance $\langle A \rangle_{\Delta\lambda} = 1 - \langle T \rangle_{\Delta\lambda}$ may be written as

$$\langle A \rangle_{\Delta\lambda} = w(\bar{z}) \left[\int_{z_1}^{z_2} S(z) n(z) \xi(s, z) dz \right] \ , \tag{D.4}$$

under expansion of the exponential function in Eq. D.2 to first order, where $\xi(s, z)$ is a transformation function from the path-coordinate s to the altitude-coordinate z. Now the atmosphere is divided in a number of layers ℓ and a fixed $w \equiv w_{\bar{\ell}}$ is chosen connected to a specific altitude layer $\bar{\ell}$, with $w_{\bar{\ell}} = w(\ell = \bar{\ell}) = \langle \sigma_{\bar{\ell}} \rangle_{\Delta\lambda} / S_{\bar{\ell}}$. The discretized absorption with respect to altitude can then be written as

$$\langle A \rangle_{\Delta\lambda} = \langle \sigma_{\bar{\ell}} \rangle_{\Delta\lambda} \left[\sum_{\ell} \frac{S(\ell)}{S_{\bar{\ell}}} N(\ell) \xi(s, \ell) \right] \ , \tag{D.5}$$

where $N(\ell)$ denotes the subcolumn density of the ℓth layer. A specific choice of $\bar{\ell}$ results in the following behavior of $S(\ell)/S_{\bar{\ell}}$, weighting the subcolumn densities of each altitude layer:
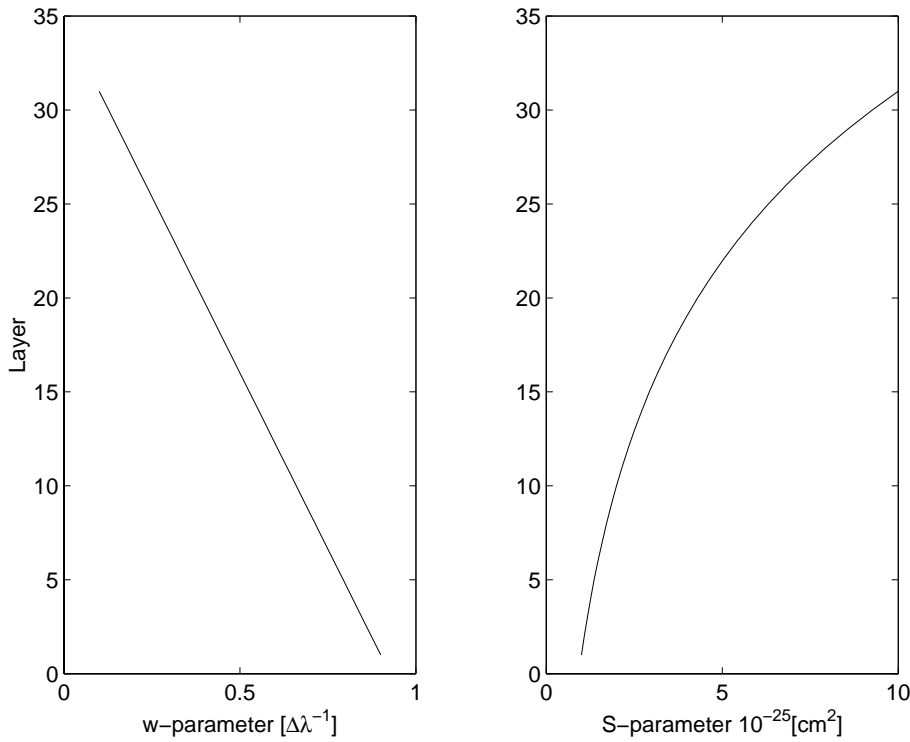
Figure D.1: Typical values for the $w(\ell)$ and $S(\ell)$ parameter (cf. chapter 5, Figure 5.2) for atmospheric water vapor absorption over a number of atmospheric layers with increasing altitude. The monotonically decreasing pressure over altitude dominates the altitude dependence of both parameters.

$$\frac{S(\ell)}{S_{\bar{\ell}}} \geq 1 \text{ for } \bar{\ell} \leq \ell$$
$$\frac{S(\ell)}{S_{\bar{\ell}}} \leq 1 \text{ for } \bar{\ell} \geq \ell. \tag{D.6}$$

From Eq. D.5 it becomes also clear that $S(\ell)/S_{\bar{\ell}}$ is basically a scaling factor of the subcolumn density, where $\langle \sigma_{\bar{\ell}} \rangle_{\Delta\lambda}$ carries the units of cross-section. From Eq. D.6 it can be followed that, providing the subcolumn profile of the absorber of interest does not have more than one maximum, the optimal choice of $\bar{\ell}$ is the layer with the expected maximum subcolumn density in order to leave the shape of the profile intact.

The left panels of Figure D.2 show two different artificial subcolumn profile, one with a maximum at the ground (a), representing, for example, an absorber like water vapor, and one with a maximum at some intermediate altitude layer (b, here the maximum subcolumn density is at layer number 16), which is the case for, for example, ozone. The

right panels show the reference absorbance by just multiplying the altitude-dependent $w(\ell)$ and $S(\ell)$ parameters as shown in Figure D.1 with the subcolumn density profile $N(\ell)$ at each layer (solid line). The dashed and the dotted lines show the result for the first order approximation of the absorbance as given by Eq. D.5 with a fixed $w_{\bar{\ell}}$ or $\langle\sigma_{\bar{\ell}}\rangle_{\Delta\lambda}/S_{\bar{\ell}}$ for $\bar{\ell} = 1$ and $\bar{\ell} = 16$, respectively. From this, the effect of $w_{\bar{\ell}}$ or $\langle\sigma_{\bar{\ell}}\rangle_{\Delta\lambda}/S_{\bar{\ell}}$ being bigger or smaller than 1 can clearly be seen. The profile above $\ell = \bar{\ell}$ is systematically overestimated, whereas the profile below $\ell = \bar{\ell}$ is systematically underestimated. Choosing an adequate $\bar{\ell}$ will lead to good results in the total column, even so the form of the profile might be disturbed. For example, when choosing layer 5 as the dominant layer in case (a) then, for this specific case, the systematic underestimation of the lower part of the profile is nearly compensated by a systematic overestimation of the upper part of the profile. In contrast, choosing layer 1 as the dominant layer leads to a systematic underestimation of the total column in a retrieval, due to the systematic overestimation of the total absorption. However, the latter choice leaves the principal shape of the profile intact, which is especially important when implementing single-scattering, where the shape of the profile determines the contribution of different scattering heights.
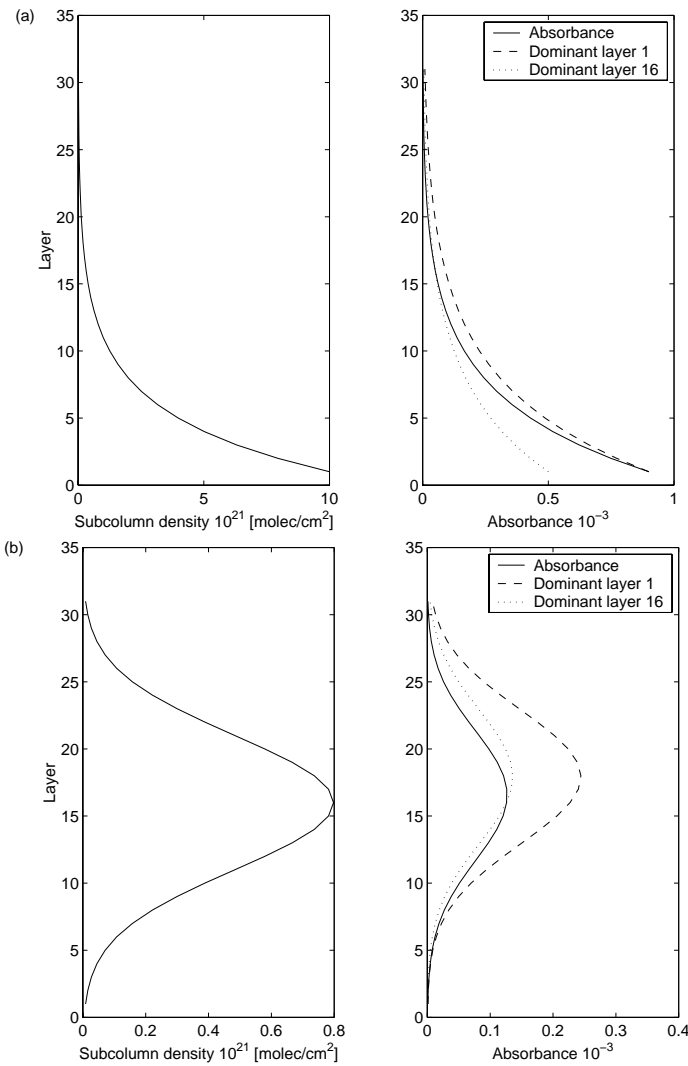
Figure D.2: The left panels show two exemplary subcolum profiles of atmospheric absorbers like, for example, water vapor (upper left panel) or ozone (lower left panel). The right panels show the reference absorbance (solid line) calculated from the altitude-dependent $w(\ell)$ and $S(\ell)$ parameter (Figure D.1) together with the subcolumn profile of the left panels. The right panels also show the absorbance but calculated using Eq. D.5 for a fixed $w_{\bar{\ell}}$ where $\bar{\ell} = 1$ (dashed line) and $\bar{\ell} = 16$ (dotted line).

List of Publications

Chapters in this Thesis

Chapter 2. Maurellis, A. N., R. Lang, and J. Landgraf, A New Determination of Extinction for Nongrey, Nonhomogeneous Atmospheres, *submitted*, 2002.

Chapter 3. Lang, R., A. N. Maurellis, W. J. van der Zande, I. Aben, J. Landgraf, and W. Ubachs, Forward modeling and retrieval of water vapor from GOME: Treatment of narrow band absorption spectra, *J. Geophys. Res.*, Vol. 107, in press, 2002.

Chapter 4. Maurellis, A. N., R. Lang, and W. J. van der Zande, A New DOAS Parameterization for Retrieval of Trace Gases with Highly-Structured Absorption Spectra, *Geophys. Res. Lett., 27*, 4069-4072, 2000.

Chapter 5. Lang, R., J. E. Williams, A.N. Maurellis, and W. J. van der Zande, Application of the Spectral Structure Parameterization Technique: Retrieval of Total Water Vapor Columns from GOME, *Atmos. Chem. Phys. Discuss., 2*, 1097-1130, 2002.

Other Publications

de Lange, A., R. Lang, W.J. van der Zande, W. Ubachs, Highly excited states of gerade symmetry in molecular nitrogen, *J. Chem. Phys., 116*, 18, 7893-7901, 2002.

Sneep, M., R. Lang, H. Nüss, and G. Moortgat, Important photochemical processes in the lower atmosphere, Chemical, Physical and Biogenic Processes in the Atmosphere, *International Research School for Cooperation on Oceanic, Atmospheric and Climate Change Studies*, Obernai, France, 2002.

Lang, R., S. van Dijk, P. Guyon, and F. Raes, Physical and chemical characteristics of aerosols: Observations and modeling, Chemical, Physical and Biogenic Processes in the Atmosphere, *International Research School for Cooperation on Oceanic, Atmospheric and Climate Change Studies*, Obernai, France, 2002.

Lang, R., Scientists and the mediation of facts, Chemical, Physical and Biogenic Processes in the Atmosphere, *International Research School for Cooperation on Oceanic, Atmospheric and Climate Change Studies*, Obernai, France, 2002.

Ubachs, W., R. Lang, I.Velchev, W.-Ü. L. Tchang-Brillet, A. Johansson, Z. S. Li, V. Lokhnygin, C.-G. Wahlström, Lifetime measurements on the c'$_4^1\Sigma_u^+$, v=0, 1 and 2 states of molecular nitrogen, *Chem. Phys., 270*, 215-225, 2001.

Maurellis, A. N., R. Lang, W. J. v. d. Zande, U. Ubachs, and I. Aben, Precipitable Water Column Retrieval from GOME Data, *Geophys. Res. Lett., 27*, 903-906, 2000.

Lang, R., A. N. Maurellis, W. J. van der Zande, I. Aben, P. Levelt, H. Naus, and W. Ubachs, DOAS-OCM Retrieval of Water Vapor from GOME and New CRD Spectroscopy, *Proc. ESA Symposium on Measurements from Space, 1,* 391-394, 1999.

Doornbos, R. M. P., R. Lang, M. C. Aalders, F. W. Cross, and H. J. C. M. Sterenborg, The determination of *in vivo* human tissue optical properties and absolute chromophore concentrations using spatially resolved steady-state diffuse reflectance spectroscopy, *Phys. Med. Biol.*, 44, 967-981, 1999.

Summary

The retrieval of atmospheric trace gas concentrations from space-borne spectral measurements of radiation reflected through the earth atmosphere requires computationally efficient sampling techniques in order to accurately model the spectral absorption and scattering signatures of the gases under study. Spectral sampling techniques connect laboratory measurements of molecular parameters like transition-line intensities, line width and line positions with spectral remote sensing measurements. Their task is to provide the best possible transfer of information between the well defined laboratory environment and the measured state of the atmosphere. They therefore establish an important link between laboratory and *in situ* atmospheric measurements which offers the possibility for validating one set of measurements by the other. Due to this tight link, both accurate sampling techniques as well as accurate spectral parameters measured in the laboratory are essential for the accurate retrieval of atmospheric trace gas concentrations from remote sensing measurements.

The modeling of water vapor absorption spectra, and retrieval of water vapor concentrations, serves as an excellent test for the performance of such spectral sampling techniques. The water vapor absorption spectrum is highly structured, i.e. the monochromatic absorption coefficient ranges over several orders of magnitude, and the widths of the absorption lines are often well below 1 wavenumber even for low altitudes, high pressure situations. Therefore, in spectral regions of water vapor absorption, the spectral dependence of the measured radiance is highly non-linear and requires sampling techniques dealing with the averaged exponent of the optical density over some spectral interval, instead of simply taking the arithmetic mean of the optical density directly. In addition, water vapor is not well mixed in the atmosphere, i.e. its density profile decreases by nearly three orders of magnitude over the first 10 kilometers. Therefore, the sampling technique has to account for changes in optical density over altitude, due to both changes in the density profile and changes of the monochromatic cross-section with respect to pressure and temperature.

The first applications of spectral sampling techniques for atmospheric modeling date back to the 1930s. Since then such techniques have been improved continuously, from the simple sampling of optical densities of a single homogeneous layer to the sampling of exponential functions of opacity over many different atmospheric layers. In the introduction to this theses (chapter 1) the commonly used correlated k-distribution sampling technique has been described in some detail and discussed with respect to how well it fulfills the aforementioned tasks. Problems in accuracy arise for the correlated k-distribution method for cases of strong inhomogeneity of the light path together with overlapping lines of significantly different strength. These problems have been briefly described in chapter 1.

In chapter 2 the Opacity Coefficient Method (OCM) has been introduced and derived from first principles, together with a detailed description of how OCM may be implemented in the equation of radiative transfer for nonhomogeneous multiple-scattering atmospheres. One of the principal benefits of both the OCM and the correlated k-

distribution method, with respect to a line-by-line spectral (integral) sampling, is that the basic spectroscopic parameters can be stored in an offline look-up table for a standard atmosphere and interpolated upon the specific scenario of the measurement case. Therefore, these methods are superior to line-by-line integral sampling with respect to computational efficiency. In addition, OCM is not based on any 'correlation assumption' and can therefore also be applied to highly structured absorbers over very nonhomogeneous paths. Chapter 2 also discusses some difficulties with the implementation of the correlated k-distribution method when dealing with spectral sampling intervals containing only a few absorption lines, as is the case for measurements of water vapor absorption in the visible and near infrared by high resolution satellite instruments such as GOME and SCIAMACHY. Also here OCM performs better than the correlated k-distribution method.

In chapter 3 the OCM spectral sampling technique has been applied to the retrieval of water vapor total column concentrations from GOME measurements. Here, a detailed study on how OCM can be applied to a specific measurement and radiative transfer scenario has been presented, where, in addition to the effect of water vapor on the measured spectra, all other absorbing and scattering atmospheric species within the spectral region of interest have to be taken into account. For this case study the weakest of the three water vapor absorption bands detectable by GOME, which is situated around 590 nm, has been exploited. A full treatment of singly scattered photons and a linear multiple-scattering approach have been used for which accuracies of the retrieved water vapor column (WVC) range between 1 and 4% for retrievals from synthetic GOME spectra and for which an upper error limit of 18% on the retrieved columns (for cloud-free GOME retrievals including the impact of aerosols) has been estimated. This study has been the first to report on water vapor total column retrieval from the 590 nm absorption band using GOME.

Whereas the OCM spectral sampling technique aims predominantly for high accuracies and wide ranges of applicability the spectral structure parameterization technique (SSP) introduced in chapter 4 predominantly aims at computational efficiency in order to make global water vapor column retrieval feasible. The basic concept of SSP is comparable to the concept of band models because of its use of spectrally averaged absorption line properties, as there are the effective line intensity and the effective line width. Similar to OCM, SSP uses look-up tables of standard atmospheres for these averaged parameters and establishes a direct link between the line parameters at a certain altitude and the gas concentration of the absorber of interest at the same altitude. Note, that due to the latter, for both sampling techniques subcolumn profiles are retrieved from which the total columns are calculated. This is a major difference to most other water vapor retrieval methods which usually retrieve total columns as a single parameter. Chapter 4 also shows retrievals of WVC from synthetic spectra, neglecting instrumental noise and systematic error contributions and assuming absorption of light travelling through a homogeneous layer only, can be performed with very high accuracy. The chapter also shows that the principal SSP parameters, the averaged line intensity and the averaged line width, may be used to gain some measure of the spectral structure of a specific absorber. This measure gives a handle on the question if a simple arithmetic mean may or may not be used for a specific absorber in order to calculate the spectrally averaged transmittance, and it defines the domain of applicability for non-linear sampling techniques like SSP and OCM.

In chapter 5 SSP has been applied for the real retrieval of WVC from GOME measurements. The step from synthetic retrievals from single homogeneous layers to multi layer real retrievals from light travelling through nonhomogeneous atmosphere includes the implementation of a SSP-sampled single-scattering contribution, as well as the modeling of all additional background absorbers within the spectral region of interest and the contribution Rayleigh scattering makes to the total extinction. In order to make use of altitude dependent averaged line parameters and, by this, account for the inhomogeneity of the light paths, a so-called dominant layer assumption has been developed and described in more detail in appendix D. This results in the retrieval of subcolumn water vapor profiles from GOME by SSP from which total WVC are calculated. As for the OCM retrievals performed in chapter 3, the weak 590 nm absorption band has been exploited. Results have been compared to results from ECMWF, SSM/I and OCM. A sensitivity study including the impact of aerosols revealed that the error on the retrieved WVC is expected to be smaller than 6% for clear sky cases and 19% for a maximum aerosol impact upon correction for a systematic bias, which has been referred to the dominant layer assumption.

As for the OCM retrievals from GOME measurements, the error on the retrieved WVC due to the presence of clouds can not be estimated. Comparisons to satellite retrievals from SSP which are not effected by clouds (SSM/I) show that cloud pixel fractions above 10% may result in both an underestimation or an overestimation of the WVC. This is because clouds may cause the photons to travel a longer or shorter path as expected by the model, depending on if they are multiply scattered inside the cloud or reflected directly at the cloud top, respectively. The effects of clouds on the WVC can, therefore, predominantly be related to cloud top height and cloud thickness but can not be accurately modeled at present.

Finally, chapter 6 gives an introduction on how to use both the OCM or SSP sampling techniques for the retrieval of water vapor profiles. In general, the problem of profile retrieval is a problem of regularizing an ill-posed problem, meaning that contributions such as the noise of the instrument and the retrieval method related bias cause some scatter in the retrieved profile, which may be filtered out by separating such noise and bias contributions from the real profile information content. The retrieval problems we have dealt with in this thesis are ill-posed because the number of retrieval parameters usually exceeds the number of independent pieces information on the physical parameters contained in the measurement and sustained by the retrieval method. In order to perform the specific regularization used for the purpose of profile retrieval in chapter 6, the maximum profile information content of the problem has been analyzed using a standard singular value decomposition scheme. From this it has been concluded that a maximum of 7 independent pieces of profile information can be retrieved from synthetic spectra using the OCM sampling technique depending on the amount of spectroscopic information used. The impact of the spectroscopy depends on the inclusion of additional water vapor absorption bands accessible by GOME, such as those around 640 and 720 nm, and, in addition, on the implementation of different water vapor line-parameter databases. In the final outlook section preliminary profile retrievals from GOME have been performed. From these it has been estimated that a maximum of 3 to 4 independent pieces of water vapor profile information can be expected from such retrievals.

Samenvatting

Het bepalen van atmosferische sporengasconcentraties met behulp van spectrale metingen vanuit de ruimte vereist efficinte numerieke technieken om de absorptie en de verstrooiingsignalen van de relevante gassen nauwkeurig te kunnen berekenen. Deze spectrale middelingtechnieken leggen een verband tussen moleculaire parameters gemeten in het laboratorium, zoals de sterkte, breedte en positie van moleculaire overgangen, en spectrale metingen vanaf grote afstand, zoals vanuit een satelliet. Hun functie is dus de informatieoverdracht tussen metingen uitgevoerd binnen een goed gedefinieerde laboratoriumomgeving en metingen van een bepaalde toestand van de atmosfeer. Numerieke spectrale middelingtechnieken scheppen dus een belangrijke verbinding tussen laboratoriumproeven en in situ-metingen waardoor de ene meting met behulp van de andere kan worden getest. Naast accurate metingen zijn ook accurate benaderingtechnieken noodzakelijk voor een nauwkeurige bepaling van atmosferische gasconcentraties met behulp van satellieten instrumenten.

Het berekenen van waterdampabsorptiespectra en het bepalen van waterdampconcentraties is een uitstekende test voor de werkwijze van de genoemde middelingtechnieken. Een waterdamp absorptiespectrum is sterk gestructureerd. Dit betekent dat de monochromatische absorptiecofficint over vele ordes van grootte varieert en dat de absorptielijnen vaak smaller zijn dan een golfgetal, ook op lage hoogte en dus bij relatief hoge atmosferische druk. Vandaar dat in spectrale gebieden van waterdampabsorptie de gemeten radiantie sterk niet-lineair is en niet de optische dikte maar de transmissie, de exponent van de optische dikte, gemiddeld moet worden. Bovendien is waterdamp in de atmosfeer niet ongelijkmatig verdeeld en slecht gemengd. Bijvoorbeeld de dichtheid van waterdamp daalt over bijna drie ordes van grootte over de eerste 10 kilometer. De numerieke methode moet rekening houden met veranderingen van de optische dikte zowel door veranderingen in het dichtheidprofiel van het gas als door variaties van de werkzame doorsnede door veranderingen in druk en temperatuur.

De eerste spectrale middelingtechnieken werden rond 1930 ontwikkeld. Sindsdien zijn deze technieken steeds verbeterd. Het begon met eenvoudige middelingen van de optische dikte van een enkele homogene laag maar het omvat heden ten dage het middelen van exponentile functies van optische dikten over vele, niet-homogene atmosferische lagen. In de inleiding van dit proefschrift wordt de op dit moment meest gebruikte k-distributie-techniek beschreven en uiteengezet in hoe verre deze techniek aan de beschreven eisen voldoet. Problemen bij het gebruik van de k-distributie-techniek doen zich vooral voor als deze aan fotonpaden over sterk niet-homogene lagen en voor overlappende absorptielijnen van sterk verschillende intensiteit wordt toegepast. Deze problemen komen in hoofdstuk 1 aan de orde.

Hoofdstuk 2 introduceert de grondslagen van de Optische Dikte Cofficinten Methode (OCM). Tegelijkertijd wordt uitgelegd hoe OCM in de straling transportvergelijking voor niet-homogene, meervoudig verstrooiende lagen kan worden gemplementeerd. Een van de belangrijke voordelen van OCM en de k-distributie-techniek boven het monochromatische berekenen van een spectrale middeling is dat de spectrale basisparameters in een offline-

tabel kunnen worden opgeslagen, van waaruit deze op een specifieke meetsituatie kunnen worden genterpoleerd. Deze methoden zijn, wat de numerieke efficintie betreft, daarom superieur aan een monochromatische middeling. Bovendien is OCM niet gebaseerd op een zogenaamde correlatieaanname en daardoor ook te gebruiken in het geval van sterk niet-homogene fotonpaden met hoge lijndichtheid en sterke variaties in de lijnintensiteit. Ook aan de orde komen in dit hoofdstuk de problemen die ontstaan bij het gebruik van de k-distributie-methode bij kleine spectrale intervallen met weinig absorptielijnen. Deze situatie doet zich voor bij metingen van waterdampabsorpties in het zichtbaar regime met behulp van hoogopgeloste metingen zoals van de satelliet instrumenten GOME en SCIAMACHY. Ook in dit geval werkt OCM beter dan de gecorreleerde k-distributie-methode.

In hoofdstuk 3 wordt de OCM-middelingtechniek gebruikt om waterdampkolommen met behulp van GOME-metingen te bepalen. In detail wordt uitgelegd hoe OCM voor een specifieke meet- en stralingtransportsituatie kan worden toegepast. Daarvoor moet ook met de effecten van alle andere absorbers en verstrooiers op de meting rekening worden gehouden. Voor deze pilotstudie is de zwakste van alle door GOME gemeten waterdampabsorptiebanden rond 590 nm gebruikt. Met behulp van een volledige simulatie van enkelvoudig verstrooide fotonen en een lineaire benadering van meervoudig verstrooide fotonen is een nauwkeurigheid tussen 1 en 4

De OCM spectrale middelingtechniek mikt op een grote precisie en zo breed mogelijke toepasbaarheid. Daarentegen concentreert de spectrale parametrisatietechniek (SSP), die in hoofdstuk 4 gentroduceerd wordt, zich op numerieke efficintie om een wereldomvattende bepaling van waterdampkolommen mogelijk te maken. Het basisprincipe van SSP is verglijkbaar met dat van bandmodellen in het gebruik van gemiddelde lijnparameters zoals de intensiteit en de breedte van absorptielijnen over een bepaald spectraal gebied. Net zoals OCM gebruikt ook SSP parametertabellen voor een bepaalde standaardatmosfeer. En net zoals OCM legt ook SSP een direct verband tussen de gemiddelde lijnparameter voor een bepaalde hoogte en de concentratie van het absorberende gas op dezelfde hoogte. Daardoor bepaalt zowel OCM als ook SSP subkolomprofielen van het betreffende gas waarvan totale kolommen worden berekend. Dit is een van de belangrijkste verschillen met de meeste andere waterdampbepalingtechnieken, die gewoonlijk maar een enkele parameter voor de totale waterdampkolom gebruiken. In hoofdstuk 4 worden bepalingen van waterdampkolommen met behulp van synthetische spectra gedemonstreerd zonder rekening te houden met de ruis van het instrument en de instrumentfunctie. Aangetoond wordt dat in dit geval, en voor een enkele homogene laag, waterdampkolommen zeer nauwkeurig kunnen worden bepaald. Bovendien konden de basis SSP-parameters worden gebruikt om de spectrale structuur van een specifieke absorber in te schatten. Daardoor kon de vraag worden beantwoord of een eenvoudige numerieke spectrale middeling van de optische dikte kan worden gebruikt voor het berekenen van een gemiddelde transmissie. Het antwoord bepaalt tegelijk het gebied van toepasbaarheid voor niet-lineaire spectrale middelingtechnieken zoals OCM en SSP.

In hoofdstuk 5 wordt de SSP-techniek voor het bepalen van waterdampkolommen met behulp van GOME-metingen uiteengezet. De hierin beschreven overgang van synthetische bepalingen van waterdampkolommen van een enkele homogene laag naar subkolomprofielen over een aantal niet-homogene lagen omvat ook een spectraal gemiddelde bepaling van de contributie van enkelvoudig verstrooide fotonen op de metingen. Bovendien moest ook

hier de contributie van alle andere absorbers en de contributie van Rayleigh-verstrooiing op de totale extinctie worden berekend. Om van hoogteafhankelijke, gemiddelde parameters gebruik te kunnen maken moest eerst een zogenaamde 'dominante-laag'-benadering worden ontwikkeld. Deze is in appendix D meer in het detail beschreven. Het uiteindelijke resultaat van een SSP-toepassing op echte GOME-metingen zijn waterdamp subkolomprofielen die opgeteld de totale waterdampkolommen geven. Ook hier is van de 590 nm absorptieband gebruik gemaakt. De resultaten worden met gegevens van ECMWF, SSM/I en OCM berekeningen vergleken. Een gevoeligheidonderzoek naar de invloed van arosolen op de berekeningen concludeerde dat de verwachte fout op de berekende kolommen kleiner is dan 6

Net als voor de OCM-berekening van waterdampkolommen met behulp van GOME-metingen kon ook hier het effect op de resultaten door de invloed van wolken op de metingen niet worden afgeschat. Vergelijkingen tussen de SSP-resultaten en waarden die niet door wolken benvloed zijn (zoals de gegevens van SSM/I), laten zien dat wolkenfracties boven de 10

Het laatste hoofdstuk, hoofdstuk 6, beschrijft hoe beide middelingtechnieken, OCM en SSP, kunnen worden gebruikt voor het bepalen van waterdampprofielen. In mathematische termen betekent de vraagstelling van profielbepaling een regularisatie van een 'slecht' gedefinieerd probleem. Ruis en systematische fout worden met behulp van een regularisatietechniek gescheiden van de echte profielinformatie in de meting. Het bepalen van waterdampprofielen, zoals in dit proefschrift is uitgevoerd, is 'slecht' gedefinieerd; het aantal modelparameters overstijgt het aantal onafhankelijke informatie-eenheden in de meting. Om een specifieke profielregularisatie toe te passen wordt het aantal onafhankelijke profielinformatie-eenheden met behulp van een standaard singuliere-waardendecompositie-procedure bepaald. Daaruit kon geconcludeerd worden dat het maximum aantal van zeven onafhankelijke profielinformatiedelen uit synthetische spectra met behulp van de OCM middelingtechniek kan worden bepaald, afhankelijk van de kwantiteit en kwaliteit van de spectroscopische informatie die voor het berekenen van de absorptiespectra wordt gebruikt. De invloed van de spectroscopie op de resultaten werd bestudeerd door gebruik te maken van extra, door GOME gemeten, waterabsorptiebanden. Bijvoorbeeld door gebruik te maken van de absorptiebanden rond de 640 nm en 700 nm, maar ook door het gebruik te maken van verschillende lijnparametertabellen. Hoofdstuk 6 eindigt met een eerste poging om waterdampprofielen uit GOME-metingen te berekenen. Deze berekeningen bevatten in totaal 3 tot 4 onafhankelijke profielinformatie-eenheden.

Acknowledgement